Prediction of viscoelastic fluid flow in contractions.

Vallejo, Juan Pablo Aguayo

How to cite:

Vallejo, Juan Pablo Aguayo (2006) *Prediction of viscoelastic fluid flow in contractions..* thesis, Swansea University.
http://cronfa.swan.ac.uk/Record/cronfa42918

Prediction of Viscoelastic Fluid Flow in Contractions

by

JUAN PABLO AGUAYO VALLEJO
B.Sc., M.Sc.

THESIS SUBMITTED TO THE UNIVERSITY OF WALES
IN CANDIDATURE FOR THE DEGREE OF
PHILOSOPHIAE DOCTOR
INSTITUTE OF NON-NEWTONIAN FLUID MECHANICS

Department of Computer Science
University of Wales Swansea
JULY 2006

DEDICATION

To my incredible son, Fernando.
To my wife, Leticia.
To my niece, Mariana.
To my family.
To my mother, Aurora.
And, to my father, José.

I dedicate this work,
giving thanks to them and to
GOD.

Acknowledgements

I wish to express my sincere thanks to my supervisor Prof. M. F. Webster for his guidance and contributions during this study.

I acknowledge especially, the always friendly assistance, guidance and contributions of Dr. H. Tammadon-Jahromi.

Special thanks to Mr. B. Puangkird, Mr. J. Banaai, Mr. J. Harvey, Dr. H. Matallah, Dr. K. S. Sujata, Dr. F. Belblidia, Dr. I. J. Keshtiban and Dr. M. Aboubacar, friends from the Computer Science department.

I gratefully acknowledge the financial support from Schlumberger Cambridge Research, and give thanks to J. P. Crawshaw and collaborators.

Support from the ministry of education in Mexico (SEP) is also gratefully acknowledged.

I wish to express also, my thanks to Dr. O. Manero, Dr. E. Chavez, Prof. G. Maitland, Prof. T. N. Phillips, Prof. Malcolm Mackley and Prof. David Gethin.

- Muchas gracias -

Summary

This thesis is concerned with the numerical prediction of two-dimensional viscoelastic flows through channels, contractions and contraction/expansion geometries. In this study, a hybrid finite element/finite volume (*fe/fv*) scheme has been employed to solve the governing equations (mass and momentum conservation and constitutive model). The *fe/fv* algorithm employs a time-stepping procedure to evolve to steady-state.

A number of rheological models have been used to stimulate desired rheological behaviour. Amongst these are the recent Pom-Pom type models (in particular the eXtended or XPP variants), which are considered as a breakthrough due to their strong physical background and their ability to reproduce qualitatively the response of polymer melts in rheometrical flows. The Phan-Thien/Tanner (PTT) class of models is also employed to compare simulation results for concentrated systems with other models. In addition, for Oldroyd-B, PTT and XPP models, Boger-like response has been represented under increasing levels of solvent within the systems. This has addressed the issue capturing enhanced excess pressure-drops (*epd*) in contraction-type flows, phenomena that appear only in axisymmetric geometries not planar and has constituted a major challenge for to date numerical simulations. A further chapter is included where the recently introduced Bautista-Manero (BM) class of models is considered, to simulate worm-like micellar systems, this is, surfactants solutions. The worm-like micelles can provoke highly viscoelastic effects, similar to those apparent with polymer systems.

Vortex intensity decline is observed for fluids displaying extension softening in 4:1 contraction flows, in sharp and rounded corner. The suppressive effect of inertia in vortex cell-size is also gathered. Through a parameter adjustment in the SXPP model, larger stress and stretch values are observed for fluids with higher degree of extension-hardening and consequently, a reduction in numerical convergence has been found. Similar vortex dynamics trends are followed for fluids (PPT and XPP) with similar rheological properties. Excess pressure-drop over the corresponding Newtonian fluid is observed in small extent in contraction/expansion flows. Axisymmetric flows display much larger stress values than planar flows, which ultimately causes the increasing trend in *epd.* The response of the BM models in planar and contraction flows is gathered and an analytical solution for the steady Poiseuille flow is presented.

Contents

1 Introduction **1**

2 Governing Equations and Rheology **6**

2.1 Introduction 6
2.2 Rheometrical flows 7
2.2.1 Simple shear (Coutte) flow 8
2.2.2 Extensional flows 9
2.3 Constitutive models and basic equations 11
2.3.1 Maxwell and Oldroyd-B models 13
2.3.3 Phan-Thien/Tanner models 15
2.3.3 Pom-Pom models 16
2.3.3a Alternative Pom-Pom models 19
- Double eXtended Pom-Pom model *19*
- λ^2*XPP model* *20*
- Modified eXtended Pom-Pom model *20*
- Semi-linear SXPP variation *21*
2.4 Non-dimensional form 23
2.5 Material fuctions 25

3 Numerical Algorithms **31**

3.1 Introduction 31
3.1.1 Brief description of the Galerkin finite element method 34
3.1.2 Brief description of the finite volume method 35
3.2 Problem specification 37
3.3 Time discretisation 38
3.4 Spatial discretisation 41
3.4.1 Finite element scheme 42
3.4.2 Finite volume scheme 44

4 Pom-Pom Modelling for Planar Channel Flows **46**

4.1 Introduction 47
4.2 Plane poiseuille flow 50
4.2.1 Influence of increasing Weissenberg number 51
4.2.2 Influence of viscosity ratio 53
4.2.3 Influence of relaxation times ratio 54
4.2.4 Influence of the number of dangling arms 55
4.2.5 Influence of anisotropy 57
4.2.6 Pressure gradient and shear-rate 59
4.3 Conclusions 60

5 Pom-Pom Modelling for Contraction Flows **62**

5.1 Introduction 62
5.2 Problem specification 67
5.3 Numerical results 70
5.3.1 Mesh convergence and vortex dynamics 71
5.3.2 Stretch, stress and deformation-rate fields 76
5.3.3 Pressure-drop and an alternative Pom-Pom model 86
5.4 Conclusions 87

6 Influence of Extensional Viscosity on Pom-Pom Modelling **90**

6.1 Introduction 91

6.2 Problem specification 94

6.3 Numerical results 97

6.3.1 Pom-Pom solutions with q-variation ($\alpha = 0.15$) 97

6.3.1a Critical Weissenberg number and vortex dynamics 97

6.3.1b Centreline and downstream wall profiles 105

6.3.1c Stretch, stress and deformation-rate fields and pressure-drop 106

- Trends in λ *107*

- Trends in N_1, τ_{yy} *and* τ_{xy} *109*

- Trends in d_{xx}, d_{xy} *and pressure-drop 110*

6.3.2 Pom-Pom solutions with α-variation {0.15, 0.25, 0.5} 113

6.3.3 Extensional response across models: Pom-Pom and PTT 116

6.3.3a Match on severe strain-hardening: EPTT($\varepsilon_{PTT} = 0.02$), η_e and Tr 119

6.3.3b Match on modest strain-hardening: EPTT($\varepsilon_{PTT} = 0.25$), ηe and Tr 120

6.3.3c Fluid-(I)a and Fluid-(I)b: similarities and differences 124

6.4 Conclusions 126

7 Excess Pressure-Drop in Contraction and Expansion Flows for Boger Fluids **129**

7.1 Introduction 130

7.2 Problem specification 134

7.2.1 Pressure-drop calibration 137

7.3 Results and discussion 138

7.3.1 Excess pressure-drop in 4:1:4 and 4:1 geometries: Oldroyd-B model 138

7.3.1a Solution data – 4:1:4 flow 140

- Axisymmetric contraction/expansion flow; $\beta = 0.9$ *141*

- Pressure profiles at centreline and along the wall; axisymmetric, $\beta = 0.9$ *142*

- Pressure profiles at boundary wall; axisymmetric and planar, $\beta = 0.9$ *143*

- Planar and Axisymmetric stress and deformation-rate field data, $\beta = 0.9$ *146*

- Axisymmetric contraction/expansion flow; $\beta = 0.99$ *153*

- Pressure profiles at boundary wall; axisymmetric and planar, $\beta = 0.99$ *153*

- Stress and deformation-rate field data; $\beta = 0.99$ *155*

- Comments on pressure-gradient: planar and axisymmetric, $\beta = 1/9, 0.9, 0.99$ *157*

7.3.1b Comparison with 4:1 contraction flow results: $[p\text{-}p_{Newt}]$-data 159

7.3.2 Vortex development and structure (4:1:4 and 4:1) 162

7.3.3 Alternative model representations: 4:1:4 axisymmetric 165

7.3.3a *epd* for Old-B, LPTT(ε_{PTT}=0.15×10^{-4}), LPTT(ε_{PTT}=0.75×10^{-4}): β=0.9 166

7.3.3b *epd* for LPTT(ε_{PTT}=0.15×10^{-4}): β=0.95 166

7.3.3c *epd* for Old-B, LPTT, EPTT and SXPP models: high β=0.99 166

7.3.3d Very high β=0.999 predictions for Old-B 171

7.3.3e Location of upstream pressure sampling point – experimental *epd* 171

7.4 Conclusions 178

8 Bautista-Manero Models in Planar Flows 182

8.1 Introduction 182
8.2 Modified Bautista Manero model 184
8.3 Discussion on results 186
    8.3.1 Material functions for the MBM model 188
    8.3.2 Pressure-drop estimation in planar channels 191
    8.3.3 An analytical solution 198
    8.3.4 Pressure distributions 202
    8.3.5 Transient solutions 202
8.4 Conclusions 204

9 Concluding Remarks 206

Appendix I: More on the SXPP model 210

I.1 Non-Dimensional Stress Relations for Steady State for Channel Flow 210
I.2 Fully expanded equations for the SXPP model in planar flows 212
I.3 Fully expanded equations for the SXPP model in axisymmetric flows 213

Appendix II: Streamlines 217

List of figures 219

List of tables 225

List of publications 226

References 227

CHAPTER 1

Introduction

Computer modelling has been one of the most effective tools to predict fluid response in simple and complex flows. It has also been invaluable to realize phenomena occurring in these flows that otherwise would be difficult to observe. Computer Fluid Dynamics (CFD) has emerged as a fast evolving branch of physical science. Computational rheology may be considered as the part of CFD which deals with non-Newtonian (complex) fluids. However, there is still a serious need for improvement in numerical methods and simulation tools, in general.

On the other hand, new constitutive models are currently emerging to represent more complex systems, or those whose adequate description has been elusive. Among these, are polymer melts and micellar (surfactant) systems. The representation of branched polymer melt behaviour in both extensional and shear flows has been improved with the introduction of Pom-Pom models. In contrast the Bautista-Manero class of models are intended to predict the diverse phenomena typically exhibited by worm-like micellar systems.

Simulation of polymer melt flow is an issue that needs continuous attention. The relatively new Pom-Pom type of models, derived mostly from theoretical analysis, are considered as a breakthrough in rheology, due to their capacity to represent qualitatively some monodisperse polymeric systems. Polymer solutions and melts are essential in industry involving materials such as plastics, paint and ink.

Surfactant solutions, capable of grouping in extremely large worm-like micelles, can reproduce rheometrical response similar to that exhibited by polymeric systems. These micellar solutions are capable of rapid change in structure, and hence, in rheological behaviour [21]. One of their most important uses is in oil-recovery, where they serve as a transporting mechanism for ceramic particle packs, into the sand of the well to keep fractures open. Worm-like micellar solutions, presenting high viscosity, can deliver the particles and once in contact with oil, the surfactant agglomerates into different, much smaller, types of micelles. This produces a considerable decrease in viscosity and avoids blockage of the ceramic packing, allowing an easier flow of oil. To model these types of solutions, an equation that takes into consideration structure formation and destruction must be included within the analysis. Recently, the Bautista-Manero models have been introduced for this purpose. They are based on the Oldroyd-B model coupled with an additional equation for viscosity, containing parameters that govern structure formation.

For some problems, improvement in both directions of constitutive modelling and numerical methods, is more than *vital*. The proper representation of excess pressure-drop is one such problem. Such excessive drop in pressure is observed in axisymmetric contraction and contraction/expansion flows, for highly viscoelastic constant shear viscosity (Boger) fluids over that presented by an equivalent Newtonian fluid of similar viscosity. Interestingly in planar contraction flows no departure between Boger and Newtonian flows is gathered. As discussed in chapter 7, the modelling of such phenomena requires suitable rheological models, capable of predicting extremely large values of extensional viscosity, whilst keeping constant values of shear-viscosity. The Oldroyd-B model, one of the simplest [101], exhibits constant shear-viscosity, though the levels of extensional viscosity are without limit. Even if other models with severe, but bounded, strain-hardening are employed, attaining high levels of viscoelasticity may prove difficult. This drawbacks is commonly referred to as the "high-Weissenberg number" problem. That is, the simulation procedure, when starting from low levels of elasticity, cannot continue due to loss of numerical convergence. Failure often occurs at viscoelastic flow-settings which are not sufficiently high.

This study is concerned with the simulation of viscoelastic fluid flows in channel, contraction and contraction/expansion settings, for both planar and axisymmetric configurations. Emphasize is given to relate the flow response of the constitutive models employed to their behaviour in simple rheometrical flows. Material functions such as shear and extensional viscosity can help to gain some insight into the nature of the deformation occurring in complex flows, and this information may be used as a guide to select the material functions required to stimulate certain desired response. Contraction and contraction/expansion flows are present in many industrial processes, such as injection moulding. They have also become a standard benchmark for testing numerical procedures. In this area, vortex dynamics, pressure-drop and centreline velocity are common features reported in the literature (see for example references [2,3,41,74]). They are also subject of theoretical analysis such as that performed by Binding, which is one of the most important analysis in contraction flows that under certain conditions, can approximate extensional viscosity through pressure-drop data ([14,15,59,60]).

Finite element and finite volume algorithms are some of the most powerful tools in numerical simulation. They have proven their capability in a number of complex geometries in many areas, such as aircraft design, noise minimization in acoustics, chemical reactor engineering and computational rheology. Here, a method consisting in a hybrid formulation of finite element and finite volume analysis is employed to solve the range of flow-settings and configurations investigated.

In chapter 2, the basic equations of fluid mechanics and rheology are introduced. Rheometrical flows are explained, providing the basis for a large part of the analysis presented in this study. Focus is given to Pom-Pom models and their material functions, describing some of the numerous modifications proposed for this type model. Note that, further rheological plots are included in other chapters when more relevant. For example, the Bautista-Manero model is discussed in chapter 8.

Chapter 3 deals with the numerical procedure employed, the hybrid finite element/finite volume (*fe/fv*) method, explaining its basic equations. This method has been configured to well represent viscoelastic flow in complex geometries. The *fe/fv* algorithm has been generated upon considering the different mathematical nature of the momentum equation (balance of forces) and the constitutive models. It has proven its capability in solving problems with Oldroyd-B and Phan-Thien/Tanner models, amongst others (see [2,3,7,105]).

Planar flows are considered in chapter 4 for the Pom-Pom model. Pressure driven channel (Poiseuille) are simple flows that present no geometrical singularities. They represent pipe/channel sections in an extremely large number of fluid flow processes. In numerical studies, the solution of Poiseuille flow yields the necessary inlet boundary conditions for contraction configurations.

Flow through sharp-corner planar 4:1 contractions is analysed in chapter 5, for the single extended Pom-Pom model. Polymeric stress, stretch, deformation-rates and vortex dynamics are reported and related to the corresponding rheometrical functions. A comparison between two contrasting finite volume procedures is also included in chapters 4 and 5.

The effect of extensional viscosity in planar 4:1 contraction flows is observed in chapter 6, where different levels of viscosity are stimulated by adjusting molecular configuration parameters. To allow for higher Weissenberg numbers, the geometry is changed to rounded-corner instead of abrupt entry. Again, stress, vortex growth, deformation rates and stretch are reported and interpreted in terms of the material functional response. The effect of constitutive model singularities on the flow is also studied. A comparison between Pom-Pom and Phan-Thien/Tanner model solutions in contraction flows is provided, for model versions with similar rheometrical properties.

In chapter 7, the excess pressure-drop problem for Boger fluids is considered in detail, that is for strongly strain-hardening, constant shear-viscosity fluids of various solvent fractions. An analysis of flow through both planar and axisymmetric configurations of contraction and contraction/expansion geometries is presented. This study covers the relationship between the pressure-drop and material functions, stress and deformation-rates. Chapter 7 also shows the necessity to adopt other points of view in the flow-field. Centreline data does not provide clues of the complex phenomena that take place in the vicinity of the boundary walls, phenomena that relate the excess pressure-drop to stress development. Additionally, the necessary conditions are specified to obtain effective excess pressure-drops in terms of entry pressure and rate-of-dissipation.

The Bautista-Manero model is studied in chapter 8, including a sensitivity analysis over its rheological parameterisation. Vortex dynamics in 4:1 contractions are reported for two sets of parameters, matching corresponding Phan-Thien/Tanner fluids. A finite difference procedure is implemented to obtain pressure-drop values in steady Poiseuille flows. The analytical solution for this problem is also deducted, proving to be in excellent agreement with the finite differences procedure. Some transient results in planar channel are also provided.

CHAPTER 2

Governing Equations and Rheology

The basic equations of fluid mechanics are presented that allow the description of motion and conservation of mass. In addition, rheological models are considered, which relate surrounding forces with the internal response from the fluid. This fluid response is studied first for some simple flows, giving the tools to analyse more complex flow-settings. Models such as Maxwell, Oldroyd-B, Phan-Thien/Tanner, are briefly explained. A more recent type of constitutive equation, the Pom-Pom fluid and its response in rheometrical flows, is also considered in some detail.

2.1 Introduction

Rheology is part of physical science and is primarily concerned with the description of the flow of matter. Normally rheologists are interested in the flow of *complex* fluids. The term non-simple refers, here, to any fluid whose viscosity can vary even at fixed temperature and pressure. Water is the classical example of a simple fluid, and paint, which requires to be stirred before application to a surface, is one of the most common liquids with variable viscosity.

A special case of non-Newtonian fluids is that of viscoelastic materials. To explain the term viscoelastic, it is appropriate to define terms of what is called *solids* and *liquids.* If a material does not change its shape continuously when subjected to a given stress, it is referred to as a solid; whilst, if the change in shape is continuous (flow) with the applied stress, without consideration of how small the stress is, the material is termed a liquid (definitions from Barnes et al. [13]). Solid-like elasticity can often be modelled with Hooke's law and liquid-like viscous behaviour through Newton's law. Viscoelastic materials are those which exhibit both solid-like and liquid-like response. A material presents viscoelastic properties if, when after cessation of applied stress, the time of the fluid to adopt a rest state can be observed (measured).

All the research conducted in the present study uses continuum theory. This is an idealization of the description of matter, where distances between molecules and the change in properties due to these lengths are ignored, by looking at an arbitrary large number of molecules to average properties, and adequately represent the fluid *element.* To obtain the response of the element under deformation, energy, mass and force balances (*conservation laws*) are applied via differential and integral operators over small volumes, yet sufficiently large to satisfy the continuum assumption. This formulation is referred as *continuum mechanics.* Approximating the response of real materials in flow lies across the fields of both, rheology and continuum mechanics. The use of *constitutive relations* is a fundamental connection between these two areas. A constitutive equation contains specific information (internal stress, pressure, molecular extension) that relates to the behaviour of idealized fluids.

2.2 Rheometrical flows

The study of fluid behaviour in *simple flows* is regarded as essential in correlating the response of a fluid in more complex flow-settings. *Simple shear* and *extensional deformation* are examples of such simple *rheometrical* flows.

2.2.1 Simple shear flow

For a fluid contained between two (extremely large) parallel planes, separated by a gap h, with the upper-plate moving at constant velocity U, the force per unit area (stress σ) necessary to maintain the constant velocity of the plate is proportional to the velocity gradient (shear-rate $\dot{\gamma}$), i.e.

$$\sigma = \eta_s(\dot{\gamma})\dot{\gamma}. \tag{2.1}$$

A Newtonian fluid presents a constant coefficient of proportionality η_s (viscosity or *resistance to flow*). Under this type of flow, a volume of fluid is deformed, loosing its original shape. For example, if a cubic element of fluid is observed at any other time, the volume of fluid has internal angles that differ from 90° (see Figure 2.1).

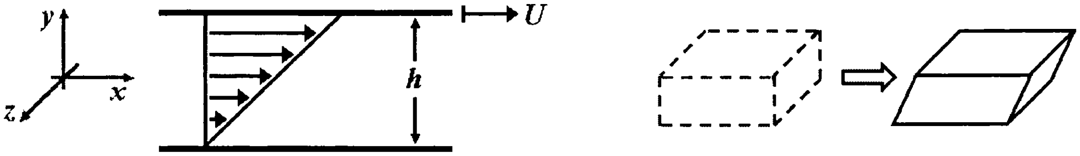

Figure 2.1. Schematic representation of simple shear flow.

The velocity field $\mathbf{u} = (u, v, w)$ and deformation-rate tensor $\mathbf{d}$ under simple shear deformation are given by:

$$\begin{aligned} u(y) &= \dot{\gamma} y \\ v &= 0 \\ w &= 0 \end{aligned} \qquad \text{and} \qquad \mathbf{d} = \frac{1}{2}\begin{bmatrix} 0 & \dot{\gamma} & 0 \\ \dot{\gamma} & 0 & 0 \\ 0 & 0 & 0 \end{bmatrix}. \tag{2.2}$$

Other properties that vary between Newtonian and non-Newtonian fluids are the first and second normal stress difference, N_1 and N_2, respectively. Their magnitudes are zero for Newtonian fluids, whilst for non-Newtonian fluids, their definitions are:

$$N_1(\dot{\gamma}) = \sigma_{xx} - \sigma_{yy} = \psi_1(\dot{\gamma})\dot{\gamma}^2, \tag{2.3}$$

$$N_2(\dot{\gamma}) = \sigma_{yy} - \sigma_{zz} = \psi_2(\dot{\gamma})\dot{\gamma}^2, \tag{2.4}$$

normally leading to relations,

$$N_1 > 0 \qquad \text{and} \qquad N_1 >> |N_2|. \tag{2.5}$$

2.2.2 Extensional flows

Considering in particular uniaxial deformation, in this flow the fluid volume is *stretched* in one particular direction, and due to incompressibility, compression takes place in the remaining axes. The fluid sample depicted in Figure 2.2 presents a cubic shape control volume at a chosen reference time (dotted line). After that and because of the stretching deformation, the fluid volume is extended in one (x) direction, whilst compression occurs along the remaining two (y, z) axes, to preserve the original volume.

The constant deformation-rate in this elongational flow is called the strain-rate $\dot{\varepsilon}$. In this case, there is no shear deformation, the fluid volume maintain essentially the same internal angles, but with modified lengths. The velocity field and deformation-rate tensor can be expressed as:

$$\begin{aligned} u(x) &= \dot{\varepsilon}\, x \\ v(y) &= -\tfrac{1}{2}\dot{\varepsilon}\, y \\ w(z) &= -\tfrac{1}{2}\dot{\varepsilon}\, z \end{aligned} \qquad \text{and} \qquad \mathbf{d} = \begin{bmatrix} \dot{\varepsilon} & 0 & 0 \\ 0 & -\tfrac{1}{2}\dot{\varepsilon} & 0 \\ 0 & 0 & -\tfrac{1}{2}\dot{\varepsilon} \end{bmatrix}. \tag{2.6}$$

The resistance, or extensional viscosity is then expressed through the relationship,

$$\sigma_{xx} - \sigma_{yy} = \sigma_{xx} - \sigma_{zz} = \eta_e(\dot{\varepsilon})\dot{\varepsilon}. \tag{2.7}$$

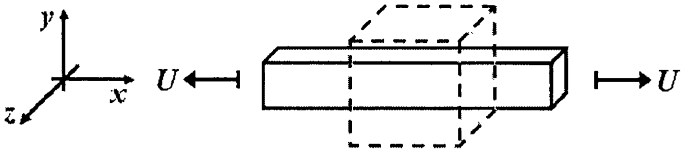

Figure 2.2. Schematic representation of uniaxial flow.

For a Newtonian fluid, η_e is constant under all strain-rates, and the following relation is satisfied:

$$\eta_e = 3\eta_s . \tag{2.8}$$

Additionally, it is expected that all fluids, including those with viscoelastic properties, satisfy (2.8) at low deformation-rates, that is,

$$\eta_e\left(\dot{\varepsilon} \to 0\right) = 3\eta_s\left(\dot{\gamma} \to 0\right). \tag{2.9}$$

Pure extensional deformation occurs in contraction and contraction/expansion flows along the centreline, while near the contraction a mix of shear and extension is present.

Trouton ratio (Tr) is defined as the quotient of extensional and shear viscosities. In order to relate $\dot{\gamma}$ and $\dot{\varepsilon}$ to evaluate shear and extensional viscosities, Jones et al. [52] proposed the following definition for the Trouton ratio:

$$Tr = \frac{\eta_e\left(\dot{\varepsilon}\right)}{\eta_s\left(\dot{\gamma} = \sqrt{3}\,\dot{\varepsilon}\right)}. \tag{2.10}$$

For inelastic fluids Tr is three for all values of $\dot{\varepsilon}$ and for viscoelastic this ratio is anticipated to satisfy

$$Tr\left(\dot{\varepsilon} \to 0\right) = 3. \tag{2.11}$$

In contraction flows, pure extension takes place along the centreline. In axisymmetric configurations this elongation is uniaxial, whilst in 2D planar flows, such deformation is that of *planar extension,* where the fluid sample is stretched in one direction and compressed in another, leaving one dimension without change. Equations governing planar extension are similar to those for uniaxial flow,

$$\eta_e = 4\eta_s \qquad (Newtonian), \tag{2.12}$$

$$\eta_e\left(\dot{\varepsilon} \to 0\right) = 4\eta_s\left(\dot{\gamma} \to 0\right) \qquad (viscoelastic), \tag{2.13}$$

$$Tr = \frac{\eta_e\left(\dot{\varepsilon}\right)}{\eta_s\left(\dot{\gamma} = 2\,\dot{\varepsilon}\right)}, \tag{2.14}$$

$$Tr\left(\dot{\varepsilon} \to 0\right) = 4 \qquad (viscoelastic). \tag{2.15}$$

A detailed discussion of these types of rheometrical flows can be found in Barnes et al. [13]. For more reference on these subjects and in rheology in general see additionally references [56,58,91].

2.3 Constitutive models and basic equations

The basic principle of mass conservation must be satisfied at every instant in the type of flow problems considered. This principle is expressed mathematically through the continuity equation (see [30,55,65]),

$$\frac{\partial \rho}{\partial t} + \nabla \cdot \left(\rho \mathbf{u}\right) = 0. \tag{2.16}$$

In equation (2.16), ρ is the fluid density, $\mathbf{u}$ the velocity vector and t, time. For incompressible flows, even if time-dependant, this reduces to

$$\nabla \cdot \mathbf{u} = 0. \tag{2.17}$$

Newton's second law of motion can be applied to a fluid element, this law states that the change of linear momentum in a system is equal to the sum of the forces acting upon it (also known as the principle of conservation of linear momentum). The forces acting on the system may be classified into two types: *body* forces acting on the volume of fluid, such as gravitational and electromagnetic forces, and *internal* forces, representing the friction between fluid molecules, affecting the fluid volume through its bounding surfaces. In differential form this is stated as [18]:

$$\rho\left(\frac{\partial \mathbf{u}}{\partial t}+\mathbf{u}\cdot\nabla\mathbf{u}\right)=-\nabla p+\nabla\cdot\mathbf{T}+\rho\mathbf{F}\,, \tag{2.18}$$

where p is the pressure, $\mathbf{T}$ is the stress without the hydrostatic contribution* and accounts for viscous/viscoelastic phenomena. Body forces, $\mathbf{F}$, are neglected since contributions from gravity are less significant than those from other forces such as pressure or stress.

As discussed above, Newtonian fluids present a constant viscosity in shear and elongational flows. Another characteristic is the instantaneous response to deformation. The general expression for the Newtonian (incompressible) model is,

$$\mathbf{T}=2\mu\mathbf{d}\,. \tag{2.19}$$

Substitution of equation (2.19) into (2.18) produces the Navier-Stokes equations. All flow settings in this study are assuming isothermal conditions and laminar flow. In equation (2.19) the deformation-rate tensor for general flows is defined as,

$$\mathbf{d}=\tfrac{1}{2}\left(\nabla\mathbf{u}+[\nabla\mathbf{u}]^{\mathrm{T}}\right). \tag{2.20}$$

Constitutive or rheological models must satisfy the following basic criteria to adequately represent fluid response from a mathematical point of view [65,88].

---

* Tensor $\boldsymbol{\sigma}$ is called the Cauchy stress tensor and is related to the tensor $\mathbf{T}$ by $\boldsymbol{\sigma}=-p\mathbf{I}+\mathbf{T}$, where $\mathbf{I}$ is the identity tensor.

- *Determination of stress*: stress for a viscoelastic fluid is determined by the history of the motion of that body.
- *Local action*: stress at any point in the fluid is determined by the history of the deformation of an arbitrarily small vicinity of fluid around that point.
- *Frame invariance*: The form of constitutive equations must be independent of the coordinate system.
- *Invariance under superposed rigid body motion*: the constitutive equations must reflect independence of absolute motion in space; that is, if the equations are correct, any rigid body motion imposed on the whole fluid must not affect the response of the material.

2.3.1 Maxwell and Oldroyd-B models

The Maxwell model [67] is considered as the first to model viscoelastic fluids via a differential system of equations. The one-dimensional form of this model is obtained by a combination of a Hookean spring and a Newtonian dashpot in series (see Barnes et al. [13]).

$$\mathbf{T}+\frac{\mu_0}{G_0}\frac{\partial}{\partial t}\mathbf{T}=2\mu_0\mathbf{d}\,, \tag{2.21}$$

where G_0 and μ_0 are the elastic modulus and the viscosity, respectively. The relaxation time for a Maxwell fluid is defined by $\lambda=\mu_0/G_0$.

Applying the principles stated above, this equation (2.21) can be re-written as the upper-convected Maxwell (UCM) model,

$$\mathbf{T}+\lambda\overset{\nabla}{\mathbf{T}}=2\mu_0\mathbf{d}\,, \tag{2.22}$$

or the lower-convected (LCM) form

$$\mathbf{T}+\lambda\overset{\vartriangle}{\mathbf{T}}=2\mu_0\mathbf{d}\,, \tag{2.23}$$

where for an arbitrary tensor $\mathbf{A}$, the upper- ($\overset{\triangledown}{\mathbf{A}}$) and lower- ($\overset{\vartriangle}{\mathbf{A}}$) convected derivatives are defined, respectively, as

$$\overset{\triangledown}{\mathbf{A}}=\frac{\partial}{\partial t}\mathbf{A}+\mathbf{u}\cdot\nabla\mathbf{A}-\left(\nabla\mathbf{u}\right)^{\mathrm{T}}\cdot\mathbf{A}-\mathbf{A}\cdot\nabla\mathbf{u}\,, \tag{2.24}$$

$$\overset{\vartriangle}{\mathbf{A}}=\frac{\partial}{\partial t}\mathbf{A}+\mathbf{u}\cdot\nabla\mathbf{A}+\left(\nabla\mathbf{u}\right)^{\mathrm{T}}\cdot\mathbf{A}+\mathbf{A}\cdot\nabla\mathbf{u}\,. \tag{2.25}$$

The Maxwell model does not contain a term to account for solvent presence (purely viscous component). To overcome this, a retardation time, λ_J, is introduced in equation (2.22):

$$\mathbf{T}+\lambda\overset{\triangledown}{\mathbf{T}}=2\mu_0\left(\mathbf{d}+\lambda_J\overset{\triangledown}{\mathbf{d}}\right). \tag{2.26}$$

Equation (2.26) is known as the Oldroyd-B model. However, numerical (discretisation) difficulties arise when dealing with the term $\overset{\triangledown}{\mathbf{d}}$, due to the presence of second-order derivatives of velocity and the model is split into two different equations, one for the polymeric component and other for the solvent, i.e.

$$\boldsymbol{\tau}+\lambda\overset{\triangledown}{\boldsymbol{\tau}}=2\mu_p\mathbf{d}\,, \tag{2.27}$$

$$\boldsymbol{\tau}_s=2\mu_s\mathbf{d}\,, \tag{2.28}$$

$$\mathbf{T}=\boldsymbol{\tau}_s+\boldsymbol{\tau}\,,\qquad \mu_0=\mu_s+\mu_p\,,\qquad \text{and}\qquad \lambda_J=\frac{\mu_s}{\mu_s+\mu_p}\lambda\,. \tag{2.29}$$

In equations (2.27)-(2.29) $\boldsymbol{\tau}$ and μ_p represent the stress and zero shear-rate viscosity contributions from the polymeric component, respectively; in a similar way, $\boldsymbol{\tau}_s$ and

μ_s are the contributions to the solvent part. The extensional viscosity predicted by Maxwell and Oldroyd-B models tends to infinity as the strain-rate approaches to $1/(2\lambda)$; additionally, the shear viscosity is constant at every shear-rate and the second normal stress difference is zero (except for the lower-convected Maxwell model which excessively predicts N_2).

A more reasonable prediction of N_2 is achieved by using the lower-convected operator mixed with the upper-convected derivative. The Johnson-Segalman model introduces an operator consisting of both convected derivatives. However, the extensional viscosity remains unbounded at low strain-rates. The model is:

$$\mathbf{T}+\lambda\overset{\square}{\mathbf{T}}=2\mu_0\mathbf{d}, \tag{2.30}$$

where the new operator is defined on an arbitrary tensor by:

$$\overset{\square}{\mathbf{A}}=\left(1-\tfrac{1}{2}\zeta\right)\overset{\nabla}{\mathbf{A}}+\tfrac{1}{2}\zeta\overset{\Delta}{\mathbf{A}}=\overset{\nabla}{\mathbf{A}}+\zeta\left(\mathbf{d}\cdot\boldsymbol{\tau}+\boldsymbol{\tau}\cdot\mathbf{d}\right). \tag{2.31}$$

ζ is the parameter controlling the proportion of the two derivatives, and generally its value lies within the interval $0\le\zeta\le 2$, where $N_2/N_1=-\tfrac{1}{2}\zeta$ and $\zeta=0.2$ yields reasonable N_2 (see reference [88]).

2.3.2 Phan-Thien/Tanner models

This prediction of unphysical values of extensional viscosity by the Johnson-Segalman model is corrected with the Phan-Thien/Tanner (PTT) constitutive equations. This model considers the creation and destruction of network junctions. Shear-thinning and extension-hardening/softening are predicted by this class of models which is expressed as:

$$f\left(\boldsymbol{\tau}\right)\mathbf{T}+\lambda\overset{\square}{\mathbf{T}}=2\mu_p\mathbf{d}, \tag{2.32}$$

the extra function $f(\boldsymbol{\tau})$ is,

$$f(\boldsymbol{\tau})=\begin{cases} e^{\left(\varepsilon_{PTT}\frac{\lambda}{\mu_p}tr(\boldsymbol{\tau})\right)} & \textit{exponential,} \\ 1+\varepsilon_{PTT}\dfrac{\lambda}{\mu_p}tr(\boldsymbol{\tau}) & \textit{linear.} \end{cases} \tag{2.33}$$

The linear form is extracted from a Taylor series expansion of the exponential form. Both forms predict shear-thinning behaviour and extension-hardening; strain-softening is anticipated for the exponential form, whilst the linear form displays sustained hardening, although, for some extreme values ($\varepsilon_{PTT}\rightarrow 1$) moderate softening is also observed.

2.3.3 Pom-Pom models

Rheological modelling of polymer melts has been proven to be a difficult task when the behaviour in both extensional and shear flows is sought. Constitutive models such as Phan-Thien/Tanner, Giesekus and Kaye-Bernstein-Kearsley-Zapas (K-BKZ) present difficulties to adequately model these polymer melt systems. Employing a modified multi-mode K-BKZ model, Mitsoulis et al. [70] were able to successfully predict vortex dynamics for low density polyethylene (LDPE) melts. Although PTT models can model a number of rheometrical responses in both shear and elongational flows, the parameter which governs the degree of extension-hardening, ε_{PTT}, controls simultaneously the shear-viscosity response (see Aboubacar et al. [2]).

The pom-pom model was introduced by McLeish and Larson [68] to represent the behaviour of idealized polymer molecules (see Figure 2.3), and as such, is considered as a major step forward. It takes into account the topological structure of the polymer chains, based on tube theory, in which polymer chains are represented by a backbone segment with the same number of dangling-arms (q) attached at both extremes of the backbone section. The drag that the melt exerts on these arms causes the backbone to stretch. The presence of branching points, slows down the reptation of the backbone. The ends of the arms are still able to move and the process of arm-retraction helps the molecule to free the polymer chain from the tube formed by its surroundings. This arm-retraction is triggered when the molecule reaches its maximum stretched state. The arms gradually free from the tube by diffusion. Once the arms have relaxed, the backbone can subsequently relax by moving the branch points. The extension of the polymer chain is represented by the parameter λ, which is the actual extension of the molecule scaled by its equilibrium length, $\lambda = L_{backbone} / L_{0_{backbone}}$.

A key aspect of this new type of model is the separation of relaxation times, one for stretch and other for orientation. The model consists of two decoupled equations, one for each relaxation process. In the original formulation of the model, the maximum backbone stretch (finite extensibility constraint) introduces a discontinuity in the gradient of the steady-state extensional viscosity. Two drawbacks remain however, the prediction of a zero second normal stress difference and the unboundedness of the backbone orientation equation at large strain-rates.

For the multimode approach proposed by Inkson et al. [51], the deficiencies of the Pom-Pom model are detected. By modifying the evolution equation for stretch (λ), Blackwell et al. [20] allowed branch point displacement. This had the effect of attenuating the non-smooth peaks in η_e [75], though discontinuities can be detected due to imposing a finite extension. To the same end Verbeeten et al. [96] introduced the eXtended Pom-Pom (XPP) model (see additionally [97]).

The evolution for the polymeric extra-stress in the single equation version of the XPP (SXPP) model is

$$\lambda_{0b}\overset{\nabla}{\boldsymbol{\tau}}+ f\left(\boldsymbol{\tau}\right)\boldsymbol{\tau}+\frac{\alpha}{G_0}\boldsymbol{\tau}\cdot\boldsymbol{\tau}+G_0\left[f\left(\boldsymbol{\tau}\right)-1\right]\mathbf{I}=2\lambda_{0b}G_0\mathbf{d}, \tag{2.34}$$

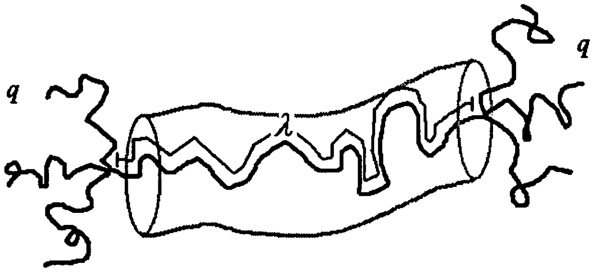

Figure 2.3. Idealized Pom-Pom molecule.

where

$$f(\boldsymbol{\tau})=2\frac{\lambda_{0b}}{\lambda_{0s}}\left(1-\frac{1}{\lambda}\right)e^{\nu(\lambda-1)}+\frac{1}{\lambda^2}\left(1-\frac{\alpha}{3G_0{}^2}tr(\boldsymbol{\tau}\cdot\boldsymbol{\tau})\right). \tag{2.35}$$

Here, $\lambda_{0b}>\lambda_{0s}$ are the orientation and backbone stretch relaxation times, respectively, and G_0 is the linear relaxation modulus. To account for a non-zero second normal stress difference (N_2), Verbeeten et al. [96] incorporated a Giesekus-type parameter, α. When the anisotropy parameter is set to zero, N_2 is also zero, and by increasing α, this stress difference becomes more significant. However, Clemeur et al. [37] have shown that 'numerical defects' appear for certain values of α and q (see section 6.3.2 for further details).

With the SXPP model, the backbone stretch is directly coupled to the extra-stress tensor

$$\lambda=\sqrt{1+\frac{1}{3G_0}\left|tr(\boldsymbol{\tau})\right|}. \tag{2.36}$$

In equation (2.36), the absolute value functions is not included in the original SXPP formulations. Here, this modification is necessary to increase the levels of attainable elasticity by avoiding problems when $tr(\boldsymbol{\tau})<0$ in complex flows (which may only happen numerically). The parameter ν in (2.35) was incorporated to remove the discontinuity in the derivative of the extensional viscosity. Its value is estimated by data-fitting and found to be inversely proportional to the number of arms (q). More precisely $\nu = 2/q$. Finally, the extra-stress tensor can be written as the sum of polymeric and solvent contributions, $\mathbf{T} = \boldsymbol{\tau} + 2\mu_s\mathbf{d}$.

Note that in the XPP model (2.34), the stress component τ_{zz} is not necessarily zero, even in 2D planar flows.

2.3.3a Alternative Pom-Pom models

- Double eXtended Pom-Pom model

The Double eXtended Pom-Pom (DXPP) model was introduced simultaneously with the SXPP version by Verbeeten et al. [96]. In this form, instead of the stress $\boldsymbol{\tau}$, the solution lies in terms of the orientation tensor $\mathbf{S}$. The model can be expressed as,

$$\boldsymbol{\tau} = G_0\left(3\lambda^2\mathbf{S} - \mathbf{I}\right), \tag{2.37}$$

$$\overset{\nabla}{\mathbf{S}} + f(\mathbf{S})\mathbf{S} + \frac{\alpha - 1}{3\lambda_{0b}\lambda^2}\mathbf{I} + \frac{3\alpha\lambda^2}{\lambda_{0b}}\mathbf{S}\cdot\mathbf{S} = \mathbf{0}, \tag{2.38}$$

$$\frac{\partial\lambda}{\partial t} + \mathbf{u}\cdot\nabla\lambda = \lambda\,\mathbf{d}{:}\mathbf{S} - \frac{(\lambda - 1)}{\lambda_{0s}}e^{\nu(\lambda-1)}, \tag{2.39}$$

$$f(\mathbf{S}) = 2\mathbf{d}{:}\mathbf{S} + \frac{1}{\lambda_{0b}\lambda^2}\left[1 - \alpha - 3\alpha\lambda^4 tr(\mathbf{S}\cdot\mathbf{S})\right], \tag{2.40}$$

where $\mathbf{I}$ is the identity tensor and as in the SXPP model, $\nu = 2/q$. In contrast to the SXPP model, here, the stretch is computed through a partial differential equation. Both single and double XPP models are expected to produce identical response as they adopt the same assumptions. The difference is that taking advantage of a traceless orientation tensor, the stretch equation may be obtained in a purely algebraic form through a single equation version of the Pom-Pom model.

- λ^2XPP model

In order to implement the XPP models within a spectral element solver, van Os and Phillips [76] proposed a modification for the extended Pom-Pom version. The resulting model consists in a combination of the equation for stress evolution and extra function of the SXPP version, equations (2.53) and (2.54), respectively, with the stretch equation from the Double eXtended Pom-Pom model in terms of the polymeric stress $\boldsymbol{\tau}$ instead of the orientation tensor $\mathbf{S}$ (see section 5.3.3 for further comments on this model).

$$\frac{\partial \lambda}{\partial t}+\mathbf{u}\cdot\nabla\lambda=\frac{1}{3\lambda G_0}\mathbf{d}:\boldsymbol{\tau}-\frac{\lambda-1}{\lambda_{0s}}e^{\nu(\lambda-1)}. \tag{2.41}$$

- Modified eXtended Pom-Pom model

Having implemented comments of van Meerveld [69] to improve the extended Pom-Pom version, Verbeeten et al. [98] presented a modification of the single XPP model by replacing the term $\left(1-1/\lambda\right)$ in equation (2.35) with $\left(1-1/\lambda^2\right)$. This modified eXtended Pom-Pom (mXPP) model is anticipated to avoid the non-physical values of stretch that may occur numerically. Stress evolution is given by equation (2.34), the absolute value in equation (2.36) for stretch is no longer necessary, and the extra function now becomes,

$$f\left(\boldsymbol{\tau}\right)=2\frac{\lambda_{0b}}{\lambda_{0s}}\left(1-\frac{1}{\lambda^2}\right)\mathrm{e}^{\nu(\lambda-1)}+\frac{1}{\lambda^2}\left(1-\frac{\alpha}{3{G_0}^2}tr\left(\boldsymbol{\tau}\cdot\boldsymbol{\tau}\right)\right). \tag{2.42}$$

However, as mentioned above, the parameter α can introduce analytical singularities into the solution for sufficiently large α and enough number of arms q. This singularities are present in both SXPP and mXPP models and is a direct consequence of the incorporation of the Giesekus-type parameter, α. In section 6.3.2 this issue is considered for the SXPP model and its influence on contraction flows; the same abnormal response is present also with the mXPP model as observed in

Figure 2.4, where a sudden increase in shear viscosity appears around a non-dimensional shear-rate of $\lambda_{0b}\dot{\gamma} \approx 13$.

- *Semi-linear SXPP variation*

In order to simplify the analysis, the anisotropy parameter, α, is set to zero. In doing so, the extra function for the SXPP model becomes a function of stretch (λ) alone, and indirectly, of the stress. Moreover, the terms eliminated by the zero α-value allow the extra function to be dependant on the trace of stress, $tr(\boldsymbol{\tau})$, which then, can be considered as a single variable.

By means of the chain rule of differentiation:

$$\frac{\partial f(\boldsymbol{\tau})}{\partial tr(\boldsymbol{\tau})} = \frac{\partial f(\boldsymbol{\tau})}{\partial \lambda}\frac{\partial \lambda}{\partial tr(\boldsymbol{\tau})}. \tag{2.43}$$

For notational simplicity, tr is taken to denote $tr(\boldsymbol{\tau})$ and an expansion in Taylor series provides,

$$f(tr) = f(tr \to 0) + \left.\frac{\partial f}{\partial \lambda}\frac{\partial \lambda}{\partial tr}\right|_{tr \to 0} tr + O\left(tr^2\right). \tag{2.44}$$

Obtaining the required derivatives:

$$\frac{\partial f}{\partial \lambda} = \frac{2}{\lambda^3}\left(\frac{\left[2\lambda(\lambda-1)+q\right]e^{\frac{2}{q}(\lambda-1)}\lambda_{0b}\lambda}{q\lambda_{0s}} - 1\right), \tag{2.45}$$

and

$$\frac{\partial \lambda}{\partial tr} = \frac{1}{6G_0\sqrt{1+\frac{1}{3G_0}tr}}, \tag{2.46}$$

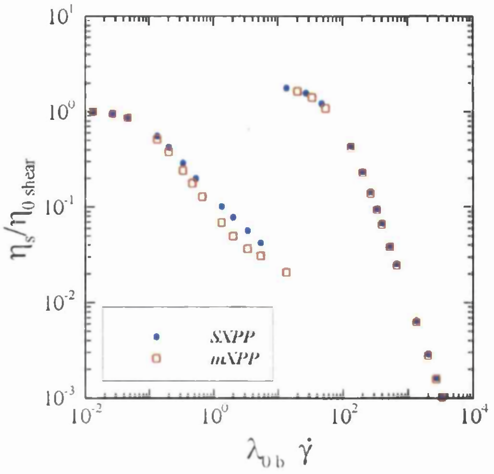

Figure 2.4. Singularities in shear viscosity for SXPP and mXPP models: $\beta = 0$, $\varepsilon = 1/3$, $q = 20$, $\alpha = 0.3$.

note that $tr(\boldsymbol{\tau}) \to 0 \Rightarrow \lambda \to 1$, so that,

$$\left.\frac{\partial f}{\partial \lambda}\right|_{\lambda \to 1} = 2\left(\frac{\lambda_{0b}}{\lambda_{0s}} - 1\right) \qquad \text{and} \qquad \left.\frac{\partial \lambda}{\partial\, tr}\right|_{tr \to 0} = \frac{1}{6G_0}. \tag{2.47}$$

Finally, the linearised extra function is gathered as:

$$f(\boldsymbol{\tau}) \approx 1 + \frac{1}{3G_0}\left(\frac{\lambda_{0b}}{\lambda_{0s}} - 1\right) tr(\boldsymbol{\tau}). \tag{2.48}$$

If equation (2.48) is used instead of (2.35), a semi-linear approximation for SXPP is obtained (where λ is still non-linear). It is unfortunate that the dependence on the number of arms (q) has been lost through the linearisation procedure. Here, the only parameter that controls the degree of extension hardening is $\lambda_{0b}/\lambda_{0s} = 1/\varepsilon$. Yet, this version can be used to emulate the response of the linear Phan-Thien/Tanner (LPTT) model.

If the same procedure is applied to the mXPP model, the resulting extra function is similar, being

$$f(\boldsymbol{\tau}) \approx 1+\frac{1}{3G_0}\left(2\frac{\lambda_{0b}}{\lambda_{0s}}-1\right)tr(\boldsymbol{\tau}). \tag{2.49}$$

2.4 Non-dimensional form

The governing equations are expressed in non-dimensional terms via length scale L (unit length), velocity scale U (twice the mean velocity[†] - taking a unit flowrate over half the channel), time scale L/U, and pressure and extra-stress scale of $\mu U/L$. The parameter $\mu=\mu_s+\mu_p$ is the total viscosity, made up from consistent viscosity fractions for solvent and solute.

In order to preserve similarity between the form of the non-dimensional Oldroyd-B and SXPP models, the relaxation time for the Pom-Pom model is chosen as λ_{0b}, with the polymeric viscosity defined as $\mu_p=G_0\lambda_{0b}$.

With these definitions, the group numbers and dimensionless parameters Re, We, β and ε are given by,

$$Re=\rho\frac{UL}{\mu},\qquad We=\lambda_{0b}\frac{U}{L},\qquad \beta=\frac{\mu_s}{\mu_s+\mu_p},\qquad \varepsilon=\frac{\lambda_{0s}}{\lambda_{0b}}, \tag{2.50}$$

the governing equations may be expressed in non-dimensional form[‡]

$$\nabla\cdot\mathbf{u}=0, \tag{2.51}$$

$$Re\left(\frac{\partial\mathbf{u}}{\partial t}+\mathbf{u}\cdot\nabla\mathbf{u}\right)=-\nabla p+\nabla\cdot\boldsymbol{\tau}+\beta\nabla^2\mathbf{u}, \tag{2.52}$$

[†] A unit flowrate would correspond naturally to a channel flow of one unit cross-width.

[‡] Equation (2.52) is the non-dimensional form of (2.18), see also equation (2.56).

$$We\overset{\nabla}{\boldsymbol{\tau}}+f(\boldsymbol{\tau})\boldsymbol{\tau}+\frac{\alpha We}{1-\beta}\boldsymbol{\tau}\cdot\boldsymbol{\tau}+\frac{1-\beta}{We}\left[f(\boldsymbol{\tau})-1\right]\mathbf{I}=2(1-\beta)\mathbf{d}, \tag{2.53}$$

where $f(\boldsymbol{\tau})$ and λ are given by

$$f(\boldsymbol{\tau})=\frac{2}{\varepsilon}\left(1-\frac{1}{\lambda}\right)e^{\nu(\lambda-1)}+\frac{1}{\lambda^2}\left[1-\frac{\alpha}{3}\left(\frac{We}{1-\beta}\right)^2 tr(\boldsymbol{\tau}\cdot\boldsymbol{\tau})\right], \tag{2.54}$$

and

$$\lambda=\sqrt{1+\frac{1}{3}\left(\frac{We}{1-\beta}\right)\left|tr(\boldsymbol{\tau})\right|}, \tag{2.55}$$

respectively. The extra-stress tensor, $\mathbf{T}$, is given by

$$\mathbf{T}=\boldsymbol{\tau}+2\beta\mathbf{d}. \tag{2.56}$$

Note, that the Oldroyd-B model corresponds to setting $\alpha=0$ and $f(\boldsymbol{\tau})=1$ in equation (2.53). If in addition, $\beta=0$ then the UCM model is obtained.

The solvent viscosity ratio, β, is an indirect measure of the concentration of polymer particles in the system. These polymer molecules are responsible for the viscoelastic nature of the system. As β tends to unity, the system is more diluted, while $\beta=0$ is the limiting state for polymer melts, where no solvent is present.

The parameter ε, the ratio of stretch to orientation relaxation times, is inversely proportional to the entanglement molecular weight of the backbone segments. Values of ε approaching unity correspond to molecules with relatively short backbone lengths but long arms to slow down the dynamics, and small values of ε correspond to highly entangled backbones.

The number of dangling arms q, has an effect on the entanglement of the system. A larger number of arms, is anticipated to cause an increase in backbone extension. In fact, for the original pom-pom formulation, the extensibility constraint is exactly equal to q.

2.5 Material functions

The Single eXtended Pom-Pom model represents a fluid displaying shear-thinning and extension-hardening/softening. The base set of parameters for the SXPP fluid used in this study are $\beta = 1/9$, $\varepsilon = 1/3$, $q = 2$ and $\alpha = 0.15$, corresponding to shear-thinning properties with low (weak) strain-hardening followed by softening. Apart from the base case, some variation in the number of arms (q) is also considered. Figure 2.5 presents the rheometrical response for the SXPP model covering a range of dangling-arms; the base case can be identified from the ($q = 2$)-line. At the selected solvent fraction, $\beta = 1/9$, increasing the number of arms has an insignificant impact upon the shear viscosity, and a major influence upon response in planar extensional flow. By increasing the number of arms from $q = 2$ to 15, the peak-value of the extensional viscosity rises about one decade in the log-log plot. This peak occurs at strain-rates between 10 to 20 units approximately for $q \geq 5$. Planar Trouton ratio (Figure 2.5b) reflects such an increase in the extensional viscosity, and combined with the shear-thinning response, this ratio (Tr) increases one decade to its extrema. Non-significant influence of the branching-arms upon the first normal stress coefficient, ψ_1, is detected up to moderate shear-rates ($\dot{\gamma} < 5$). For higher deformation-rates, increasing q results in larger values of ψ_1, that is, via a decrease in its rate-of-decline with $\dot{\gamma}$ (Figure 2.5c). The same adjustment in the number of arms (from 2 to 15) causes a significant increment in backbone stretch (λ), the parameter that governs molecular extension. This becomes apparent when deformation-rates exceed 0.5 units (Figure 2.5d).

Considering briefly the extensional response of the mXPP variant, some departure from the SXPP-η_e response can be observed over the decade of extension

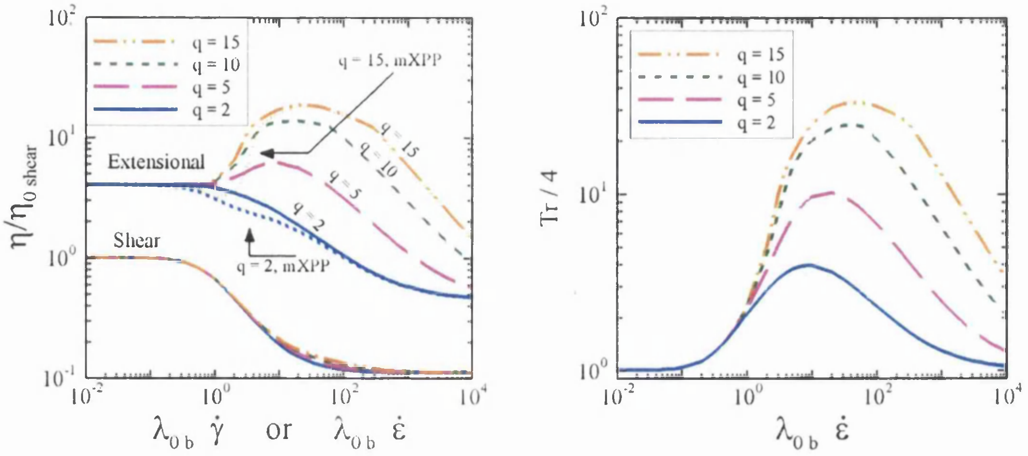

a) Shear and planar viscosity

b) Planar Trouton ratio

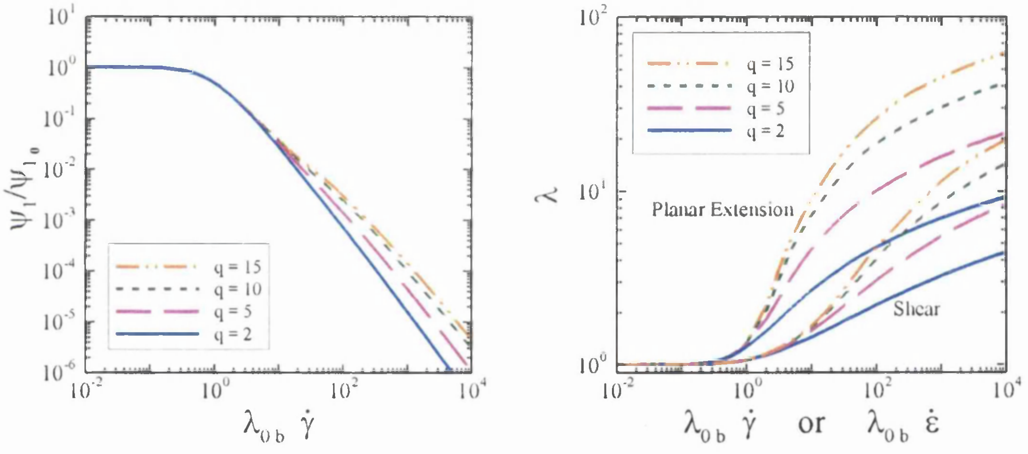

c) First normal stress coefficient

d) Backbone stretch

Figure 2.5. Shear and planar-extension response varying q; $\beta = 1/9$, $\varepsilon = 1/3$, $\alpha = 0.15$.

rates [10^0, 10^1]. For $q = 2$, the strain-softening begins before its SXPP counterpart; although some change in the rate-of-decline in η_e is detected at larger strain-rates, both model versions soften in a similar manner. For an increasing in the number of branched-arms q, the mXPP version displays extension-softening at moderate strain-rates, followed by rapid hardening that ultimately, follows the hardening/softening behaviour of the single Pom-Pom model variant. Transient evolution of viscosity and backbone stretch in shear and planar-extensional flows is depicted in Figure 2.6. The solution is generated from rest to the establishment of steady-state. Time is scaled with λ_{0b}; transient viscosities (planar and shear) are scaled with the steady-state shear viscosity at zero shear-rate, η_0. These variables (η_e, η_s, λ)[§] reach their steady-state values more rapidly for larger fixed values of deformation-rate ($\dot{\varepsilon}$ or $\dot{\gamma}$). In addition, backbone stretch for $\dot{\varepsilon}$ and $\dot{\gamma}$ at levels of 0.01 and 1, do not show any significant overshoot. Under increasing deformation-rate, the overshoot becomes more evident. This is also enhanced for systems with a larger number of arms to the molecule. Note that, in contraction and contraction/expansion flows, unsteady Lagrangian influences are not anticipated to be particularly significant in the contraction region, even if the fluid experiences large deformation-rates. This is due to the short residence times of fluid element/particles across the constriction region. In contrast, considering the exit channel in the contraction configuration, large shear-rates are developed above the boundary-wall and residence times are sufficient to allow steady-state values to be reached some units of length after the contraction. For example, in the case of the rounded corner 4:1 contraction with, the steady-state is reached at the wall around 3 units beyond the end of the corner (see Figure 6.9). These material functions were extracted from expressions for simple shear and planar extension transient flows, subject to initial condition $\tau_{ij}=0$ at $t=0$.

For transient shear flow:

$$
\begin{aligned}
\frac{\mathrm{d}}{\mathrm{d}t}\tau_{xx} &= 2\tau_{xy}\dot{\gamma} - \frac{\alpha}{\lambda_{0b}G_0}\left(\tau_{xx}{}^2+\tau_{xy}{}^2\right) - \frac{1}{\lambda_{0b}} f(\boldsymbol{\tau})\tau_{xx} - \frac{G_0}{\lambda_{0b}}\left[f(\boldsymbol{\tau})-1\right],\\
\frac{\mathrm{d}}{\mathrm{d}t}\tau_{yy} &= -\frac{\alpha}{\lambda_{0b}G_0}\left(\tau_{yy}{}^2+\tau_{xy}{}^2\right) - \frac{1}{\lambda_{0b}} f(\boldsymbol{\tau})\tau_{yy} - \frac{G_0}{\lambda_{0b}}\left[f(\boldsymbol{\tau})-1\right],\\
\frac{\mathrm{d}}{\mathrm{d}t}\tau_{zz} &= -\frac{\alpha}{\lambda_{0b}G_0}\tau_{zz}{}^2 - \frac{1}{\lambda_{0b}} f(\boldsymbol{\tau})\tau_{zz} - \frac{G_0}{\lambda_{0b}}\left[f(\boldsymbol{\tau})-1\right],\\
\frac{\mathrm{d}}{\mathrm{d}t}\tau_{xy} &= \tau_{yy}\dot{\gamma} - \frac{\alpha}{\lambda_{0b}G_0}\tau_{xy}\left(\tau_{xx}+\tau_{yy}\right) - \frac{1}{\lambda_{0b}} f(\boldsymbol{\tau})\tau_{xy} + G_0\dot{\gamma}.
\end{aligned}
\qquad (2.57)
$$

[§] In this study, extensional viscosity is represented by η_e in both planar and uniaxial extensional flows.

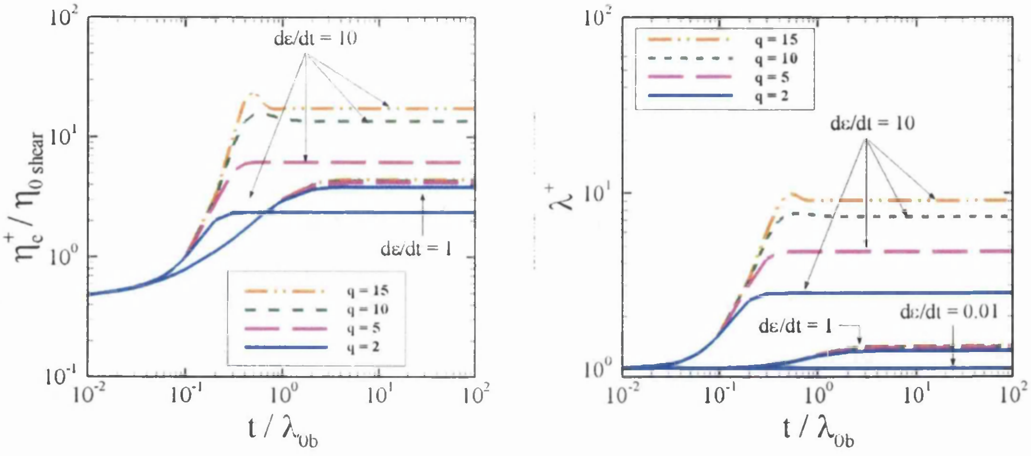

a) Transient planar extensional viscosity *b) Backbone stretch in planar extension*

c) Transient shear viscosity *d) Backbone stretch in shear flow*

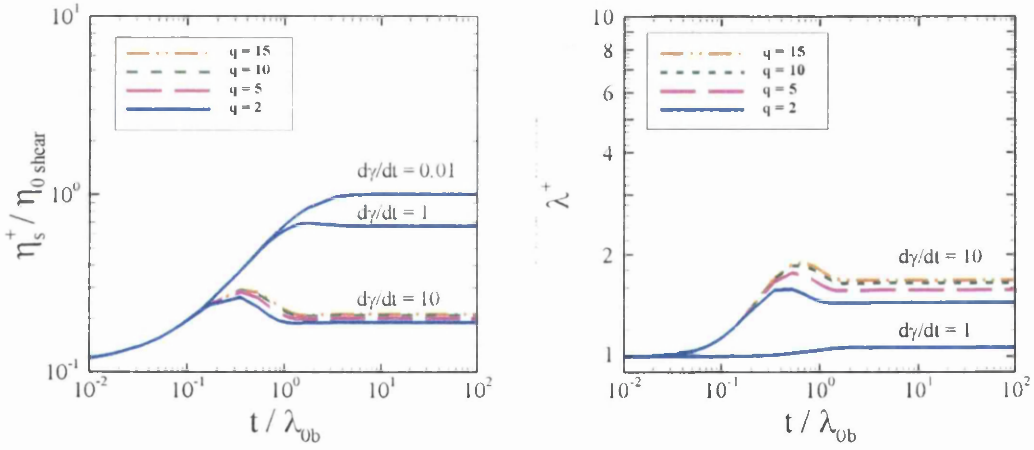

Figure 2.6. Transient shear and planar-extension response varying q; $\beta = 1/9$, $\varepsilon = 1/3$, $\alpha = 0.15$.

And for transient planar elongation:

$$
\begin{aligned}
\frac{\mathrm{d}}{\mathrm{d}t}\tau_{xx} &= 2\dot{\varepsilon}\left(\tau_{xx}+G_0\right)-\frac{\alpha}{\lambda_{0b}G_0}\tau_{xx}^{\;2}-\frac{1}{\lambda_{0b}}f\left(\boldsymbol{\tau}\right)\tau_{xx}-\frac{G_0}{\lambda_{0b}}\left[f\left(\boldsymbol{\tau}\right)-1\right],\\
\frac{\mathrm{d}}{\mathrm{d}t}\tau_{yy} &= -2\dot{\varepsilon}\left(\tau_{yy}+G_0\right)-\frac{\alpha}{\lambda_{0b}G_0}\tau_{yy}^{\;2}-\frac{1}{\lambda_{0b}}f\left(\boldsymbol{\tau}\right)\tau_{yy}-\frac{G_0}{\lambda_{0b}}\left[f\left(\boldsymbol{\tau}\right)-1\right],\\
\frac{\mathrm{d}}{\mathrm{d}t}\tau_{zz} &= -\frac{\alpha}{\lambda_{0b}G_0}\tau_{zz}^{\;2}-\frac{1}{\lambda_{0b}}f\left(\boldsymbol{\tau}\right)\tau_{zz}-\frac{G_0}{\lambda_{0b}}\left[f\left(\boldsymbol{\tau}\right)-1\right].
\end{aligned}
\tag{2.58}
$$

The dynamic response is the solution through time of systems (2.57) and (2.58) at any fixed deformation-rate $\dot{\gamma}$ or $\dot{\varepsilon}$. Standard numerical procedures such as Euler or Runge-Kutta methods can be employed to solve these systems of ordinary differential equations. Transient viscosity is gathered from the solution of (2.57) or (2.58), and applying equations (2.1) or (2.7) (depending upon whether under shear or elongational deformation). The steady-state at each deformation-rate is obtained by taking the transient solution at sufficiently large times.

To conclude this chapter, Table 2.1 displays the expression for material functions for some common models. The functions for the SXPP model were obtained by setting $\alpha = 0$, to facilitate the analysis. Additionally, Table 2.2 and Figure 2.7 summaries the influence of the non-dimensional variables on SXPP rheology, under the setting of zero anisotropy.

Table 2.1. Material function expressions of some common models

	$\eta_{s(\dot{\gamma})}$	$\psi_{1(\dot{\gamma})}$	$\eta_{e(\dot{\varepsilon})}$
UCM	μ_0	$2\mu_0\lambda$	$\frac{2\mu_0}{1-2\lambda\dot{\varepsilon}}+\frac{\mu_0}{1+\lambda\dot{\varepsilon}}$
Oldroyd-B	μ_0	$2\mu_0(\lambda-\lambda_J)$	$\frac{2\mu_p}{1-2\lambda\dot{\varepsilon}}+\frac{\mu_p}{1+\lambda\dot{\varepsilon}}+3\mu_s$
SXPP	$\frac{\mathrm{G}_0\,\lambda_{0\mathrm{b}}}{f(\boldsymbol{\tau})^2}+\mu_{\mathrm{s}}$	$\frac{2\,\lambda_{0\mathrm{b}}{}^2\,\mathrm{G}_0}{f(\boldsymbol{\tau})^3}$	$\frac{3\,\mathrm{G}_0}{\left[\lambda_{0\mathrm{b}}\,\dot{\varepsilon}+f(\boldsymbol{\tau})\right]\left[-2\,\lambda_{0\mathrm{b}}\,\dot{\varepsilon}+f(\boldsymbol{\tau})\right]}+3\mu_{\mathrm{s}}$

Table 2.2. Influence of increasing non-dimensional numbers in shear and extensional viscosity

Increasing in:	η_S	η_e
$\beta = \mu_S/\mu_T$	• Declining of thinning level value of the second plateau increases	• Major drop in level of softening • value of the second plateau increases
$\varepsilon = \lambda_{0S}/\lambda_{0b}$	• Slight increase in thinning region	• Visible effect in hardening region, not as significant as for q
q	• No significant effect	• Strong increase in the hardening level

β-variation

ε-variation

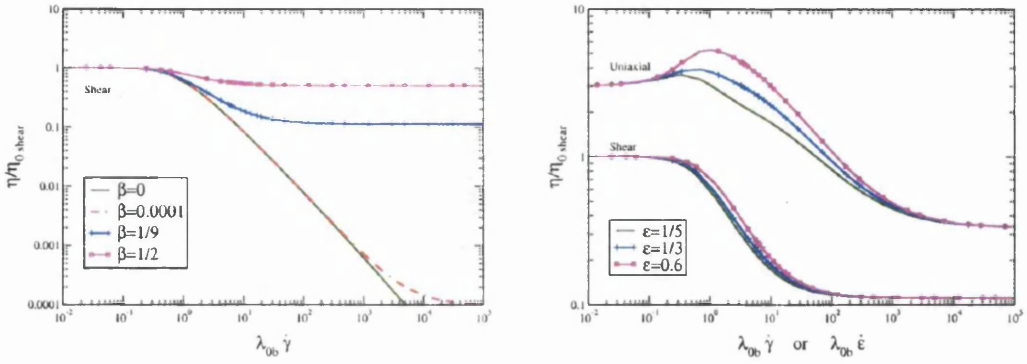

a) Shear viscosity

b) Shear and uniaxial viscosity

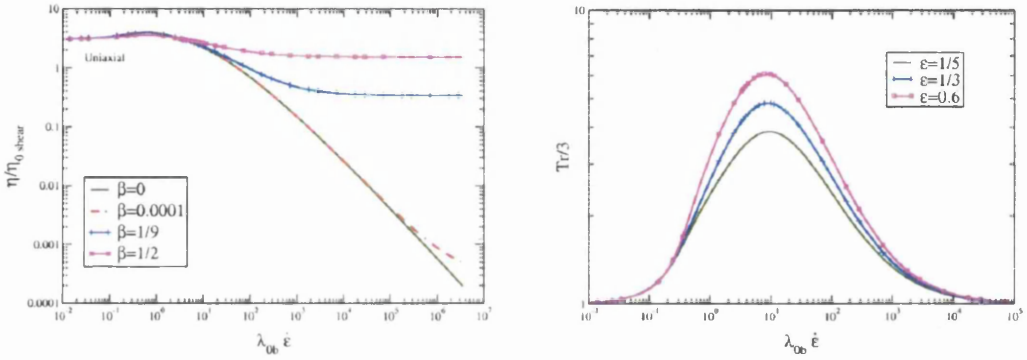

c) Uniaxial viscosity

d) Uniaxial Trouton ratio

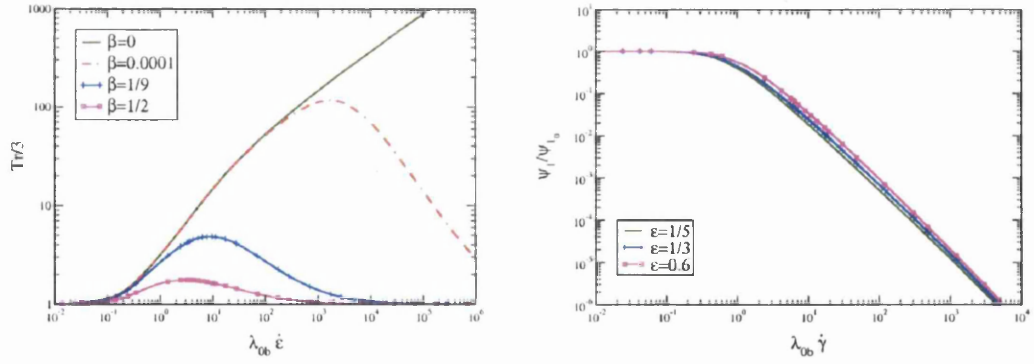

e) Uniaxial Trouton ratio

f) First normal stress coefficient

Figure 2.7. Influence of β and ε on SXPP material functions: $\beta = 1/9$, $\varepsilon = 1/3$, $q = 2$, $\alpha = 0$.

CHAPTER 3

Numerical Algorithms*

The numerical procedure employed in this study is a hybrid method consisting of a finite element method (FEM) for the momentum and continuity equations and the finite volume method (FVM) for the constitutive law. Both methods had been applied separately with success for a wide variety of computational fluid dynamics (CFD) problems. This hybrid implementation takes advantages of features of both algorithms to produce a stable high-order finite element/finite volume (*fe/fv*) scheme.

3.1 Introduction

Numerical modelling has been improved extraordinary with modern developments in computer processors. Nowadays, systems consisting in very large number of equations can be solved within minutes. In CFD modelling, three numerical methodologies have been applied successfully to a range of flow-problems involving simple and complex flow domains. These methods are typically, finite difference, finite element and finite volume schemes (for viscoelastic flows refer to

---

* The basic numerical algorithms used in this thesis are those developed previously in the Institute of Non-Newtonian Fluid Mechanics (INNFM), Swansea group. These have been extended through incorporating the associated constitutive equations discussed in this study.

[11,77,101]). In the field of computational rheology, these three methods have been adapted to cope with a variety of constitutive law for stress, and have proven to be an invaluable tool for the analysis of flow-phenomena.

The finite difference method was the first to emerge, and although it is generally simple to implement, dealing with complex geometries and boundary conditions can lead to a lost in accuracy and a much more difficult discretisation scheme. This has given rise to the need for conformal mapping. FE and FV methods are commonly used for non-uniform grids, allowing simulation of non-simple flow geometries with a reduced number of equations when compared to standard finite differences schemes.

FEM and FVM are commonly referred to as the same type of algorithm. In both, the problem domain is divided into a non-overlapping finite number of sub-domains. The model equations are applied over each finite element or finite volume, and solution unknowns are approximated by 'shape' functions and nodal values over these sub-domains. Low order polynomials are commonly used for this purpose in FEM and FVM[†]. The equations describing the problem are producted with weighting functions and integrated over the domain, producing a system of algebraic equations where the nodal solution of unknowns is sought.

The hybrid scheme employed in this study consists in a combination of FEM and FVM procedures. The finite element approach is used to solve the momentum equation, with a time discretisation via a semi-implicit formulation on a Taylor-Galerkin procedure. Incompressibility is enforced through a fractional-staged procedure termed pressure-correction, producing a three-staged algorithm. A finite volume technique is used for spatial discretisation of the constitutive equation. The finite volume grid is formed via a partition of each finite element triangle by connecting the mid-side nodes of that element. Accuracy is achieved through a consistent treatment of the flux and source terms of the constitutive equation. Flux

---

[†] Using high-order polynomials introduces the complementary spectral element method.

and source residuals are distributed to the vertices of each finite volume control cell through the use of fluctuation distribution (FD) schemes. Stability in terms of attainment of high Weissenberg number is improved via the use of a median-dual-cell (MDC) approach for evaluation of flux and source terms.

The basis of the finite element implementation used is the Taylor-Galerkin/pressure-correction (TGPC) algorithm, proposed by Townsend and Webster [94] to simulate the flow of viscous and viscoelastic fluids. The main idea is to solve the hyperbolic-type constitutive equation with an algorithm suitable for this kind task. As the FVM has often been found superior to the FEM for this purpose, the present hybrid finite element/finite volume algorithm has appeared. Donea [43] was the first to work on Taylor-Galerkin schemes for convection-diffusion problems, with a discretisation based upon Euler, leapfrog and Crank-Nicolson time-stepping procedures. Temam [93] and Chorin [33] proposed the earliest forms of pressure-correction schemes for viscous incompressible flows. Second-order pressure-correction versions were introduced by van Kan [53], through a finite difference discretisation and Crank-Nicolson time-splitting. The combination of these ideas under a finite element discretisation is the basis of the algorithm proposed by Townsend and Webster [94]. Hawken et al. [47] improved upon the initial explicit time-discretisation proposed, advancing to a semi-implicit form for viscous flows. Carew et al. [28] and Baloch et al. [12] took these basic implementations forward to cover the viscoelastic case.

The main aspects of the Galerkin finite element (see [35,40,111] for example) are discussed below. Also, an outline of the finite volume [30,49] procedure is considered.

In chapters 4 and 5, solutions obtained through the *fe/fv* algorithm for the flow in channels and contractions are compared against data computed with a semi-Lagrangian finite volume (SLFV) method. This is a pure finite volume scheme implemented by the research group of fluid dynamics of Cardiff University. Detail of this method can be found in references [1,81].

3.1.1 Brief description of the Galerkin finite element method

Briefly, the finite element method consists in the splitting of the domain (geometry) over which the problem is to be solved, into a set of finite elements (mesh). This geometry can be simple or complex. Consider for example the following time independent Poisson equation,

$$\frac{\partial^2 u}{\partial x^2} = f(x). \tag{3.1}$$

The unknown solution variables are interpolated by suitable functions, typically of polynomial type of first or second order. The resulting problem residuals are weighted and applied to each of the finite elements that contributes to the original domain.

$$u(x) = \sum_{i}^{nt} \phi_i(x) u_i, \tag{3.2}$$

where nt is the total number of nodes in an element, $\phi_i(x)$ the trial functions, u_i, unknown solution nodal values. With $w_j(x)$ weighting functions, substitution of (3.2) in (3.1) yields

$$\int_{\Omega_e} \frac{\partial^2}{\partial x^2}\left[\phi_i(x) u_i\right] w_j(x) \mathrm{d}\Omega_e = \int_{\Omega_e} f(x) w_j(x) \mathrm{d}\Omega_e. \tag{3.3}$$

In the case of the Galerkin method, weighting functions are chosen from the same space of functions as the trial functions, that is $w_j(x) = \phi_j(x)$. Then, by integration by parts,

$$\left.\frac{\partial \phi_{i(x)}}{\partial x} \phi_{j(x)}\right|_{\Gamma_e} - u_i \int_{\Omega_e} \frac{\partial \phi_{i(x)}}{\partial x} \frac{\partial \phi_{j(x)}}{\partial x} \mathrm{d}\Omega_e = \int_{\Omega_e} f_{(x)} \phi_{j(x)} \,\mathrm{d}\Omega_e. \tag{3.4}$$

Summing all such elemental contributions assembles the system over the domain ($\Omega = \sum_{e} \Omega_e$). The term evaluated on the boundary (Γ_e) of the element cancels out on interior elements and is set to zero when the solution values are known at the outer domain boundary. This is the case in the present study, where typically the velocity is imposed at the boundaries.

In matrix notation, the full system of equations emerging from (3.4) can be expressed as

$$\mathbf{K}\mathbf{u} = \mathbf{b}, \tag{3.5}$$

the column-matrix $\mathbf{u}$ contains the nodal values, $\mathbf{K}$ and $\mathbf{b}$ are defined as

$$K_{ij} = \int_{\Omega} \frac{\partial \phi_i(x)}{\partial x} \frac{\partial \phi_j(x)}{\partial x} \mathrm{d}\Omega, \qquad b_j = \int_{\Omega} f(x) \phi_j(x) \mathrm{d}\Omega, \tag{3.6}$$

which can be evaluated either analytically or numerically. The assembly of all single elements into a total system must take into account the specified boundary conditions. For instance, as known values of the solution are imposed in this example, nodal values at both sides of the domain (boundary Γ) are then specified and can be substituted directly in the corresponding positions for $\mathbf{K}$, $\mathbf{b}$ and eliminated from $\mathbf{u}$. Solution of problem (3.5) requires algebraic procedures. Depending on the number of elements/nodes and the complexity of the shape functions, these procedures can be either of direct or iterative nature.

3.1.2 Brief description of the finite volume method

With the finite volume technique, instead of solving the differential expression for a conservation law, an integral form is considered instead. This is the case for the differential constitutive model, which is integrated over an *fv*-subdomain. This can be considered as a subclass of the finite element procedure with weighting functions set to unity, $w(x) = 1$. Considering a general conservation law

$$\frac{\partial}{\partial t}\int_{\Omega}\varsigma\,\mathrm{d}\Omega+\int_{\Gamma}\mathbf{f}\cdot\mathbf{n}\,\mathrm{d}\Gamma=\int_{\Omega}\mathbf{q}\,\mathrm{d}\Omega, \tag{3.7}$$

where ς is the quantity to 'conserved' such as mass, momentum or energy, $\mathbf{f}$ is the flux that can be separated in convective and diffusive parts, $\mathbf{n}$ an outward unit vector normal to the surface Γ that encloses the volume Ω and $\mathbf{q}$, the source terms or body forces. Mean values in a *fv*-cell are defined as

$$\varsigma_i=\frac{1}{|\Omega_i|}\int_{\Omega_i}\varsigma\,\mathrm{d}\Omega_i. \tag{3.8}$$

Then, applying (3.7) on a single finite volume, with mean values ς_i and q_i, one gathers

$$\frac{\partial}{\partial t}\varsigma_i+\frac{1}{|\Omega_i|}\sum_k\int_{\Gamma_k}\mathbf{f}\cdot\mathbf{n}_k\mathrm{d}\Gamma_k=q_i, \tag{3.9}$$

where k is the number of 'faces' of the *fv*-subcell and Γ_k is the area of those faces. One advantage of the FVM is that the variables in integral form are naturally conserved over the entire domain and on each individual *fv*-cell.

Using numerical integration procedures, the mean values can be approximated,

$$\int_{\Omega_i}\varsigma(x)\,\mathrm{d}\Omega_i\approx\sum_{i=0}^{nc}\varphi_i\varsigma_i(x), \tag{3.10}$$

where $\varphi_i\geq 0$ are weights, and nc is the number of nodes of the integration procedure. Surface integrals are computed as

$$\int_{\Gamma_k}\mathbf{f}\cdot\mathbf{n}_k\mathrm{d}\Gamma_k\approx\sum_k F_k. \tag{3.11}$$

In this expression, F_k is an approximation of $\mathbf{f}\cdot\mathbf{n}_k$ and k is again the number of faces of the *fv*-cell.

The use of all such approximations over each finite volume, with their assembly to represent the total domain, constitute the discretised form of equation (3.7). This generates the system of algebraic equations to be solved, as similar to that for the finite element approach, given in equation (3.5).

3.2 Problem specification

The model for the isothermal incompressible flow of a viscoelastic fluid with no volumetric forces is specified by the following expressions for continuity and momentum (non-dimensional form extracted from chapter 2)

$$\nabla \cdot \mathbf{u} = 0, \tag{2.51}$$

$$Re\left(\frac{\partial \mathbf{u}}{\partial t} + \mathbf{u} \cdot \nabla \mathbf{u}\right) = -\nabla p + \nabla \cdot \boldsymbol{\tau} + \beta \nabla^2 \mathbf{u}. \tag{2.52}$$

In addition, a constitutive equation must be included to account for the response of the particular fluid. The non-dimensional form of the Oldroyd-B model is

$$We\overset{\nabla}{\boldsymbol{\tau}} + \boldsymbol{\tau} = 2(1-\beta)\mathbf{d}. \tag{3.12}$$

If other models are specified, then (3.12) is replaced by the selected model equations. For example, in the particular case of the Single eXtended Pom-Pom (SXPP) model, equations (2.53)-(2.55) are used instead.

Appropriate boundary and initial conditions must be applied in order to correctly specify the flow problem in question. In general, the boundary conditions may be of a mixed form,

$$\mathbf{u}_{\Gamma_1} = \mathbf{g}_1, \qquad (\boldsymbol{\sigma} \cdot \mathbf{n})_{\Gamma_2} = \mathbf{g}_2, \qquad \boldsymbol{\tau}_{\Gamma_3} = \mathbf{g}_3, \tag{3.13}$$

where $\Gamma_{k=1,2,3}$ are non-overlapping subsection of the boundary Γ enclosing the domain Ω, $\boldsymbol{\sigma}$ is the Cauchy stress tensor (see section 2.3) and $\mathbf{n}$ is the outward unit normal vector to the boundary. In this study only 2D flows are considered, specifying no-slip conditions (vanishing velocity) at the boundary-walls. For domain inlet and exit, velocity profiles for the Oldroyd-B model are imposed, providing sufficiently large inlet/exit channel sections are established for fully-developed flow to apply. In addition, inlet stress conditions must be imposed.

Simulation at low elasticity (or Weissenberg) levels (typically $We = 0.1$) starts from some initial state in all variables, typically rest. Then, continuation in We number is employed to evolve to higher levels of elasticity, using the solution at the previous level as the initial condition for the next We-step. These initial conditions can be expressed as

$$\mathbf{u}_{(\mathbf{x},t_0)} = \mathbf{u}^0{}_{(\mathbf{x})}, \qquad \nabla \cdot \mathbf{u}^0 = 0, \qquad \mathbf{T}_{(\mathbf{x},t_0)} = \mathbf{T}^0{}_{(\mathbf{x})}, \tag{3.14}$$

where the superscript "0" indicates evaluation at time $t = t_0$.

3.3 Time discretisation

The basis of the time-stepping procedure is a Taylor series expansion. Improved accuracy may be gained through a two-step Lax-Wendroff approach, which may be explained assuming a one-dimensional problem of the form,

$$\frac{\partial u}{\partial t} + \frac{\partial}{\partial x} f(u) = 0. \tag{3.15}$$

Here, x and t are independent spatial/temporal variables, and $u(x,t)$ is a scalar field dependent solution variable.

The two-step Lax-Wendroff procedure, over time-step $t \in \left[t^n, t^{n+\frac{1}{2}}\right]$ and $t \in \left[t^n, t^{n+1}\right]$, is

$$u^{n+\frac{1}{2}} = u^n + \tfrac{1}{2}\Delta t\left[-\frac{\partial}{\partial x}f(u)\right]^n, \tag{3.16}$$

$$u^{n+1} = u^n + \tfrac{1}{2}\Delta t\left[-\frac{\partial}{\partial x}f(u)\right]^{n+\frac{1}{2}}. \tag{3.17}$$

In these equations and in the rest of the chapter, the terms with n indicate evaluation at a specific time step.

Following the ideas of van Kan [52], an approximation of $O(\Delta t^2)$, may be derived by applying these predictor-(3.16)/corrector-(3.17) equations to the momentum equation in non-dimensional form, see equation (2.52)[‡]. This yields,

- *step* 1: $$\mathbf{u}^{n+\frac{1}{2}} - \mathbf{u}^n = \frac{\Delta t}{2\,Re}\left[\nabla\cdot(\boldsymbol{\tau} + 2\beta\mathbf{d}) - Re\,\mathbf{u}\cdot\nabla\mathbf{u} - \nabla p\right]^n, \tag{3.18}$$

- *step* 2: $$\mathbf{u}^{n+1} - \mathbf{u}^n = \frac{\Delta t}{Re}\left[\nabla\cdot(\boldsymbol{\tau} + 2\beta\mathbf{d}) - Re\,\mathbf{u}\cdot\nabla\mathbf{u} - \nabla p\right]^{n+\frac{1}{2}}. \tag{3.19}$$

The pressure term ($\nabla p^{n+\frac{1}{2}}$) in equation (3.19) is approximated by

$$p^{n+\frac{1}{2}} = \theta p^{n+1} + (1-\theta)\,p^n, \tag{3.20}$$

If in equation (3.20), the weighting parameter is set to $\theta = \frac{1}{2}$ (Crank-Nicolson) the temporal discretisation error is $O(\Delta t^2)$; otherwise, the error is $O(\Delta t)$. Equation (3.19) can be re-written in the form,

$$\mathbf{u}^{n+1} - \mathbf{u}^n = \frac{\Delta t}{Re}\left[\left(\nabla\cdot[\boldsymbol{\tau} + 2\beta\mathbf{d}] - Re\,\mathbf{u}\cdot\nabla\mathbf{u}\right)^{n+\frac{1}{2}} - \theta\nabla p^{n+1} - (1-\theta)\nabla p^n\right]. \tag{3.21}$$

[‡] Equation (2.52) can also be expressed as $Re\left(\dfrac{\partial\mathbf{u}}{\partial t} + \mathbf{u}\cdot\nabla\mathbf{u}\right) = -\nabla p + \nabla\cdot(\boldsymbol{\tau} + 2\beta\,\mathbf{d})$.

In order to implement the incompressibility constraint of equation (2.51), an auxiliary variable $\mathbf{u}^*$ may be introduced, which is non-divergence-free (non-solenoidal), satisfying

$$\mathbf{u}^* - \mathbf{u}^n = \frac{\Delta t}{Re}\left[\left(\nabla\cdot[\boldsymbol{\tau}+2\beta\mathbf{d}] - Re\,\mathbf{u}\cdot\nabla\mathbf{u}\right)^{n+\frac{1}{2}} - \nabla p^n\right]. \tag{3.22}$$

Subtracting (3.22) from (3.21) and defining $q^{n+1} = p^{n+1} - p^n$, the velocity at the proceeding time-step becomes

$$\mathbf{u}^{n+1} - \mathbf{u}^* = \theta\frac{\Delta t}{Re}\nabla q^{n+1}. \tag{3.23}$$

Taking advantage of the fact that $\mathbf{u}^{n+1}$ obeys equation (2.51), the pressure increment on the time-step may be obtained through the divergence of equation (3.23),

$$\nabla^2 q^{n+1} = \frac{Re}{\theta\,\Delta t}\nabla\cdot\mathbf{u}^*, \tag{3.24}$$

where $\nabla^2 q = \nabla\cdot\nabla q$.

Hawken et al. [47] presented a more stable approach by adopting a Crank-Nicolson time-split on diffusion terms, whilst leaving an explicit form for other terms. In this particular case, where boundary conditions are specified on the boundary, only the term $\nabla\cdot\mathbf{d}$ is affected. Then, the fractional stages of the temporal discretisation can be expressed as[§]:

- *Stage 1a:*

$$\frac{2\,Re}{\Delta t}\left[\mathbf{u}^{n+\frac{1}{2}} - \mathbf{u}^n\right] = \left(\nabla\cdot[\boldsymbol{\tau}+2\beta\mathbf{d}] - Re\,\mathbf{u}\cdot\nabla\mathbf{u}\right)^n + \beta[\nabla\cdot\mathbf{d}]^{n+\frac{1}{2}} - \nabla\left(p^n + \theta_1\left[p^n - p^{n-1}\right]\right), \tag{3.25}$$

[§] Stress equations are written for the Oldroyd-B model, see equation (3.12).

$$\frac{2We}{\Delta t}\left[\boldsymbol{\tau}^{n+\frac{1}{2}}-\boldsymbol{\tau}^{n}\right]=\Big(-We\,\mathbf{u}\cdot\nabla\boldsymbol{\tau}+2[1-\beta]\mathbf{d}-\boldsymbol{\tau}+ \\ We\left[(\nabla\mathbf{u})^{\mathrm{T}}\cdot\boldsymbol{\tau}+\boldsymbol{\tau}\cdot\nabla\mathbf{u}\right]\Big)^{n}. \tag{3.26}$$

- *Stage 1b:*

$$\frac{Re}{\Delta t}\left[\mathbf{u}^{*}-\mathbf{u}^{n}\right]=\left(\nabla\cdot\boldsymbol{\tau}-Re\,\mathbf{u}\cdot\nabla\mathbf{u}\right)^{n+\frac{1}{2}}+\nabla\cdot\left(2\beta\left[\frac{\mathbf{d}^{*}+\mathbf{d}^{n}}{2}\right]\right)- \\ \nabla\left(p^{n}+\theta_{1}\left[p^{n}-p^{n-1}\right]\right), \tag{3.27}$$

$$\frac{We}{\Delta t}\left[\boldsymbol{\tau}^{n+1}-\boldsymbol{\tau}^{n}\right]=\Big(-We\,\mathbf{u}\cdot\nabla\boldsymbol{\tau}+2[1-\beta]\mathbf{d}-\boldsymbol{\tau}+ \\ We\left[(\nabla\mathbf{u})^{\mathrm{T}}\cdot\boldsymbol{\tau}-\boldsymbol{\tau}\cdot\nabla\mathbf{u}\right]\Big)^{n+\frac{1}{2}}. \tag{3.28}$$

- *Stage 2:*

$$\nabla^{2}\left(p^{n+1}-p^{n}\right)=\frac{Re}{\theta_{2}\,\Delta t}\nabla\cdot\mathbf{u}^{*}. \tag{3.29}$$

- *Stage 3:*

$$\frac{2Re}{\Delta t}\left(\mathbf{u}^{n+\frac{1}{2}}-\mathbf{u}^{*}\right)=-\theta_{2}\,\nabla\left(p^{n+1}-p^{n}\right). \tag{3.30}$$

This three-stage structure must be solved over each time-step, $\left[t^{n},t^{n+1}\right]$ until convergence to a limiting steady-state is secured.

3.4 Spatial discretisation

The numerical scheme employed in the present study is that from a class of hybrid methods. In particular, spatial discretisation for velocity and pressure is performed through a Galerkin finite element method, whilst for the stress equation (3.26) and (3.28), a finite volume scheme is implemented.

3.4.1 Finite element scheme

In the finite element scheme, scalar velocity components and pressure fields are approximated by

$$u(x,t)=\phi_j(x)\,U_j(t), \qquad p(x,t)=\psi_j(x)\,P_j(t), \tag{3.31}$$

where $U_j(t)$, $P_j(t)$ are nodal values of velocity and pressure; the set of functions $\phi_j(x)$ is that of piecewise quadratic basis functions for velocity, and $\psi_j(x)$ are linear basis functions for pressure. Triangular elements are employed in the *fe*-implementation, with velocity computed at vertex and midside nodes, and pressure only at vertex nodes. The exterior parent triangle in Figure 3.1a represents a typical finite element, indicating the information computed at each node. The problem statement in fully-discrete matrix-vector form may be expressed as,

- *Stage 1a*

$$\left(\frac{2Re}{\Delta t}\mathbf{M}+\tfrac{1}{2}\beta\mathbf{S}\right)\left[\mathbf{U}^{n+\frac{1}{2}}-\mathbf{U}^{n}\right]=\left(-\left[\beta\mathbf{S}+Re\,\mathbf{N}(\mathbf{U})\right]\mathbf{U}-\mathbf{B}\mathbf{T}\right)^{n}+\mathbf{L}^{T}\mathbf{P}^{n}. \tag{3.32}$$

- *Stage 1b*

$$\left(\frac{Re}{\Delta t}\mathbf{M}+\tfrac{1}{2}\beta\mathbf{S}\right)\left[\mathbf{U}^{*}-\mathbf{U}^{n}\right]=\left(-\left[\beta\mathbf{S}+Re\,\mathbf{N}(\mathbf{U})\right]\mathbf{U}-\mathbf{B}\mathbf{T}\right)^{n+\frac{1}{2}}+\mathbf{L}^{T}\mathbf{P}^{n}. \tag{3.33}$$

- *Stage 2*

$$\mathbf{K}\left(\mathbf{P}^{n+1}-\mathbf{P}^{n}\right)=-\frac{Re}{\theta_2\Delta t}\mathbf{L}\mathbf{U}^{*}. \tag{3.34}$$

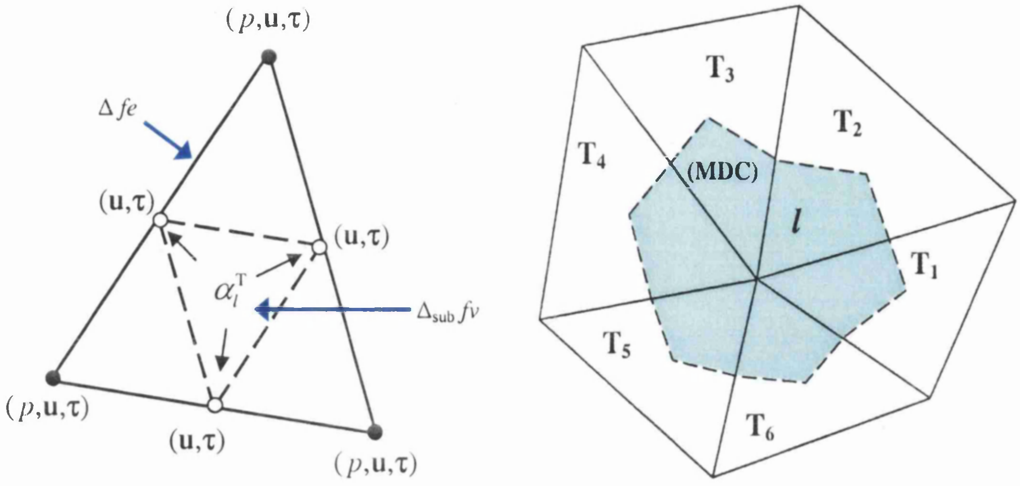

Figure 3.1. Element grid; a) *fe*- parent triangle and *fv*-subcells, b) median-dual-cell configuration.

. *Stage 3*

$$\frac{Re}{\Delta t}\mathbf{M}\left(\mathbf{U}^{n+1}-\mathbf{U}^{n}\right)=\tfrac{1}{2}\mathbf{L}^{T}\left(\mathbf{P}^{n+1}-\mathbf{P}^{n}\right). \qquad (3.35)$$

In equations (3.32) and (3.33) the weighting parameter θ_1 has been set to zero. $\mathbf{U}$, $\mathbf{T}$, and $\mathbf{P}$ are solution nodal vectors for velocity, stress and pressure. The weighting shape functions may be manipulated to give the matrix-vector terms,

$$M_{ij}=\int_{\Omega}\phi_i\phi_j\,\mathrm{d}\Omega, \qquad K_{ij}=\int_{\Omega}\frac{\partial\psi_i}{\partial x}\frac{\partial\psi_j}{\partial x}\mathrm{d}\Omega, \qquad S_{ij}=\int_{\Omega}\frac{\partial\phi_i}{\partial x}\frac{\partial\phi_j}{\partial x}\mathrm{d}\Omega,$$

$$B_{ij}=\int_{\Omega}\frac{\partial\phi_i}{\partial x}\phi_j\,\mathrm{d}\Omega, \qquad \left(L_k\right)_{ij}=\int_{\Omega}\psi_i\frac{\partial}{\partial x_k}\phi_j\,\mathrm{d}\Omega, \qquad (3.36)$$

$$N_{ij}\left(\mathbf{U}\right)=\int_{\Omega}\phi_i\left(\phi_k\,\mathrm{U}_k\frac{\partial\phi_j}{\partial x}+\phi_k\,\mathrm{V}_k\frac{\partial\phi_j}{\partial y}+\phi_k\,\mathrm{W}_k\frac{\partial\phi_j}{\partial z}\right)\mathrm{d}\Omega,$$

3.4.2 Finite volume scheme

In order to consistently represent flow problems with the finite volume method, an appropriate split of the flux ($\mathbf{R}$) and source ($\mathbf{Q}$) residuals must be made to the vertices of each *fv*-triangle. With cell-vertex methods, nodal variables are located at the vertices of the *fv*-cell. Values at any other position must be obtained by interpolation. In contrast, rates-of-changes (or fluctuation) of flow variables are integrated over each *fv*-cell (surface flux or volume integrals). This implies that fluctuation is cell-centered and must be adequately distributed to the *fv*-cell vertices. The hybrid *fe/fv* algorithm employed in this study, utilizes fluctuation distribution (FD) procedures to achieve this.

The FVM mesh is generated by partitioning, at the midside nodes of each finite element (parent) triangle, into four triangular *fv*-subcells (see Figure 3.1a). The type of *fv*-algorithm employed is a cell-vertex scheme, which is employed to obtain values for stress at each node, similar to the treatment for velocity in the *fe*-scheme.

The constitutive model such as equation (3.12) can be rewritten for the FVM implementation in terms of flux and source terms,

$$\frac{\partial}{\partial t}\boldsymbol{\tau} = -\mathbf{R} + \mathbf{Q}, \tag{3.37}$$

with expressions for the flux ($\mathbf{R}$) and source ($\mathbf{Q}$) of

$$\mathbf{R} = \mathbf{u} \cdot \nabla \boldsymbol{\tau}, \tag{3.38}$$

$$\mathbf{Q} = \frac{1}{We}\left(2[1-\beta]\mathbf{d} - \boldsymbol{\tau}\right) + \left(\nabla \mathbf{u}\right)^{\mathrm{T}} \cdot \boldsymbol{\tau} + \boldsymbol{\tau} \cdot \nabla \mathbf{u}. \tag{3.39}$$

Integration of equations (3.37)-(3.39) for each scalar component of the stress τ, yields the associated residuals. These must be evaluated on the *fv*-cells and/or on the median-dual-cell (MDC) associated (Figure 3.1b) with each given node *l*. The MDC for any node is formed by taking one third of each triangular cell containing that node,

$$\int_{\hat{\Omega}_l} \frac{\partial}{\partial t} \tau \, \mathrm{d}\Omega = - \int_{\Omega_T} R \, \mathrm{d}\Omega + \int_{\hat{\Omega}_l} Q \, \mathrm{d}\Omega . \tag{3.40}$$

Time discretisation is shown in equations (3.26) and (3.28), stages 1a and 1b, respectively. The proportion of contribution to the cell-vertex l for each *fv*-cell (T) from the evaluation of source and flux integrals is controlled by fluctuation distribution coefficients (α_l^T, see Chandio [30] and Chandio et al. [31]). The update for node l is constructed by summing contributions from its control volume Ω_l, formed by all *fv*-triangles sharing that node. For this purpose, Aboubacar et al. [4,6] proposed a generalised area-weighting stencil for such schemes, of the form

$$\begin{aligned} \left[\sum_{\forall T_l} \delta_T \, \alpha_l^T \, \Omega_T + \sum_{\forall MDC_l} \left(1-\delta_T\right) \hat{\Omega}_l^T \right] \frac{\Delta \tau_l^{n+1}}{\Delta t} = \sum_{\forall T_l} \delta_T \, \alpha_l^T \, b^T + \\ \sum_{\forall MDC_l} \left(1-\delta_T\right) b_l^{MDC} \end{aligned} \tag{3.41}$$

where $b^T = \left(-R_T + Q_T\right)$, $b_l^{MDC} = \left(-R_{MDC} + Q_{MDC}\right)^l$. Here, Ω_T is the area of the *fv*-triangle T, whilst $\hat{\Omega}_l^T$ is the area contribution of the same triangle to the median-dual-cell. In formula (3.41), the parameter δ_T directs the balance taken between the contributions from the median-dual-cell and the triangle T. This completes the necessary detail for the *fe*- and *fv*-discretisations used.

CHAPTER 4

Pom-Pom Modelling for Planar Channel Flows*

This chapter is concerned with the numerical solution of steady-state viscoelastic flows using two different numerical schemes, a hybrid finite element/finite volume (*fe/fv*) and a semi-Lagrangian finite volume procedure (SLFV). In particular, the Single eXtended form of the Pom-Pom model (SXPP) is considered here, making comparison between the results of these two different finite volume schemes. Time-stepping is employed within both numerical algorithms. The pure finite volume, which is based on area-weighting, is a staggered-grid cell-centred scheme. Together with a semi-Lagrangian formulation, this is employed particularly for unstructured rectangular grids, implementing backtracking along the solution characteristics as a function of time. The momentum and continuity equations are solved for the hybrid scheme via a fractional-staged Taylor-Galerkin/pressure-correction procedure (finite element part) and for the constitutive system a cell-vertex finite volume scheme is adopted. To achieve the above goal, a variety of combinations of 'flux' and 'median-dual-cell' spatial discretisations are made upon fluctuation distribution schemes

---

* Material of this chapter has been shaped in the paper "Modelling pom-pom type models with high-order finite volume schemes" by M. Aboubacar,.J. P. Aguayo, P. M. Phillips, H. R. Tamddon-Jahromi, B. A. Snigerev and M. F. Webster, and published in *Journal of Non-Newtonian Fluid Mechanics* **126** (2005) 207-220.

(upwinding) and time-term treatments. Triangular-based grids may be used with this *fe/fv* implementation on both structured and unstructured meshes. Comparison of the two finite volume approaches is provided, emphasizing the new aspects posed by Pom-Pom above Oldroyd modelling.

4.1 Introduction

Two accurate and stable finite volume methods for solving viscoelastic flow, are compared for the Pom-Pom class of models: a hybrid finite element/finite volume scheme and a semi-Lagrangian finite volume procedure. Steady-state solution is achieved through evolution by a time-splitting procedure for both schemes. A semi-implicit Taylor-Galerkin formulation is employed for the cell-vertex hybrid *fe/fv* for discretisation of momentum equations; incompressibility is enforced via a pressure-correction step. The pure finite volume scheme is based upon a backward Euler procedure and convection terms, in momentum and constitutive equations, are treated with a semi-Lagrangian step.

Under the hybrid implementation, discretisation of conservation equations is performed through a finite element procedure and through finite volume for the constitutive equation system. The finite volume grid is constructed by dividing each (parent) triangular finite element using its mid-side nodes to generate four (child) triangular-cells. The resulting approximation is close in philosophy to the so-called 4×4 stress subelements, introduced by Marchal and Crochet [63]. In order to prevent spurious oscillation in the velocity field, discretisation in the mixed finite element context requires compatible approximation spaces for velocity and extra-stress. Here, distribution of flux and source residuals to each of the vertices of a finite volume cell is enforced through Fluctuation-Distribution (FD) schemes. Conservation of convected terms is satisfied on each control volume; this is a convenient feature of all FD schemes. Linearity preserving (second-order accuracy in space for linear solutions) is another feature of the Low Diffusion B (LDB) scheme (linear FD-schemes class) used in this hybrid *fe/fv* context. A consistent treatment of flux and source terms in the constitutive equation is necessary to achieve high-order accuracy. Enhanced stability, with respect to large elasticity (De or We) attainment, is improved by taking into account contributions from flux and source terms, based on the median-dual-cell construct (MDC). This is a fundamental step to develop a stable scheme and to obtain convergent solutions in complex flows. A generalised finite volume nodal-update has emerged that includes additional consideration for time-term discretisation.

A semi-Lagrangian treatment for convection terms and a staggered grid arrangement for variables are some key features of the pure finite volume scheme. The SIMPLER scheme, improved to include constitutive equations, is used to solve the resulting discrete system. Second-order area-weighting, developed by Phillips and Williams [81], is employed for the conservation equations. A variant of this scheme has been successfully applied in complex flows problems [82]. This conservative stable scheme eludes problems associated with high-order upwinding schemes.

By solving an Oldroyd-B model problem, Aboubacar and Webster [6] demonstrated second-order accuracy in space represented by the hybrid schemes. Stability for a range of Weissenberg (We) numbers of both schemes has been shown for the transient start-up of an Oldroyd-B fluid in a planar channel and their temporal accuracy was established when compared to the analytical solution of Waters and King [104] for this problem.

Over the past several years, a new class of tractable differential constitutive models, capable of describing the behaviour of polymer melts, has emerged. These fluid models are based on the developments of Doi and Edwards [42] of the tube kinetic model for entangled melts. The double-convection-reptation (DCR) model of Ianniruberto and Marrucci [50], the Pom-Pom model introduced by McLeish and Larson [68] and the subsequent extended versions proposed by Verbeeten et al. [96] are all examples of models derived from the work of Doi and Edwards. Such models incorporate two important aspects that are non-existent in phenomenological equations. The first aspect is that via the proposing molecular relaxation mechanisms, the models include the fact that melt rheology depends on polymer molecular structure. The second aspect, is the introduction of a spectrum of relaxation times to be taken into account, leading to a system of two partial differential equations, one for orientation and another for stretch.

Chain stretch, reptation and Rouse friction have been included in the DCR model (a multi-mode convection-constraint release 'CCR'-version). The introduction of the CCR-mechanism [64] is a major step forward, since it resolves the problem of excessive shear-thinning predicted by the Doi-Edwards model at high shear-rates. Nevertheless, a two-mode DCR model exhibits a narrow window of shear-thickening [103]. The Pom-Pom model emerged to represent an idealised polymer molecule, composed of a backbone with the same number of dangling arms (q) at both ends. In the original formulation, three dynamical variables appear in the differential approximation of the model: backbone orientation tensor ($\mathbf{S}$), backbone stretch (λ), and arms-withdrawal (S_c). Arms-withdrawal takes place when the molecule reaches its maximum stretched state (number of arms, q) provoking an abrupt finite extensibility constraint[†] which results in a discontinuity in steady-state extensional viscosity (see [19,20,51,68]). The decouple nature of orientation and stretch relaxation times is a key feature in this class of models. It is significant that such a simple molecular topology, with only one mode, has been able to qualitatively predict transient viscosities (shear and elongational) of the IUPAC A LDPE (low density polyethylene) melt.

The original Pom-Pom model suffers from three major drawbacks: discontinuities in steady-state extensional viscosity, the equation for orientation is unbounded and the model predicts a zero second normal stress difference in shear flow. Despite a number of modifications (extension to multi-mode [51], drag-strain

---

[†] A finite extensibility constraint is present in the DCR model too, but the switch is provided smoothly and automatically through the definition of chain-orientation relaxation-time.

coupling [20], modification of the backbone orientation relaxation-time to allow for retraction as well as stretch [57]) these disadvantages remain still to be corrected. Verbeeten et al. [96] have proposed an extended version of the model with the following adjustments: *first*, the backbone orientation is not required to obey Doi and Edwards theory for linear polymers; *second*, although they retained the drag-strain coupling [20], the finite extensibility constraint is discarded. Following Inkson et al. [51], model parameters are determined by linear and nonlinear response, instead of linking them directly to molecular data. Additionally, for a nonzero second normal stress coefficient, the authors have introduced a Giesekus-like parameter, α, to account for some anisotropic relaxation. In this manner, the so-called eXtended Pom-Pom model (XPP) was able to quantitatively predict the rheology of a commercial LDPE melt. Hence, the SXPP model is considered in the present study.

4.2 Plane Poiseuille flow

Adequate imposition of time-dependent boundary conditions at inflow sections of simple and complex geometries is required when solving transient flow problems. Analytical solution for velocity and stress in transient Poiseuille flow of Maxwell/Oldroyd-B model fluids was obtained by Waters and King [104]. However, for Pom-Pom models an analytical solution for Poiseuille flow is not readily available, and transient inflow boundary conditions and fully-developed steady-state solution must be determined numerically. Influence of the model parameters on steady-state velocity profiles, polymeric stress and backbone stretch is described.

Given a flowrate, a steady-state solution for the SXPP model is obtained utilising an Oldroyd-B solution as inflow boundary conditions (velocity and extra-stress) at the selected flowrate. No-slip conditions are imposed at walls and natural boundary conditions at exit for velocity. Solutions at high Weissenberg number are obtained through parameter continuation in elasticity number. Once velocity and stress profiles have developed away from the inlet, desired SXPP profiles are obtained at the domain exit, providing that significantly long computational domains are employed.

Structured 20×60 meshes with computational domains of [0,16]×[0,2] are employed for both *fe/fv* and SLFV schemes; a typical time-step is $\Delta t = 10^{-3}$. There are no geometric singularities in the flow and the problem is solved for half of the channel, imposing symmetry about the centreline. Computations were also performed on a structured 40×60 mesh, to ensure that mesh convergence was achieved. The maximum run time for computations on the 20×60 mesh was of the order of 10 minutes, performed on (single-user/single-job basis) several computing platforms PC/Unix, including an Intel Pentium 4 (2.5GHz, 512MB) and a Compaq XP1000 (500MHz, 256MB) workstation.

4.2.1 Influence of increasing Weissenberg number

In order to observe the influence of the Weissenberg number, on velocity, extra-stress and backbone stretch, the other SXPP parameters are fixed and taken to be $\beta = 1/9$, $\varepsilon = 1/3$, $q = 2$ and $\alpha = 0.15$. Some inertia is imposed through the Reynolds number, setting $Re = 1$. Figure 4.1 demonstrates the influence of We on solutions obtained separately with both finite volume schemes.

For this shear-thinning fluid, the velocity attains a lower maximum value than for the Oldroyd-B fluid (0.75) at the same flowrate. Maximum values of velocity (centreline) at $We = 1$ are 0.725 for the *fe/fv* scheme and 0.727 for the SLFV scheme. These values lower to 0.663 and 0.660, at $We = 10$. On the refined mesh maximum velocity values for the two methods are 0.663 and 0.660, respectively, at $We = 10$. The difference in maxima between both schemes is less than 0.5%. For the present case, mesh refinement reduces this difference by less than 0.1%.

As the shear-rate (velocity gradient) at the centreline is zero, the stretch assumes its equilibrium value ($\lambda = 1$) along this symmetry line. Its maximum value occurs at the wall, the position where the shear-rate reaches its largest value. This maximum stretch rises as Weissenberg number increases (stretch maxima are 1.436 for *fe/fv* and 1.432 for SLFV at the level of $We = 10$).

The polymeric contribution to the extra-stress tensor τ_{xx} starts to grow before relaxing at higher values of We. The extra stress τ_{xy} is almost linear at $We = 1$, and for the three elasticity levels shown, this stress component maintains its linear form next to the centreline, where the backbone stretch is close to unity (value of equilibrium). Both numerical scheme solutions lie in excellent agreement (see Figure 4.1).

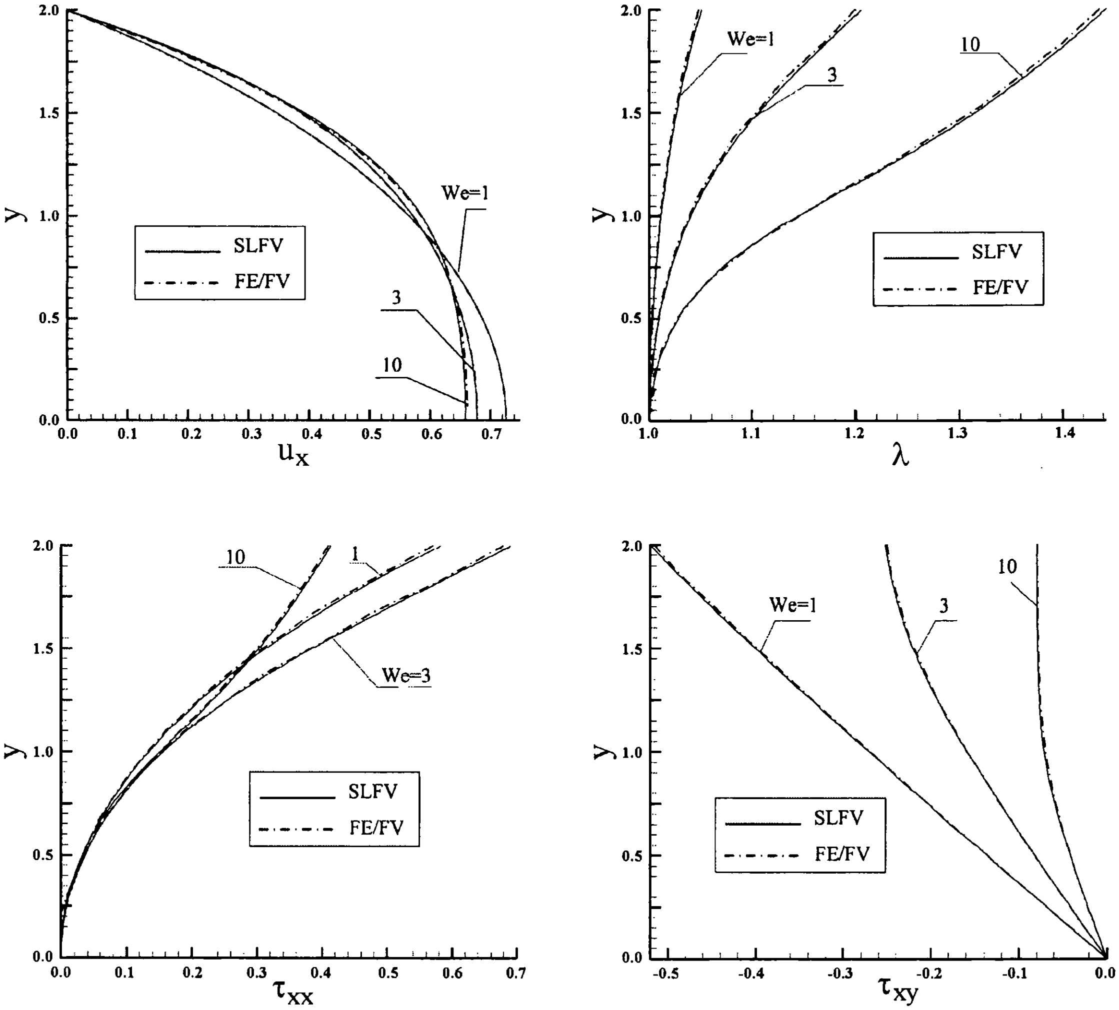

Figure 4.1. Channel flow; SLFV vs. *fe/fv*, $Re = 1$, $\beta = 1/9$, $\varepsilon = 1/3$, $q = 2$, $\alpha = 0.15$.

4.2.2 Influence of viscosity ratio

Figure 4.2 illustrates the influence of the viscosity ratio β (solvent/total) on velocity, stretch and polymeric stress (τ_{xx} and τ_{xy}) profiles. Systems with high polymer content correspond to low values of β, whilst dilute or less-entangled solutions correspond to high β-values.

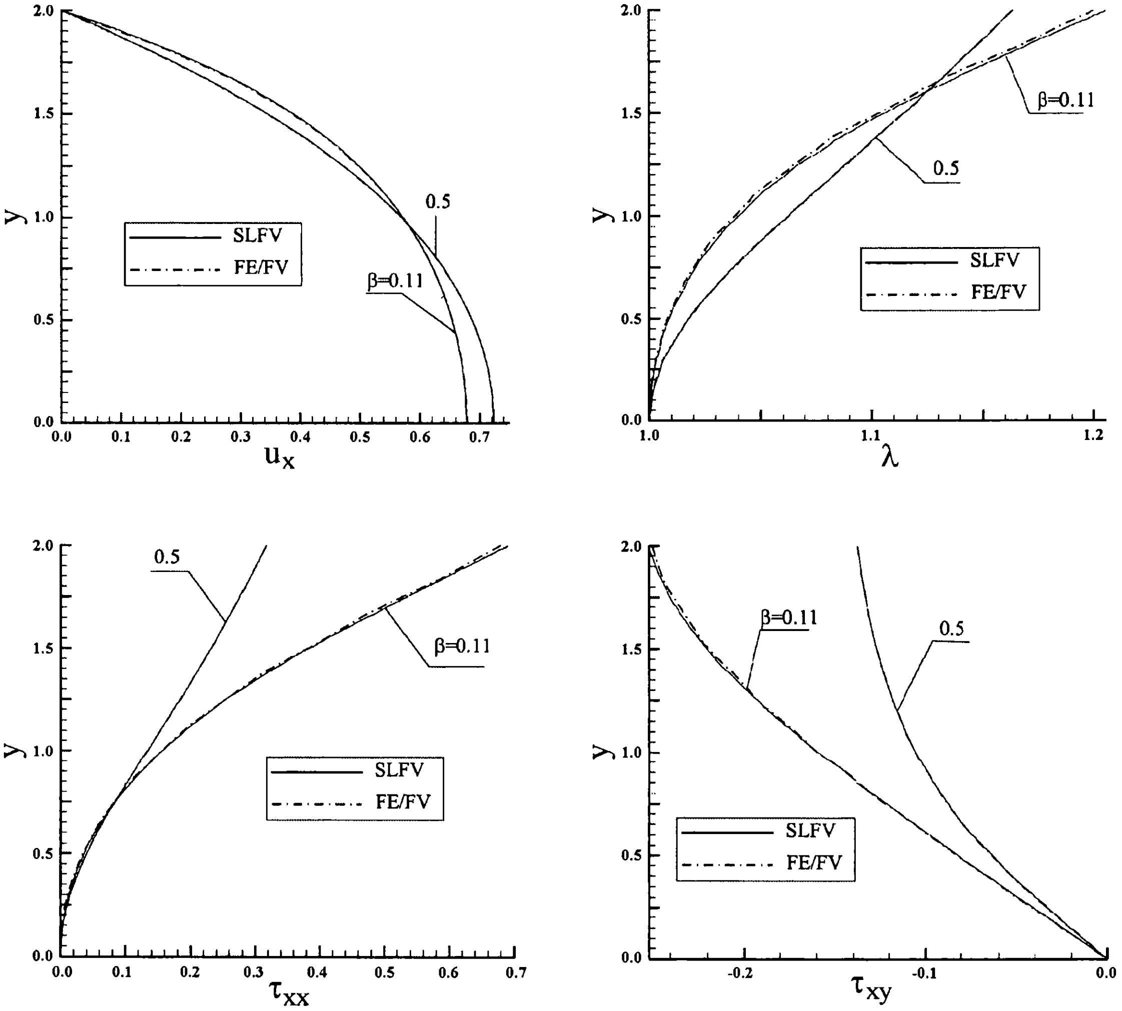

Figure 4.2. Channel flow; SLFV vs. *fe/fv*, $Re = 1$, $We = 3$, $\varepsilon = 1/3$, $q = 2$, $\alpha = 0.15$.

The smallest value of β that ensures a monotonically increasing shear-stress as a function of shear-rate for the Johnson-Segalman model is 1/9. Although this lower bound of β is not strictly necessary for the Oldroyd-B model, which is a particular instance of the Johnson-Segalman model, $\beta = 1/9$ is the value commonly adopted in benchmark numerical simulations. It is important to note that, in order to reflect quantitative comparisons with the so-called Boger fluids in experiments, the value of β should be taken of at least 0.9. Values of β ranging from 0.1 to 0.5 have been used here.

For a decrease in β, the velocity profile becomes flatter. This behaviour may be anticipated, if we associate the decrease of β with an increase of the relaxation time of the backbone orientation, according to the definitions of β and μ_p used here. As high β-values represent more dilute systems, the magnitude of the polymeric stresses is expected, in general, to be less when the solvent contribution becomes more important. Therefore, for larger values of β, reduction in stress and stretch is observed. Agreement between both numerical schemes (*fe/fv* and SLFV) is excellent, as can be gathered from Figure 4.2.

4.2.3 Influence of relaxation times ratio

The ratio of relaxation times through backbone stretch/orientation, ε, is related to the degree of entanglement of the system, where high ε-values correspond to more dilute, or less entangled, polymer systems. For this less entangled case, $\varepsilon \to 1$, orientation and stretch relax almost simultaneously, whilst for low ε-values ($\varepsilon \to 0$), the relaxation time for orientation is much slower than that of the backbone stretch; then, the system can be considered as highly entangled. The influence of ε on profiles of velocity, stretch, and polymeric contributions to the extra-stress components τ_{xx} and τ_{xy} is presented in Figure 4.3. It can be observed that a decrease in ε flattens the velocity profile. However, from $\varepsilon = 0.6$ to 0.2 this effect is almost unnoticeable, as shown in the figure. Stretch and polymeric components of the stress reflect a significant increase in magnitude as ε increases, an effect that becomes more pronounced close to the wall.

The agreement between the *fe/fv* and SLFV schemes is good, with minor differences observed near the boundary wall for $\varepsilon = 0.6$.

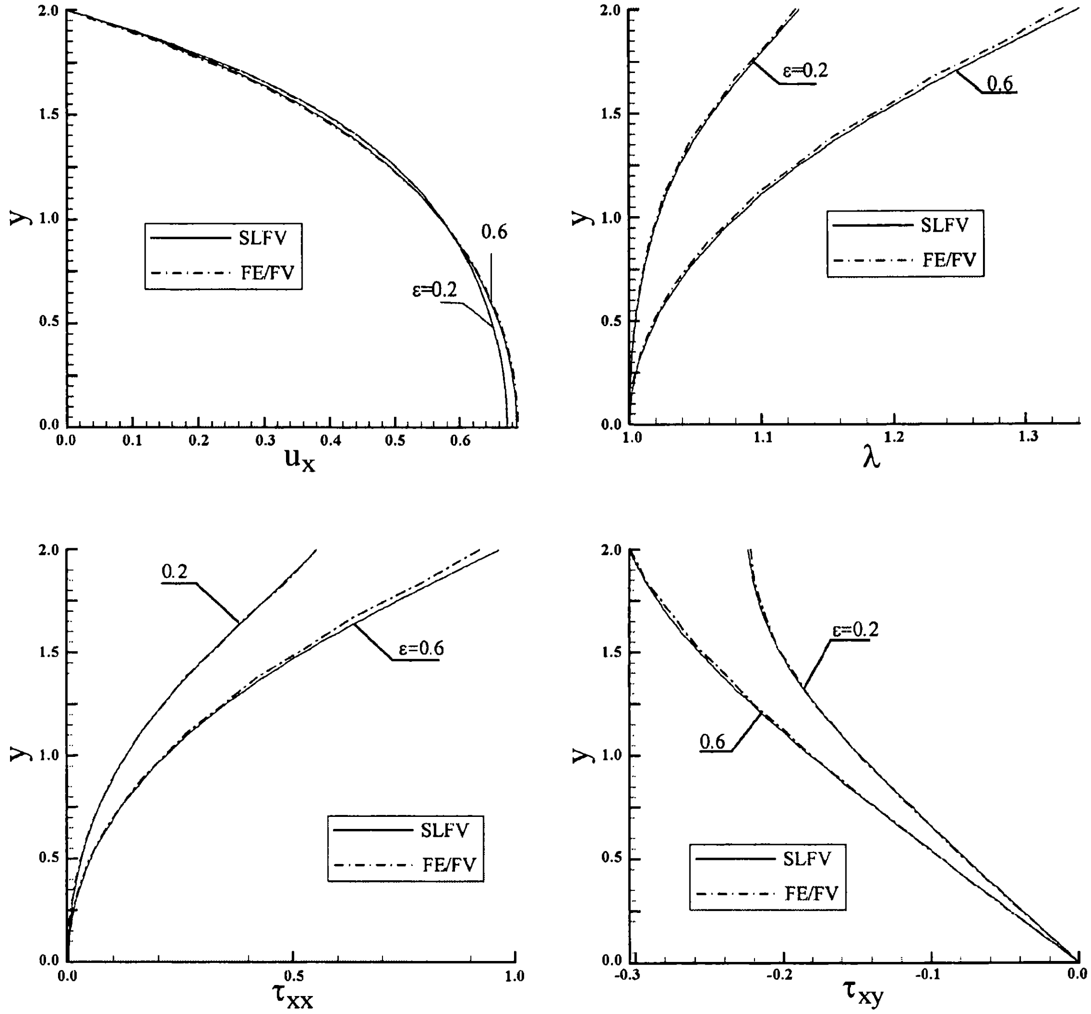

Figure 4.3. Channel flow; SLFV vs. *fe/fv*, *Re* = 1, *We* = 3, β = 1/9, q = 2, α = 0.15.

4.2.4 Influence of the number of dangling arms

The influence of the number of arms on the profiles of velocity, stretch, and polymeric contributions to the extra-stress components τ_{xx} and τ_{xy} is shown in Figure 4.4.

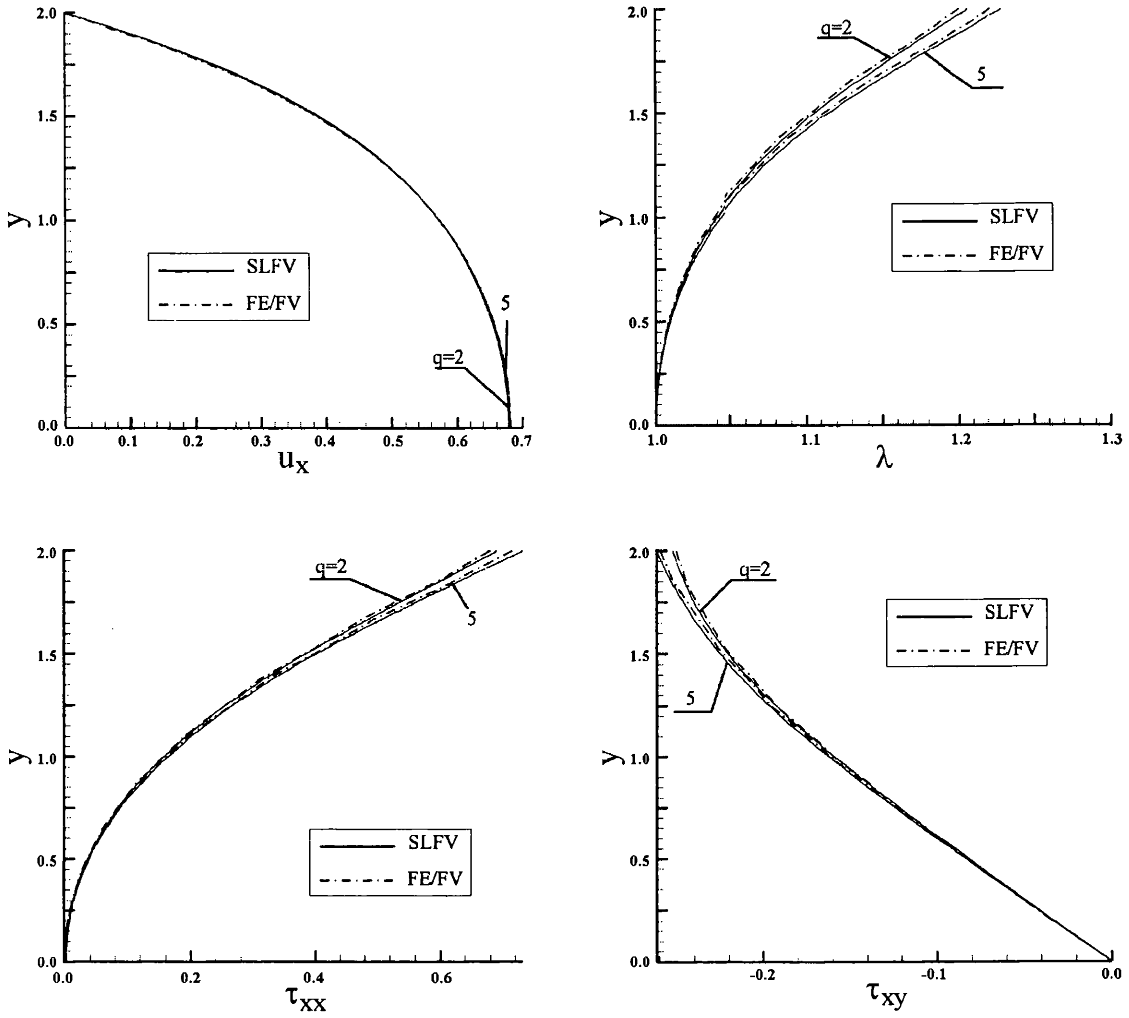

Figure 4.4. Channel flow; SLFV vs. *fe/fv*, $Re = 1$, $We = 3$, $\beta = 1/9$, $\varepsilon = 1/3$, $\alpha = 0.15$.

Varying the number of arms (q) at each end of the Pom-Pom molecule should affect the level of entanglement of the system. However, for shear flow with fixed relaxation time ratio (ε) and solvent to total viscosity ratio (β), a variation of q is not anticipated to provoke significant differences in flow response. For the field-variables presented in Figure 4.4, a variation from $q = 2$ to 5 produces minor differences in their solution. Stretch for $q = 5$ is slightly larger, for both *fe/fv* and SLFV schemes. No tangible effect of q on the velocity profile is detected. Differences near the boundary wall for stress and stretch can be appreciated, still these are not significant in magnitude. The SLFV scheme exhibits slightly larger values of stretch, τ_{xx} and τ_{xy} over those for the *fe/fv* scheme.

4.2.5 Influence of anisotropy

The influence of α on velocity, stretch and stress profiles is presented in Figure 4.5. As explained earlier, this parameter was included in the eXtended versions of the Pom-Pom models to account for anisotropy of the material.

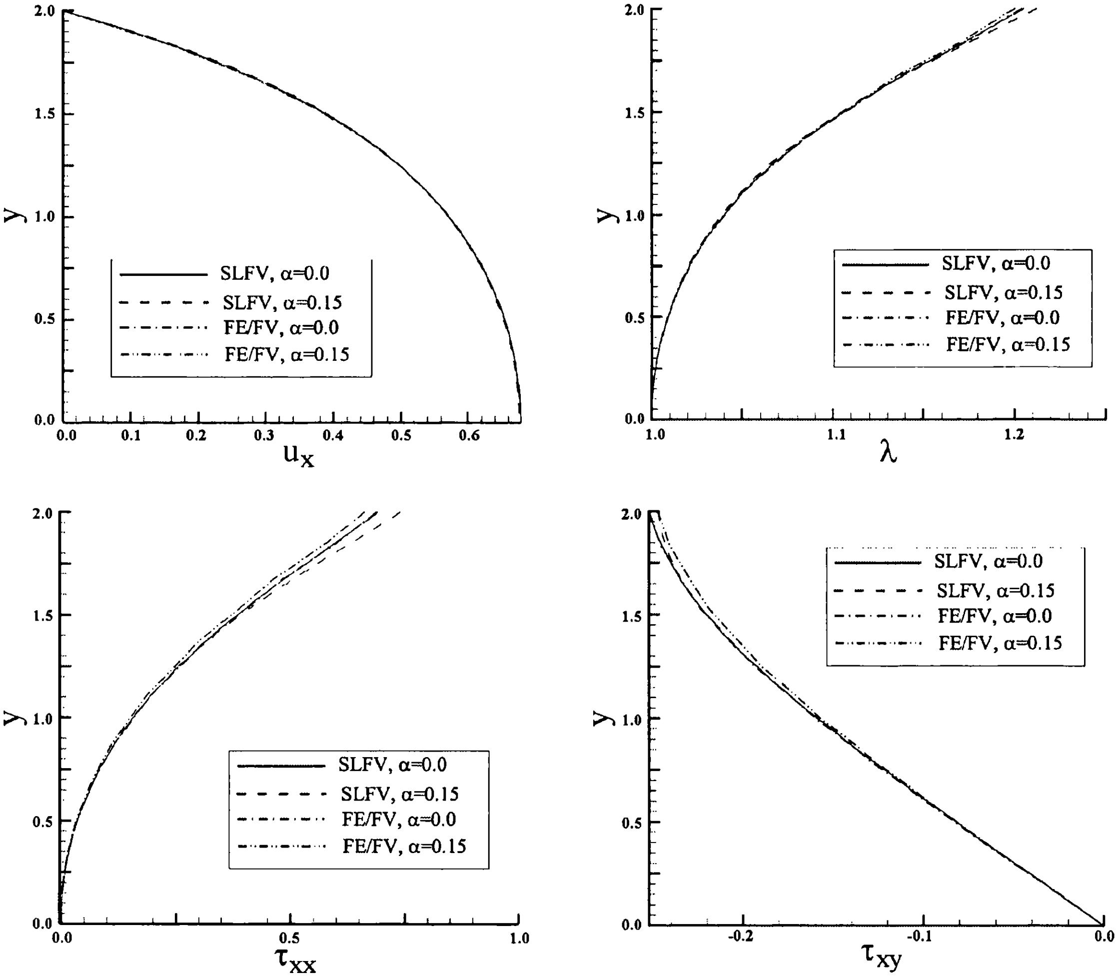

Figure 4.5. Channel flow; SLFV vs. *fe/fv*, $Re = 1$, $We = 3$, $\beta = 1/9$, $\varepsilon = 1/3$, $q = 2$.

A vanishing α produces a vanishing second normal stress difference (N_2) in shear flow. In all sets of model parameters where $\alpha = 0$, second and third normal stress components are equal ($\tau_{yy} = \tau_{zz}$). This is confirmed in the numerical computations. Here, the *fe/fv* and SLFV schemes provide barely any differences for the chosen values of this parameter ($\alpha = 0$ and 0.15).

Figure 4.6 exhibits the effect or varying the anisotropy of the material through the *fe/fv* solution. As this is planar channel flow, second normal stress difference is expected to be small and the influence of α is negligible. Nevertheless, it is important to note that stress components τ_{yy} and τ_{zz} are nonzero (in contrast to the response of an Oldroyd-B fluid in Poiseuille flow, where τ_{xx} is the only non-zero normal stress component). As mentioned above, with no anisotropy, the τ_{yy}-profile is exactly the same as that of τ_{zz} (see curve for $\alpha = 0$ in Figure 4.6). Whilst the effect of anisotropy at $\alpha = 0.15$ is insignificant for τ_{yy}, for τ_{zz}, a slight decrease in magnitude can be appreciated.

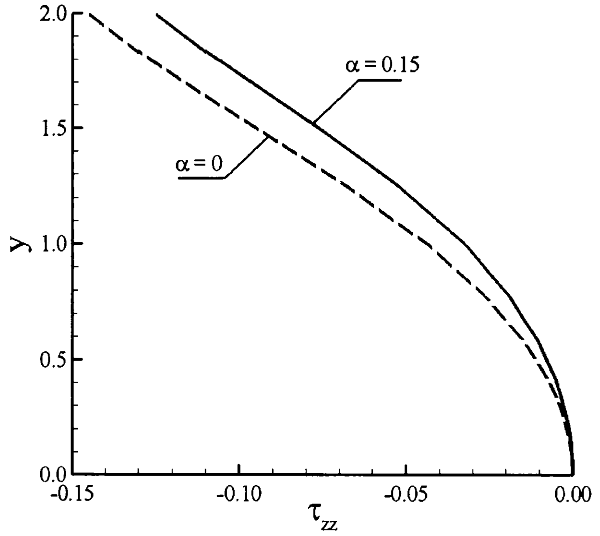

Figure 4.6. Polymeric stress τ_{zz} profiles: α variation; $We = 3$, $\beta = 1/9$, $\varepsilon = 1/3$, $q = 2$.

4.2.6 Pressure gradient and shear-rate

Pressure gradient[‡], ∇p, as a function of Weissenberg number is charted in Figure 4.7, with selected parameter values of: $Re=1$, $q=2$, $\varepsilon=1/3$, $\beta=1/9$ and $\alpha=0.15$. Due to the shear-thinning behaviour of the SXPP fluid model, the pressure gradient decreases with increasing elasticity, throughout the *We* range considered. Any differences between scheme solutions are practically undetectable.

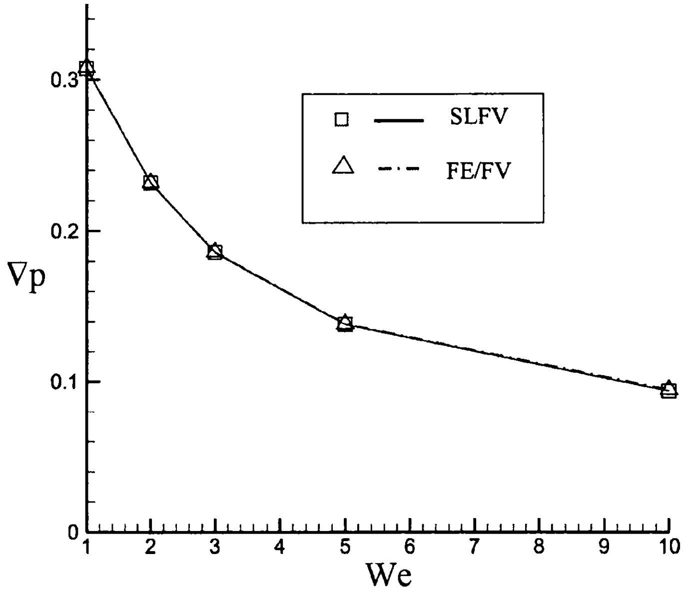

Figure 4.7. Dependence of pressure gradient on elasticity. Re = 1, β= 1/9, ε= 1/3, q = 2, α= 0.15.

Figure 4.8 displays the effect on shear-rate ($\dot{\gamma}$) under these steady-state Poiseuille flow conditions when We, β, ε and q are varied. Profiles against $\dot{\gamma}$ are displayed only for the *fe/fv* scheme. Shear-rate is a linear function of cross-stream position for Newtonian fluids. As such, this response is anticipated to match that at low *We* for the viscoelastic model used here. One needs to note that along the symmetry line $\dot{\gamma}$ is zero. As elasticity increases, shear-thinning reduces the viscosity, producing a zone of relatively low shear-rate values around the centreline. At large

---

[‡] Equivalent to pressure drop/channel length for this problem.

We, the $\dot{\gamma}$-profile tends to recover linear shape, indicating that the second plateau in viscosity has been reached (see Figure 2.5).

The effect of 'adding' more solvent to the system (from $\beta = 1/9$ to $1/2$) results in a more linear profile at the same Weissenberg number level ($We = 3$). It was shown above that changes in ε and q are hardly noticeable on velocity, and consequently, the impact upon shear-rate is insignificant.

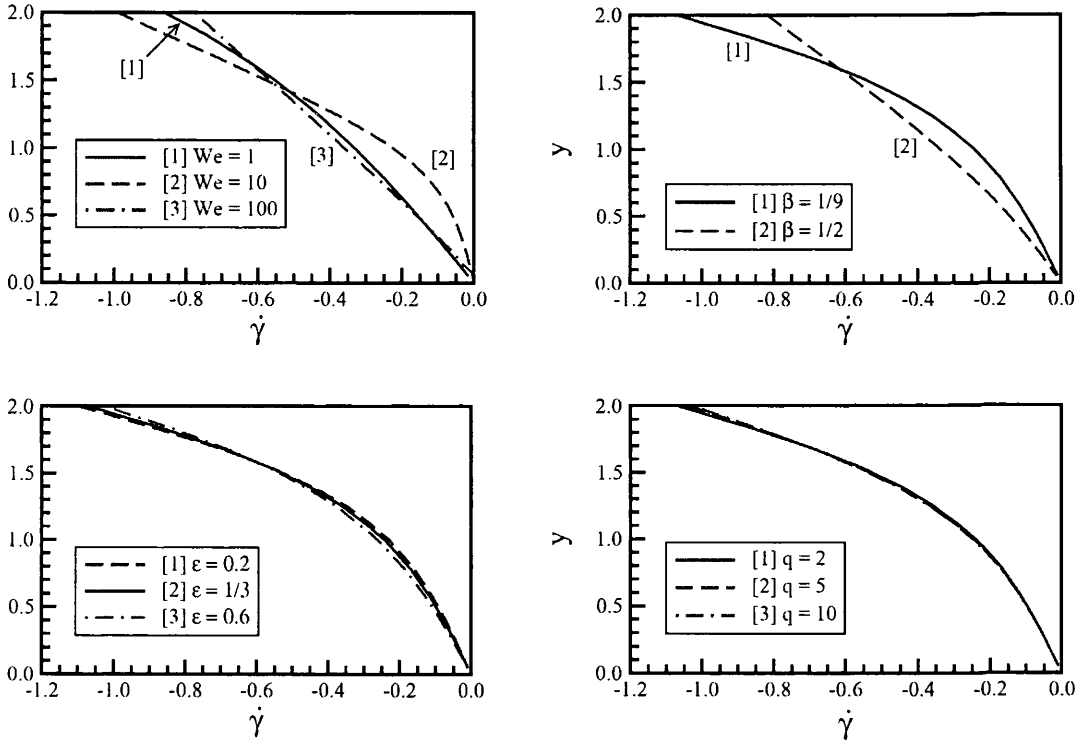

Figure 4.8. Shear-rate in Poiseuille flow: $We = 3$, $\beta = 1/9$, $\varepsilon = 1/3$, $q = 2$, $\alpha = 0.15$.

4.3 Conclusions

In this chapter solutions for planar channel flow have been presented employing two contrasting finite volume schemes. The model used has been the Single eXtended Pom-Pom model for branched polymers. Generation of steady-state profiles (velocity, stretch and extra-stress), that can be used as inlet boundary conditions, is key in the simulation of complex flows. Typically, Poiseuille flow has been solved for a range of parameters relating to the polymer structure and concentration in the system.

The Pom-Pom class of models considers two relaxation times, one for orientation and another for backbone stretch. Unlike the corresponding situation for Maxwell/Oldroyd-B models, an analytical solution for the SXPP governing equations is unavailable. In previous studies [4], the performance of both schemes on plane Poiseuille flow of an Oldroyd-B fluid has been compared in terms of accuracy. As mentioned above, there is an analytical solution for the transient development of the Oldroyd-B model on this problem flow. The numerical schemes have been shown to be second-order accurate in space. Here, for this SXPP Poiseuille flow, both procedures (*fe/fv* and SLFV) have been compared over a range of material parameters and lie in excellent agreement.

CHAPTER 5

Pom-Pom Modelling for Contraction Flows*

Previously, steady Poiseuille flow for the Single eXtended Pom-Pom (SXPP) model was solved with two time-stepping finite volume schemes, a hybrid finite element/finite volume (*fe/fv*) and a semi-Lagrangian pure finite volume (SLFV) procedure. In this chapter, the scope is extended to planar 4:1 sharp contraction flows for the same fluid model. Vortex behaviour and field variable solutions are provided for two different inertia levels and for a range of elasticity numbers. Once more, a comparison of the two finite volume approaches is presented for this complex flow setting, concentrating upon the new features posed by the Pom-Pom class of models. An alternative double equation version of the Pom-Pom type model (λ^2XPP) is also tried against the single equation form.

5.1 Introduction

The prediction of polymer melts flow, using an extended Pom-Pom (XPP) model, though planar 4:1 sharp contractions is presented in this chapter. This class of models, proposed by McLeish and Larson [68], represents an extension of the Doi

---

* Material of this chapter has been shaped, submitted and accepted for publication to the *Journal of Computational Physics*.

and Edwards' tube kinetic model for entangled melts. The original Pom-Pom formulation presents three major disadvantages: discontinuous extensional viscosity, unbounded orientation and does not predict a second normal stress difference, N_2, in shear. Verbeeten et al. [96] introduced two extended versions of the Pom-Pom model to overcome these drawbacks; namely, the Single and Double eXtended Pom-Pom models, (SXPP and DXPP, respectively). Their main difference lies in the equation for the stretch (λ): for the DXPP model, λ is computed through the evolution in time of a partial differential equation, whilst for the SXPP model, λ is obtained through the evaluation of an algebraic equation. These new type of models recognize the dependency of the rheology on the internal structure of the polymer.

Significant differences can be appreciated between the flow response of diluted polymer solutions with constant shear viscosity (Boger fluids) and concentrated/melts systems; vortex behaviour and pressure-drop are examples where strong dependence of rheometrical properties may be observed.

Vortex growth dynamics in contraction flows has been extensively studied, for different contraction ratios ($\hat{\beta}$) in both axisymmetric and planar configurations. However, the link between vortex enhancement and rheometrical functions is still an open research area. The experimental work of Nguyen and Boger [72] showed that, for polyacrylamide (PAA) in a highly viscous glucose solvent with no shear-thinning effects (i.e. a Boger fluid), vortex cell-size grows with elasticity in a variety of contraction ratios for axisymmetric flows. These authors were able to correlate vortex cell-size with suitable definitions of elasticity, deformation-rates and contraction ratio. Boger et al. [26] concluded that information on shear flow is not sufficient to correlate vortex behaviour, when studying the contrasting response of two Boger-type solutions in circular contractions; the first system is a solution of polyacrylamide in corn syrup and the other consists of polyisobutylene/polybutene (PIB/PB), both exhibiting similar shear properties.

Cogswell [38,39] was the first to point out the necessity of taking into account the influence of extensional viscosity on vortex development. Having studied the flow of a low density polyethylene (LDPE), in comparison to the response of a polystyrene (PS) melt at two temperatures to provoke variation in the material functions, White and Baird [106,107] concluded that shear-thinning response must be considered along with extensional effects. Such a conclusion was reached from the fact that similar extensional viscosity (compared to that of LDPE) could be attained for the PS melt at higher flowrates and still no similar vortex growth was achieved. Raiford et al. [84] found a suppressive effect of inertia on vortex enhancement for a shear-thinning solution of polyisobutylene in tetradecane (PIB/C14) flowing through axisymmetric contractions. Byars et al. [27] pointed out that steady-state extensional viscosity in 4:1 axisymmetric contractions, is far from being attained due to the transient effects in a Lagrangian sense. Therefore, extensional stress growth at low deformation rates must be considered. On the other hand, a "Binding analysis" [14,15], based on the ideas of Cogswell, considered both steady-state shear and extensional viscosities (by means of power-law models) and their impact on vortex dynamics in contraction flows. This analysis has proven useful in providing extensional viscosities from entry pressure data (see reference [16]) for shear-thinning liquids (although not for Boger fluids) and in obtaining vortex attachment lengths [112]. However, Maia [59] and Maia and Binding [60] observed significant departures from experimental data when applying this analysis.

Rothstein and McKinley [85] studied the flow through axisymmetric contraction/expansion geometries. They associated the presence of lip vortices at $\hat{\beta} = 2$ with shear dominated flow in the case of a polystyrene PS/PS solution, and the presence of salient-corner vortices, at larger contraction ratios, with a dominant extensional effect. This transition was not detected for a PIB/PB Boger fluid, where lip-vortices were present for contraction ratios less than eight. In conclusion, Rothstein and McKinley proposed that transitions from lip to salient-corner vortices may be related to a normal stress ratio, $\aleph$, (shear/extensional deformation, see [85]). These authors explained their results referring to the different values of the normal stress ratio for the polymer solutions investigated. They found that higher values of $\aleph$ for a given polymer system and contraction ratio are related to lip-vortices.

Changing the geometry from circular to planar contractions has been found to suppress vortex enhancement for Boger fluids. This is not the case for shear-thinning polymer solutions/melts, where enhancement can be observed in both geometries [101]. Another important phenomenon present in contraction flows of viscoelastic fluids is the occurrence of enhanced pressure-drop, above that expected without considering elasticity. This would appear to be directly related to vortex growth [101]. Such behaviour has proved quite difficult to simulate, and in chapter 7, this problem is considered in depth.

A detailed review of experimental and computational work can be found in the text of Owens and Phillips [77] and the review paper of Walters and Webster [101]. The 4:1 contraction ratio has been widely used as a benchmark problem to asses the accuracy and stability of numerical schemes. Experimentally, for a Newtonian fluid, contraction ratios greater than 4:1 do not exhibit significant changes in flow characteristics. This statement does not hold for elastic liquids (see reference [101]).

Purnode and Crochet [83], via the numerical simulation of a single-mode of the Peterlin modification of the Finite Extensible Non-linear Elastic spring (FENE-P) model, were able to predict the planar contraction experimental results obtained by Evans and Walters [44,45] for polyacrylamide aqueous solutions with mild strain hardening and shear-thinning properties. In reference [83], streamlines are presented both from experiments and simulations, displaying in general, similar vortex characteristics (salient corner and lip vortices) although not matching on flowrate settings. This discrepancy in flowrates may be explained by appealing to three-dimensional effects, which are difficult to eliminate in experimental work, and the limited capability of the FENE-P model to represent adequately the rheology of PAA solutions. These numerical solutions were achieved with a finite element scheme proposed by Marchal and Crochet [62,63].

With a finite volume scheme based on the SIMPLER methodology, Yoo and Na [109] observed lip-vortex growth for an Oldroyd-B fluid, both in size and intensity with increasing Deborah number (De), whilst changes in salient-corner vortices were difficult to detect. In their work, inertia was found to exert a suppressive effect on vortex growth, though lip-vortices could still be observed. Lip-vortex activity for two linear Phan-Thien/Tanner (LPTT) fluids was reported by Carew et al. [28] with the use of a finite element method. The degree of hardening was controlled by the parameter ε_{PTT}; $\varepsilon_{PTT}=0.02$ corresponds to a strongly hardening fluid and $\varepsilon_{PTT}=0.25$ to a weakly hardening form. None of these fluids display extension-softening. A solvent to total viscosity ratio was chosen to be $\beta=1/9$ (a low solvent content polymer solution) and the Reynolds number was set to unity. For the strongly hardening LPTT fluid, the lip vortex was observed to increase with Weissenberg number; this increase continued until it became the single established vortex. For the LPTT($\varepsilon_{PTT}=0.25$)-case no lip-vortex activity was detected. Studies of Alves et al. [10] for the Upper Convected Maxwell (UCM) model, Phillips and Williams [80], Aboubacar and Webster [6] and Xue et al. [108] for an Oldroyd-B fluid, all based on finite volume discrete systems, report similar conclusions on lip-vortex activity. However, the capability of a numerical scheme to detect such lip-vortices, depends on the refinement of the mesh; whilst coarse meshes capture this feature, refined grids are unable to do so (see [6]).

For the original differential Pom-Pom model, Bishko et al. [19] simulated the transient flow of a polymer melt in a planar 4:1 contraction, the numerical procedure was a Lagrangian finite element method. An increase in the salient-corner vortex was observed upon increasing the number of arms, q, and the level of elasticity. Verbeeten et al. [98] simulated the transient flow of an LDPE melt in a 3.29:1 contraction using a multi-mode modified eXtended Pom-Pom (mXPP) and an exponential Phan-Thien/Tanner (EPTT) fluid model. The use of the mXPP was required in order to improve stability by modifying the stretch dynamics of the XPP model variants. Comparison against experimental data was also provided, showing excellent agreement in velocity profiles and stress related data. The method used is based on a finite element procedure with the Discrete Elastic Viscous Stress Splitting (DEVSS) technique, in combination with the Discontinuous Galerkin (DG) method. Sirakov et al. [87] studied the steady-state response of the XPP model for a 3D contraction geometry. The numerical results were tested against experimental information for a LDPE melt, finding errors within 15% for vortex cell-size measurements. Numerical deficiencies in the finite element study of Sirakov et al. were attenuated by setting $\alpha = 0$ and, additionally, modifying the square root term for stretch, λ. This modification introduces a smoothing function which accepts negative values of the trace of $\boldsymbol{\tau}$, and gives almost the same values of stretch as the original SXPP equation. Negative values of the trace of stress are unphysical; however, they may arise near the constriction plane in numerical simulations.

Numerical solutions in this chapter are obtained employing two finite volume schemes: a hybrid cell-vertex scheme (*fe/fv*) and a pure cell-centred (SLFV) scheme. Aboubacar et al. [4] reported results demonstrating spatial and temporal accuracy for the start-up and steady-state planar Poiseuille flow of an Oldroyd-B model fluid. The *fe/fv* scheme is described in chapter 3 and in reference [6], and the SLFV in [1,82], respectively. Steady-state solutions for channel flows have been obtained and found in excellent agreement in the previous chapter 4. Here, both schemes are tested on a complex 4:1 contraction flow of a kinetic model representing a low solvent content polymer system; the comparison is in terms of the influence of Weissenberg on stress, stretch, pressure-drop and salient-corner vortex dynamics. Simulations are generated for two levels of inertia ($Re = 0$ and $Re = 1$)[†]. A time-splitting procedure is applied within both methods to evolve the solution towards a steady-state.

5.2 Problem specification

Flow of a viscoelastic fluid through planar 4:1 sharp-corner contraction geometries is considered here. This type of complex flow, although not so complex

---

[†] Extremely low experimental levels of inertia are approximated here by setting $Re = 0$.

in geometry, exhibits regions with mixed shear and extensional phenomena. Large shear-rates are expected at the boundary walls, while pure extensional deformation is attained along the centreline (or centreplane) near the constriction plane; see Figure 5.1 for a diagram of this 4:1 contraction flow. Vortex growth dynamics, pressure-drop across the contraction, velocity overshoot along the symmetry-line, the numerical high Weissenberg number problem and how these responses are influenced by material functions, such as shear and extensional viscosity, are all features of considerable interest in the literature of viscoelastic contraction flows (see [77] for further details). Under creeping flow conditions, vortices can assume different shapes (see the works of Boger [25] and Evans and Walters [44,45]). For shear-thinning fluids, the cell-size tends to increase with elasticity. In reference [44], for a 1% aqueous solution of polyacrylamide, no lip vortex was observed. This is in agreement with the numerical results of Alves et al. [9].

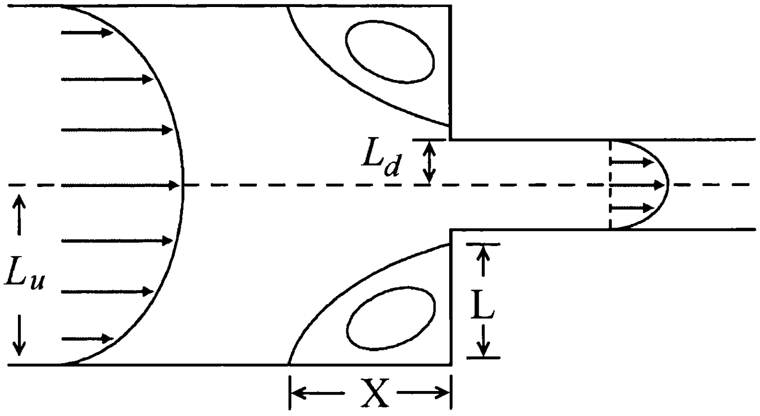

Figure 5.1. Schematic 4:1 contraction geometry: sharp-corner.

The velocity profile for the transient flow of an Oldroyd-B fluid in planar channel is imposed as an inlet boundary condition. Upstream channel distance is large enough for this Oldroyd-B model solution to evolve into the desired Pom-Pom profile. Natural boundary conditions are specified for velocity and extra-stress at the outflow of the domain, with no-slip boundary conditions imposed along the stationary walls.

The two alternative finite volume procedures described before are used to solve this 4:1 contraction flow. Comparison between both schemes is provided in terms of vortex dynamics and field variable computation results. Spatial convergence is ensured through the use of a series of meshes, each of increasing degree of refinement (element size). Details on the number of elements (*fe/fv*) or volumes (SLFV), degrees of freedom and minimum size of element for the meshes used, are reported in Table 5.1. The SLFV scheme employs non-uniform structured rectangular meshes. Cell-volume size reduces in the plane of the constriction and increases via a geometric progression of grid point spacing, as position moves away from the re-entrant corner in the axis parallel to the symmetry line. Unstructured triangular elements/volumes are utilized in the *fe/fv* procedure with finer discretisation around the re-entrant corner. Figure 5.2 displays the finest meshes (m3 for *fe/fv* and M4 for SLFV) used. The contraction is located at $x=0$ in all meshes. Upstream and downstream channel lengths are $27.5L_d$ and $49L_d$, respectively.

Table 5.1. Mesh characteristics parameters, *fe/fv* and SLFV schemes

	Mesh	***Elements/ volumes***	***Nodes***	***Degrees of freedom*** $(\mathbf{u}, p, \boldsymbol{\tau})$	R_{min}
fe/fv	***m1***	980	2105	13193	0.0243
	m2	1542	3279	20543	0.0190
	m3	2987	6220	38937	0.0063
SLFV	***M1***	2240		26880	0.1000
	M2	3200		38400	0.0900
	M3	3600		43200	0.0800
	M4	7200		86400	0.0400

Time-stepping procedure is stopped when the L_2-norm relative maximum difference between two successive time steps falls below 10^{-7}. Solutions at high Weissenberg numbers are derived via continuation in the elasticity parameter, starting from $We = 0.1$, followed typically by $We = 0.5$, 1, 3, 5, 10, 15, 20, ... until convergence is lost.

5.3 Numerical results

Results have been computed for a base set of SXPP parameters, namely: $\beta = 1/9$, $\varepsilon = 1/3$, $q = 2$ and $\alpha = 0.15$. This represents a low-hardening/extension softening fluid in uniaxial deformation with shear-thinning properties. Two levels of inertia are considered ($Re = 0$ and 1). Calculations have been performed for Weissenberg numbers in the range $0 \leq We \leq 60$[‡].

a) Unstructured (m3)

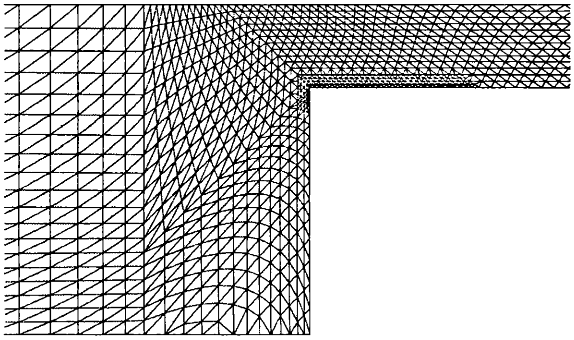

b) Structured (M4)

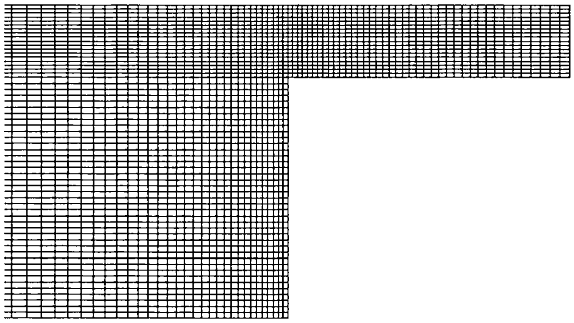

Figure 5.2. *fe/fv* mesh (m3) and SLFV (M4), in contraction zone.

[‡] Results beyond $We = 20$ are for *fe/fv* only.

5.3.1 Mesh convergence and vortex dynamics

Figure 5.3 presents creeping flow centreline profiles of velocity (u_x) component, stretch (λ), normal stress component (τ_{xx}) and pressure (p) for $We=0.1$ and $We=10$. Centreline velocity displays a small overshoot at $We=10$, which is difficult to detect for $We=0.1$. The effect of increasing elasticity of the fluid, is reflected in the large increment of the required length for relaxation of the backbone stretch and stress τ_{xx}, once the contraction has been passed.

Note that for $We=10$, normal stress has not recovered its fully-developed centreline value ($\tau_{xx}=0$) even 20 units after the contraction plane, while for $We=0.1$ this occurs before roughly 3 units after the constriction. This increase in elasticity reduces the pressure-drop from around 145 to 23 units due to shear-thinning (exit pressure is set to zero for both numerical procedures). The reduction in the peak value of τ_{xx} with increasing elasticity is due to strain-softening that becomes more prominent for $We \geq 5$. The *fe/fv* scheme predicts slightly larger and sharper overshoots in λ and τ_{xx} than those computed with the SLFV scheme at $We=10$, although simulation results for both schemes are in close agreement.

Contour lines for stream function are provided in Figure 5.4 for $Re=0$ and 1, covering Weissenberg numbers in the range $0.1 \leq We \leq 60$. Here, focus is on the dimensionless salient-corner vortex size parallel to the symmetry line, X (see Figure 5.1), which is normalised by the height of the inlet channel ($2L_u$).

For creeping flow, this vortex cell-size gradually grows with elasticity (see Figure 5.5a). This behaviour is also reported by Bishko et al. [19] for the differential approximation to the original Pom-Pom model. The opposite response is obtained for the ($Re=1$)-case.

a) Centreline profiles, low We

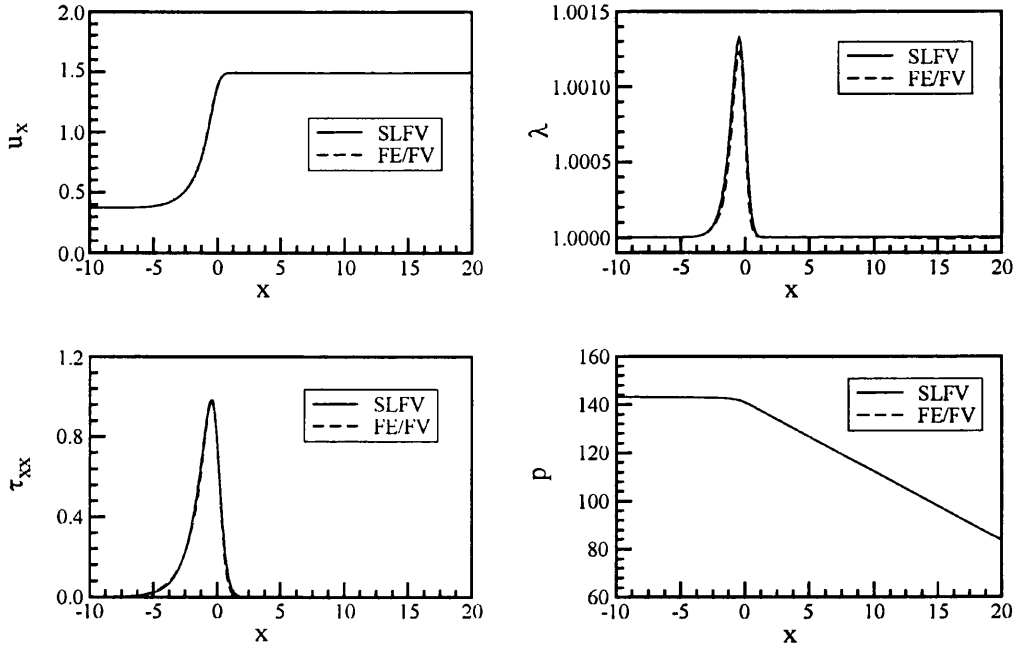

b) Centreline profiles, high We

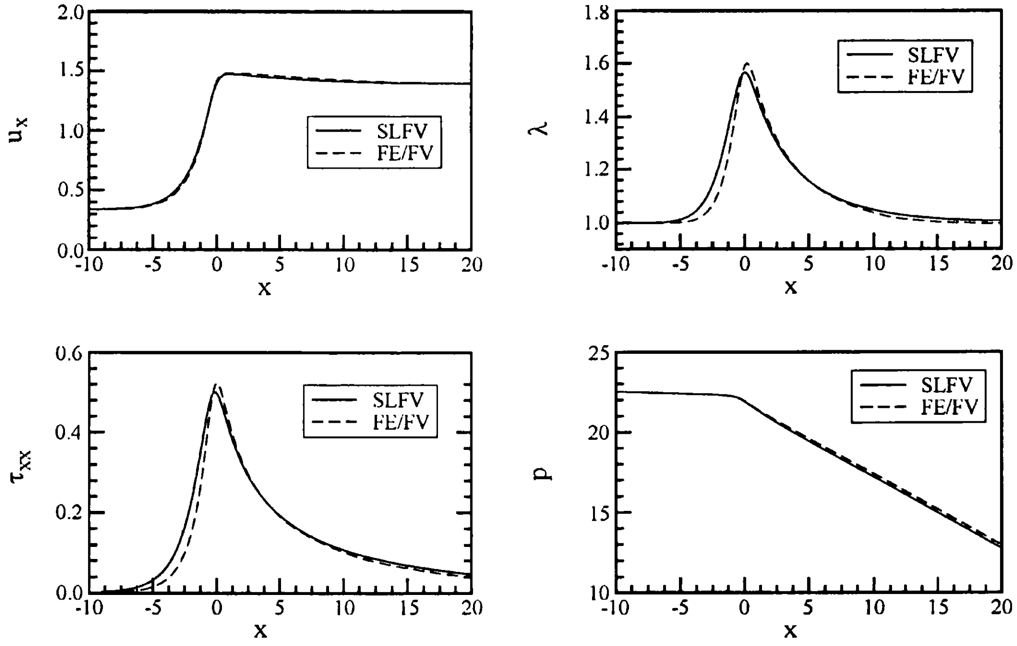

Figure 5.3. Symmetry line flow results at $Re = 0$: $\beta = 1/9$, $\varepsilon = 1/3$, $q = 2$, $\alpha = 0.15$; a) $We = 0.1$, b) $We = 10$.

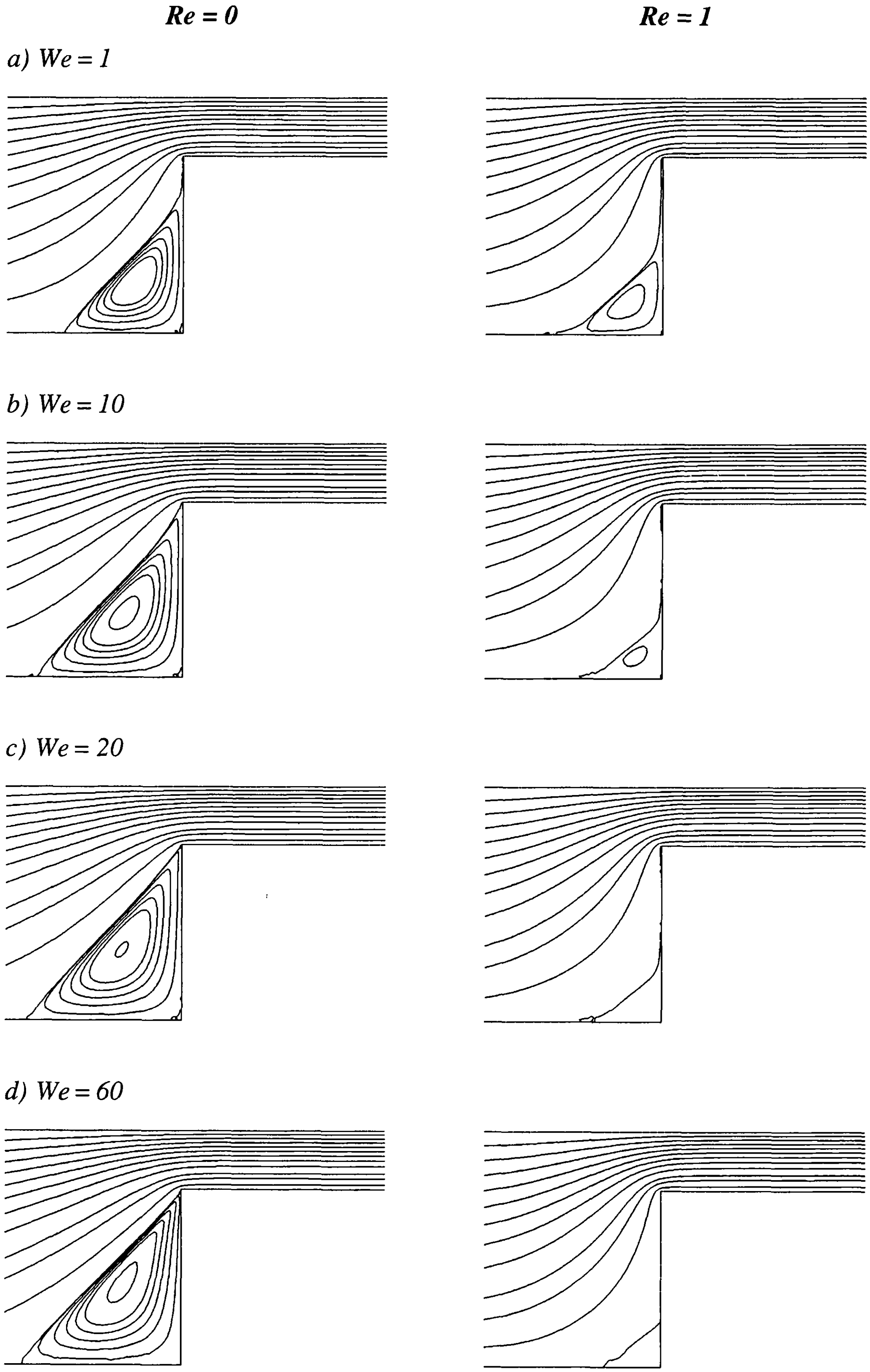

Figure 5.4. Stream function with increasing *We*: $\beta = 1/9$, $\varepsilon = 1/3$, $q = 2$, $\alpha = 0.15$; $Re = 0$ and 1.

a) Cell-size

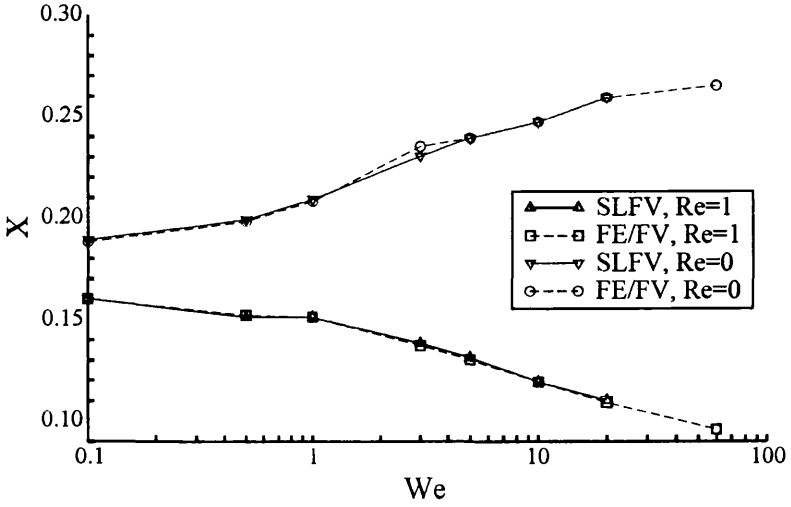

b) Intensity

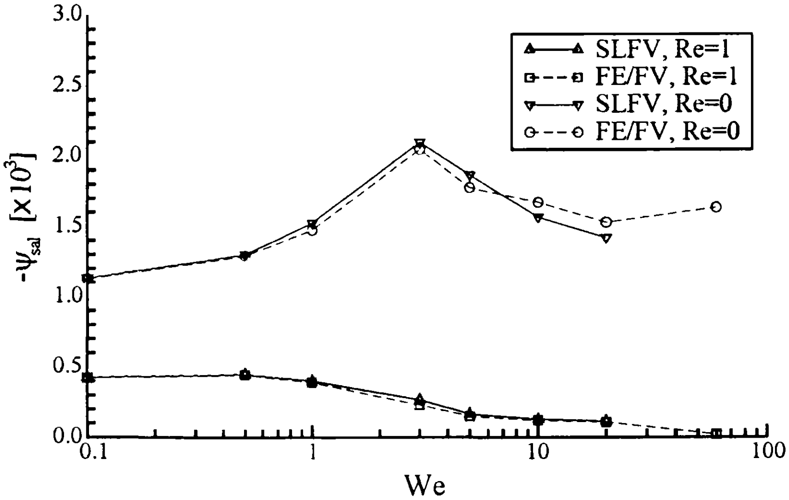

Figure 5.5. Salient-corner vortex trends with increasing We: $\beta = 1/9$, $\varepsilon = 1/3$, $q = 2$, $\alpha = 0.15$, $Re = 0$ and 1; a) cell-size, b) intensity.

A similar trend in this flow geometry, was obtained by Aboubacar et al. [2,3] for a PTT fluid with $\varepsilon_{PTT} = 0.25$ - a fluid with comparable extensional behaviour. Contrasting these moderate responses in uniaxial extension, Oldroyd-B model and EPTT($\varepsilon_{PTT} = 0.02$) both display severe strain-hardening, even at moderate extension rates, reducing critical We. No lip-vortex is detected with either of the schemes. This is consistent with Carew et al. [28] for a Linear Phan-Thien/Tanner (LPTT) model at $\varepsilon_{PTT} = 0.25$, and with Bishko et al. [19] for the original differential Pom-Pom model.

Contrary to the increase in vortex intensity and cell-size growth for $Re = 0$, there is vortex reduction in both their magnitudes when elasticity increases and upon the introduction of inertia. Although a slight increase in intensity can be observed up to $We = 0.5$ a monotonic decrease occurs afterwards. Considering $We = 20$, for example, the suppressive vortex growth effect at $Re = 1$ reduces intensity by about 90% from that of the ($Re = 0$)-case.

The two finite volume schemes are in excellent agreement, with slight departures in intensity when inertia is absent. Information is provided to confirm satisfactory mesh convergence in Table 5.2 and Table 5.3, covering the salient-corner vortex cell-size in the range $0.1 \le We \le 20$ for $Re = 0$ and $Re = 1$, respectively.

Table 5.2. Mesh convergence: salient-corner vortex cell-size (*X*), *Re=0*

	fe/fv			SLFV	
We	***m1***	***m2***	***m3***	***M3***	***M4***
0.1	0.185	0.188	0.188	0.189	0.189
1	0.206	0.208	0.208	0.209	0.209
5	0.236	0.239	0.239	0.239	0.239
10	0.242	0.247	0.247	0.247	0.247
20	0.255	0.259	0.259	0.259	0.260

For the SXPP model, meshes must be sufficiently fine in order to obtain converged solutions for larger Weissenberg numbers. This lies in contrast to other models, such as Oldroyd-B, where convergence fails if the mesh is too fine for moderate values of *We* (typically ≈ 3).

Table 5.3. Mesh convergence: salient-corner vortex cell-size (*X*), *Re = 1*

	fe/fv			SLFV			
We	***m1***	***M2***	***m3***	***M1***	***M2***	***M3***	***M4***
0.1	0.163	0.160	0.160	0.162	0.161	0.161	0.160
1	0.153	0.151	0.151	0.153	0.152	0.151	0.151
5	0.133	0.130	0.130	0.134	0.133	0.131	0.131
10	0.122	0.119	0.119	-	-	0.119	0.119
20	0.113	0.109	0.109	-	-	0.110	0.110

5.3.2 Stretch, stress and deformation-rate fields

Following the work of Bishko et al. [19], the inflow section can be divided into two regions of relatively unstretched fluid, and a third of highly stretched material. These "unstretched" zones are located near the centreline and in the vortex region. The third region is a banded zone between the other two, in which the fluid moves to the downstream channel. It is possible to recognize this feature for creeping flow in Figure 5.6 for the We-range covered. Large stretch zones are detected near the re-entrant corner and along the downstream wall.

Stretch increases in magnitude with We. Extensional effects dominate in the banded region (see Figure 2.5d). Note that for $We = 20$ and 60, in a small zone above the re-entrant corner, the stretch exceeds the number of dangling arms, breaking the extensibility constraint $\lambda \leq q$, proposed in the original formulation of the Pom-Pom model. As mentioned earlier, this constraint has been removed in the XPP versions.

Contour field plots for polymeric stress τ_{xx} and τ_{xy} are shown in Figure 5.7 and Figure 5.8, respectively. In general, reduction in both normal and shear stress magnitudes can be seen in the flow field as elasticity increases. This is consistent with the planar channel flow simulation results obtained by van Os and Phillips [76] and those presented in the previous chapter. The decrease in τ_{xy} is more noticeable in the banded region, where extension dominates over shear deformation.

The polymeric stress difference, N_1, follows similar trends to those exhibited by τ_{xx}, with a net reduction in magnitude under increasing elasticity across the flow domain. Such a response may be attributed to the strain softening of the extended Pom-Pom fluid modelled. Corresponding contour lines plots are displayed in Figure 5.9.

Since for this study the anisotropy parameter is set at $\alpha = 0.15$, a nonzero second normal stress difference, N_2, is expected even in regions where shear deformation is the dominant effect (refer to Figure 5.10). There is some resemblance in N_2-fields with vortex growth and curvature structure as We increases for the two different levels of inertia. This response has been detected likewise by Aboubacar et al. [2] working with EPTT fluids.

The extensional component of the rate of deformation tensor, d_{xx}, exhibits two regions of extreme values: a positive one located just before the contraction along the symmetry line, and another with negative (and larger in magnitude) values in the inflow section reaching the re-entrant corner. As can be observed in Figure 5.11, elasticity and inertia only slightly influence d_{xx}-profiles, apart from in the recirculation vortex region, where the magnitude of the rate of deformation is close to zero.

Peak values of d_{xy} arise within a zone near to the sharp corner. For this shear component, there are two regions where any influence of elasticity may be gathered. The first, is the negative d_{xy}-region situated just before the re-entrant corner (see between the two contour lines where $d_{xy} = 0$ in Figure 5.12), which suffers a reduction in size but only for the zero inertia case. The other We-influenced zone lies above the downstream wall, where a reduction in the value of this shear component is also detected, but now for both values of the Reynolds number.

Re* = *0　　　　***Re* = *1***

a) We = 1

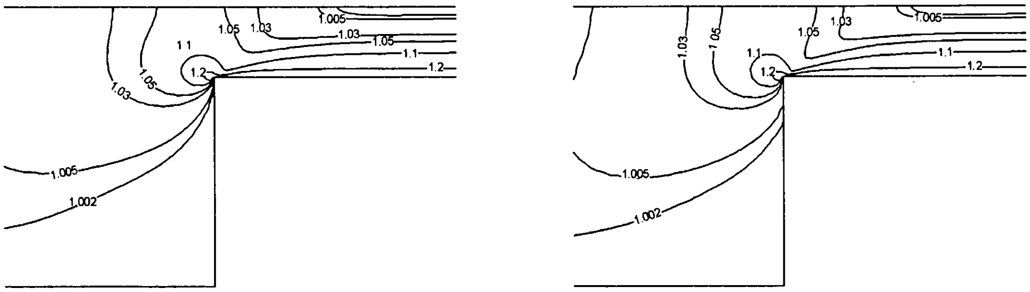

b) We = 10

c) We = 20

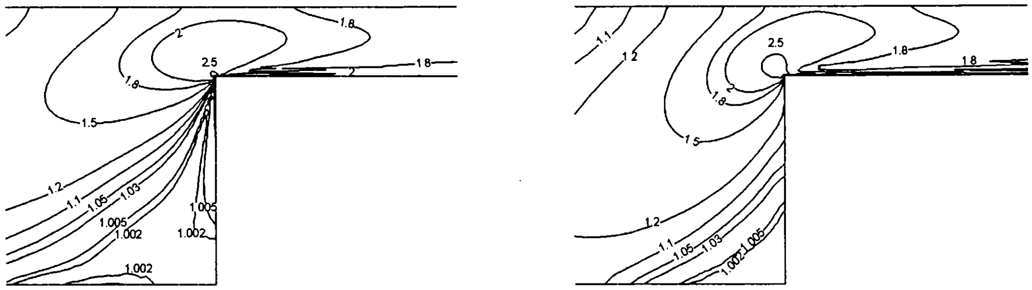

d) We = 60

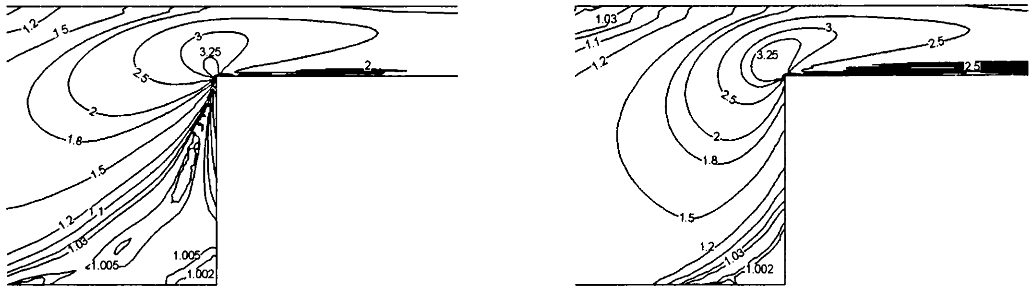

Figure 5.6. Backbone stretch λ-fields, increasing *We*: $\beta = 1/9$, $\varepsilon = 1/3$, $q = 2$, $\alpha = 0.15$, $Re = 0$ and $Re = 1$.

Re = 0 ***Re = 1***

a) We = 1

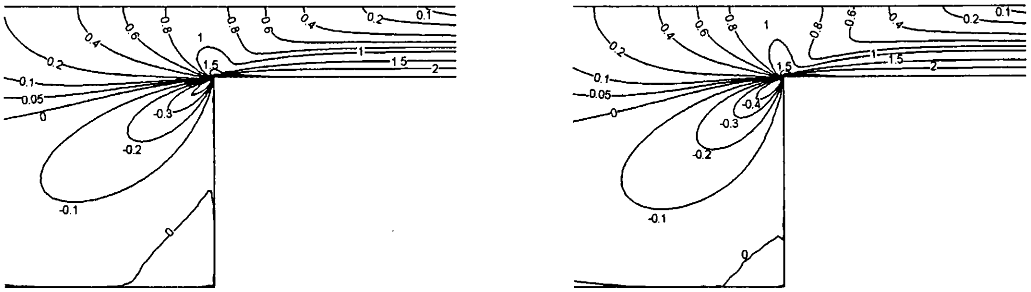

b) We = 10

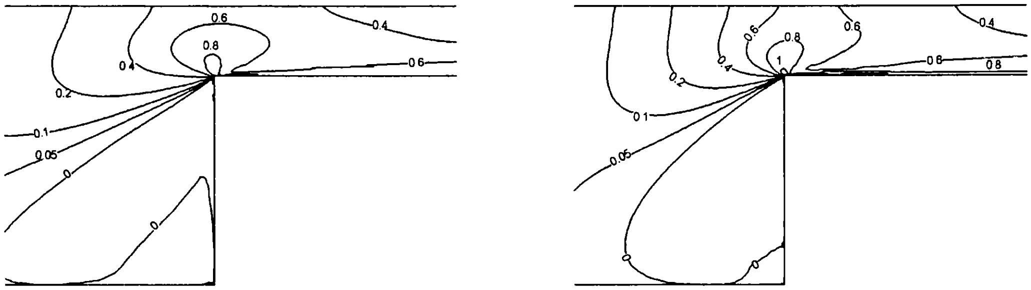

c) We = 20

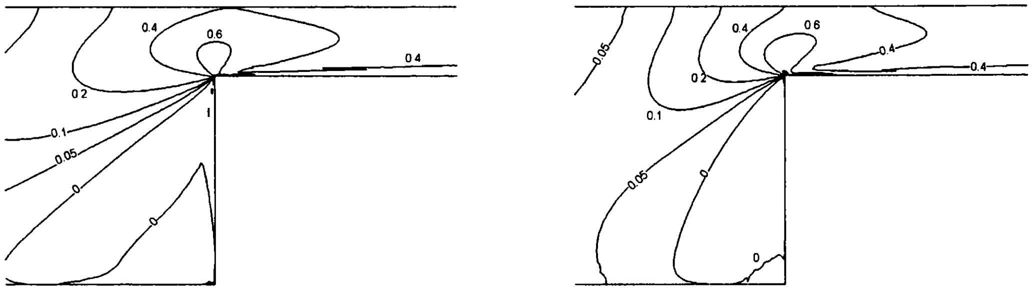

d) We = 60

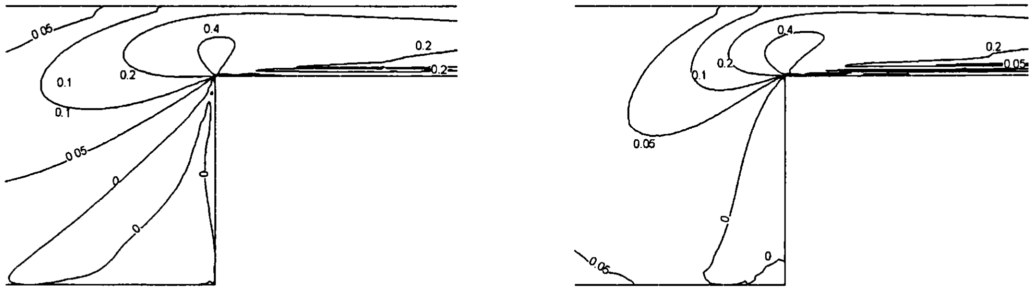

Figure 5.7. Normal stress τ_{xx}-fields, increasing *We*: $\beta = 1/9$, $\varepsilon = 1/3$, $q = 2$, $\alpha = 0.15$; $Re = 0$ and $Re = 1$.

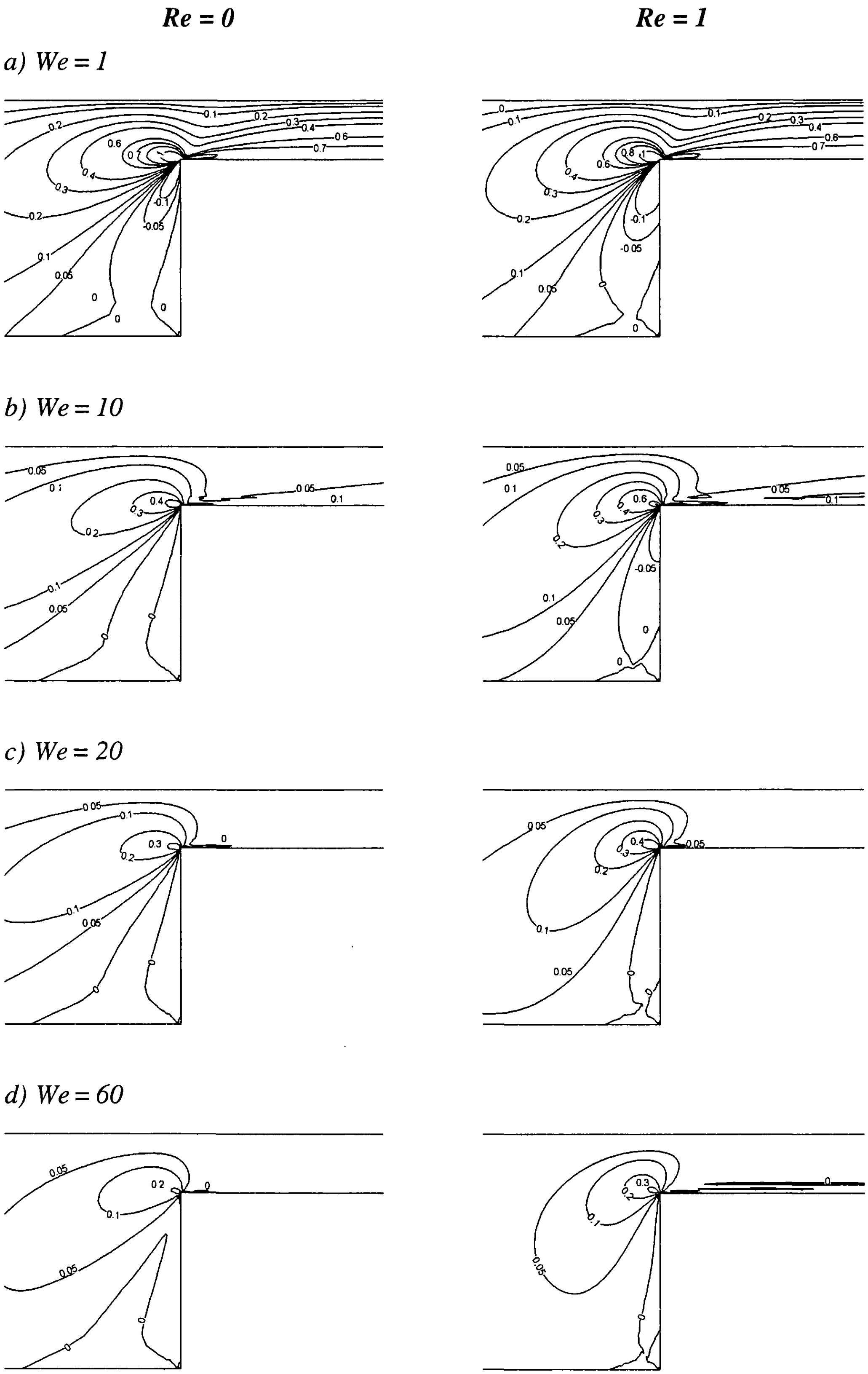

Figure 5.8. Shear stress τ_{xy}-fields, increasing We: $\beta = 1/9$, $\varepsilon = 1/3$, $q = 2$, $\alpha = 0.15$; $Re = 0$ and $Re = 1$.

Re = 0 ***Re = 1***

a) We = 1

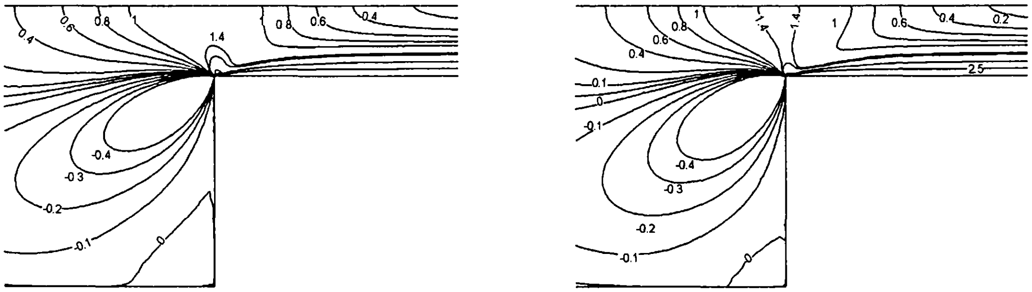

b) We = 10

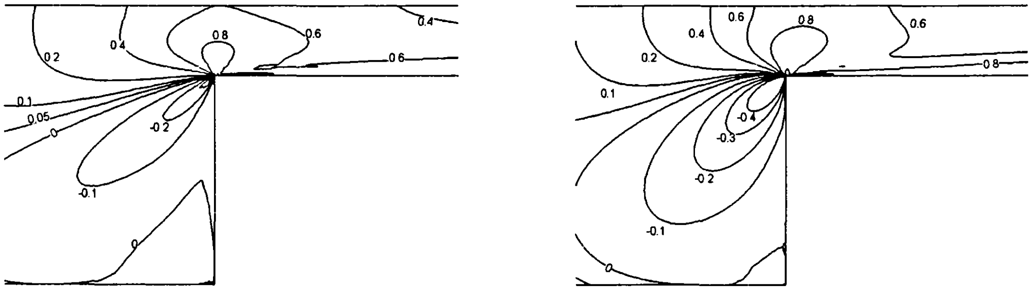

c) We = 20

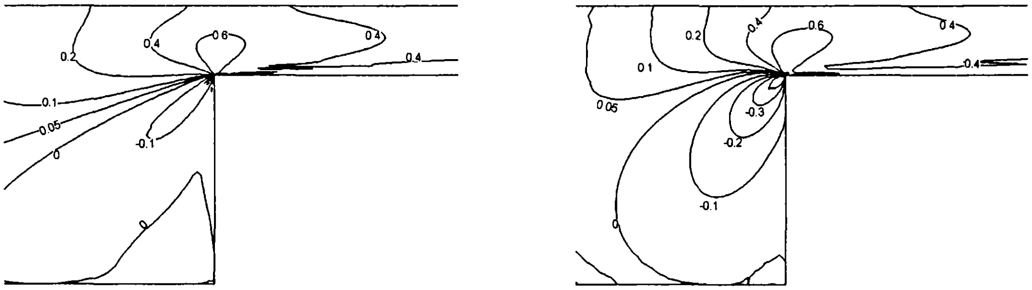

d) We = 60

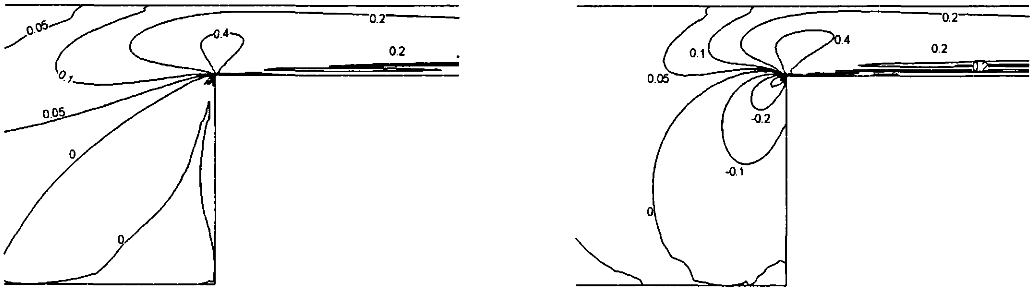

Figure 5.9. First normal stress difference (polymeric): N_1-fields, increasing We: $\beta = 1/9$, $\varepsilon = 1/3$, $q = 2$, $\alpha = 0.15$; $Re = 0$ and $Re = 1$.

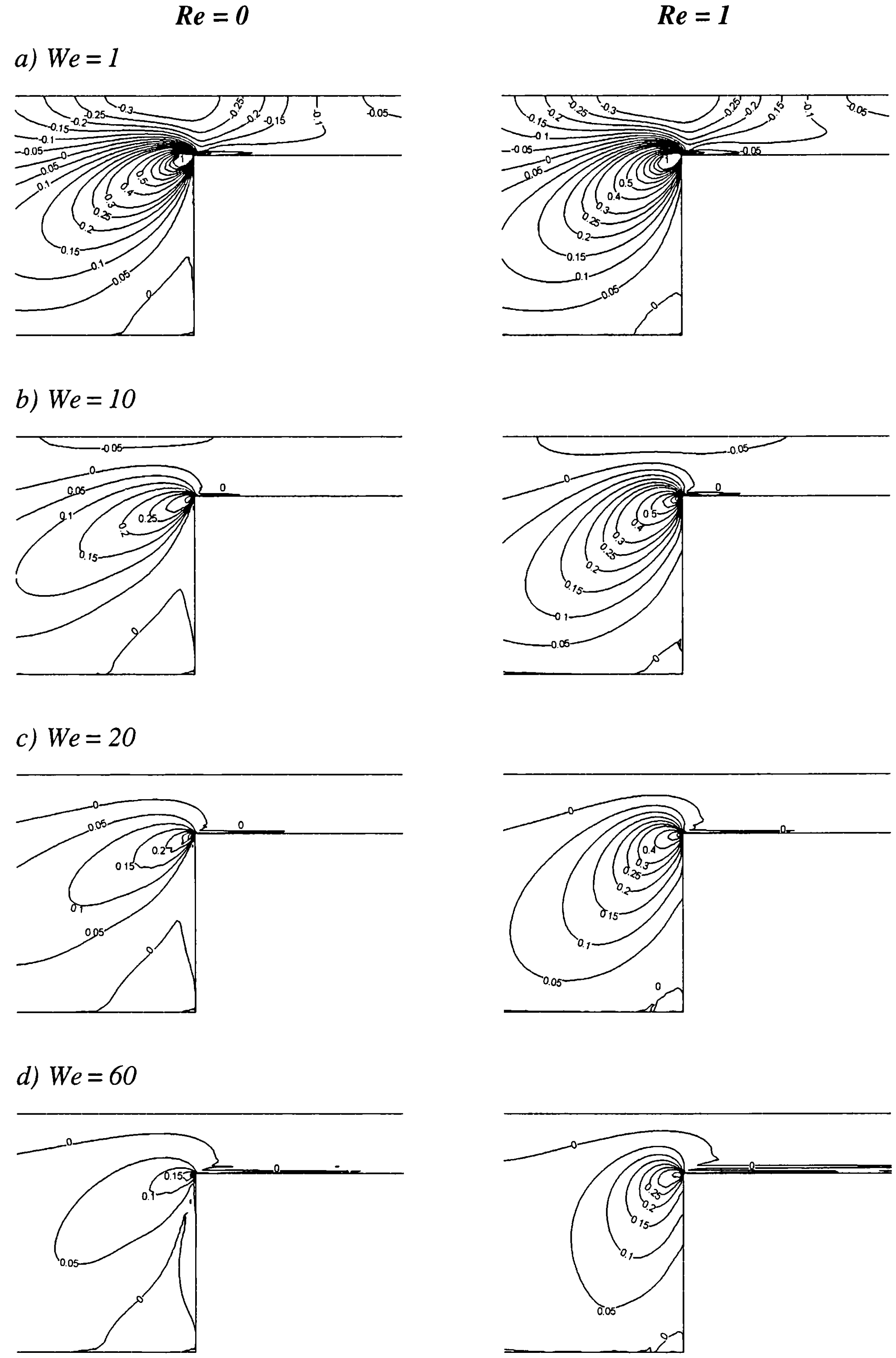

Figure 5.10. Second normal stress difference N_2-fields, increasing We: $\beta = 1/9$, $\varepsilon = 1/3$, $q = 2$, $\alpha = 0.15$; $Re = 0$ and $Re = 1$.

Re = 0 ***Re = 1***

a) We = 1

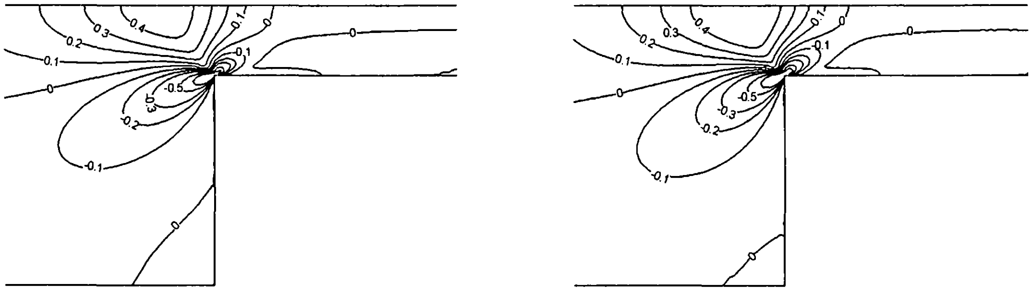

b) We = 10

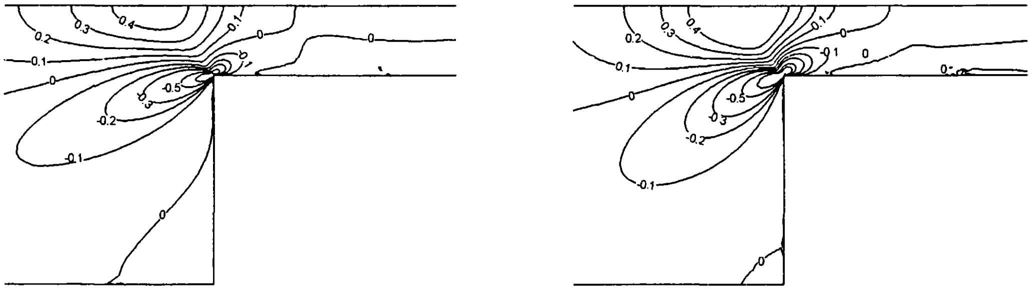

c) We = 20

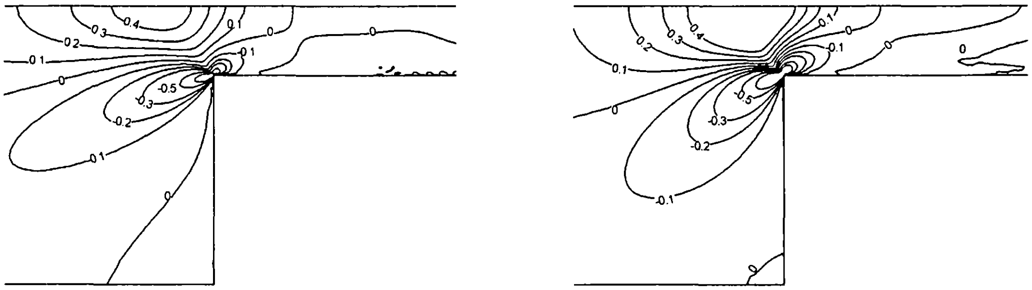

d) We = 60

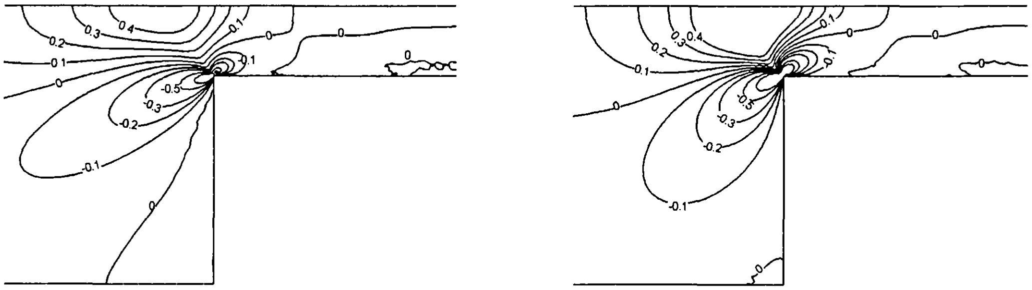

Figure 5.11. Rate of strain d_{xx}-fields, increasing We: $\beta = 1/9$, $\varepsilon = 1/3$, $q = 2$, $\alpha = 0.15$; $Re = 0$ and $Re = 1$.

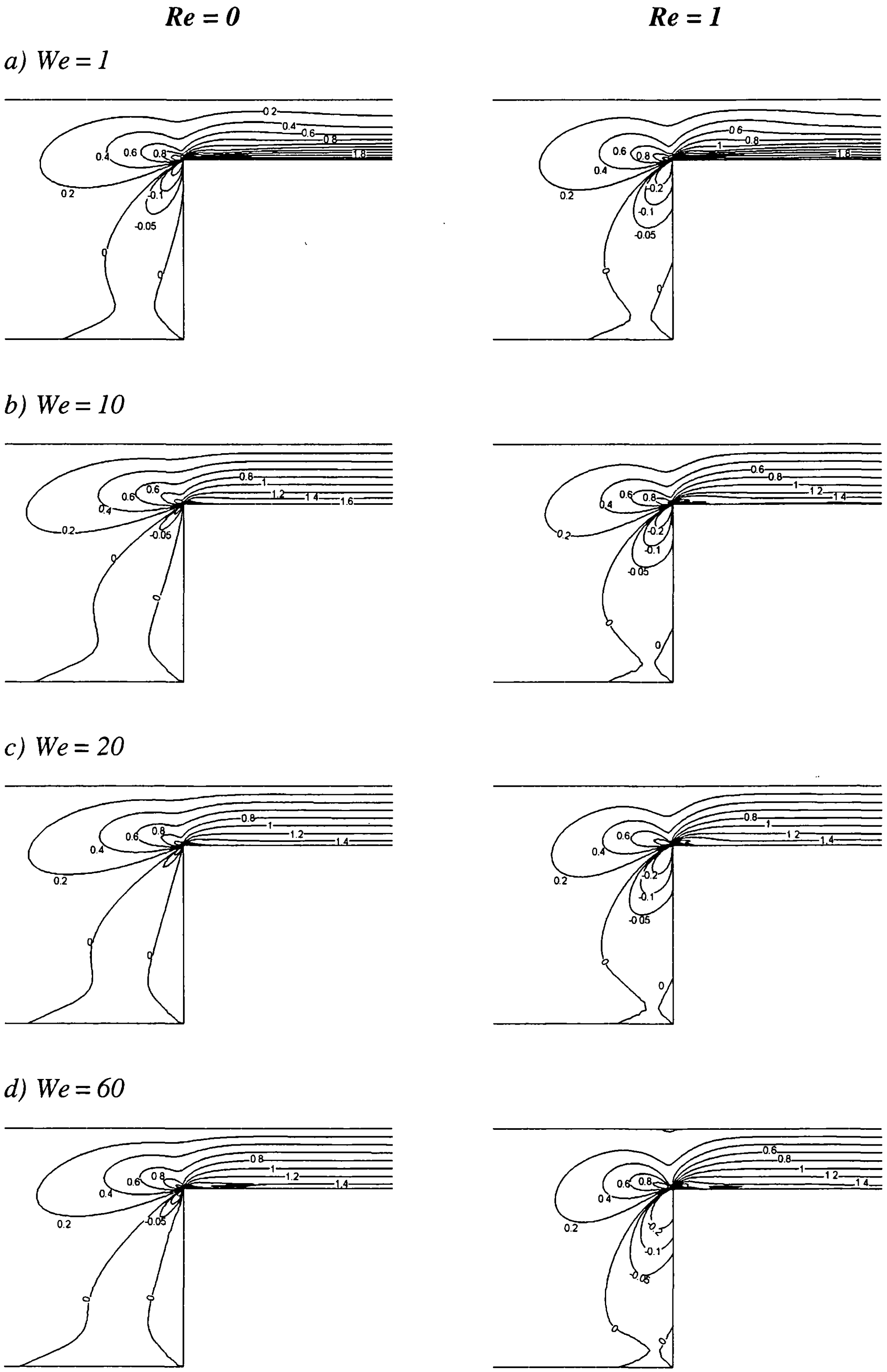

Figure 5.12. Rate of strain d_{xy}-fields, increasing *We*: $\beta = 1/9$, $\varepsilon = 1/3$, $q = 2$, $\alpha = 0.15$; $Re = 0$ and $Re = 1$.

Note that, the regions of largest backbone stretch λ in the inflow section of the contraction, are located where peak values of d_{xx} occur (the negative peak in the sharp corner). Values of stretch and polymeric first normal stress difference at selected points (see Figure 5.13) are reported in Table 5.4 to allow for further detailed comparison between the performance of the two numerical schemes employed.

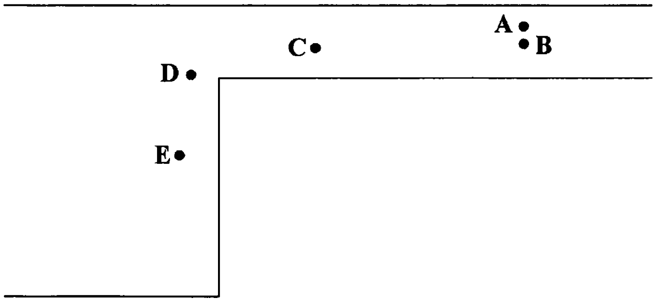

Figure 5.13. Sample points used in the 4:1 contraction domain.

Table 5.4. Values of stretch (λ) and first normal stress difference (N_1) at sample points, *Re=0* (contraction point at *x=0.0*, *y=3.0*)

		fe/fv			SLFV		
Sample-points	***We***	***1***	***10***	***20***	***1***	***10***	***20***
A	λ	1.01	1.16	1.35	1.01	1.18	1.35
$(x=19.9, y=3.78)$	N_1	0.13	0.22	0.2	0.14	0.23	0.2
B	λ	1.05	1.5	1.72	1.06	1.55	1.7
$(x=19.9, y=3.50)$	N_1	0.76	0.53	0.37	0.81	0.58	0.37
C	λ	1.05	1.49	1.65	1.06	1.55	1.71
$(x=9.99, y=3.78)$	N_1	0.76	0.52	0.34	0.8	0.57	0.37
D	λ	1.01	1.26	1.45	1.01	1.36	1.55
$(x=-1.94, y=3.07)$	N_1	0.24	0.21	0.18	0.25	0.27	0.2
E	λ	1.01	1.23	1.41	1.01	1.26	1.39
$(x=-2.00, y=2.07)$	N_1	-0.23	0.04	0.02	-0.19	0.03	0.05

5.3.3 Pressure-drop and an alternative Pom-Pom model

Pressure drop as function of *We* is plotted for the two inertia levels set in this study. This quantity is normalised through the correspondent pressure-drop for a Newtonian fluid with the same zero shear-rate viscosity η_0 of the viscoelastic fluid and set at equal flowrate. As the SXPP fluid selected is shear-thinning, $\Delta p/\Delta p_{Newt}$ decreases monotonically with increasing elasticity, seeming to reach a plateau at $We = 20$. This decrease is less sharp for $Re = 1$. No differences can be detected between solutions with *fe/fv* and SLFV (see Figure 5.14).

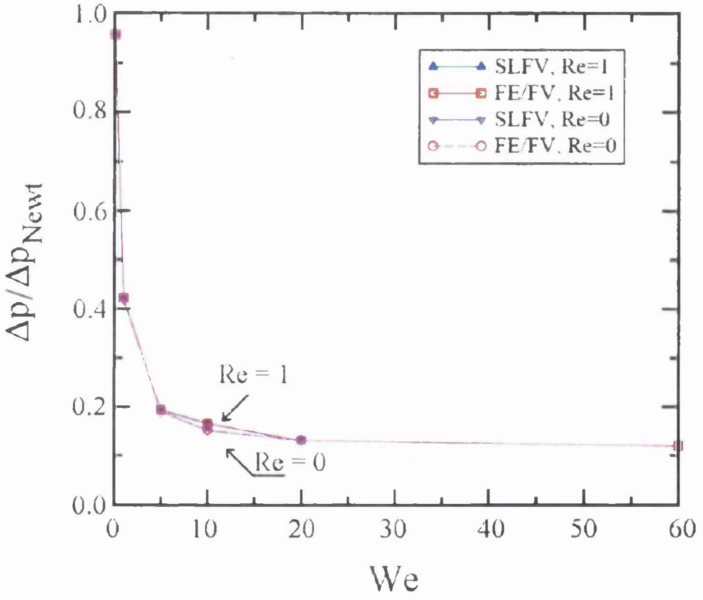

Figure 5.14. Pressure-drop vs. *We*: $\beta = 1/9$, $\varepsilon = 1/3$, $q = 2$, $\alpha = 0.15$; SLFV and *fe/fv* schemes, $Re = 0$ and 1.

A modification of the DXPP model was performed to well-suit implementation in a coupled solver of a spectral element technique, implemented by van Os and Phillips [76]. In the double extended Pom-Pom model, the stretch, λ, is governed by a partial differential equation and, instead of solving for the extra-stress, this formulation should be solved for the orientation tensor $\mathbf{S}$. Then, an explicit equation must be evaluated in order to extract $\boldsymbol{\tau}$. With a change of variable ($\mathbf{A} = \lambda^2\mathbf{S}$) made in the double extended model, the resulting modification can be considered as a hybrid of SXPP and DXPP models (see section 2.3.3). This alternative formulation was implemented in reference [76]. In the present work, the new modification is termed the λ^2XPP model (section 2.3.3a).

A comparison between predictions of velocity and stretch profiles in planar Poiseuille flow is provided in Figure 5.15. This comparison is at a high elasticity level ($We = 10$) and no departure between the two steady-state model solutions can be appreciated.

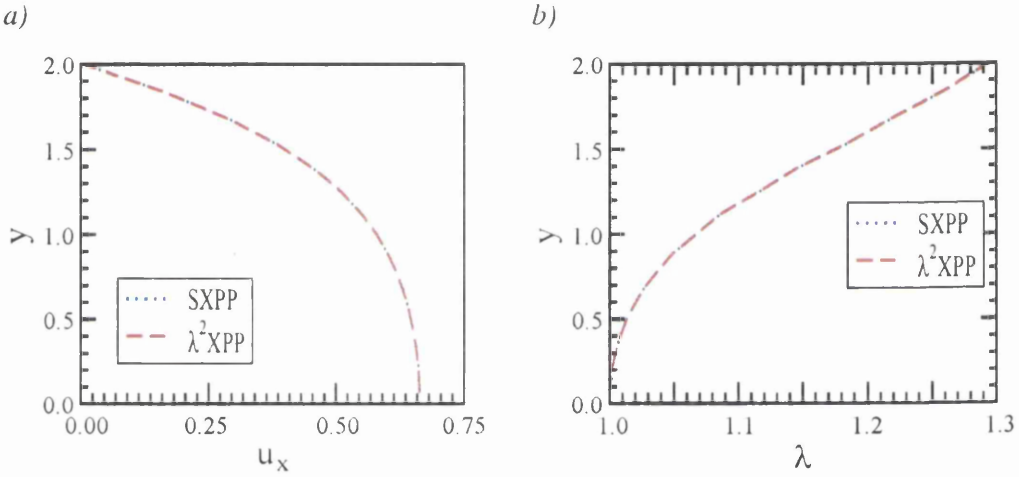

Figure 5.15. SXPP vs. λ^2XPP profiles in planar channel flow with the *fe/fv* scheme: $We = 10$, $Re = 1$, $\beta = 1/9$, $\varepsilon = 1/3$, $q = 2$, $\alpha = 0.15$; a) velocity, b) stretch.

For 4:1 planar contraction flow, centreline results are presented in Figure 5.16. Again, no discrepancy can be observed between either model, even in peak values. The numerical technique used for the Poiseuille and 4:1 contraction flow of the two XPP models is the *fe/fv* scheme.

5.4 Conclusions

The problem studied here is the flow through a 4:1 sharp contraction geometry of a fluid exhibiting low-strain-hardening/softening in uniaxial deformation and

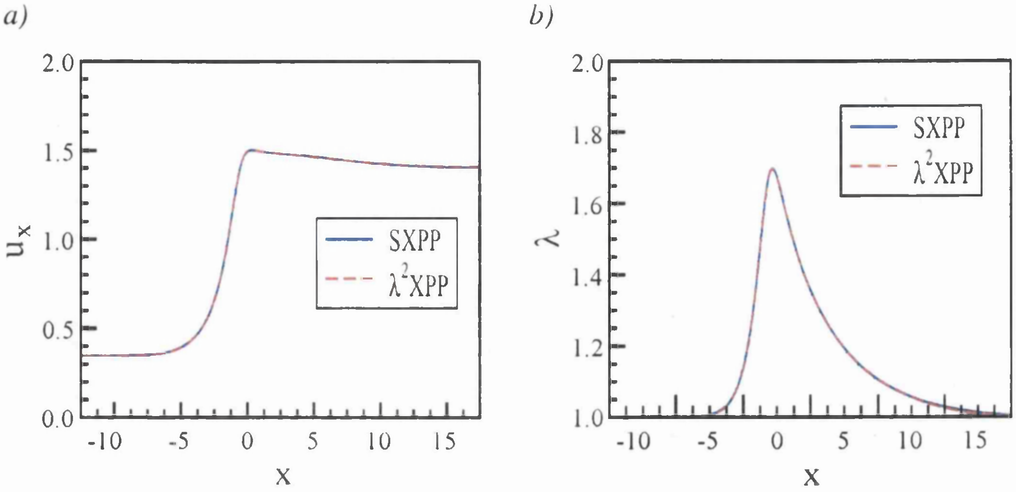

Figure 5.16. SXPP vs. λ^2XPP centreline results in planar 4:1 sharp contraction flow with the *fe/fv* scheme: $We = 10$, $Re = 0$, $\beta = 1/9$, $\varepsilon = 1/3$, $q = 5$, $\alpha = 0.15$; a) velocity, b) stretch.

thinning in shear flow. Fluid response under such complex flow is explained in terms of the rheometrical properties exhibited by the particular XPP fluid selected here.

Two contrasting finite volume schemes have been tested for this benchmark complex flow. The first is a cell vertex hybrid finite element/finite volume procedure with consistent treatment of flux and source terms. The second is a pure finite volume method with a semi-Lagrangian treatment on convection terms; contributions from previous time-step are evaluated with a second-order area-weighting procedure. Data qualifying mesh convergence has been reported in terms of vortex growth. Both schemes are in excellent agreement over a range of Weissenberg numbers for the chosen XPP fluid.

For the ($Re = 0$)-case, vortex cell-size has been found to increase with increasing Weissenberg number. Correspondingly, vortex intensity also increases up to $We = 3$; after this stage, a decrease in intensity is observed for further increments in elasticity. Inertia has the opposite influence on the cell-size of the vortex (monotonic decrease for $Re = 1$). Initially, vortex intensity has grown slightly, from $We = 0.1$ to 0.5, followed by a steady decline thereafter. Qualitative agreement has been achieved between the XPP model and the exponential PTT($\varepsilon_{PTT} = 0.25$) model, both fluids exhibit similar extensional viscosity and the same levels of shear-thinning under rheometrical flows. As reported by Bishko et al. [19], the entry flow section has been identified as a zone where extensional deformation dominates over shear flow. Therefore, large backbone stretch is observed in this region. The fluid lying above the downstream wall is subjected to shear and practically zero extensional deformation.

CHAPTER 6

Influence of Extensional Viscosity on Pom-Pom Modelling*

The Pom-Pom class of models present the advantage that by increasing the dangling arms at each end of the Pom-Pom molecule, the extensional viscosity (η_e) may be increased considerably without provoking significant variation in the correspondent shear viscosity (η_s). This is so for a range of deformation rates, at a given viscosity ratio (β). In this chapter, the influence of extensional viscosity is studied in a complex flow setting, involving shear and extensional deformation. The problem chosen is flow through a 4:1 rounded-corner contraction geometry. Additionally, a comparison with the exponential Phan-Thien/Tanner (EPTT) phenomenological network-based model is provided for fluid parameters with similar response in rheometrical flows. The stability of a hybrid finite element/finite volume (*fe/fv*) scheme for the Single eXtended Pom-Pom (SXPP) model is investigated for a range of Weissenberg (We) numbers. Considering the deformation-rates attained for

---

* Material of this chapter has been shaped in the paper "Extensional response of the pom-pom model through planar contraction flows for branched polymer melts" by J. P. Aguayo, H. R. Tamddon-Jahromi and M. F. Webster, and published in *Journal of Non-Newtonian Fluid Mechanics* **134** (2006) 105-126.

this particular complex flow setting, distinction may be drawn between fluids that display either extension softening or extension-hardening properties. This may be gathered through observation of vortex behaviour, stretch, stress and pressure-drop. Special attention is given to the anisotropy parameter introduced in the XPP model to account for non-vanishing second normal stress difference in simple shear flow.

6.1 Introduction

In Chapter 5 the flow of a SXPP fluid was considered through a planar 4:1 sharp contraction geometry. In this chapter, the scope is extended to consider the influence of variation in the extensional viscosity in such a complex flow situation. With the objective of improving the maximum level of elasticity attainable (We_{crit}), the sharp contraction is replaced by a rounded re-entrant corner. By doing so, the influence of extensional response may be studied for a wider range of We.

The finite element/finite volume (*fe/fv*) scheme used here has been successfully applied to simulate phenomenological models, in particular, the constant shear viscosity Oldroyd-B and a variety of Phan-Thien/Tanner (PTT) versions, for transient Poiseuille [4] and planar/axisymmetric 4:1 contraction flows [2,3]. Numerical results show qualitative agreement when predicting experimental features of contraction flows, such as vortex inhibition for Boger fluids in planar contractions and vortex growth in its axisymmetric counterpart [2][†]. This applies also to vortex dynamical trends in terms of cell-size and structure for shear-thinning fluids, with comparable response as observed for linear low density polyethylene (LLDPE) and low density polyethylene (LDPE) blends [95].

In order to obtain quantitative agreement with experimental data, models capable of representing well the rheometrical response of real fluids must be considered.

[†] Boger fluids are solution systems with sufficiently low content of viscoelastic component to detect any variation in the shear viscosity of the solvent; however, models such as Oldroyd-B and FENE-CR, which predict constant shear viscosity, can behave similarly to Boger fluids even with the high viscoelastic content employed in reference [2].

PTT, Giesekus, and the Kaye-Bernstein-Kearsley-Zapas (K-BKZ) models are phenomenological constitutive equations commonly used to model polymer melt behaviour. Giesekus models in extensional deformation sustain hardening with increase in strain-rates; yet ultimately, a plateau is reached. Mitsoulis et al. [70] employed a modified multi-mode K-BKZ to simulate the contraction flow of LDPE melts. There, vortex cell-size was successfully predicted. These authors considered both extension and shear stress to make the comparison. Moreover, PTT models can reproduce a variety of rheological responses (see sections 2.3.2 and 6.3.3) in both planar and uniaxial extensions, though the parameter controlling the degree of extension, ε_{PTT}, also affects the shear-viscosity (see Matallah et al. [66]).

The eXtended Pom-Pom (XPP) models, proposed by Verbeeten et al. [96], are capable of reproducing the response of polymeric systems in rheometrical flows. These versions are derived from the kinetic-based Pom-Pom model introduced by McLeish and Larson [68] and is based on reptation dynamics of an idealized linear molecule with an equal number of branched arms at both ends (see Figure 2.3). An important aspect of the SXPP model is the capability of increasing the extensional viscosity levels with minor variation of shear-viscosity for a range of deformation rates and solvent to total viscosity ratios, β (see Figure 2.5).

Inkson et al. [51] found that a multi-mode Pom-Pom model with a physically reasonable distribution of branching is able to reproduce the material functions of a LDPE melt, covering four decades in deformation-rates. In general, an excellent fit of steady-state shear and extensional viscosity was obtained by Zatloukal [110], for three polymer melts being, LDPE, metallocene-catalyzed LLDPE (mLLDPE) and Polyvinyl butyral (PVB). The performance of the XPP model was tested against a modified White-Metzner and Leonov models. Bogaerds et al. [23] found that setting low values of the anisotropy parameter α, i.e. having some second normal stress difference (N_2) contribution, produces a stabilizing effect on Couette and Poiseuille flows. Significant differences in the dynamic response between the material functions of the Exponential PTT (EPTT) and the XPP model were also found.

Tanner and Nasseri [92] proposed a new modification to the XPP model. This modification reproduces the steady elongational behaviour of the extended Pom-Pom of Verbeeten et al. [96]. The authors neglect the anisotropy of the material by setting $\alpha = 0$, and ignore the $\left[f(\boldsymbol{\tau}) - 1 \right] \mathbf{I}$ term in the evolution equation for stress. The new model is considered as a new type of Phan-Thien/Tanner models and is called the PTT-XPP model. One important feature of this new model is the slower thinning of shear viscosity (η_s), compared with the original XPP shear response.

Bishko et al. [19] simulated the transient flow through a 4:1 planar contraction, using the original differential Pom-Pom model. These authors concluded that incrementing the branching (controlled by the number of arms, q) produces larger vortices at any given Weissenberg number. This conclusion is in agreement with experimental observations of vortex growth of branched (represented by higher q-values) and linear polyethylene melts, where smaller vortices were found for the linear melt. Clemeur et al. [37] presented an alternative Pom-Pom version called the Double-Convected Pom-Pom (DCPP) model. In a subsequent study, Clemeur et al. [36] compared the numerical solutions of planar contraction flows in terms of birefringence measurements of a LDPE melt, obtaining good quantitative agreement. Excellent comparisons with experimental observations were also reported by Verbeeten et al. for a LDPE melt, covering flow through a cross-slot device, confined flow around a cylinder [99] and for a 3.29:1 planar contraction flow [98]. Numerical results in references [98,99] were obtained with a discrete elastic viscous stress splitting technique, in combination with a discontinuous Galerkin (DEVSS/DG) method. Unrealistic values of stretch, λ, were detected at stagnation point stations in flow around a cylinder and close to the sharp re-entrant corner in the contraction flow. The numerical convergence was improved by introducing a modified eXtended Pom-Pom (mXPP) model, which differs from the original only in the extra function, $f(\boldsymbol{\tau})$, see equation (2.42).

Steady-state solutions for a multi-mode Pom-Pom model in a three-dimensional contraction geometry have been presented by Sirakov et al. [87]. A comparison of vortex size observed for the flow of a LDPE melt is also provided showing good agreement. Sirakov et al. [87] modified the SXPP model in order to improve stability, by setting the anisotropy equal to zero and proposed a suitable equation of stretch which handles the negative (unphysical) values $tr(\tau)$ that may occur numerically. Wapperom and Keunings [102] solved the flow through a planar 4:1:4 rounded-corner contraction/expansion for the integral and differential Pom-Pom fluid model. In their work, non-physical stretch values ($\lambda < 1$) were detected near the constriction.

6.2 Problem specification

The benchmark flow problem considered here is the creeping flow through a 4:1 planar, rounded-corner contraction geometry. Figure 6.1 displays a schematic representation of this choice of complex flow. Zoomed sections of the three unstructured triangular meshes employed, with different degrees of refinement, are shown in Figure 6.2.

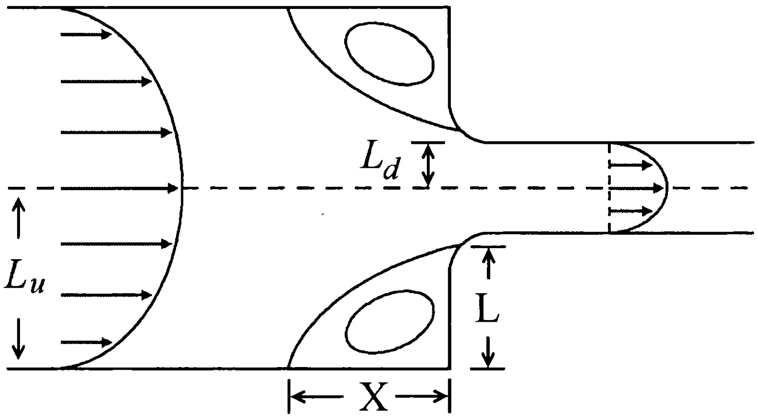

Figure 6.1. Schematic 4:1 contraction geometry: rounded-corner.

Mesh characteristics data is provided in Table 6.1. Upstream and downstream channel lengths are $27.5L_d$ and $49L_d$, respectively; $L_u = 4L_d$ (see Figure 6.1) and the curvature of the re-entrant corner is $\frac{3}{4}L_d$. The contraction is located at $x = 27.5$ units.

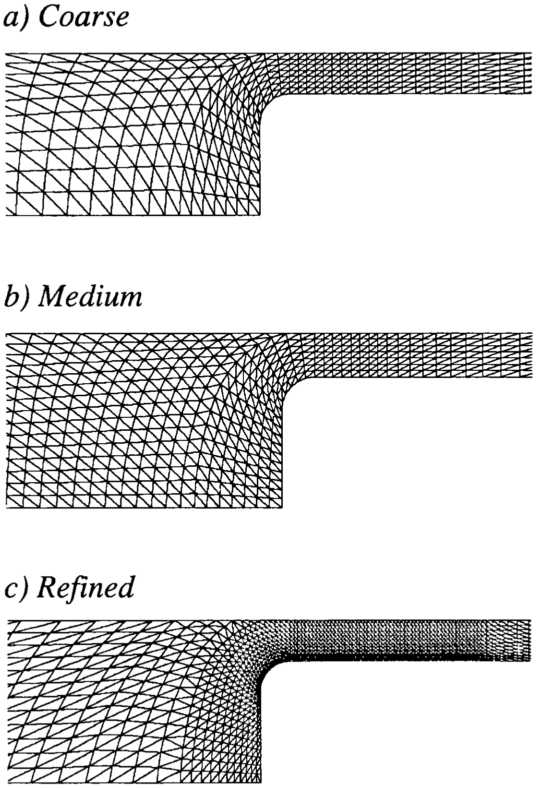

Figure 6.2. Unstructured *fe*-triangular meshing in contraction zone.

Transient Oldroyd-B solutions in Poiseuille flow have been imposed as inlet boundary conditions, employing the analytical solution for velocity (u_x) of Waters and King [104]. The upstream channel length is large enough to have fully developed SXPP profiles before the fluid reaches the entry section. No equivalent analytical solution for transient or steady-state Poiseuille flows has been obtained for the XPP class models. An alternative way to set boundary condition at the inlet is to use the numerical fully-developed solution for a channel of the same height (see chapter 4 for details). Additionally, no-slip boundary conditions are realised along the stationary walls. The stress at the inlet is computed by solving in weak-form the equivalent ordinary differential channel flow problem.

As mentioned earlier, the precise form of the extensional viscosity is varied by adjusting the number of dangling-arms attached at both ends of the Pom-Pom molecule. Solutions are computed at four different q-settings, with the notation Fluid-q_i where $i=\{2,5,10,15\}$. Other fluid parameters are $Re=0$, $\beta=1/9$, $\varepsilon=1/3$ and $\alpha=0.15$. Note that Fluid-q_2 is the default setting used throughout this study. Results for a parameterisation study in α-setting are also analysed and a comparison between Pom-Pom and EPTT solutions for fluids displaying equivalent levels of extension hardening is provided. This match in hardening is achieved by adjusting $\{q, \varepsilon\}$-parameters.

Table 6.1. Mesh characteristics parameters

Mesh	***Elements/ volumes***	***Nodes***	***Degrees of freedom*** $(\mathbf{u}, p, \boldsymbol{\tau})$	R_{min}
(4:1)$_a$	1086	2325	14570	0.0296
(4:1)$_b$	1626	3433	21502	0.0170
(4:1)$_c$	2693	5652	35392	0.0097

Solutions at high elasticity levels are obtained through continuation in Weissenberg number. Simulations are initiated from solution at $We=0.1$, subsequently incrementing and advancing solutions through steps of $We=0.5$, 1, 3, 5, 10, 15, 20, ... until convergence is lost at a critical level, We_{crit}. Vortex cell-size is reported, measured parallel to the symmetry line (X) and at right-angles (L). The L_2-norm relative maximum difference over two successive time steps is employed as a criteria for time-step termination with the selected threshold of (10^{-7}).

6.3 Numerical results

In this chapter, the analysis of the results obtained from simulation is divided into three sub-sections. The first, deals with the influence of increasing extensional viscosity by increasing the number of dangling-arms (q) for the SXPP model, commenting on the vortex, stretch and stress responses. The second sub-section considers the variation of anisotropy, and in the third, a comparison with predictions for two different EPTT model fluids is provided. These models present similar levels of extension hardening and peak values of Trouton ratio. The influence of q on SXPP rheology may be observed in section 2.5.

6.3.1 Pom-Pom solutions with q-variation ($\alpha = 0.15$)

The scope of this section covers on variation in flow field structure reflecting the influence exerted by rheological material functions. For each setting of arms-q, vortex patterns and their variation with elasticity (We) are reported up to a stage close to We_{crit}, where numerical convergence is lost.

6.3.1a Critical Weissenberg number and vortex dynamics

It has been found that an increase in the degree of hardening displayed by the extensional viscosity may produce a decline in the elasticity level attainable (see for example references [28,54,83]). A decrease in We_{crit} when 'adding' more arms to the Pom-Pom molecule may be expected. For the selected number of arms chosen here, $q = \{2,5,10,15\}$, the correspondent critical We-levels are approximately $We_{crit} = \{60,25,13,12\}$. In the case of Fluid-$q_2$, the degree of hardening is practically zero, although the softening regime is 'delayed' up to a non-dimensional strain-rate of 0.2 units. It is for this fluid, where the largest We_{crit} of 60 is obtained. Fluid-q_5 displays an increment of about 50% in extensional viscosity peak-value, when compared with the q_2-case. The critical level of elasticity is reduced to $We_{crit} = 25$.

As the extensional viscosity continues to rise, further decline is detected in We_{crit} with $q=10$ and $q=15$, reducing to $We_{crit}=13$ and $We_{crit}=12$, respectively, confirming earlier observations.

Vortex cell-size, measured at right angle with respect to the symmetry-line (L), and parallel to the symmetry line (X), are plotted as function of We in Figure 6.3a. However, in this figure, X and L are calibrated in a different manner from that proposed in chapter 5. Here, cell-size is zoomed by twice the upstream channel half-width for ready interpretation of data. Vortex lengths units follow those of the geometry specification, and vortex data is obtained from the streamlines patterns.

It can be observed that X and L follow similar increasing trends with increasing elasticity. At any given We, L is always larger than X. Growth patterns in L are similar for elasticity levels up to $We=8$, a stage at which departure (decline in rate of increase) in trends is detected for Fluid-q_2 with respect to other strongly-hardening fluids ($q\geq 5$). Figure 6.4 presents streamline patterns for $q=2$ and $q=5$, whilst Figure 6.5 equates to data for $q=5$ and $q=15$. In general, the linear shape of the separation-line is gathered across all instances, where the calibration of section 5.3.1 is employed.

Salient-corner vortex intensity ψ_{sal} is shown in Figure 6.3b. The response for $q=5$,10 and 15 follows the same continuous enhancement with We. The same trend is followed in the ($q=2$)-case with $We\leq 5$; beyond this level of elasticity, a monotonic decline in intensity is produced. Such decline may be attributed to the softening regime of Fluid-q_2, that is not expected when $q\geq 5$ (see arguments below). Shear viscosity cannot be responsible for such different behaviour as that exhibited by Fluid-q_2, due to the fact that η_s is essentially the same for the various cases selected here (see Figure 2.5). The possibility of modifying extensional response with a non- substantial variation in shear viscosity is an important feature of the Pom-Pom class models that is absent in other models, such as the PTT network variants.

a)

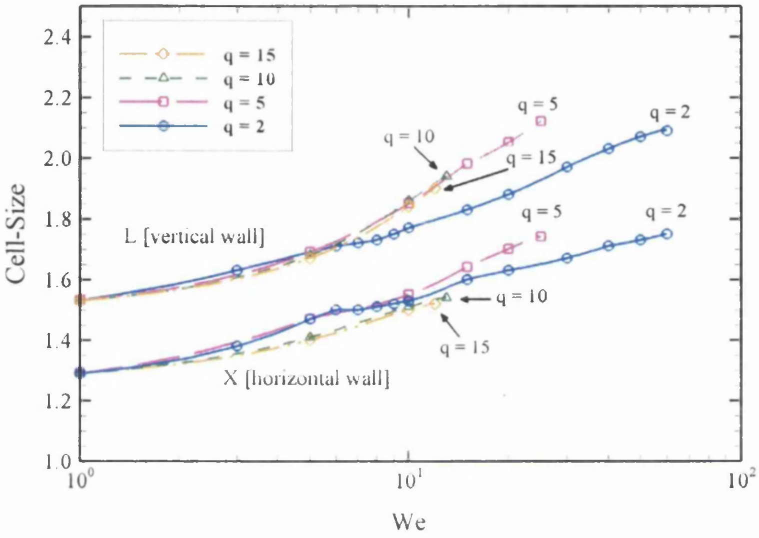

b)

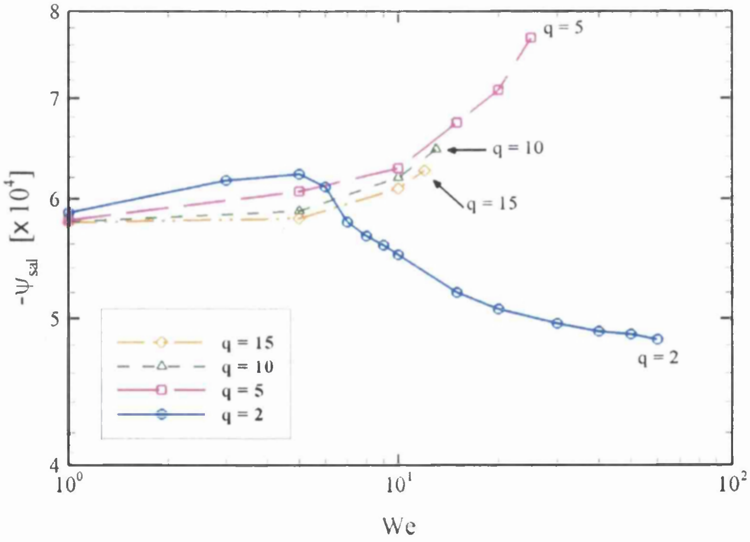

Figure 6.3. Salient-corner vortex, increasing *We*: $Re = 0$, $\beta = 1/9$, $\varepsilon = 1/3$, $\alpha = 0.15$; $q = 2, 5, 10, 15$, a) cell-size, b) intensity.

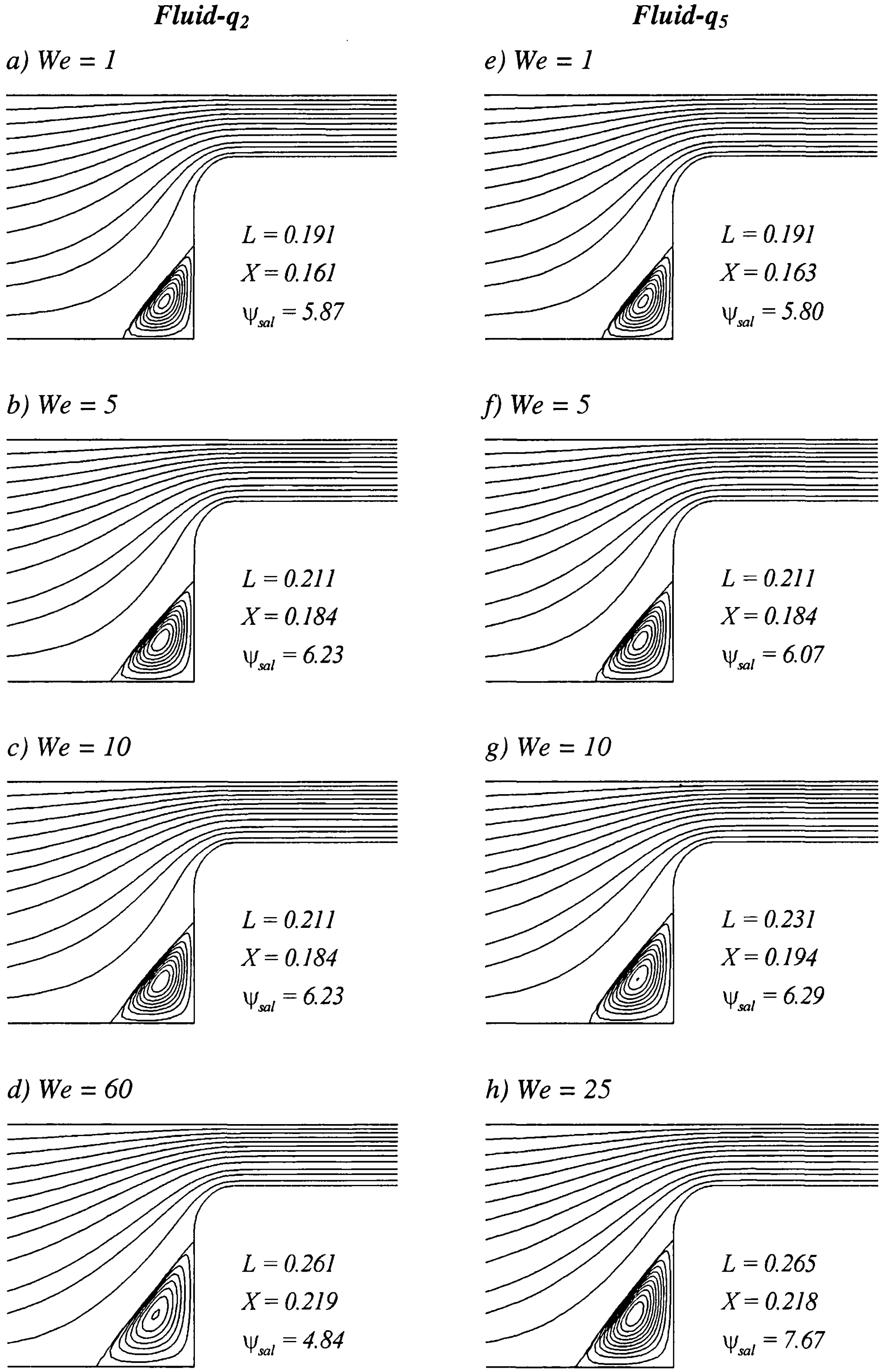

Figure 6.4. Stream function and vortex data (L, X, $\psi_{sal} \times[-10^4]$), increasing We: $Re = 0$, $\beta = 1/9$, $\varepsilon = 1/3$, $\alpha = 0.15$; $q = 2$ and 5.

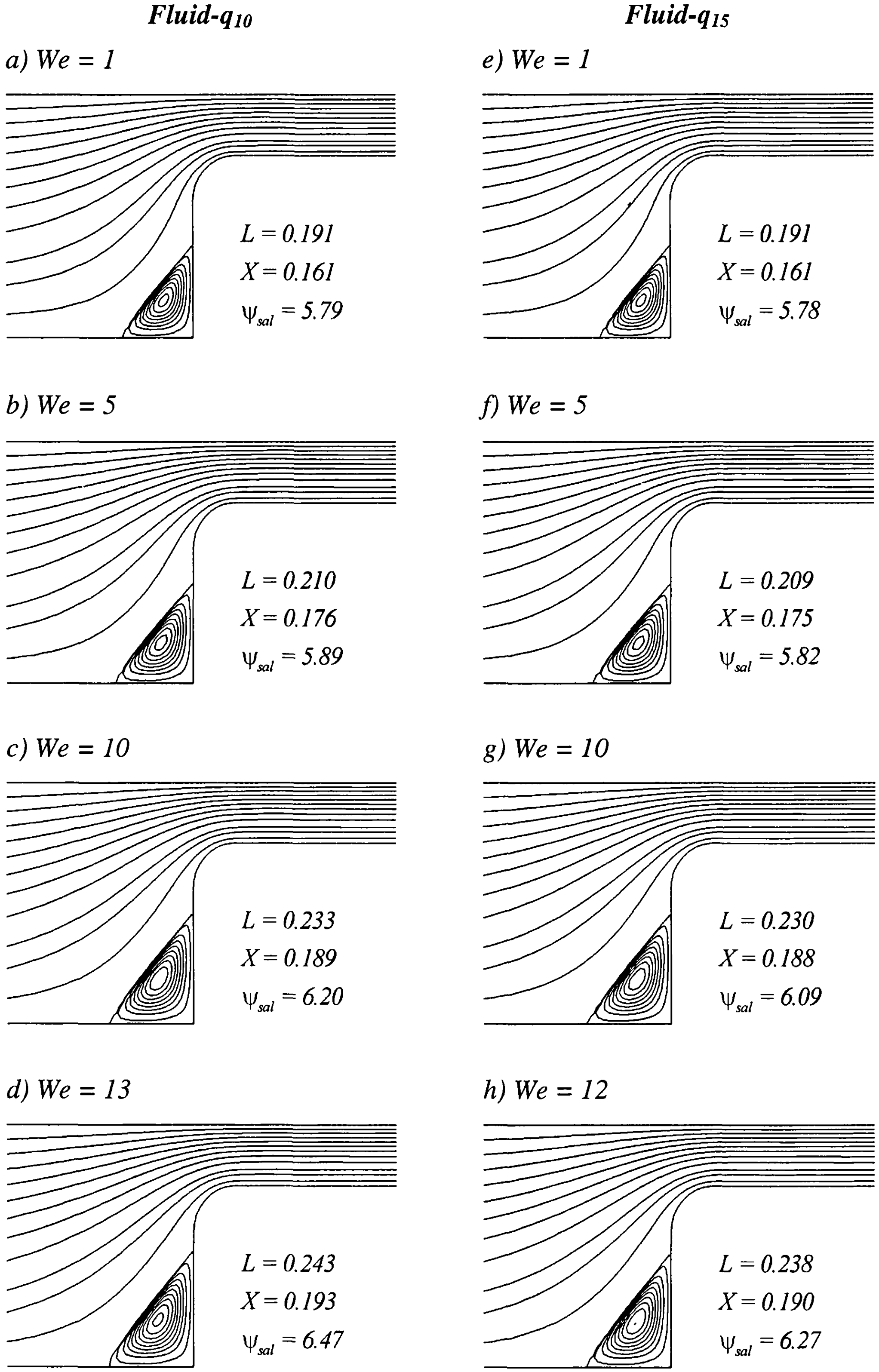

Figure 6.5. Stream function and vortex data (L, X, $\psi_{sal}\times[-10^4]$), increasing We: $Re = 0$, $\beta = 1/9$, $\varepsilon = 1/3$, $\alpha = 0.15$; $q = 10$ and 15.

The extensional component of the deformation-rate tensor, d_{xx}, conveys some insight to explain the departure of Fluid-q_2 from other settings. Figure 6.6 (left column) shows d_{xx} at an elasticity level of $We = 10$. Two d_{xx}-maxima can be detected, one on the symmetry line, just before the fluid enters the downstream channel (entry-flow region); the other is almost at the end of the rounded-corner, in contact with the boundary of the contraction. As can be observed from Figure 6.6, d_{xx}-fields are very similar for the selected fluids analysed here. Additionally, as minor variation in d_{xy}-fields (Figure 6.6-right column) with respect to increase in the number of arms is gathered, it can be concluded that the four fluids are exposed to essentially the same deformation rates. However, even at similar deformations rates, the extensional viscosity experienced by each fluid is quite different. For $q = 2$, the extension-softening regime starts at $\lambda_{0b}\dot{\varepsilon} \approx 0.2$, a regime not reached by the ($q \geq 5$)-fluids until strain-rates of $\lambda_{0b}\dot{\varepsilon} \geq 9$.

It is now convenient to show regions in the flow field where extension-softening is 'expected'. For $q = 2$, a large area of expected softening is anticipated. Fluid-q_5 may have this area reduced considerably because of the fact that softening starts at much larger strain-rates (see Figure 2.5). Figure 6.7 shows the expected extension-softening regions (shaded zones) for Fluid-q_2 and Fluid-q_5. These regions are obtained by taking ($\partial u / \partial x$) as the strain-rate in Figure 6.7a,b and the generalized flow invariant (Γ)[‡] in Figure 6.7c,d. The values indicated in the zones from the rheology at the given elasticity. That is, strain-softening of Fluid-q_2 starts at $\lambda_{0b}\dot{\varepsilon} \approx 0.2$. Then, for the selected elasticity level ($We = 10$), it is necessary to extract the correspondent orientation relaxation time λ_{0b}, following the definitions of non-dimensional numbers and values of the characteristics quantities (see section 2.4). The result for Fluid-q_2 is that softening starts at a strain-rate of $\dot{\varepsilon} \approx 0.02$ time units.

[‡] Flow invariants, $\Gamma = 2\sqrt{I_2}$ and $\Sigma = 3 I_3 / I_2$, where $I_2 = \frac{1}{2} tr\left(\mathbf{d}^2\right)$ and $I_3 = \det\left(\mathbf{d}\right)$, see [63].

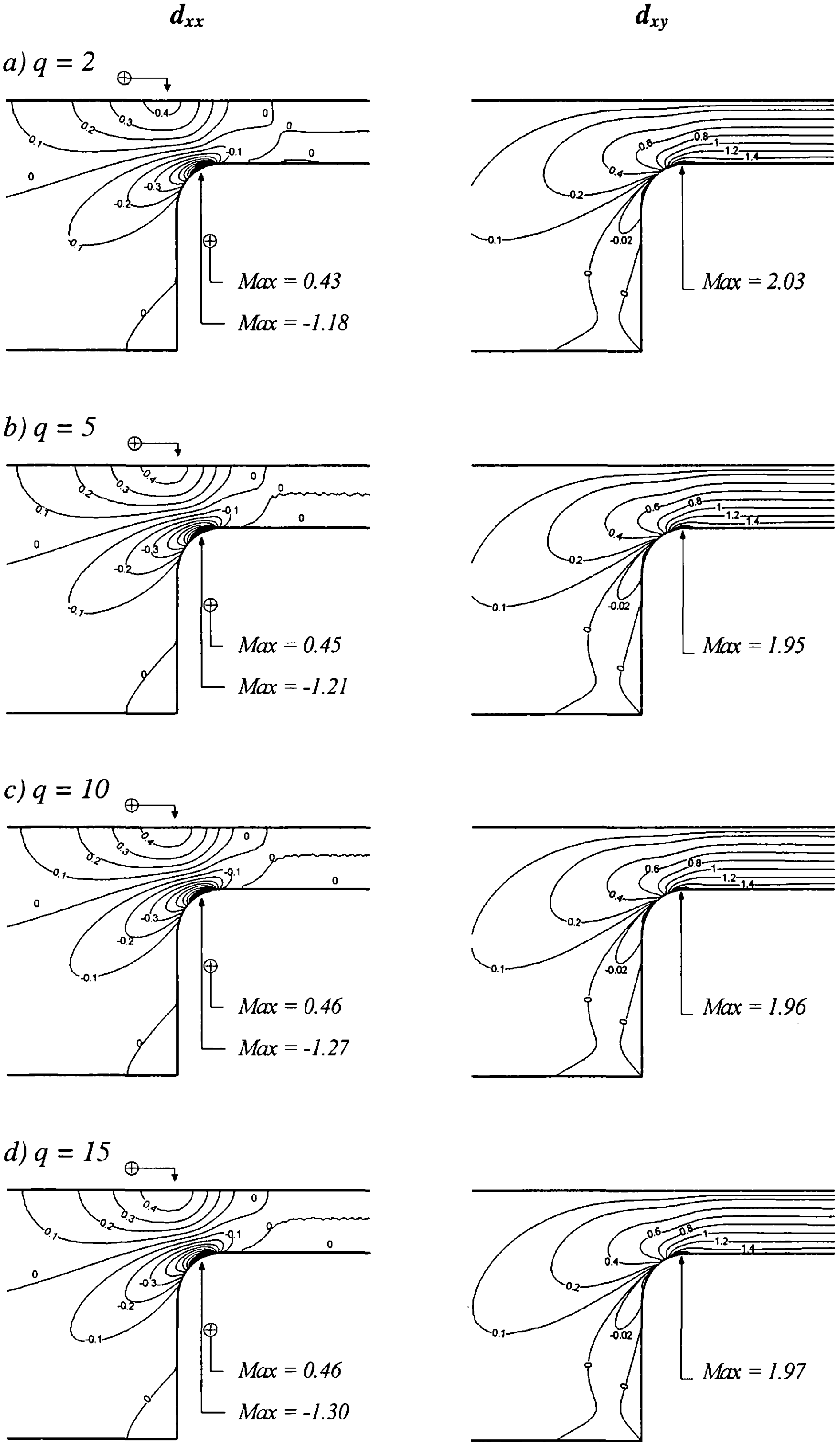

Figure 6.6. Rate-of-strain d_{xx} and d_{xy} fields, $We = 10$: $Re = 0$, $\beta = 1/9$, $\varepsilon = 1/3$, $\alpha = 0.15$; increasing q.

Following the same procedure for Fluid-q_5, the extension softening starts at $\dot{\varepsilon} \approx 0.9$ time units, meaning a difference of more than one order in magnitude when compared with the ($q = 2$)-case.

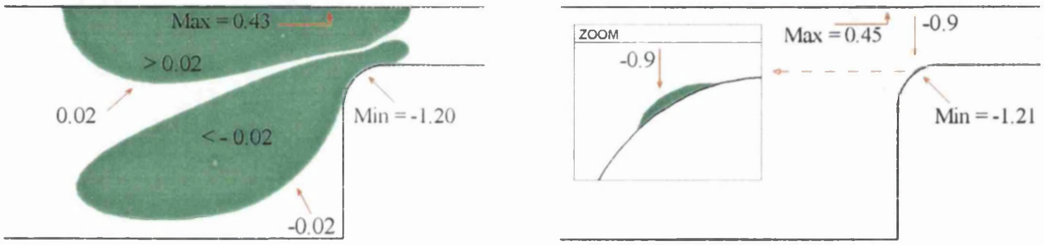

a) ∂u/∂x contourline, q = 2   *b) ∂u/∂x contourline, q = 5*

c) Γ contour line, q = 2   *d) Γ contour line, q = 5*

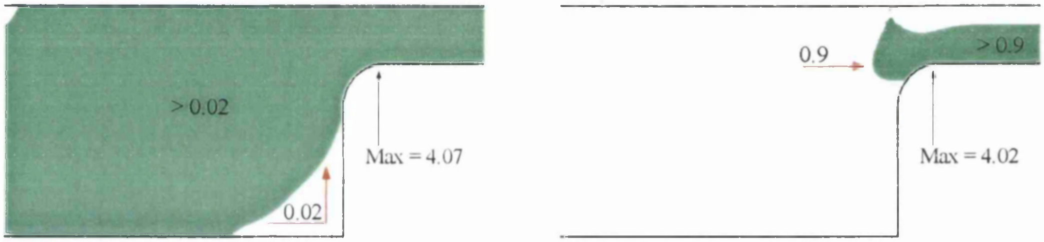

Figure 6.7. Rate-of-strain (*dxx* and *Γ*) fields, *We* = 10: *Re* = 0, β = 1/9, ε = 1/3, α = 0.15; *q* = 2 and 5.

Bearing in mind that *pure extensional flow* only occurs along the centreplane (near the constriction), hence, $\partial u/\partial x$ and Γ simply provide a guidance when applied to the complex 4:1 contraction flow. Applying the above criteria, it can be observed that the 'expected' softening region for ($q = 2$) is considerably larger than that for ($q = 5$), with both approximations of strain-rates ($\partial u/\partial x$ and Γ). Note that Γ-fields also identify shear deformation as well[§].

Mesh convergence data is provided in terms of the salient-corner vortex cell-size, X, in Table 6.2. The selected fluid for this table is Fluid-q_5, covering the range

---

[§] Invariant *Σ*, commonly associated with extensional deformation, is not defined in 2D-planar flows.

$0.1 \leq We \leq 25$ for the three meshes employed. Mesh convergence is evident through the refinement and allows higher elasticity level solutions to be attained.

Table 6.2. Mesh convergence for salient-corner vortex cell-size (X): $0.1 \leq We \leq 25$, $q = 5$

Mesh	***We***						
	0.1	***1***	***5***	***10***	***15***	***20***	***25***
(4:1)$_a$	0.151	0.162	0.182	0.190	-	-	-
(4:1)$_b$	0.152	0.163	0.184	0.194	0.205	-	-
(4:1)$_c$	0.152	0.163	0.184	0.194	0.205	0.212	0.218

6.3.1b Centreline and downstream wall profiles

Polymeric first normal stress difference, N_1, stretch λ, stress component, τ_{yy} and pressure p are plotted along the symmetry-line in Figure 6.8 for $We = 10$. From $q = 2$ to 15 the increase in N_1- and λ-peak values are around 20% and 10%, respectively. The increment in both variables may be attributed to the larger extensional viscosity, caused by 'adding' more q-arms to the molecule. No significant effect is provoked by such a change in q, as can be seen in τ_{yy} compared to that in other variables. Pressure and pressure-drop increases with q by 9% from Fluid-q_2 to Fluid-q_{15}.

Downstream wall profiles ($y = 3$) for $We = 10$ are shown in Figure 6.9 for N_1, λ, τ_{xy} and τ_{yy}. Here, large dependency of q over N_1 and λ is detected. From Fluid-q_2 to Fluid-q_{15} downstream values increase by around 135% for the normal stress difference and about 50% for stretch. Polymeric τ_{xy}-component also shows an increase with q in peak and downstream wall values. The τ_{yy}-component shows similar increment though is less evident.

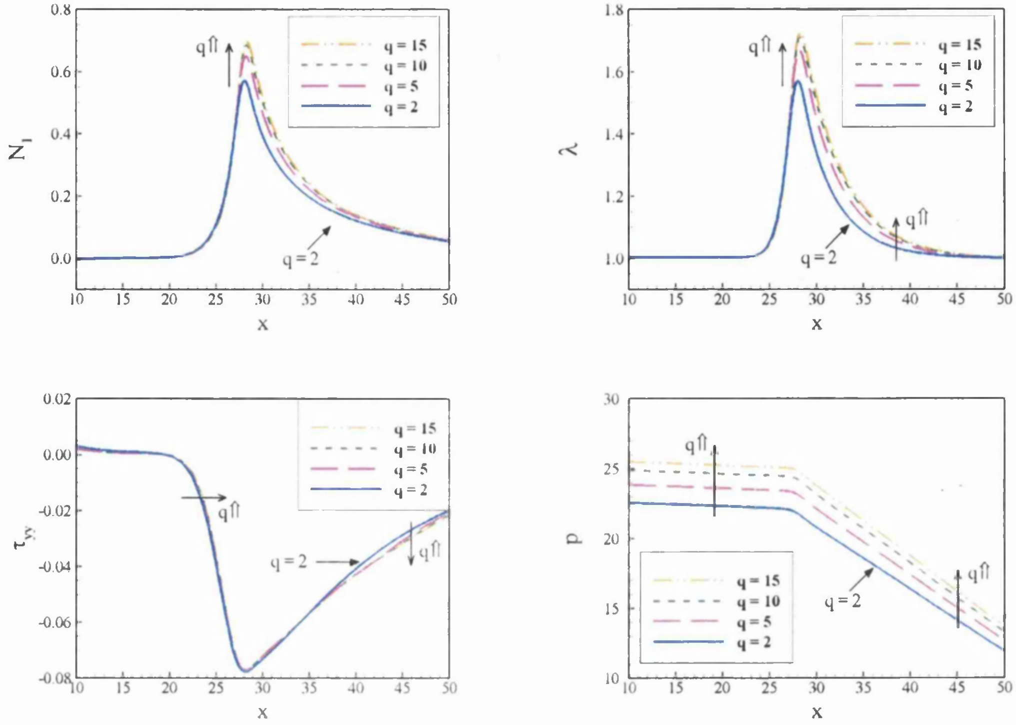

Figure 6.8. Profiles along plane of symmetry, We = 10: $Re = 0$, $\beta = 1/9$, $\varepsilon = 1/3$, $\alpha = 0.15$; increasing q.

6.3.1c Stretch, stress and deformation-rate fields and pressure-drop

Maximum values of components of the rate of deformation tensor (d_{xx} and d_{xy}) are located in the boundary of the re-entrant corner (Figure 6.6). d_{xx} exhibits a peak value at the centreline while the fluid lying above the downstream boundary wall is exposed to large values of shear deformation (d_{xy}). In addition, deformation rates are also significant in the entry zone. Far from the contraction, shear deformation is dominant, although it is strongest in the downstream channel. Hence, influence of the number of arms will be stimulated principally in these zones. Note that the *influence of q* is reflected in the significant differences of the large values of stress (τ_{xx}) and stretch (λ) along the downstream wall. These differences are related to the coefficient of the first normal stress difference, ψ_1, not to shear viscosity, which remains relatively unaffected by the choice of q. It is important to note, that the influence of the constriction upon downstream wall profiles is short. This is due to the low residence time of the flow across the contraction region.

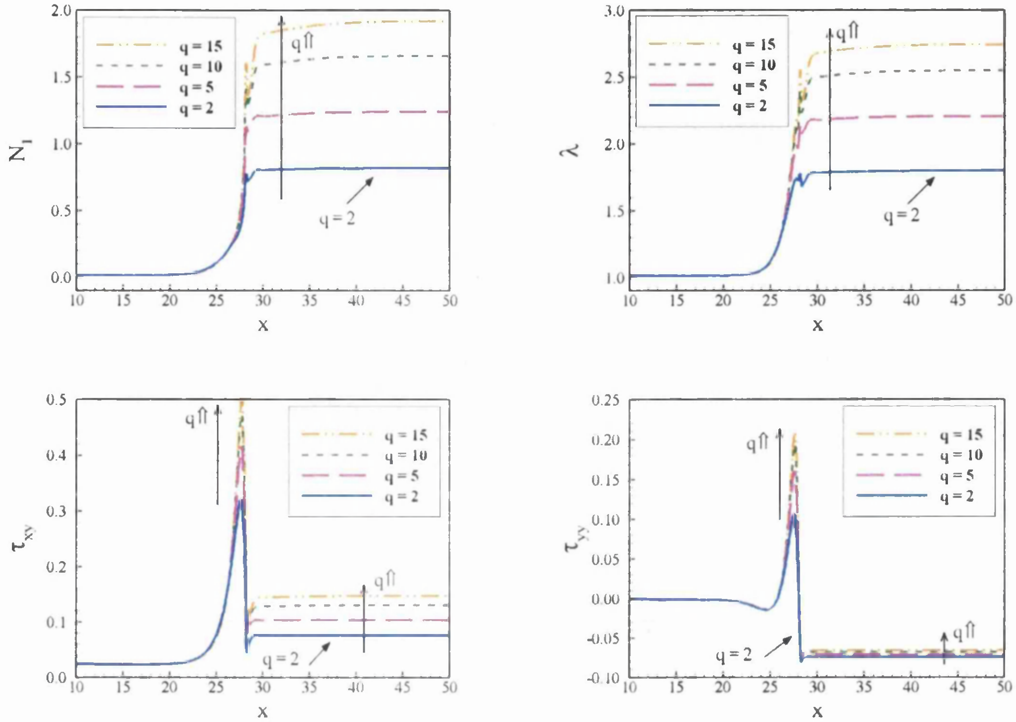

Figure 6.9. Profiles along downstream wall, $y = 3$, $We = 10$: $Re = 0$, $\beta = 1/9$, $\varepsilon = 1/3$, $\alpha = 0.15$, increasing q.

- *Trends in* λ

Backbone stretch is plotted in Figure 6.10 (left column). Regions of relatively low stretch fluid can be identified in the inflow (upstream channel before entry zone) and along/near the centreline far upstream/downstream from the constriction, see Bishko et al. [19]. The dominant deformation in these zones of low stretch is shear. In addition, low values of stretch are found in the recirculation region. A '*banded entry-flow*' zone of stretched material (termed as in [19]) can also be identified, corresponding to a dominate effect of extensional viscosity over shear deformation.

Two zones lying above the re-entrant corner with large stretch values can be appreciated from Figure 6.10. The first is part of the entry zone, and another smaller

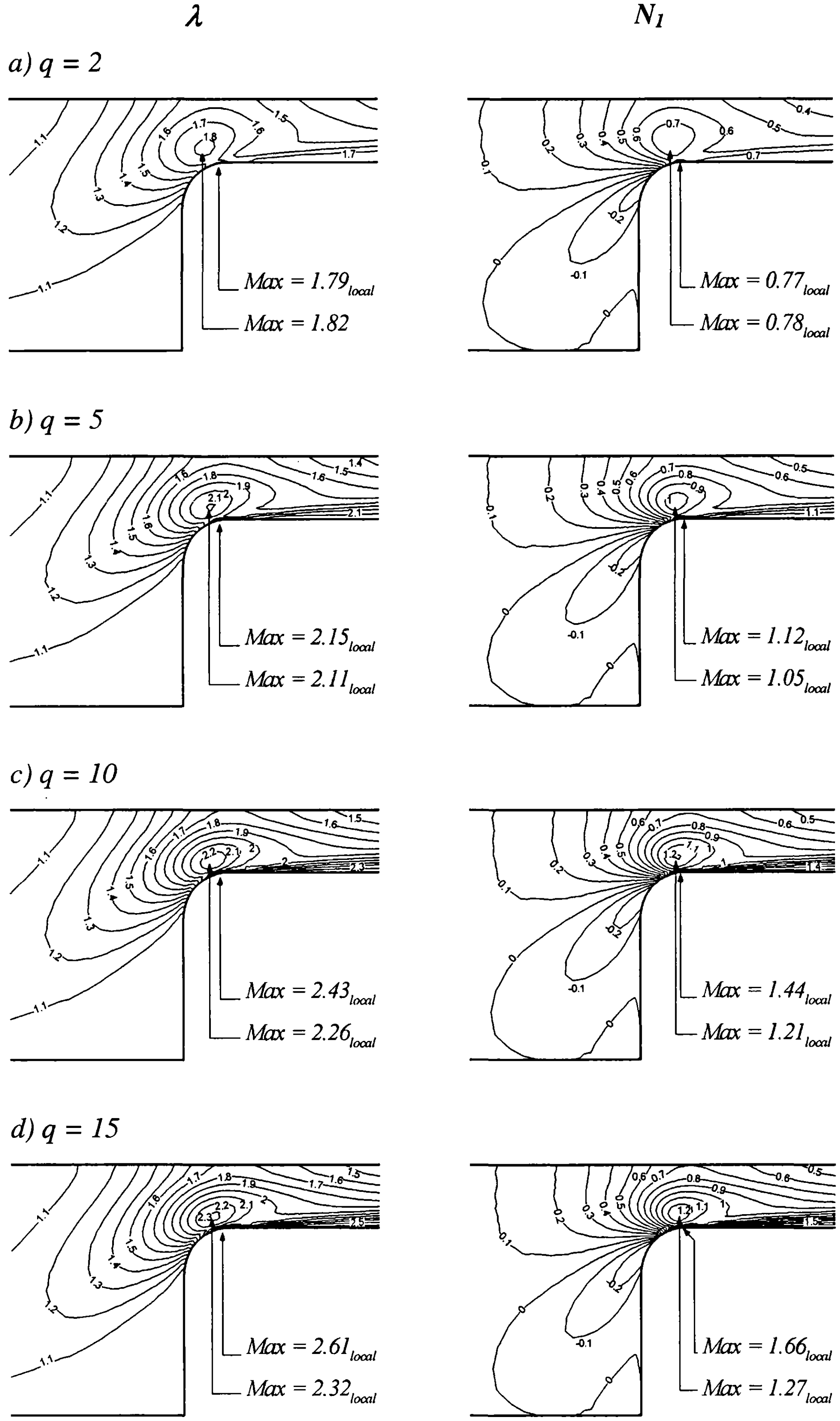

Figure 6.10. Stretch and firs normal stress difference (polymeric) fields, $We = 10$: $Re = 0$, $\beta = 1/9$, $\varepsilon = 1/3$, $\alpha = 0.15$; increasing q.

in size, is situated just below the first one, in contact with the boundary wall at the end of the rounded-corner.

Additionally, large backbone stretch is observed on the centreline just above the constriction (Figure 6.8) and along the downstream wall (Figure 6.9). Rise in peak values when increasing q for $We=10$, can be discerned from Figure 6.10, from $\lambda_{max}=1.82$ for $q=2$ to $\lambda_{peak}=2.32$ in the entry-flow zone and $\lambda_{peak}=2.61$ in the small area touching the wall for $q=15$. Note that stretch along the downstream-wall is comparable in magnitude to the peak-values in the small area discussed above. In order to detect the role of η_e on this complex flow, contour lines at a larger level of elasticity are presented in Figure 6.11 for λ and N_1 at $We=25$. However, solutions are available only for Fluid-q_2 and Fluid-q_5 at this high level of elasticity. The proposed increment in the number of arms stimulates more visible differences at this elasticity stage, when compared to the ($We=10$)-response. Relative increase in backbone stretch over the contraction zone, is around 25% for $We=25$ from $q=2$ to $q=5$, as opposed to only 10% at $We=10$.

- Trends in N_1, τ_{yy} and τ_{xy}

Contour lines for the polymeric stress difference, ($\tau_{xx}-\tau_{yy}$) are presented in Figure 6.10 (right column). Increment in the number of arms results in a general increase in N_1 over the contraction zone and along the downstream wall. Influence of q on N_1-response is amplified at the elasticity level of $We=25$. An increase of around 65% is detected for the positive N_1-peak value, when the branching varies from $q=2$ to 5. The increase in N_1-peak observed at $We=10$ is about 34%, for the same variation in the number of arms (see Figure 6.11). No noticeable differences occur far upstream of the contraction.

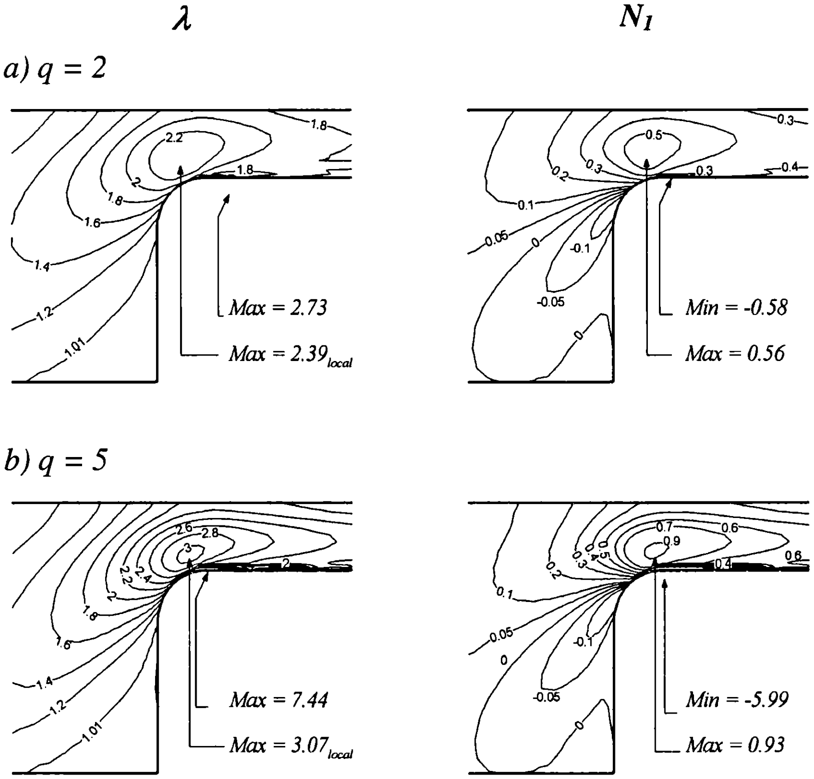

Figure 6.11. Stretch and firs normal stress difference (polymeric) fields, $We = 25$: $Re = 0$, $\beta = 1/9$, $\varepsilon = 1/3$, $\alpha = 0.15$; $q = 2$ and 5.

The polymeric τ_{yy} stress component maxima is located in the rounded-corner, near the constriction plane. Values in the centreline are about one order in magnitude less than peak-values. The *banded entry-flow* zone for stretch is also visible for τ_{yy} (Figure 6.12-left column). Negative τ_{yy}-values are found in the fluid lying close to the downstream-wall, showing a decline in magnitude with increasing q. In general, polymeric stress shear component (τ_{xy}) increases slightly with increment in arms-q in the flow field. It is possible to also identify a banded-zone for this stress component (Figure 6.12-right column).

- Trends in d_{xx}, d_{xy} and pressure-drop

Components of the deformation-rate tensor, d_{xx} and d_{xy}, display minor influence with an increase in the number of arms of the Pom-Pom molecule. There is only slight increase in peak-values for d_{xx} on the centreline and above the re-entrant corner (Figure 6.6).

As mentioned in the beginning of this section (6.3.1c), regions in the flow subjected to high deformation rates are zones where influence in variation of the number of arms is anticipated to produce the most significant differences in the 4:1 contraction flow. The reason is that rheometrical functions are expected to reach extreme values in the high deformation regions mentioned above. Hence, extensional viscosity is stimulated in large strain-rate zones while shear viscosity and first normal stress difference coefficient are stimulated in regions dominated by large shear-rates. Figure 2.5d shows that backbone stretch depends on both, shear- and strain-rates, though stretch is larger in extensional deformation than in shear for a given deformation-rate. Therefore, stretch patterns in the entry section resemble d_{xx}-fields and in the downstream channel, just beyond the re-entrant corner, stretch patterns follow the trends in d_{xy} contour lines (see Figure 6.10).

By further observation, similarity in stress and stretch behaviour can be appreciated, leaving clear evidence that molecular stretch and stress responds to the complex deformation experienced by the fluid. However, due to the fact that in the zone covering from the entry-flow section to past the re-entrant corner, there is a complex mix of shear and extensional phenomena, viscometric functions may be taken as a guidance only in anticipating any response.

Figure 6.13 presents the pressure-drop, Δp, normalized by the predicted for a Newtonian fluid (Δp_{Newt}) with same flowrate and same viscosity as the zero shear-rate viscosity for the SXPP model, $\eta_s(\dot{\gamma} \to 0)$. This normalized pressure-drop suffers a significant monotonic decline with increasing elasticity. For $We < 2$, this decline is of the order of 70% (for all Fluid-q_i) from the Newtonian reference line ($\Delta p / \Delta p_{Newt} = 1$). After this elasticity stage, the rate-of-declines is reduced considerably, to eventually reach a plateau well established at $We = 10$.

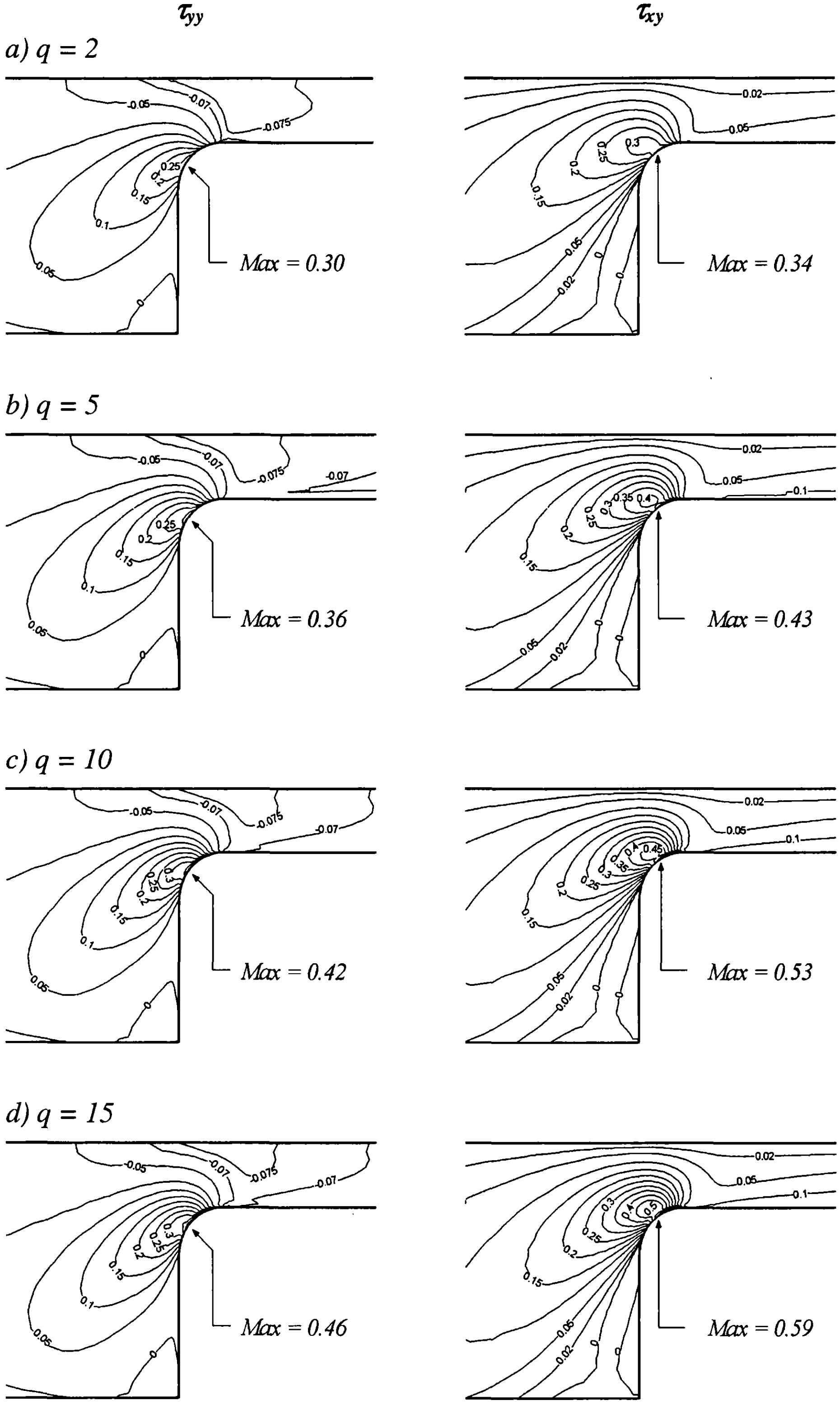

Figure 6.12. Normal stress (τ_{yy}) and shear stress fields, $We = 10$: $Re = 0$, $\beta = 1/9$, $\varepsilon = 1/3$, $\alpha = 0.15$; increasing q.

Minor differences for the q-values simulated here can be observed, producing just a slight reduction in Δp for systems with more branched-arms. The large pressure-drop detected for all fluids is due to the shear-thinning properties of the particular choice of parameters in this study. However, the slight reduction in $\Delta p/\Delta p_{Newt}$ with q may be attributed to the minor differences in shear-viscosity between fluids.

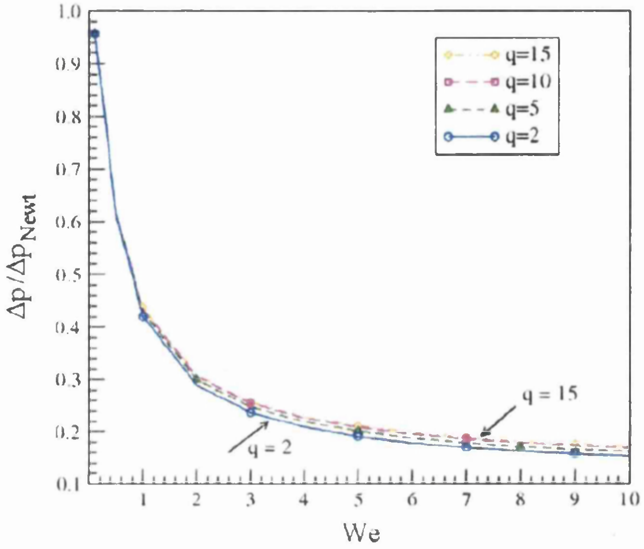

Figure 6.13. Normalised pressure-drop vs. We: $Re = 0$, $\beta = 1/9$, $\varepsilon = 1/3$, $\alpha = 0.15$; $q = 2, 5, 10, 15$.

6.3.2 Pom-Pom solutions with α-variation {0.15, 0.25, 0.5}

Rheometrical functions response for an adjustment in the anisotropy parameter α are presented in Figure 6.14 for $q = 15$. Clemeur et al. [37] have reported 'numerical defects' for the XPP class models. These authors gave particular attention to instabilities in material functions provoked by some values of α. For sufficiently low values of the anisotropy parameter, singularities in shear-viscosity and first normal stress difference coefficient are not evident, though an increase in α and/or in q may bring these about. In extensional viscosity, the instability is reflected as an unphysical flattening effect. Trouton ratio and stretch in rheometrical flows are also affected by such numerical defects.

a) Shear and planar viscosity *b) Normalised Trouton ratio (planar)*

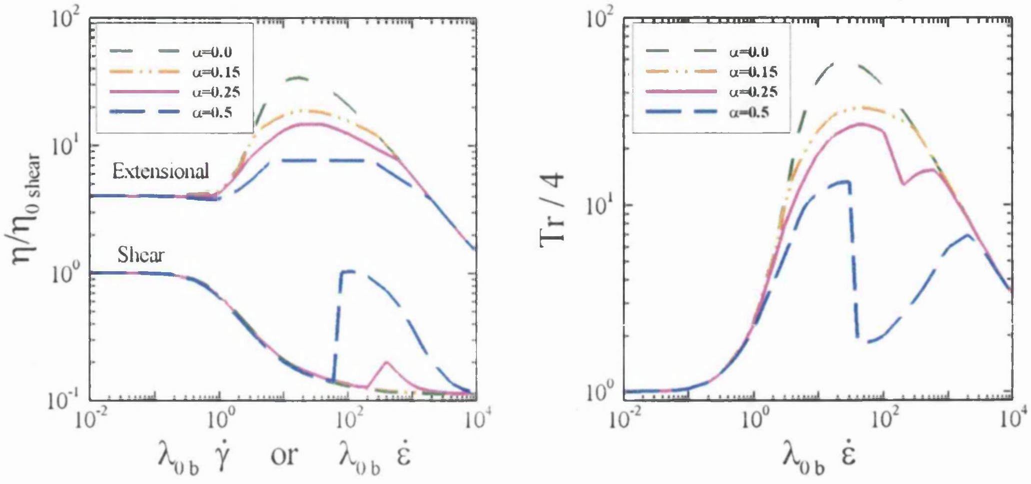

c) Firs normal stress coefficient *d) Backbone stretch*

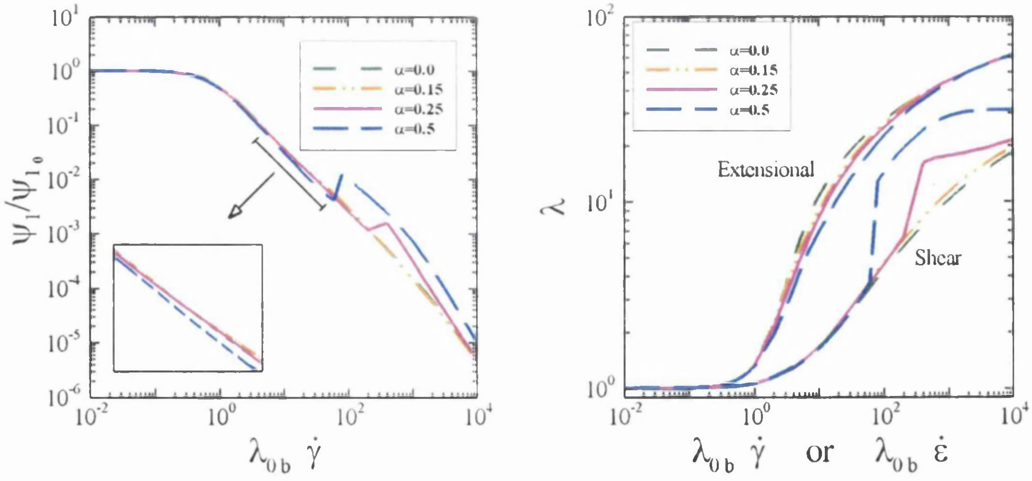

Figure 6.14. Rheological properties of SXPP model, variation in α, $\beta = 1/9$, $\varepsilon = 1/3$ and $q = 15$.

With the objective of 'capture' the effect of the instabilities upon flow response, solutions for a number of anisotropy parameters have been generated, namely:

$\alpha = \{0.15, 0.25, 0.5\}$. The number of arms is set to $q = 15$, the reason being that, for the selected values of q simulated here, this is the fluid where instabilities are more evident. Downstream-wall profiles are given in Figure 6.15 for N_1, λ, τ_{xy} and N_2.

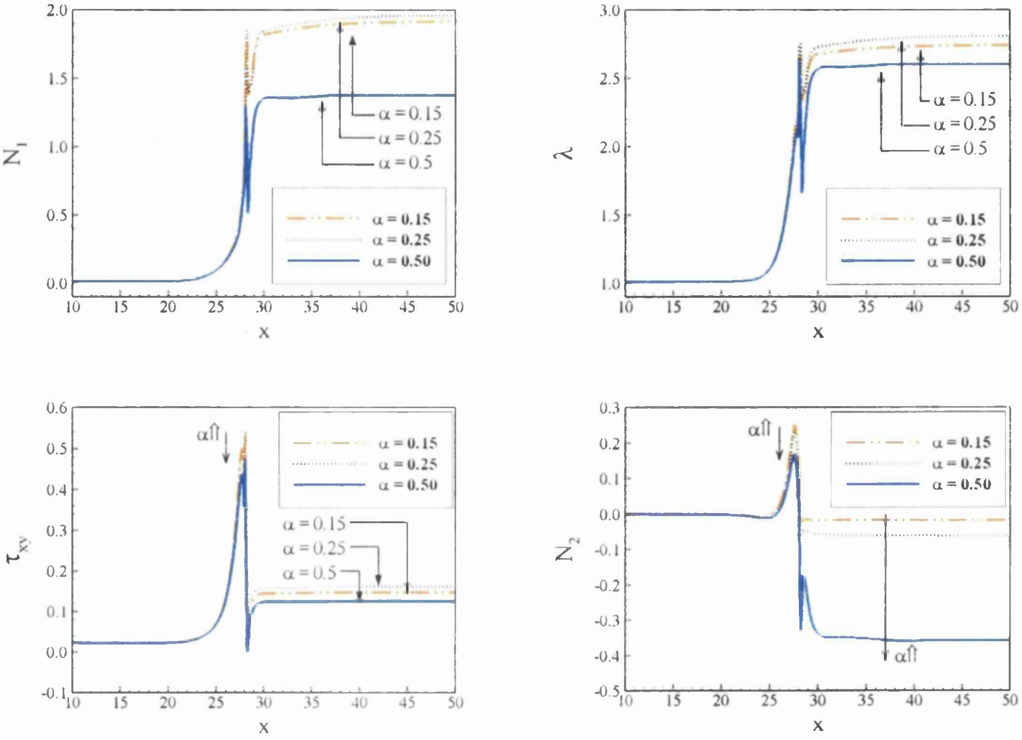

Figure 6.15. Profiles along downstream wall, $y = 3$, increasing α: $Re = 0$, $\beta = 1/9$, $\varepsilon = 1/3$; $q = 15$, $We = 10$.

For $\alpha = 0.15$ and 0.25, no significant effect is observed in these profiles. Note that N_2 practically vanishes before and after the constriction. Further increment in anisotropy ($\alpha = 0.5$) renders reduction in polymeric first normal stress difference, stretch and in polymeric shear stress, once the fluid has passed the constriction. The most significant of these variations is for N_1, where the reduction (from $\alpha = 0.15$ to $\alpha = 0.5$) is around 30%. The polymeric second normal stress difference, N_2, exhibits an increase of more than one order in magnitude from the reference line at $\alpha = 0.15$. Additionally, decay in peak-values near the constriction plane is detected.

The flattening effect on extensional viscosity may account for this response. Such reduction in peak-values is more prominent in N_1 and λ (both variables show dependence on extensional fields in the constriction zone) than in shear stress.

The decline in N_1 and λ along the wall of the exit channel at $\alpha = 0.5$ may be the consequence of the reduction in ψ_1 (compared to the case for $\alpha \leq 0.25$) prior to the onset of instability (see the zoomed box in Figure 6.14c).

As the solutions obtained for the various values of anisotropy display no discontinuity or abnormal behaviour, it must be assumed that the deformation-rates suffered by the fluid are not large enough to enter the regimes where singularities are anticipated, especially in the downstream channel section. In the constriction, the simulated deformation-rates may be sufficient in magnitude. However, the residence time across this region is relatively short and may prevent the fluid from reaching the fully steady-state regime (in a Lagrangian time sense).

6.3.3 Extensional response across models: Pom-Pom and PTT

Predicted vortex growth is compared in this section for the planar rounded-corner 4:1 contraction flow of two types of models: a kinetic-based form (single extended Pom-Pom) and a network type (exponential Phan-Thien/Tanner).

Aboubacar et al. [2,3] reported vortex data for two EPTT fluids, with different strain-hardening response. The EPTT($\varepsilon_{PTT} = 0.02$)-fluid accounts for severe strain-hardening properties, whilst the EPTT($\varepsilon_{PTT} = 0.25$)-fluid displays relatively low strain-hardening form. The objective is to perform the simulation of SXPP fluids with similar response in extensional flow to that exhibited by the two EPTT fluids employed in references [2,3]. For each EPTT fluid, two different sets of SXPP-parameters are provided, one, giving an equivalent peak in extensional viscosity (η_e) and the other in Trouton ratio (Tr). This assists to associate flow response with either the extensional properties, or otherwise, those moderated by the influence of shear. To approximate peaks in extensional viscosity and Trouton ratio, the same viscosity ratio, β, of references [2,3] is also employed here. This equates shear and extensional viscosity values at both, low and extremely high deformation rates for each EPTT and SXPP fluids. Once the viscosity ratio is fixed (i.e. the solvent content), two parameters exert influence on the strain-hardening properties of the SXPP model[**], the relaxation times ratio, ε, and the number of arms, q. An increment in either of these two variables increases the degree of strain-hardening. Additionally, for the selected β ratio, only ε has an effect upon shear response, with increasing ε delaying the onset of shear-thinning. Fine adjustment to match the EPTT material functions is sought through variation in both parameters q and ε. Four fluids that match EPTT response are enumerated as (I)*a*, (II), (III), (IV). An adjustment in α for the fluid with the strongest strain-hardening behaviour, Fluid-(I)*a*, is also included, named Fluid-(I)*b*. The SXPP-parameters used are reported in Table 6.3, whilst Figure 6.16 displays the graphical corresponding comparison against the EPTT rheometrical functions.

Table 6.3. SXPP and corresponding EPTT parameters; β = 1/9

	Corresponding PTT	q	ε	α	***Comment***
Fluid-(I)$_a$	η_e: EPTT($\varepsilon_{PTT}=0.02$)	8	0.999999	0.15	Severe-hardening
Fluid-(I)$_b$	η_e: EPTT($\varepsilon_{PTT}=0.02$)	8	0.999999	0.05	Severe-hardening
Fluid-(II)	Tr: EPTT($\varepsilon_{PTT}=0.02$)	5	0.5	0.15	Strong-hardening
Fluid-(III)	η_e: EPTT($\varepsilon_{PTT}=0.25$)	2	0.333333	0.15	Delayed-softening
Fluid-(IV)	Tr: EPTT($\varepsilon_{PTT}=0.25$)	2	0.075	0.15	Softening

The SXPP Fluid-(I)*a* approximates the extensional viscosity maximum of EPTT($\varepsilon_{PTT}=0.02$) and exhibits the highest level of hardening amongst these SXPP

[**] Extensional viscosity is also influenced by the parameter α, however this also introduces numerical defects to the model, as discussed in section 6.3.2.

fluids. However, this SXPP fluid exceeds the Trouton ratio of the same EPTT fluid, even though the shear behaviour between both models is close. In contrast, Fluid-(II), exhibits high levels of hardening, though lower than Fluid-(I)*a*, and matches *Tr* for EPTT($\varepsilon_{PTT} = 0.02$).

a) Shear and planar viscosity, $\varepsilon_{PTT} = 0.02$ *b) Shear and planar viscosity,* $\varepsilon_{PTT} = 0.25$

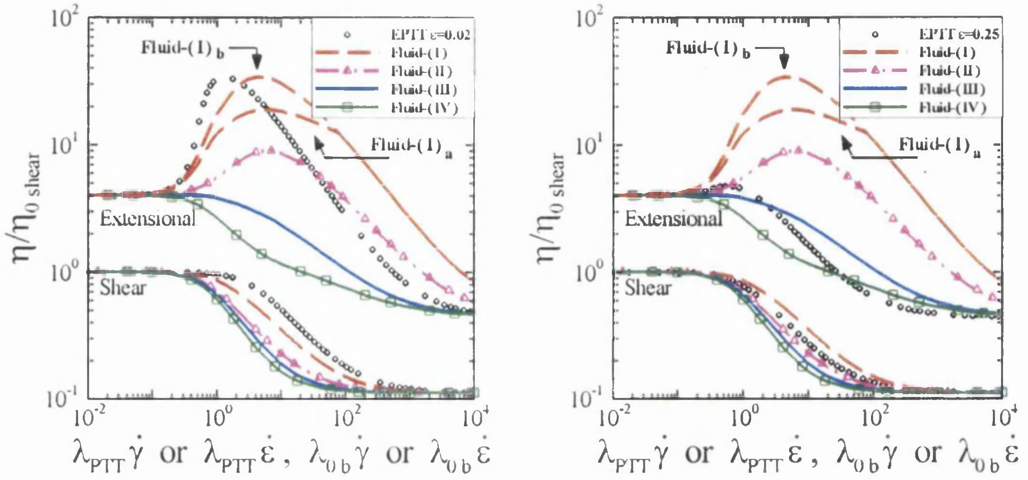

c) Normalised Trouton ratio, $\varepsilon_{PTT} = 0.02$ *d) Normalised Trouton ratio,* $\varepsilon_{PTT} = 0.25$

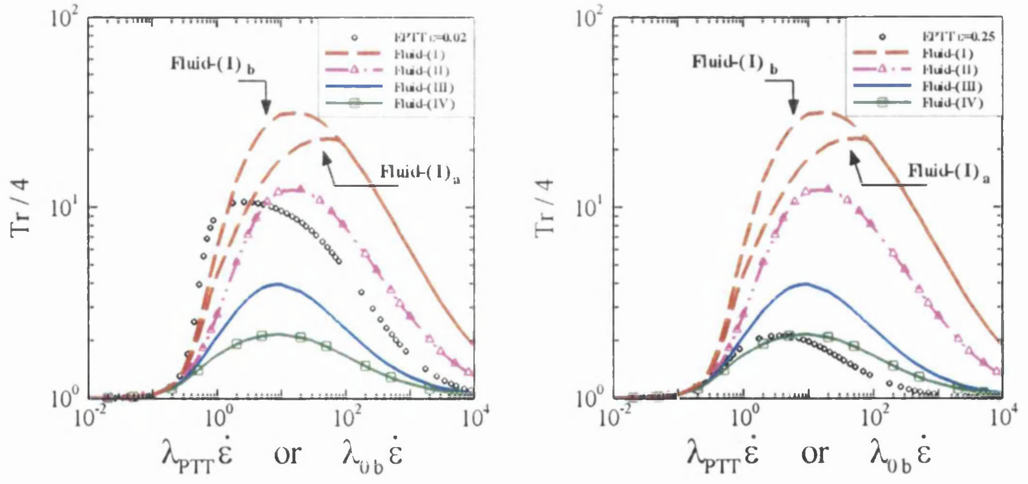

Figure 6.16. Rheological properties of SXPP and EPTT models: variation in q, ε and ε_{PTT}; $\beta = 1/9$, $\alpha = 0.15$.

Little hardening is represented by Fluid-(III) which closely approximates η_e for EPTT($\varepsilon_{PTT}=0.25$), whilst Fluid-(IV) matches the Tr for this low hardening EPTT-fluid. Note that, Fluid-(IV) softens directly without exhibiting any prior hardening in extensional flows. Fluid-(III) is the base-case in previous simulations produced here.

Elasticity influence on vortex cell-size (L along upstream-wall and X along contraction-plane wall) and intensity (ψ_{sal}) is reported for the five fluids simulated. Phan-Thien/Tanner vortex growth is reported by Aboubacar et al. [2], information that is measured and interpreted graphically.

The following sections comment upon the severe and modest strain-hardening instances separately, taking the match over η_e and Tr in turn. As explained in section 6.3.1a, for ready interpretation of data, X and L are calibrated by zooming values by twice the upstream channel half-width. Streamline patterns for the severe and low hardening scenarios are shown in Figure 6.17 and Figure 6.18, respectively. Figure 6.19 displays the trends of cell-size and intensity along with the predictions for the two EPTT fluids reported by Aboubacar et al. [2].

6.3.3a Match on severe strain-hardening: EPTT(ε_{PTT} = 0.02), η_e and Tr

A Comparable η_e-peak value for the severe hardening EPTT($\varepsilon_{PTT}=0.02$) choice is obtained by Fluid-(I)$_a$. In general, larger vortices are found for Fluid-(I)$_a$ than for Fluid-(II). For all cases, vortex intensity (ψ_{sal}) is greater for the more strongly-hardening fluid. Trends in intensity and cell-size for both Pom-Pom fluids are very similar under increasing elasticity (see Figure 6.17 and Figure 6.19). Two features are particularly noticeable: first, lower We_{crit} is attained for fluids with higher degree of strain-hardening. For Pom-Pom Fluid-(II) with less hardening response, $We \approx 17$, a value that almost doubles $We_{crit} \approx 9$ of Fluid-(I)$_a$. The second feature is that vortex cell-size and intensity are fairly similar for both fluids at their corresponding We_{crit}.

EPPT($\varepsilon_{PTT} = 0.02$) exhibits slight vortex inhibition at low elasticity levels ($We \leq 3$); this is followed by a significant enhancement in cell-size and intensity. For this fluid the reported maximum elasticity attainable is $We \approx 30$ (see original Figure 6 in Aboubacar et al. [2]). Although, no inhibition in vortex growth is observed with increasing elasticity for either SXPP fluids (I)*a* and (II), trends are similar though not in magnitude. The curvature of the separation-line differs between EPTT and SXPP fluids. The EPTT($\varepsilon_{PTT} = 0.02$) model shows linear structure at low elasticity and gradually becomes slightly concave; as elasticity approaches critical level, convex shape and very large vortex cell-size are observed. In contrast, SXPP fluids, of matching η_e and Tr, display insignificant change in orientation or shape of the vortex separation-line (linear shape) as the level of elasticity increases.

6.3.3b Match on modest strain-hardening: EPTT($\varepsilon_{PTT} = 0.25$), η_e and T_r

The extensional viscosity peak-value of EPTT($\varepsilon_{PTT} = 0.25$)-setting is approximated closely by Fluid-(III), a material representing slight hardening only, followed by strain-softening. Fluid-(IV), a setting without hardening, equates to the peak of EPTT($\varepsilon_{PTT} = 0.25$) in Trouton ratio. A decline in the level of hardening, compared with the strongly-hardening scenario, is reflected in the prediction of smaller vortices for both SXPP and EPTT models. The same decline also gives as a result higher levels of attainable elasticity, being $We_{crit} \approx 60$ for both Fluids (III) and (IV). Fluid-(III) exhibits some slight enhancement in vortex intensity, although this is difficult to detect from Figure 6.19. Such growth occurs up to an elasticity level around $We = 5$. Beyond this stage, intensity slightly declines in a monotonic fashion. When Fluid-(III) response is compared against that exhibited for EPTT($\varepsilon_{PTT} = 0.25$), similar trends are extracted, though variations are easier to observe with the network model. The largest intensity for both Fluid-(III) and EPTT($\varepsilon_{PTT} = 0.25$) is located around the same Weissenberg number of $We \approx 5$.

Fluid-I_a: matching η_e-ε_{PTT} = 0.02

a) We = 1

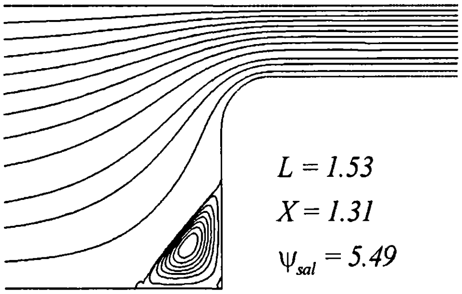

b) We = 5

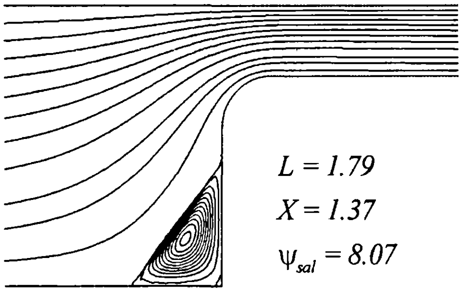

c) We = 9

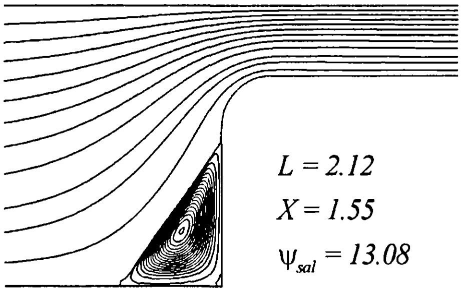

Fluid-II: matching Tr-ε_{PTT} = 0.02

d) We = 1

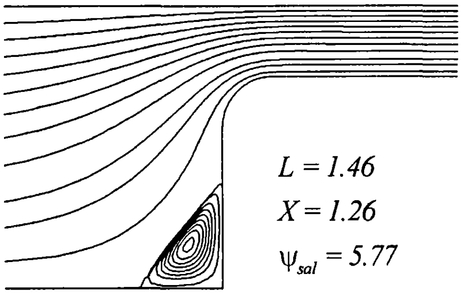

e) We = 5

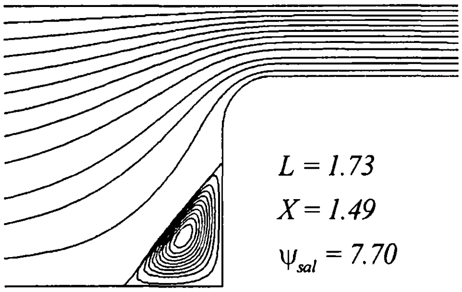

f) We = 10

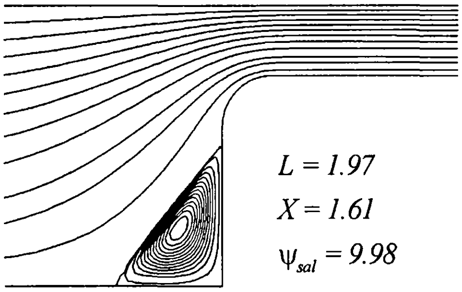

g) We = 17

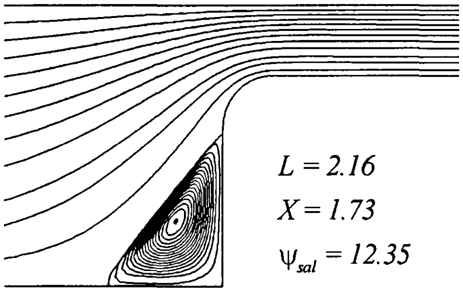

Figure 6.17. Streamlines and vortex data (L, X, $\psi_{sal}\times[-10^4]$), Fluids I_a and II, strong hardening.

Fluid-III: matching η_e-ε_{PTT} = 0.25 ***Fluid-IV: matching Tr-ε_{PTT} = 0. 25***

a) We = 1 *e) We = 1*

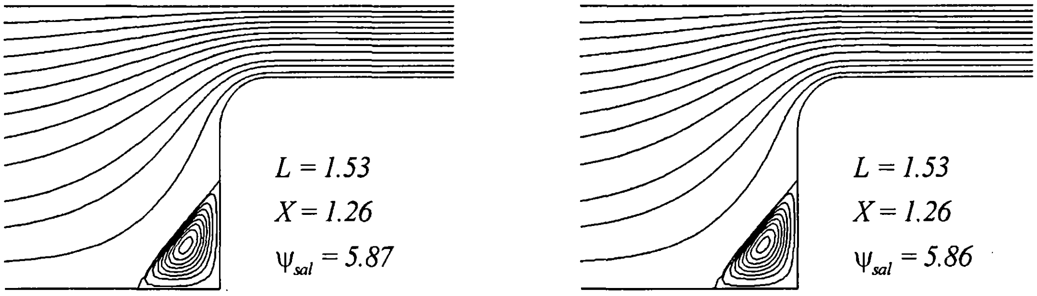

b) We = 10 *f) We = 10*

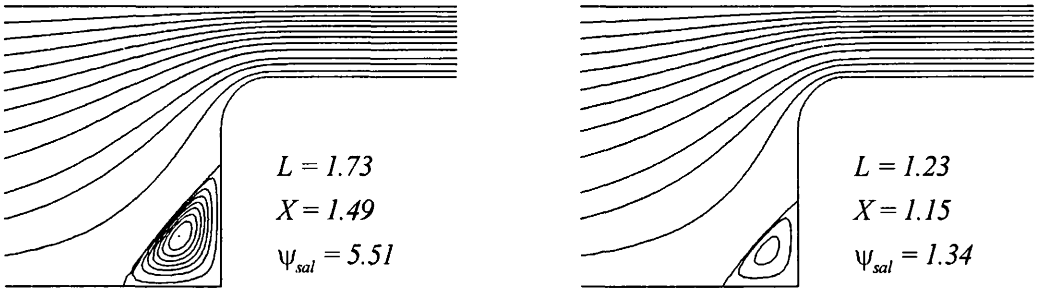

c) We = 20 *g) We = 20*

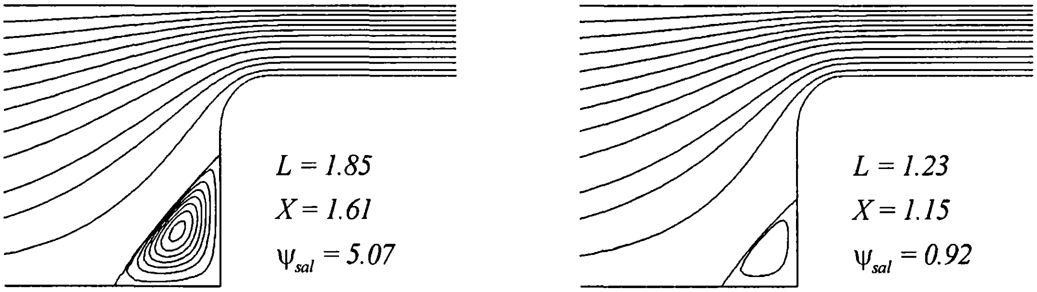

d) We = 60 *h) We = 60*

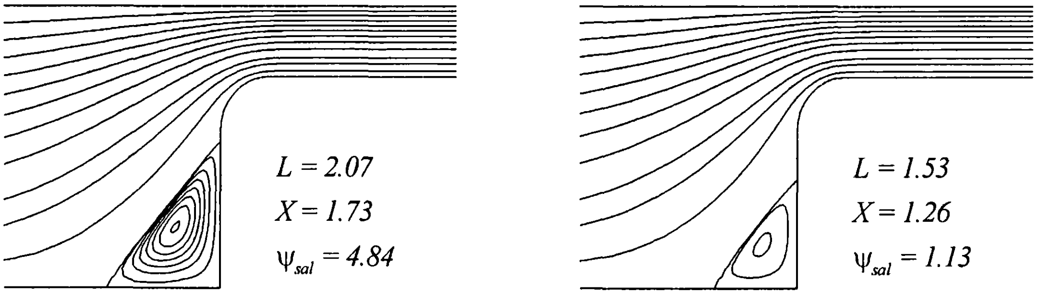

Figure 6.18. Streamlines and vortex data (L, X, ψ_{sal} ×[-10^4]), Fluids III and IV, low hardening.

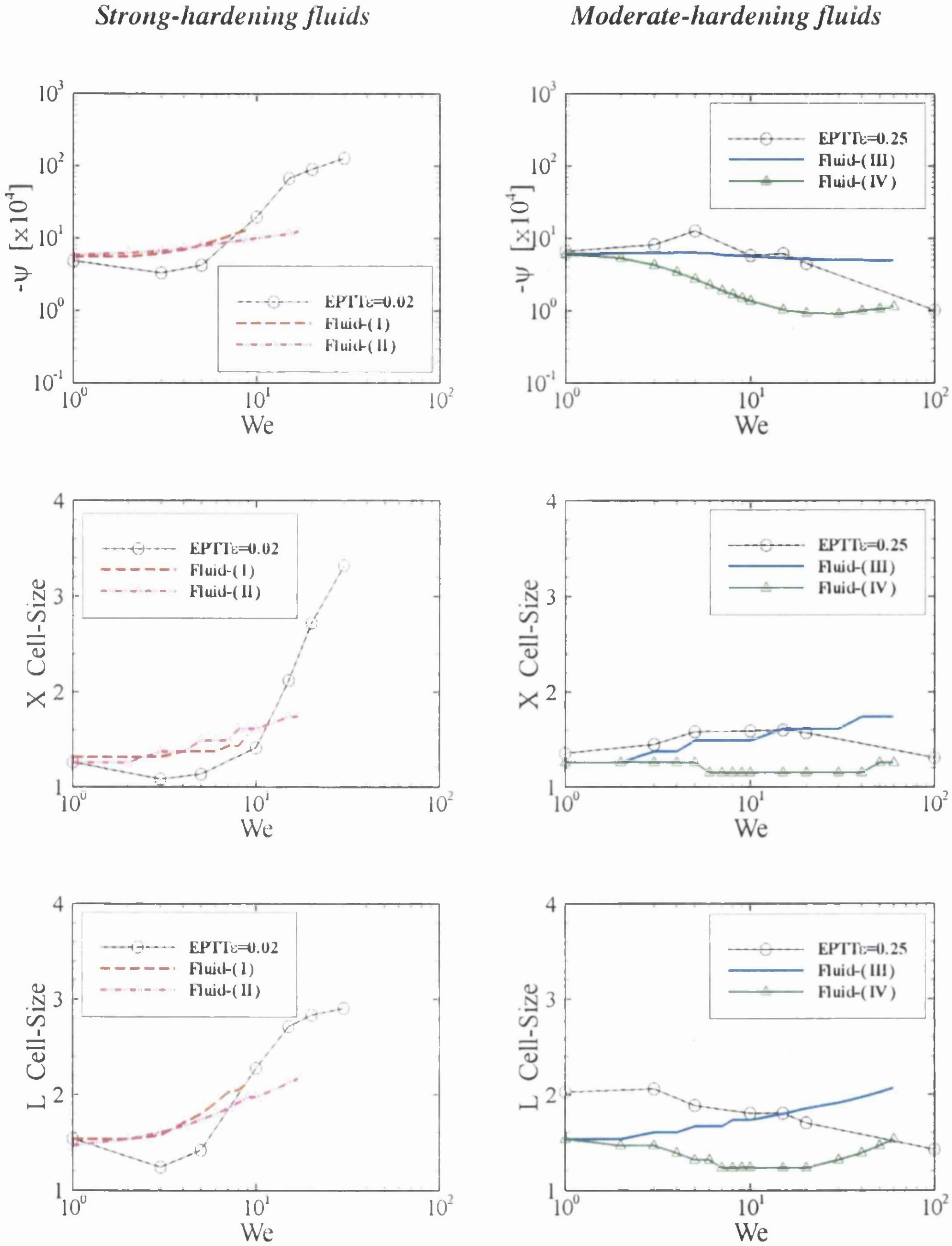

Figure 6.19. Salient-corner vortex intensity and cell-size, increasing *We*; strong and moderate hardening fluids.

There is no vortex enhancement predicted for Fluid-(IV), either in intensity or cell-size, up to a level of $We = 30$, beyond which a slight increase in these magnitudes takes place. This trend followed by Fluid-(IV) lies in opposition to that displayed for EPTT($\varepsilon_{PTT} = 0.25$). However, at $We = 100$ the EPTT model shows a similar limiting intensity with that exhibited by Fluid-(IV) at $We = 60$.

Reduction in vortex intensity and cell-size may be linked to a consequence of strain-softening behaviour and associated levels of Trouton ratio. The higher elasticity levels reached for the EPTT models, may be attributed to the fact that the extensional viscosity for EPTT($\varepsilon_{PTT} = 0.25$) is lower than that for its matching counterpart, Fluid-(III), and strain rates larger than $O(2)$ units, see Figure 6.16. The shape of the vortex separation-line is practically linear for Fluid-(III), similar to that predicted for Fluid-(I)$_a$ and (II). Alternatively, Fluid-(IV) presents a relatively convex structure. For the corresponding EPTT-setting, separation-line shape changes from linear ($We = 1$) to convex ($We = 5$), recovering linear shape at elasticity levels greater than $We = 20$ (see [2]).

6.3.3c Fluid-(I)$_a$ and Fluid-(I)$_b$: similarities and differences

In this section, the influence of α is studied for the SXPP fluid exhibiting the largest strain-hardening behaviour. Field contour plots for the polymeric first and second normal stress difference are shown in Figure 6.20 for Fluid-(I)$_a$ and Fluid-(I)$_b$. The only difference between these fluids is the level of anisotropy, governed by $\alpha = 0.15$ and $\alpha = 0.05$, respectively.

The effect of varying anisotropy on N_1 is mainly observed in two regions. One is just above the re-entrant corner, a small zone where a decline in N_1 may be related to the reduction in extensional viscosity by increasing α. The second region corresponds to the fluid lying on the downstream wall, where difference in ψ_1 at the chosen anisotropy levels, produces a decrease in N_1 from $\alpha = 0.05$ to 0.15. A similar response is discussed in section 6.3.2.

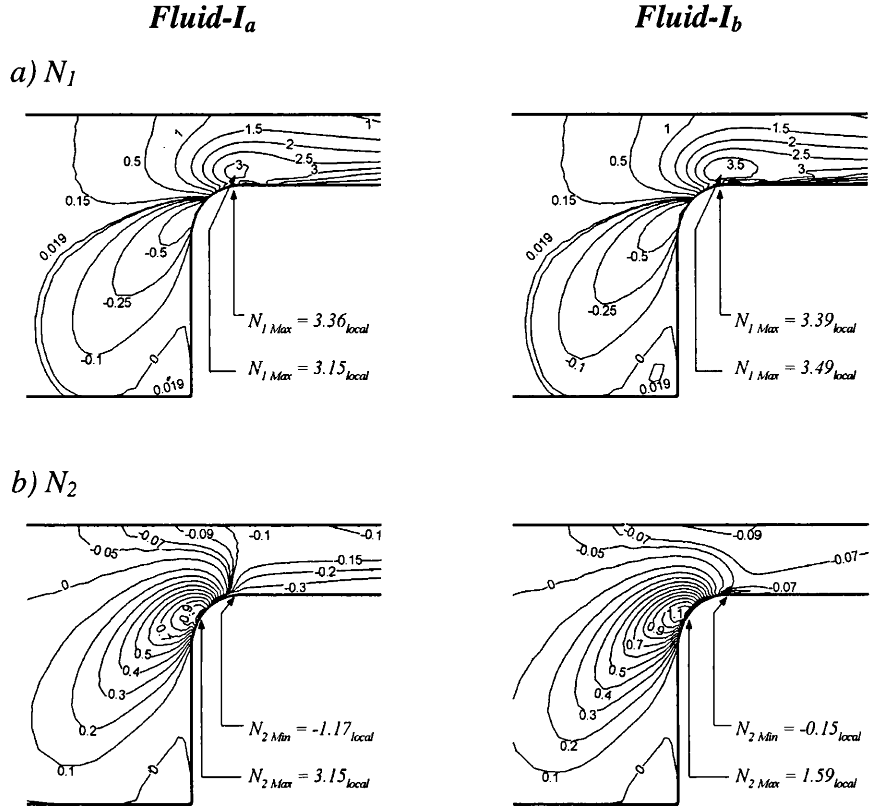

Figure 6.20. First and second normal stress difference (N_1, N_2) fields: $\alpha = 0.05$ (Fluid-I$_b$) and 0.15 (Fluid-I$_a$); $We = 8$.

The influence of α-variation is expected to have a larger effect on N_2 than on N_1. As the fluid passes across the stretch 'banded-zone' reaching the re-entrant corner, a general, though slight, decline in N_2 values can be observed with decrease in α. The most substantial variation in N_2 is along the downstream wall, just beyond the end of the rounded-corner, a region of strong shear-flow. There, an increase in magnitude of the polymeric stress difference is predicted, from 0.07 units at $\alpha = 0.05$ to 1.5 units at $\alpha = 0.15$. Near the centreline in the entry flow section, α-

adjustment has had barely any impact on N_2. Such findings lend themselves to the conclusion that variation in α is related primarily to a shear-flow response.

There is a decrease in strain-hardening provoked by increasing the anisotropy parameter from $\alpha = 0.05$ to $\alpha = 0.15$. This decrease, as anticipated, allows simulations to reach a higher level of critical elasticity, although here this increment in We_{crit} is only minor, from $We_{crit} = 8$ to $We_{crit} = 9$, for Fluid-(I)$_a$ and Fluid-(I)$_b$, respectively.

6.4 Conclusions

The influence on a complex flow of variation in the number of side branched-arms, q, dangling from the ends of a molecular chain segment, has been studied in this chapter. Extensional viscosity is largely affected by such parameterisation. The selected geometry is a planar rounded-corner 4:1 contraction. With q-variation from 2 to 15, the fluids display levels of hardening varying from slight (sometimes referred to here as 'delayed' softening) to severe, respectively. Note that, over the prevailing kinematic flow conditions, strain-softening is not anticipated for Fluids-q_{10} and q_{15} (10 and 15 arms); for Fluid-q_5 softening may occur in a minuscule region around the corner. There is significant impact upon the extensional viscosity and normal stress difference to take into account with change in q. The shear viscosity for the selected set of parameters is barely affected by this proposed variation in the number of branched-arms.

There is only relatively slight influence detected on d_{xx} and d_{xy}-fields by such variation in the number of arms. Zones with expected softening are presented in order to explain the differences between Fluid-q_2 from the other selected fluids ($q \geq 5$). Due to the differences in extensional viscosity, these zones are found to decrease significantly, and to even disappear for more severe hardening configurations. The onset of extension softening seems to have a strong impact on vortex behaviour, producing suppression of intensity. In addition, lower levels of strain-hardening may account for larger levels of attainable elasticity, as seen on [28,54,83]. Vortex cell-size follows similar trends across all Fluid-q_i studied, noting that for fluids where low or zero strain-softening is anticipated, cell-size follows essentially the same patterns.

Variables directed related to shear viscosity (τ_{xy} and Δp) exhibit minor departure between solutions for these variations in the number of arms. Pure extensional deformation applies along the centreline, whilst strong shear flow is developed in the exit-channel. In the entry-flow section, reaching the re-entrant corner, there is superposition of these two types of deformation.

In regions dominated by extensional deformation, increase in the magnitude of stress and stretch may be observed. Backbone stretch continually increases (even doubles) across the entry flow region. Such increase is more evident from Fluid-q_2 to Fluid-q_5. In the exit channel (a strong shear-flow zone), significant increase is detected in N_1 and λ with increasing q; these differences are sustained along the downstream section. Again, this change is more rapid from $q=2$ to $q=5$ than above. As mentioned earlier, the coefficient of the first normal stress difference is the cause of these variations.

Large values of the anisotropy parameter, α, may produce the onset of singularities in rheometrical flows. Discontinuities in shear functions are not captured for the kinematic conditions exhibited by the cases analysed here.

Reported vortex trends for two contrasting EPTT fluids are compared with Pom-Pom fluids, with similar degrees of hardening and peak-values in Trouton ratios. Adjustment in peak-values for both models is obtained by first, fixing the viscosity ratio (β) to that used by Aboubacar et al. [2], and then, varying the number of arms (q) and relaxation times ratio (ε) in the SXPP model. Differences in rate-of-change for shear-thinning and in extension hardening/softening, imply that even when the extensional viscosity is equivalent between EPTT and SXPP models, Trouton ratios are larger for the Pom-Pom model than for the corresponding network-type fluid. For this reason, two SXPP sets of parameters are produced, matching η_e and Tr in turn, for each PTT fluid studied.

For the strongly-hardening/softening EPTT($\varepsilon_{PTT} = 0.02$)-setting, fluids (I)$_a$ and (II) approximate η_e and Tr respectively. In this scenario, growth in cell-size and intensity follow similar trends in all three fluids (except for a small inhibition at low We for the EPTT case). Larger vortices are gathered for the severe hardening case over the slightly hardening behaviour. Switching to this moderate hardening case, EPTT($\varepsilon_{PTT} = 0.25$) and Pom-Pom Fluid-(III) display similar peak-values in extensional viscosity; vortex intensity grows up to $We \approx 5$. After this stage a decline is gathered. However, changes are much more dramatic for the PTT model. Pom-Pom Fluid-(IV) exhibits no hardening at all, it softens even at low strain-rates and its trend in intensity is opposite to that for the corresponding PTT fluid. This is the only SXPP-setting where vortex reduction in cell-size has been observed. Therefore, it can be concluded that larger strain-hardening is related to the generation of large vortices.

In this study, vortex trends are better approximated by fluids showing equivalent extensional viscosity than Trouton ratio (for moderate hardening cases). For all the different sections in the present chapter, lowering strain-hardening peak-values has produced an increase in the attainable elasticity number.

CHAPTER 7

Excess Pressure-Drop in Contraction and Expansion Flows for Boger Fluids*

Estimation of pressure-drop (Δp) for constant viscosity highly elastic (Boger) fluids in contraction and contraction/expansion flows is considered in this chapter. Experimentally, significant enhancement above that corresponding to Newtonian fluids with same viscosity and flowrate (Q), can be observed in axisymmetric contractions. In contrast, for planar configurations, pressure-drop is practically equivalent for both Newtonian and Boger fluids. Numerical analysis has failed to predict successfully such phenomena for Oldroyd-B models. Changing from a 4:1 contraction to a 4:1:4 contraction/expansion geometry helps to determinate the factors that contribute to such enhancement in pressure-drop. Amongst these factors, the extensional viscosity (η_e) of the fluid and the viscosity ratio play an extremely important role in the enhancement of pressure-drop. Alternative models capable of reproducing severe hardening response in extensional flows are investigated. A

---

* Material of this chapter has been shaped and submitted for publication to the *Journal of Non-Newtonian Fluid Mechanics.*

hybrid finite element/volume algorithm with a time-stepping procedure is employed to obtain numerical solutions.

7.1 Introduction

Enhancement in excess pressure-drop[†] (*epd*) observed for Boger fluids in axisymmetric contractions but not in planar flows is a phenomenon that has proved to be a challenge for numerical algorithms to date. The importance of these Boger fluids is that they adequately represent the response of diluted polymeric systems. Here, the addition of small quantities of polymer may produce highly elastic properties while the shear viscosity remains practically unaffected [24].

Nigen and Walters [73] compared experimental pressure-drops under increasing flowrates for two polyacrylamide/water-glucose Boger fluids (B1 and B2 [24]) and for glucose-water Newtonian liquids (NS1 and NS2) in contraction geometries. The trial contraction ratios were in the range $2 \leq \hat{\beta} \leq 32$ for axisymmetric and planar configurations; both long and short-die exit-lengths were also considered. Analysing the axisymmetric instance, no difference was detected at low flowrates between pressure-drops for Boger and Newtonian fluids at low flowrates. Incrementing values of Q (around one order of magnitude) discrepancies became clearly apparent in both short and long exit dies, although more pronounced for the short-die case. No difference could be detected between Boger and Newtonian fluids in the planar configuration.

In their experiments, Maia and Binding [60] considered the flow of the so-called S1 (polyisobutylene in a mixed solvent of polybutene and Dekalin) fluid trough axisymmetric contraction geometries. The S1 fluid is a system exhibiting shear-tinning and severe extension-hardening properties. The contraction ratios considered were in the range $24.4{:}1 \leq \hat{\beta} \leq 124.3{:}1$. Maia and Binding [60] observed that the

---

[†] In this chapter, *epd* is to identify pressure-drop of a non-Newtonian fluid, even if the trend against elasticity or flowrate is decreasing. Enhancement in *epd* is for an increasing trend.

relation between the pressure-drop and the wall shear-rate is independent of the contraction ratio and identified three different regions of Δp on wall shear-rate. Using the 'Binding analysis', these authors, reported qualitatively agreement for extensional viscosity computations with the observed pressure-drops at low strain-rates. Maia [59] tested the capability of two integral constitutive equations, the Wagner and its modification by Papanastasiou-Scriven-Macosko (PSM) models. Two differential-type models were also studied, the exponential Phan-Thine/Tanner (EPTT) and Giesekus model, to represent the response of the S1 fluid in steady shear, uniaxial extension and flow through axisymmetric contractions. The EPTT model was found to give better agreement with experimental data; moreover, using Binding analysis with this model, good agreement with predicted pressure-drop (in terms of the Couette correction) was gathered for low and high values of the downstream wall shear-rate. In the intermediate zone, the analysis overpredicts the experimental values.

The flow through axisymmetric contraction/expansion geometries ($2 \leq \hat{\beta} \leq 8$) was considered by Rothstein and McKinley [85] (see also [86]). These authors studied the pressure-drop response of a dilute monodisperse polystyrene/polystyrene Boger fluid (with estimated solvent ratio of $\beta = 0.92$) under creeping flow conditions. Large *epd* (over the correspondent Newtonian case) was observed for all trials, varying contraction ratios and curvature of the re-entrant corner.

Szabo et al. [90] simulated the flow of the Chilcott-Rallison version of the Finite Extensible Non-linear Elastic spring (FENE-CR) model - a constant shear-viscosity/strain-hardening fluid [32] - through a rounded 4:1:4 axisymmetric contraction/expansion geometry. These authors observed that, setting the extensibility parameter to $L = 5$, resulted in an initial decrease in *epd* with increasing elasticity, until a Deborah[‡] (De) number of ≈ 3 was reached and an increase in *epd* was gathered thereafter. For further increments in elasticity, pressure-drop for Boger fluids rose above the correspondent Newtonian value until convergence was lost

---

[‡] With identical definition to the used in the present study.

($De_{crit} \approx 9.5$). Setting $L = 3.26$, increase in *epd* was also computed, although convergence was lost before crossing the Newtonian reference line whilst setting $L \to \infty$ (equivalent rheometrical response to Oldroyd-B model) results in a monotonic decrease in *epd* for increasing elasticity. The L-parameter controls the maximum extension attainable by the polymer molecules. The degree of extension hardening for the FENE-CR model was larger for increments in L. The viscosity ratio used in reference [90] was[§] $\beta = 1/9$.

For $L = 3.26$, the minimum peak – *upturn* – in Δp is at $De \approx 1.2$, although the resulted enhancement was not sufficiently large to cross the Newtonian reference line due to loss in numerical convergence. Switching to $L = 5$, Δp minimum was at $De \approx 3$ and in this case *cross-over* appeared. Finally, for a polymer-molecule without limiting extension, $L \to \infty$, no *upturn* was gathered (and therefore no *cross-over*) in Δp. The behaviour of pressure-drop for this case was similar to that reported for an Oldroyd-B fluid in Aboubacar et al. [2,3,5]. The occurrence of the *upturn* and *cross-over* are highly significant phenomena, where the balance between elastic and viscous effects plays a key role. The numerical procedure employed was a finite element scheme. Szabo et al. [90] could claim to be the first to numerically simulate such increase in *epd* and its exceeding over the Newtonian value.

In the 4:1:4 contraction/expansion, the required downstream lengths for stress to relax are significantly shorter than those of the 4:1 contraction. Except for pressure, no difference between downstream and upstream values is detected at any position far from the constriction zone, in the 4:1:4 geometry. Therefore, the rate of dissipation ($\mathscr{D}$) over the domain may be equated to the flowrate times the actual pressure-drop. A similar relationship cannot be established for the contraction flow case. This important feature was pointed out by Cartalos and Piau [29]. In section 7.3.3e, this equivalence between dissipation and the product of pressure drop and

---

[§] As mentioned in chapter 5, $\beta = 1/9$ represents a system with high polymeric content, not representative of Boger fluids; however, shear viscosity for the FENE-CR model is constant, giving then, similar response to diluted systems in some instances.

flowrate helps to recognize the conditions required to obtain pressure loss (Δp_{Boger}) values larger than those of the corresponding Newtonian fluid.

A monotonic decrease with elasticity was observed for the response of a shear-thinning Pom-Pom fluid in a planar rounded-corner 4:1:4 geometry, investigated by Wapperom and Keunings [102]. In a more recent study, Binding et al. [17] predicted the *upturn* in both planar and axisymmetric 4:1:4 configurations setting the solvent ratio $\beta = 1/9$. The cross-over was detected for the planar configuration at the same β. Results for a highly polymeric content system ($\beta = 1/9$) provided a continuous decreasing trend in pressure-drop with increase in De. The finite element package POLYFLOW was employed in reference [17].

Perera and Walters [78] investigated the flow of a 4-constant shear-thinning Oldroyd fluid through expansion/contraction/expansion geometries. The main interest was on the influence of rheometrical functions on vortex growth. Keiller [54] predicted pressure-drops through an orifice into a tube for both Oldroyd-B and FENE-CR models. For these viscoelastic fluids, Δp-values were lower than the Newtonian case with equivalent shear viscosity and flowrate. Keiller [54] associated this reduction in pressure-drop with the development of a Poiseuille flow in the long exit-tube. The extra pressure-drop** for Oldroyd-B and FENE-CR models followed the same monotonic decrease with increasing Weissenberg (We) numbers. That is until elasticity is large enough and the molecules have attained their maximum extension in the FENE-CR fluid, producing a slight increase before reaching a plateau in pressure-drop. Additionally, Keiller [54] found negative values of extra pressure-drop for both axisymmetric and planar geometries.

Aboubacar et al. [2,3] compared pressure-drop for the flow through 4:1 sharp and rounded-corner axisymmetric and planar geometries for five viscoelastic fluids: an Oldroyd-B, two low-hardening and two severe-hardening PTT (linear and

---

** Definition: extra pressure-drop $\dfrac{\Delta p_{Boger} - \Delta p_{Newt}}{\Delta p_{Newt} / L_{downstream}}$.

exponential) fluids. The reported pressure-drop was normalized against the corresponding Newtonian fluid. The solvent ratio was set to $\beta = 1/9$. Incrementing elasticity, simulation results for all fluids showed a monotonic decrease in the normalized pressure-drop when compared with the Newtonian case. Trends were relatively unaffected by the two corner shapes studied there and fluid type (either shear-thinning PTT or constant viscosity Oldroyd-B). In particular, this finding raises the question - when and what conditions are required to reproduce enhanced *epd* in axisymmetric contractions for the highly-elastic constant shear-viscosity Oldroyd-B model, a model capable of reproduce Boger-fluid type response.

The numerical simulations reported in this chapter are obtained with the hybrid finite element/finite volume (*fe/fv*) scheme. The creeping flow through rounded-corner 4:1 contraction and 4:1:4 contraction/expansion geometries, both axisymmetric and planar, is considered here. The 4:1:4 geometry follows the specifications used in Rothstein and McKinley [85,86], Szabo et al. [90] and Wapperom and Keunings [102]. The Oldroyd-B model is employed to match Boger-type behaviour due to its constant viscosity and severe hardening. Alternative representation of Boger fluids is made via Phan-Thien/Tanner and Single eXtended Pom-Pom (SXPP) models. To this effect, shear-thinning properties exhibited by these two classes of models is removed almost completely, by adjustments in the level of solvent content and additionally, severe extension-hardening is achieved by the proper choice of parameter.

7.2 Problem specification

Upstream channel radius (half-height in planar case) is R_u; the radius in the mid-plane is given by $R_c = R_u/4$; the rounding of the corner is determined by fractions of R_c, see Figure 7.1 for a schematic representation of these geometries. Specifications for the contraction/expansion are the same as in reference [102]. Inlet and exit regions of the computational domain are given by $19.5L$, where $L = R_u/4$.

a) 4:1:4 Contraction/expansion

b) 4:1 Contraction

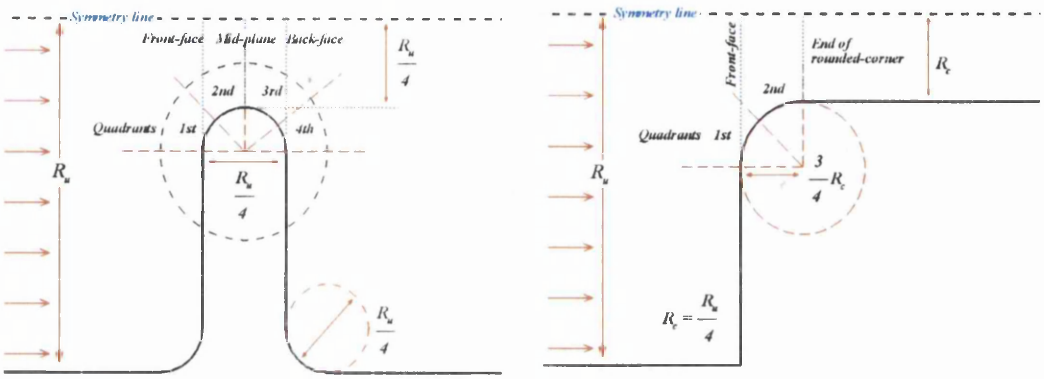

Figure 7.1. Schematic diagram for a) 4:1:4 contraction/expansion, b) 4:1 contraction.

4:1:4

4:1

a) Coarse

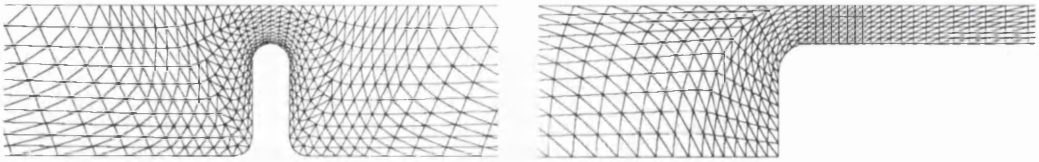

b) Medium

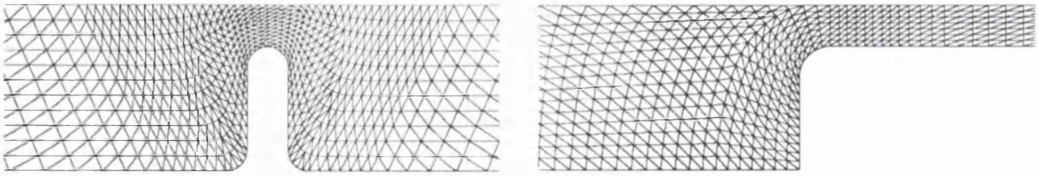

c) Refined

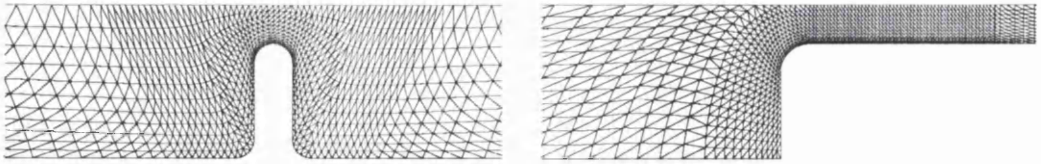

Figure 7.2. Zoomed mesh sections of 4:1:4 contraction/expansion and 4:1 contraction; a) coarse, b) medium, c) refined.

Dimensions for the contraction flow are the same as those used in chapter 6. Three meshes with different degrees of refinement (see Figure 7.2) are employed for each geometry. Element density increases especially in the vicinity of the boundary wall of the contraction. Detailed information on mesh characteristics is provided in Table 7.1.

Table 7.1. Mesh characteristics

Mesh	*Elements*	*Nodes*	*Degrees of freedom* $(\mathbf{u}, p, \tau)$	*Rmin*
$(4{:}1{:}4)_a$	1080	2289	14339	0.0099
$(4{:}1{:}4)_b$	1672	3519	22038	0.0074
$(4{:}1{:}4)_c$	2112	4439	27798	0.0058
$(4{:}1)_a$	1086	2325	14570	0.0296
$(4{:}1)_b$	1626	3433	21502	0.0170
$(4{:}1)_c$	2693	5652	35392	0.0097

In this study, comparison between planar and axisymmetric geometries has been made by imposing the same average velocity through the constriction zone, similarly to Binding et al. [17] and Phillips [79]. Flow response is analysed with increasing elasticity, in terms of the Weissenberg number. The increase in We can be achieved through a variation in the relaxation time of the fluid or in the velocity scale, (see equation (2.50)), rendering similar results. Here, Weissenberg is increased by means of the relaxation time scale.

Inlet boundary conditions are imposed through the solution of Poiseuille flow reported by Waters and King [104]. The velocity at the boundary walls is set to zero (no-slip at boundary). Upstream channel length is sufficiently large to ensure fully-developed flow is established before the contraction. Stress is determined pointwise through the derived ODE system of the particular choice of model. Continuation in elasticity is employed to obtain converged steady-state solutions; incrementation in

We is typically {0.1, 0.5, 1.0, 1.5, 2.0, 2.1, 2.2, ..., We_{crit}}. At $We = 0.1$, initial conditions for stress and velocity are those from rest. Criteria to terminate the time-stepping procedure is when the L_2-norm relative maximum difference between two consecutive time steps fall below a set threshold (10^{-7} in the present study).

7.2.1 Pressure-drop calibration

The total pressure-drop observed in a contraction flow is the sum of the corresponding Δp for fully-developed (*fd*) Poiseuille flow of the upstream and downstream channels plus an additional loss due to the presence of the contraction. This additional loss is referred to here as 'entry correction' (Δp_{en}). If the tested fluid is Boger-type, significant differences are expected to occur in axisymmetric geometries but not in planar; this, when compared to a Newtonian fluid of same viscosity and same flowrate. Excess pressure-drop (*epd*) is reported here in terms of a normalized entry correction (see for example [2,17,85,86]) and is defined as

$$\mathcal{P} = \frac{\left(\Delta p - \Delta p_{fd}\right)_{Boger}}{\left(\Delta p - \Delta p_{fd}\right)_{Newt}} = \frac{\left(\Delta p_{en}\right)_{Boger}}{\left(\Delta p_{en}\right)_{Newt}} \qquad (7.1)$$

where the Poiseuille flow contribution is $\Delta p_{fd} = \Delta p_{upstream} + \Delta p_{downstream}$ and as mentioned above, the flowrate and the shear viscosity are set to be the same for both viscoelastic and Newtonian fluids. Total pressure-drop ($\Delta p = p^{inlet} - p^{exit}$) is sampled at centreline positions, between inlet to exit, where fully-developed flow in $\boldsymbol{\tau}$, $\nabla \mathbf{u}$ or ∇p (say within 1%) can be assumed. Solvent/total viscosity ratio β is varied in order to approximate Boger-type response. Values of this ratio are {1/9, 0.9, 0.95, 0.99, 0.999}; highly polymeric content is represented by $\beta = 1/9$, whilst $\beta \geq 0.9$ represents very diluted systems. For the non-constant shear viscosity models (PTT and XPP) β controls the level of the variation in η_s. In fact, for the normalised shear viscosity (η_s/η_{s0}) the relation $\eta_s/\eta_{s0} \to \beta$ is satisfied for extremely large shear-rates ($\dot{\gamma} \to \infty$). This means that for $\beta = 0.9$, the maximum deviation from Boger-like behaviour is anticipated to be 10%. Therefore, for both PTT and XPP models, the viscosity ratio studied here is $\beta \geq 0.9$.

7.3 Results and discussion

Excess pressure-drop for the Oldroyd-B model is studied under increasing values of elasticity. The cause of the differences observed in *epd* is analysed for two different levels of solvent content: $\beta = 0.9$, where the *upturn* is more noticeable and $\beta = 0.99$, for the analysing the *cross-over* phenomena. Then, a comparison between the flow across both 4:1:4 and 4:1 geometries in terms of internal pressure (p) values is presented. Alternative constitutive equations as Phan-Thien/Tanner and Single eXtended Pom-Pom models are adjusted to represent constant shear-viscosity fluids, with large levels of extension-hardening, in order to stimulate *epd* enhancement for bounded extensional viscosity fluids. The influence of the location of sampling points is examined and comments are included on the conditions necessary to obtain larger pressure-drop values than those exhibited by Newtonian fluids.

7.3.1 Excess pressure-drop in 4:1:4 and 4:1 geometries: Oldroyd-B model

Response of excess pressure-drop (*epd*) to a variation in elasticity (We) for 4:1:4 axisymmetric and planar geometries is displayed in Figure 7.3. Considering first the solvent ratio $\beta = 0.9$ in the circular geometry, a decline with increasing We is observed until a minimum is reached at $We = 2$. Thereafter, an increasing *epd*-trend takes place until the simulation diverges at $We_{crit} = 5$, a stage that ‘touches’ the Newtonian reference line ($epd = 1$). This *upturn* in *epd* is the first important feature to be analysed. Same behaviour is gathered for the axisymmetric case with $\beta = 0.99$.

a) 4:1:4 Axisymmetric

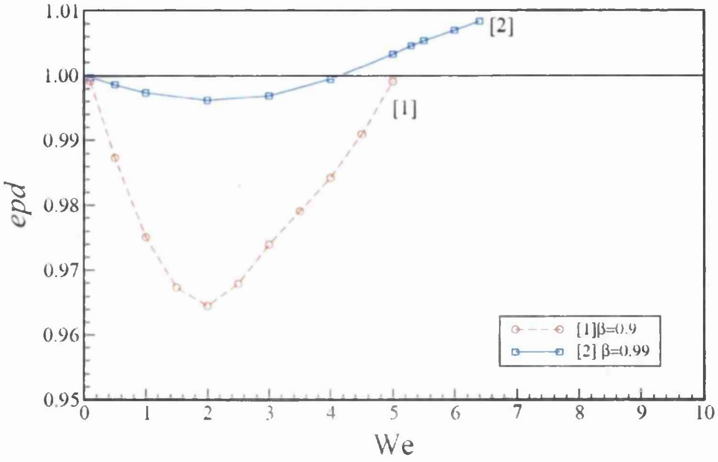

b) 4:1:4 Planar

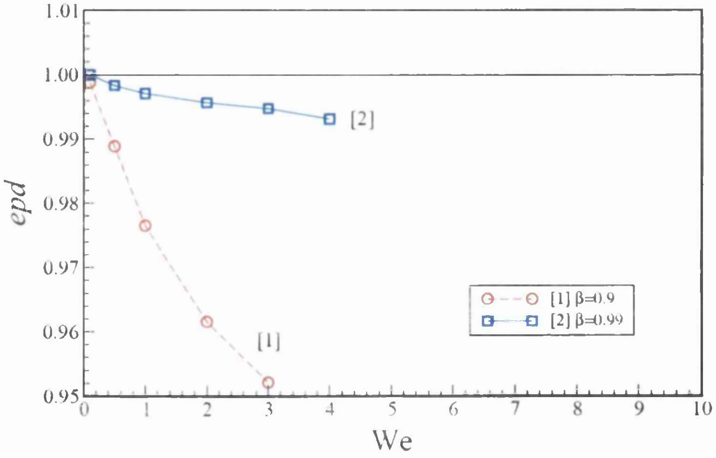

Figure 7.3. Pressure-drop (*epd*) vs. *We* (Oldroyd-B): $\beta = 0.9$ and 0.99, 4:1:4 contraction/expansion; a) axisymmetric, b) planar.

The *upturn* occurs at the same elasticity value as that for $\beta = 0.9$, although for this more diluted system, *epd* crosses the reference line at $We \approx 4.2$ and the growth continues up to the critical stage around $We_{crit} = 6.4$. Hence, the *cross-over* appears, the second feature to be studied here. Note that even when the rate-of-increase (slope) in *epd* is lower for $\beta = 0.99$ when compared to the slope for $\beta = 0.9$, two factors account for the cross-over: the larger attainable elasticity and the fact that at

$\beta = 0.99$, *epd*-trend is closer to the Newtonian reference line due to the effect of having 'more' solvent in the solution. In the planar case, monotonic decrease (concave curvature) in *epd* is observed for both levels of solvent content. Critical levels are $We_{crit} \approx 3$ and $We_{crit} \approx 4$ for $\beta = 0.9$ and $\beta = 0.99$, respectively. Switching to the 4:1 contraction setting (Figure 7.4), only monotonic decrease with We is gathered. This decline is more substantial for the axisymmetric scenario than for the planar situation, and curiously, the *epd*-trend shows some convex shape, i.e. no tendency to reach a plateau is expected for the circular contraction flow. Critical levels of elasticity are $We \approx 3.5$ ($\beta = 0.9$), $We \approx 6$ ($\beta = 0.99$) for the axisymmetric case and $We \approx 4.5$ ($\beta = 0.9$), $We \approx 8$ ($\beta = 0.99$) for the planar. Note that *epd* values for the contraction case are significantly larger than those for the contraction/expansion scenario. In fact, pressure-drops can be about twenty time greater for the 4:1 case.

In all these simulations, larger values of attainable elasticity are obtained for larger values of the solvent ratio. Decline in excess pressure-drop has been frequently reported in the simulation literature for planar and axisymmetric, rounded-corner and abrupt contraction flows [2,3,8,54].

7.3.1a Solution data – 4:1:4 flow

Figure 7.5 displays contour lines for pressure in the 4:1:4 axisymmetric instance, at $We = 2$ and $We = 3$ and setting $\beta = 0.99$, with the objective to demonstrate that mesh convergence has been achieved. By observing these contour patterns, two aspects are detected: from the coarsest to the finest mesh, a smoothing effect in the segments of the curves takes place; additionally, contour lines for any given (non-dimensional) pressure are located in the same position for each mesh employed. Therefore, predictions obtained for all meshes are adequate.

a) 4:1 Axisymmetric

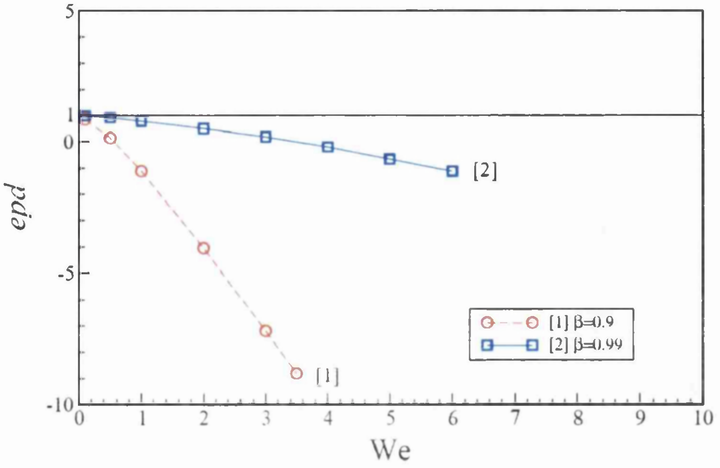

b) 4:1 Planar

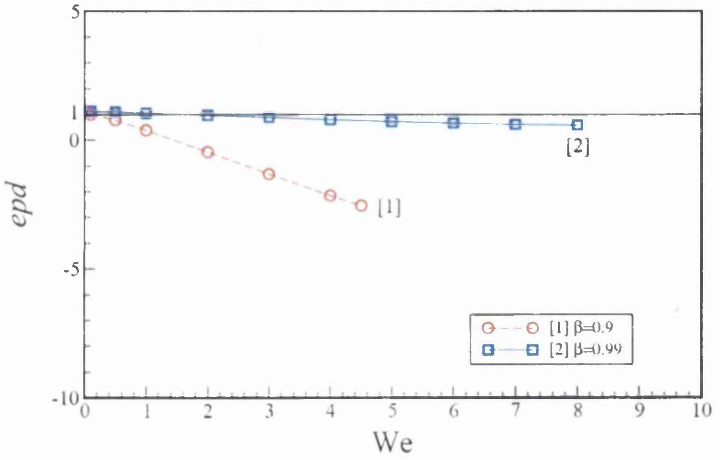

Figure 7.4. Pressure-drop (*epd*) vs. *We* (Oldroyd-B): β=0.9 and 0.99, 4:1 contraction; a) axisymmetric, b) planar.

- *Axisymmetric contraction/expansion flow;* $\beta = 0.9$

Special attention is given to the *turn-up* displayed in this case. Contour lines for pressure around the constriction are presented in Figure 7.6. Apart from the pressure levels, differences between planar and axisymmetric configurations arise in a small area in touching the front-face of the constriction. In this zone a peak in pressure is detected, and for the axisymmetric setting, a decrease in the area of this zone, from

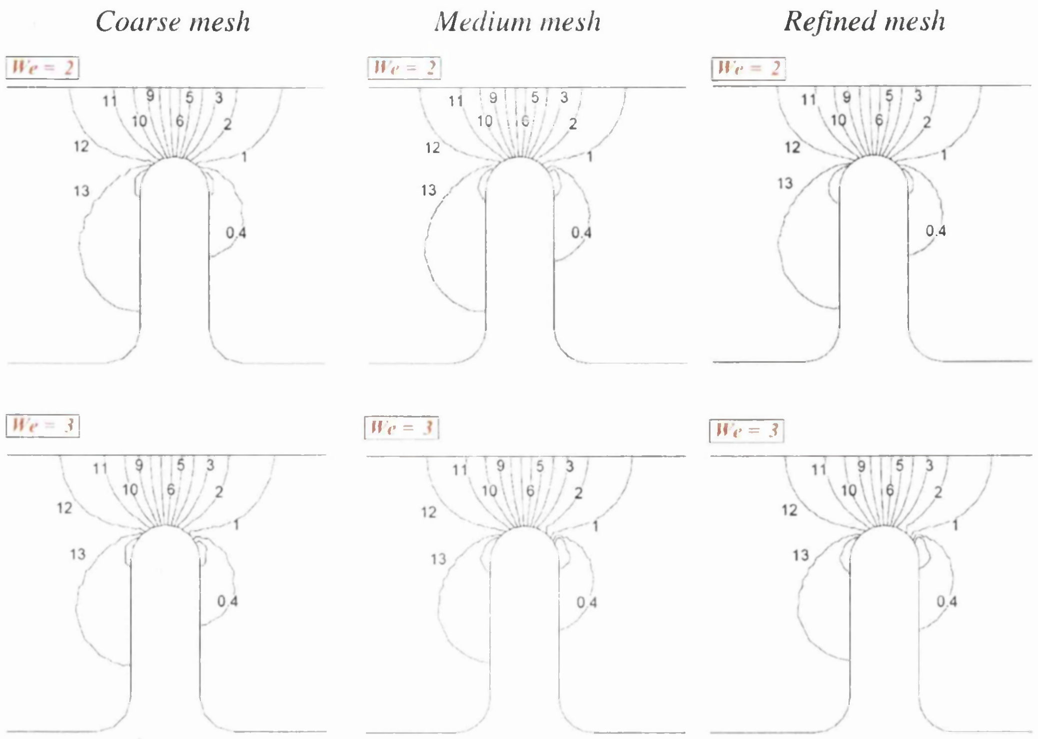

Figure 7.5. Pressure field plots around the contraction/expansion (Oldroyd-B): $\beta = 0.99$, $We = 2$ and 3, 4:1:4 axisymmetric, coarse, medium and refined meshes.

$We = 1$ and $We = 2$. After the decline, when elasticity reaches $We = 3$, an increase is gathered. Such behaviour is not reproduced by the planar situation, where only a decrease in area occurs, as it can be seen in the shaded zones presented in Figure 7.6. Note that the response in these regions for the circular contraction emulates the behaviour of the *upturn*.

- *Pressure profiles at centreline and along the wall; axisymmetric, $\beta = 0.9$*

For the axisymmetric 4:1:4 geometry, centreline plots are shown in Figure 7.7, there, the lower-left plot is for the full geometry and zoomed sections are included. Top-left plot is a zoom of the entry section, a zone in which a flip-over in p is exposed. As the flow advances through the constriction (top-right plot), pressure adjusts linearly; that is, p increases with We. For the exit section of the constriction (lower-right plot) no visible differences are gathered; the selected We-levels become

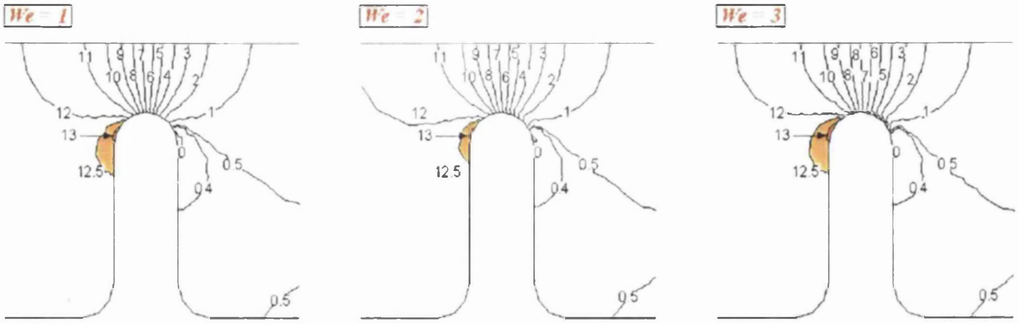

p-Axisymmetric

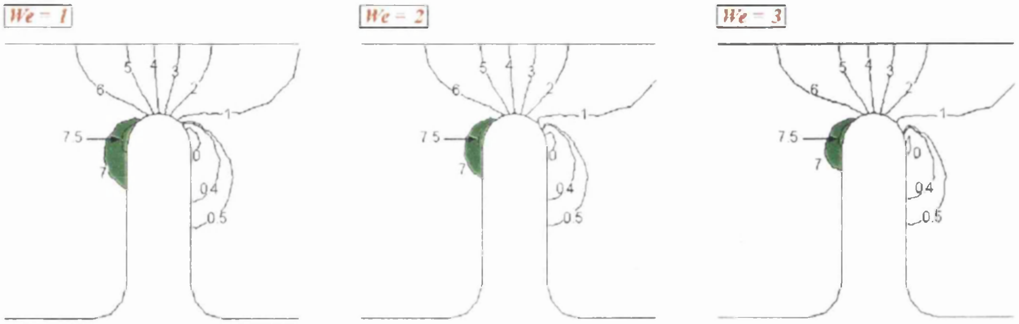

p-Planar

Figure 7.6. Pressure field plots around the contraction/expansion: increasing *We* (Oldroyd-B): $\beta = 0.9$, axisymmetric vs. planar.

coincident and gradually reach the fixed-exit value. Note that as a consequence of fixing the exit pressure reference to $p = 0$, comments made here for pressure apply also for pressure-drop.

- *Pressure profiles at boundary wall; axisymmetric and planar, $\beta = 0.9$*

Though the centreline is commonly used to report field variables, in this case, the information offers no obvious interpretation of the reason of the upturn. Therefore, p-profiles along the downstream wall are provided in Figure 7.8. A generalized curvilinear coordinate (ξ) is introduced to take into account the front- and back-faces and the curvature of the constriction. This is defined in incremental

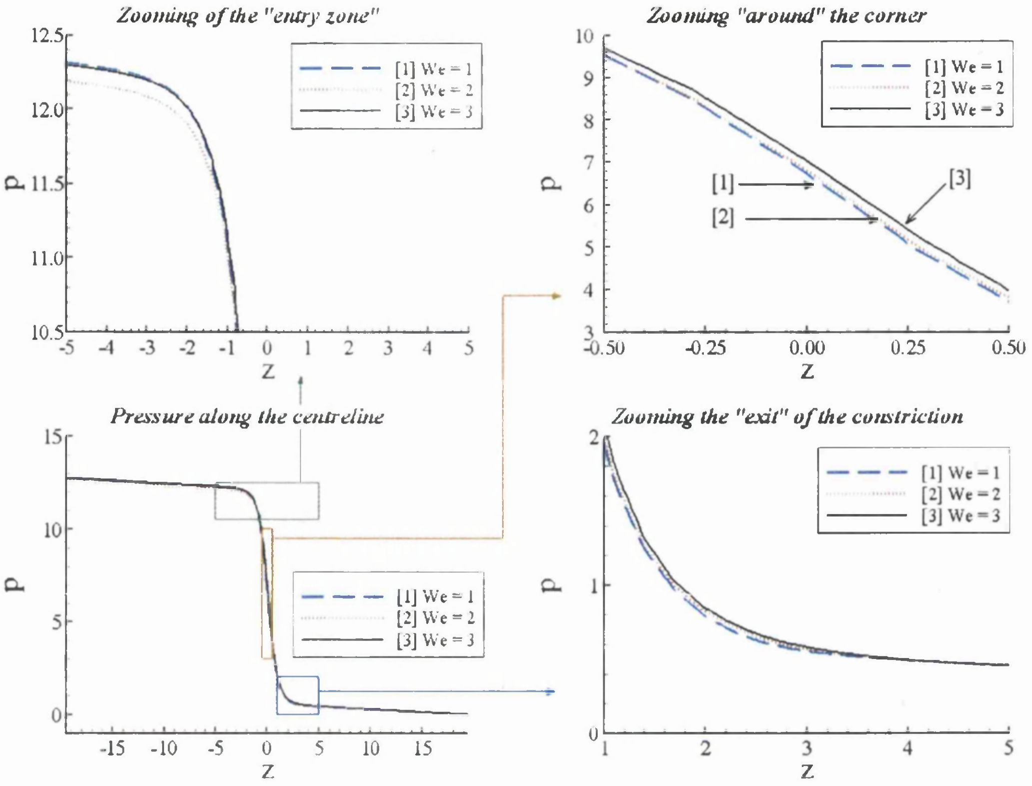

Figure 7.7. Pressure profile along *centreline*: increasing *We* (Oldroyd-B): $\beta = 0.9$. 4:1:4 axisymmetric.

form as $\delta\xi = \sqrt{\delta r^2 + \delta z^2}$, where r and z are the radial/vertical and axial coordinates, respectively, and the operator δ is the difference operator.

The flip over in pressure is also observed with increasing We in the entry section (top-left plot), that is, the level at $We = 3$ becomes larger than that for $We = 2$, being close (slightly lower) to that for $We = 1$. Lower-right plot in Figure 7.8 is a zoom of the geometry zones before and after the constriction, where minor differences in p-lines may be gathered and no discrepancy is detected as the fluid flows away from the constriction. It is the zone after the mid-plane where important differences can be discerned. The top-right plot is a further amplification of the constriction region, covering exactly from the front- to the back-face, the mid-plane is located at $\xi = 0$. Some differences for the three We-levels are detected 'before' the mid-plane (minimum-gap, see also Figure 7.1). There, the small gap between

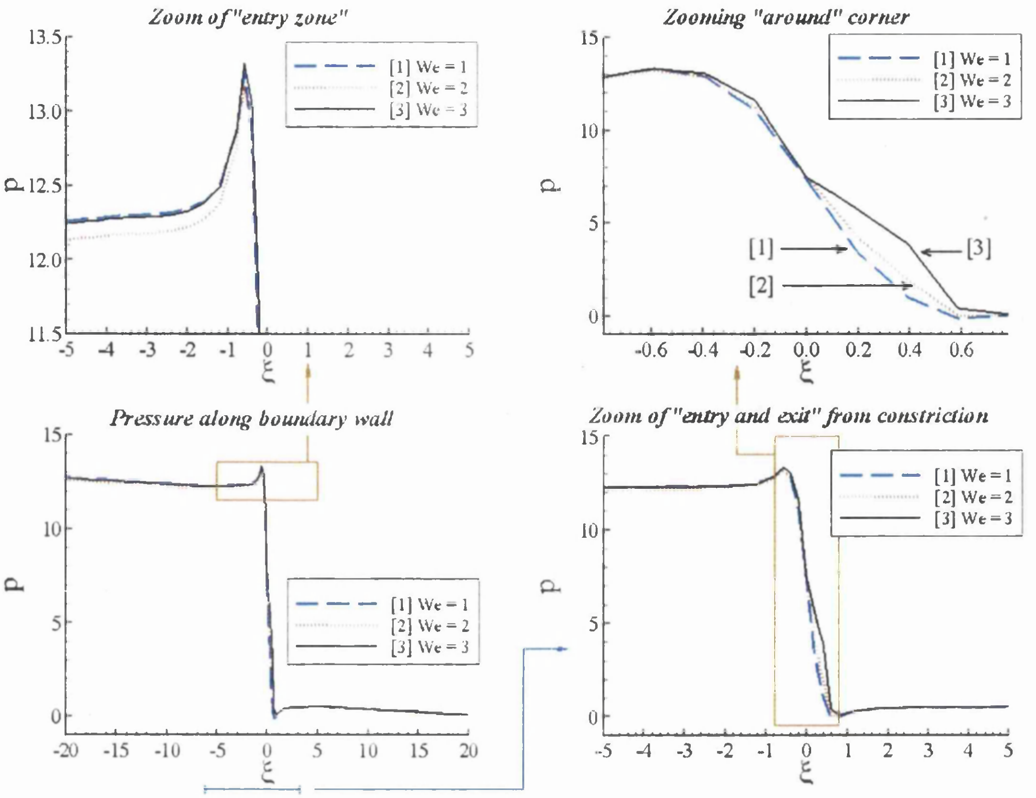

Figure 7.8. Pressure profile along *wall*: increasing *We* (Oldroyd-B): $\beta = 0.9$, 4:1:4 axisymmetric.

$We = 3$ and $We = 2$ is slightly larger than that for $We = 2$ and $We = 1$. The magnitude of the differences on the back-section of the contraction (third/fourth quadrants in Figure 7.1) is larger. Increasing We is reflected in higher levels of pressure through the third and fourth quadrants; the gap between $We = 3$ and $We = 2$ is now significantly larger.

A comparison between the 4:1:4 planar and axisymmetric pressure response at the boundary wall is provided in Figure 7.9. The region plotted lies within the front- to back-face of the constriction. For the planar case, departure in pressure values before the mid-plane is difficult to detect, whilst this is just moderate across the fourth quadrant. The 4:1:4 axisymmetric solutions provide major shifts with increment in elasticity levels throughout the rounded-constriction. The maximum gap

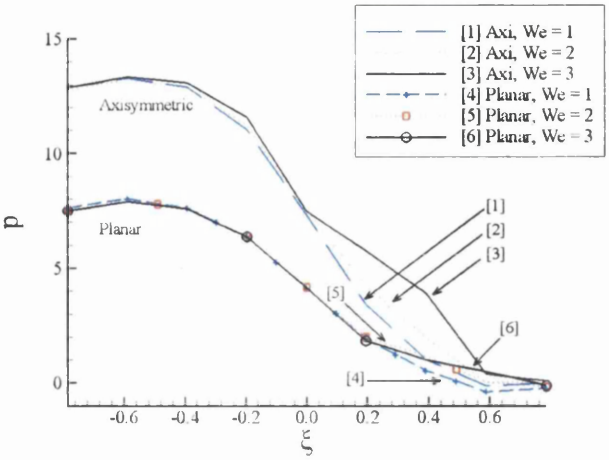

Figure 7.9. Pressure profile *along wall of constriction* zone (Oldroyd-B): $\beta = 0.9$, 4:1:4, axisymmetric vs. planar.

between We-solution from axisymmetric to planar cases is reduced by a factor around three. Additionally, note that departures in p-trends are 'localized' mostly to the fourth quadrant, in contrast to the circular contraction where substantial increase in pressure starts immediately after the mid-plane.

- *Planar and Axisymmetric stress and deformation-rate field data,* $\beta = 0.9$

Three-dimensional surface plots for the polymeric first normal stress difference, defined by[††] $N_1 = \tau_{11} - \tau_{22}$, are presented in Figure 7.10. Contour-line plots for τ_{11} and τ_{22} are also provided in Figure 7.11 and Figure 7.12, respectively. As mentioned earlier, these plots are for the half-channel due to symmetry considerations, zoomed in the constriction zone. The perspective in Figure 7.10 and in all figures is that flow direction is from left to right.

For the both planar and axisymmetric scenarios, polymeric normal stress difference and stress component τ_{11}, maxima are located just beyond the constriction

---

[††] Planar ($\tau_{xx}, \tau_{yy} \rightarrow \tau_{11}, \tau_{22}$); axisymmetric ($\tau_{rr}, \tau_{zz} \rightarrow \tau_{22}, \tau_{11}$).

N_1-Axisymmetric

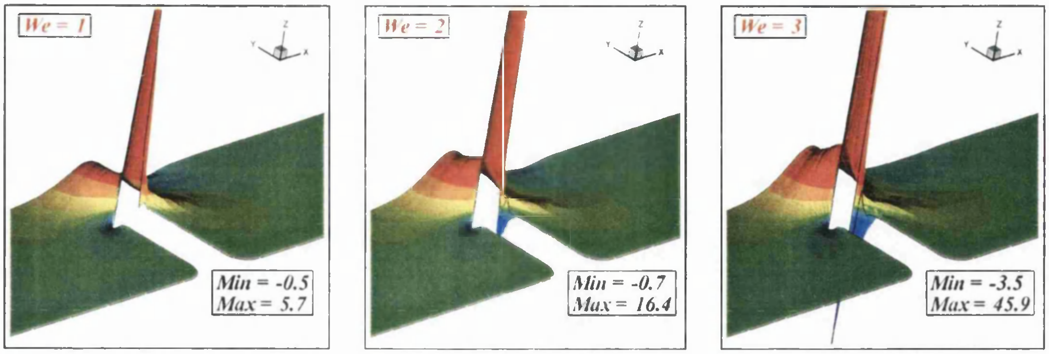

N_1-Planar

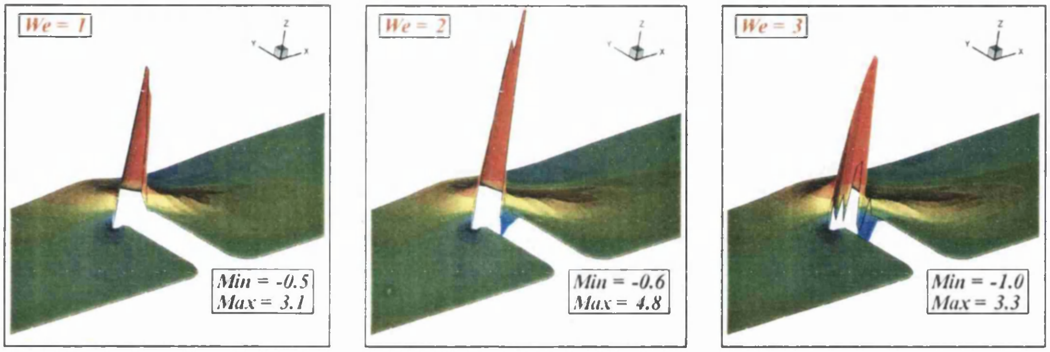

Figure 7.10. Polymeric first normal stress difference, N_1 fields (Oldroyd-B): $\beta = 0.9$, 4:1:4, axisymmetric vs. planar.

plane in the third and fourth quadrants, in contact with the constriction wall. τ_{11}-fields show that this maxima-region is relatively small in area though with large stress 'concentration' (extreme in the axisymmetric setting).

In the circular contraction case, the N_1-peak increases from 5.7 to 45.9 units (around eight times larger) when elasticity varies from $We = 1$ to $We = 3$, with a gradual but minor downstream shift in location of stress-maxima. A cross-stream diffusion of these stress-peaks is detected at the centreline, which increases with elasticity[‡‡]; however, with considerably lower values.

[‡‡] Centreline stress maximum lie about the constriction mid-plane.

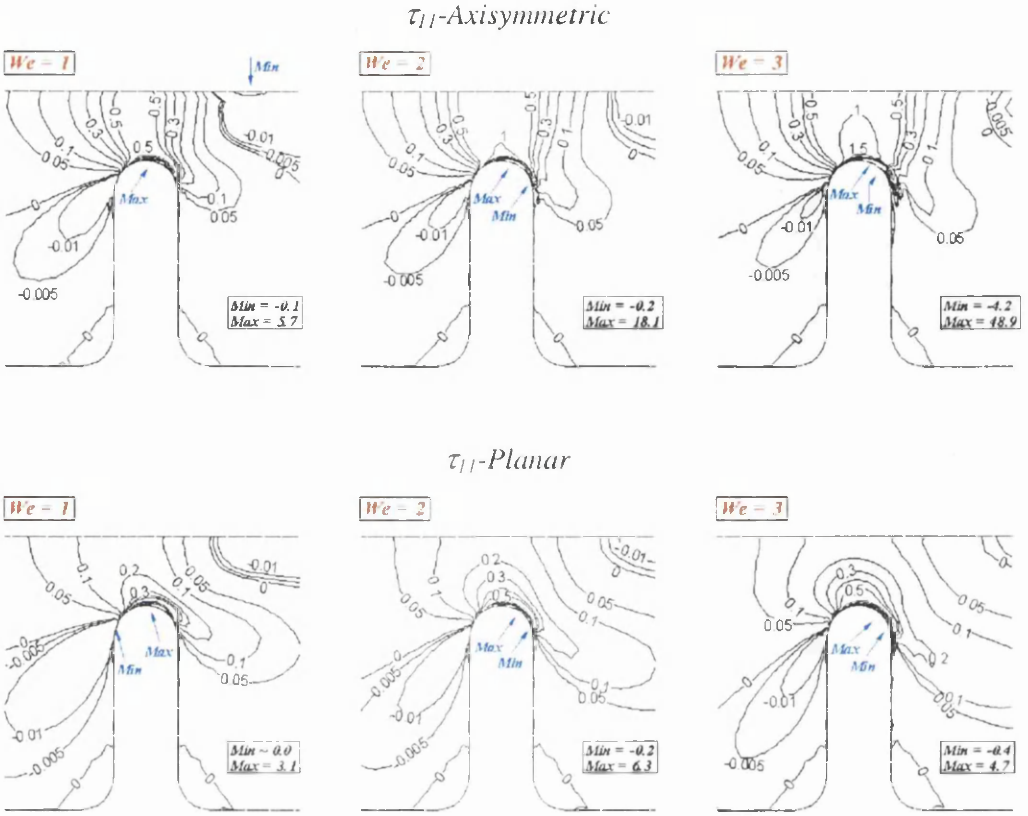
τ_{11}-Axisymmetric

τ_{11}-Planar

Figure 7.11. τ_{11} field contours (Oldroyd-B): $\beta = 0.9$, 4:1:4, axisymmetric vs. planar.

Considering now planar configurations and as mention previously, stress-peaks are located in the same regions. The gradual shift of τ_{11}-maxima is still present. Differences with respect to the axisymmetric case are that there is no substantial increase in stress (< 7 units) with elasticity and that the diffusion to the centreline is considerably lower, for further details refer to Figure 7.10 and Figure 7.11.

The secondary component of normal-stress, τ_{22}, (planar-τ_{yy} or axisymmetric-τ_{rr}) presented in Figure 7.12 displays maximum values both before and after the constriction 'touching' the boundary wall. Although τ_{22}-peaks are larger after the mid-plane than before this position, both maxima are of the same order of magnitude. Incrementation through the levels of elasticity provokes a rise in τ_{22}-maxima (larger

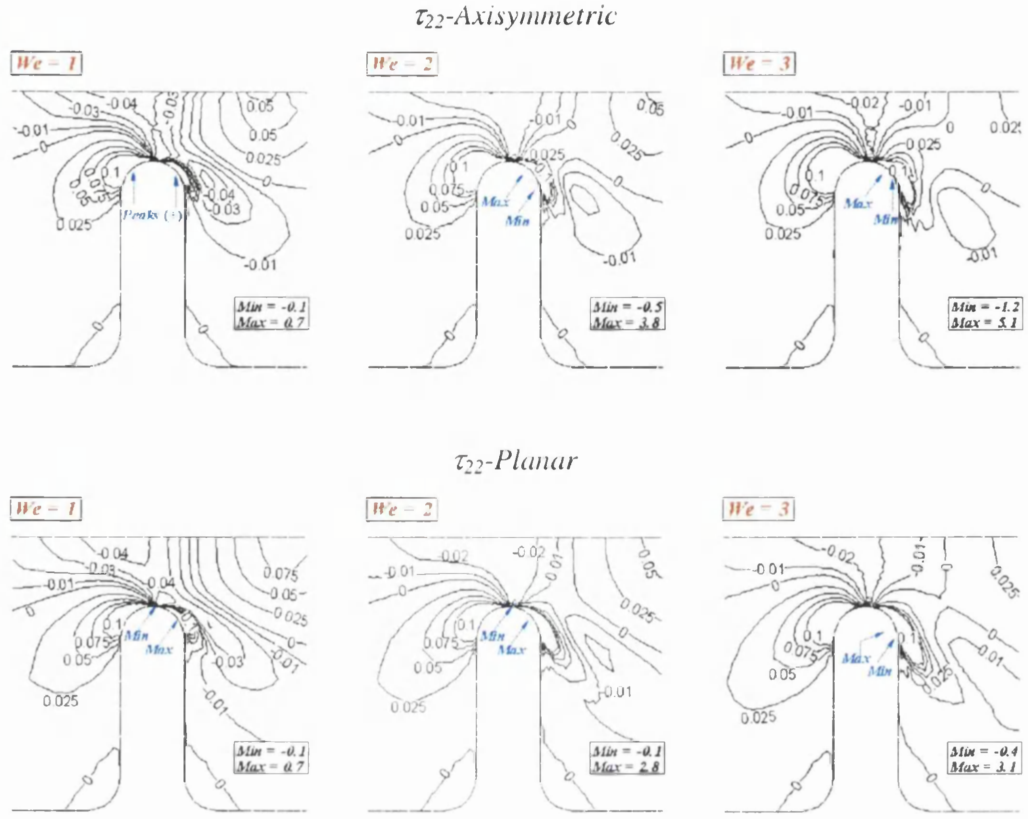

Figure 7.12. τ_{22} field contours (Oldroyd-B): $\beta = 0.9$, 4:1:4, axisymmetric vs. planar.

for the axisymmetric than for the planar case). However, the magnitude of this stress component is considerately lower when compared to those exhibited by τ_{11} (or N_1) at any given We. The τ_{22}-component shows influence on the structure and strength of the vortex regions.

Contour-lines for the polymeric shear stress component (τ_{12}) are depicted in Figure 7.13. Peak values are detected both before (maxima) and after (minima) the constriction mid-plane. Even though in the axisymmetric configuration both extrema suffer increase with elasticity, this effect is more significant for the minima (from -1.5 to -11.7 units), located just after the mid-plane. In the planar configuration, such an increasing trend is not consistently noted, the magnitude of exit-peak grows just

τ_{12}-Axisymmetric

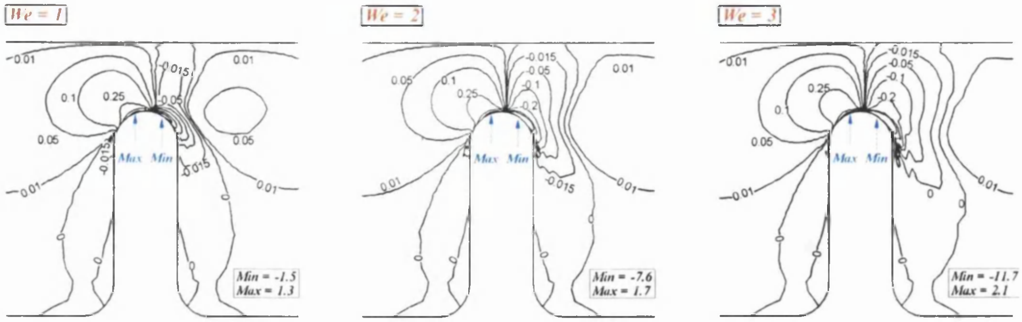

τ_{12}-Planar

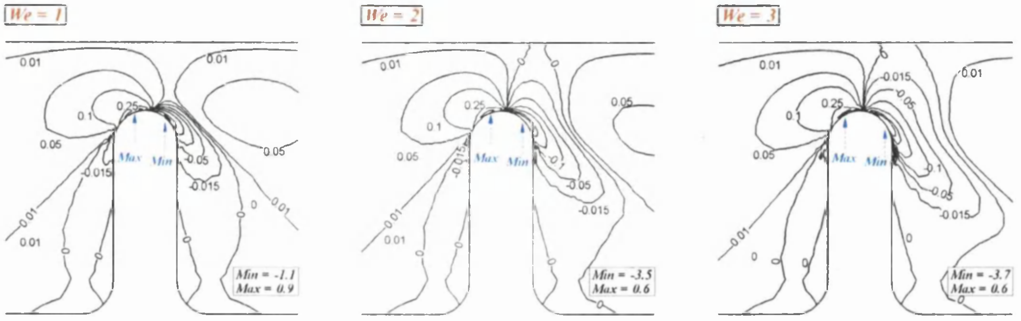

Figure 7.13. τ_{12} field contours (Oldroyd-B): $\beta = 0.9$, 4:1:4, axisymmetric vs. planar.

initially. At an elasticity level of $We = 3$, the magnitude of this τ_{12}-component is around one quarter of that for τ_{11}.

Contour field plots of d_{11} are illustrated in Figure 7.14, which uncovers little variation with *We* in both axisymmetric and planar flows. Four peaks of this deformation-rate component can be observed in the flow field near the constriction. Maximum values in contact with the boundary wall are of about $O(2)$ units and there are no significant differences noted in the magnitude between the axisymmetric and planar configurations. Centreline peaks in the circular contraction double those exhibited by their planar counterparts. Furthermore, the regions of increasing

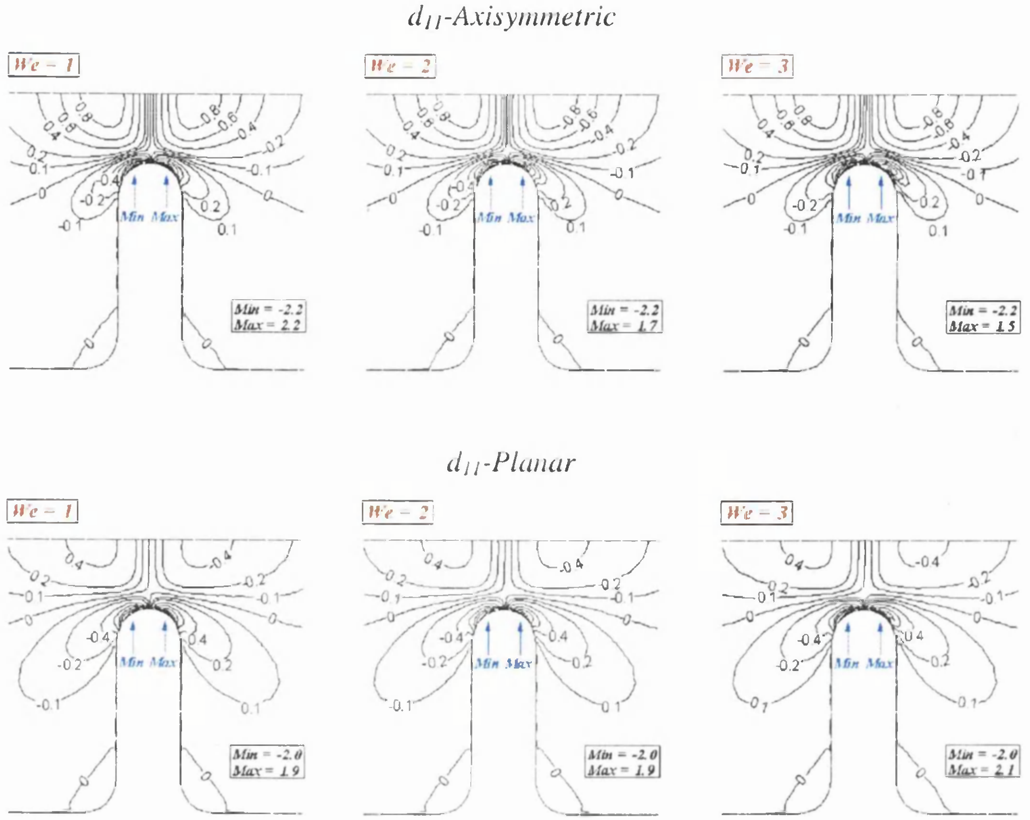

Figure 7.14. d_{11} field contours (Oldroyd-B): $\beta = 0.9$, 4:1:4, axisymmetric vs. planar.

deformation rate (in absolute value sense) are more localized in axisymmetric flows. Extension-hardening response is influenced by such deformation rates.

Polymeric stress τ_{11} (or N_1) displays only one peak in the constriction zone near the boundary wall where d_{11}-maxima occur. Note that some cross-stream influence from the main peak in normal stress is detected at the centreline, a manifestation of elastic phenomena.

As mentioned in chapter 6, d_{11} is only a guidance to extensional deformation rates when computed in such complex flow settings. In an attempt to relate τ_{11} (or N_1) with the deformation rate behaviour, standard forms of flow invariants (see section 6.3.1a for definitions), Γ and Σ are presented in Figure 7.15 and only for the

Σ-Axisymmetric

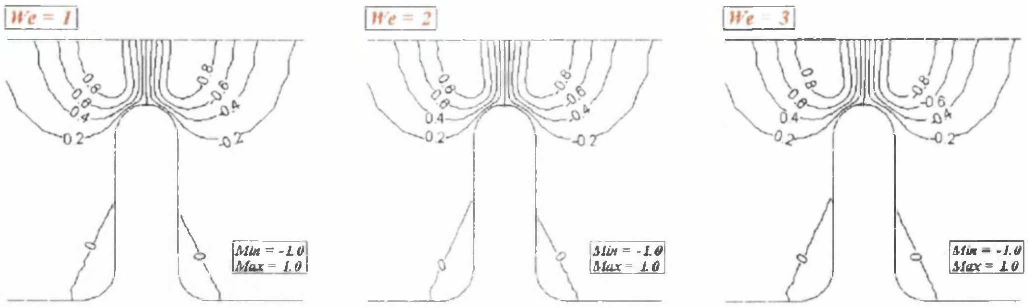

Γ-Planar

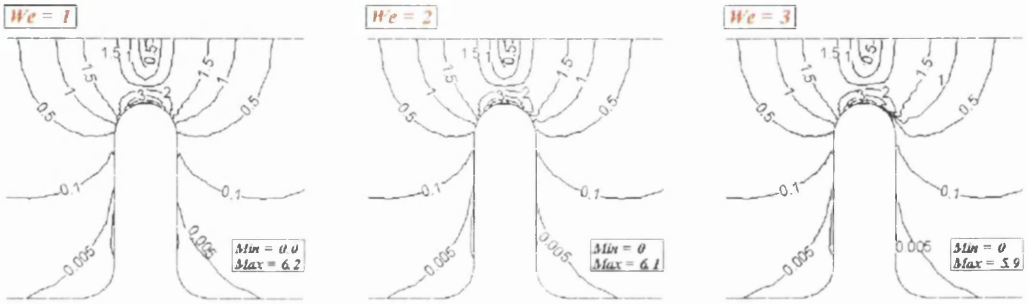

Figure 7.15. Σ and Γ field contours (Oldroyd-B): $\beta = 0.9$, 4:1:4 axisymmetric.

axisymmetric configuration. Σ-peaks are located at the centreline, presenting a maximum before the mid-plane and a minimum of equal magnitude after this position. In general, no influence of We is noticed. These two zones of large values of Σ are extended up to the constriction wall, showing larger cross-stream penetration than in d_{11}; however, no extreme values are found in contact with the boundary wall of the contraction. It is Γ representation of the deformation rate that displays a single peak at the constriction wall in the mid-plane position resembling that exhibited by τ_{11}. Γ-fields also show local maxima at the centreline with symmetry about the peak before and after the mid-plane.

It can be concluded that there is correlation between peaks in stress τ_{11} (or N_1) and deformation rates of the fluid lying above the constriction wall at the mid-plane position. Cross-stream influence is detected in these variables. In the planar counterpart such a conclusion cannot be reached. As a result, the expected degree of strain-hardening in both configurations can be quite different, being larger for axisymmetric flows. Larger (fast response) viscous influences in the converging flow into the constriction region and in the decelerating flow out of the constriction are stimulated in the axisymmetric case (see comments of Szabo et al. [90]).

- Axisymmetric contraction/expansion flow; β = 0.99

Adjusting the solvent ratio to $\beta = 0.99$ in the axisymmetric 4:1:4 contraction/expansion, the enhancement in normalized *epd* is sufficiently large for the *cross-over* phenomena to emerge. It was mentioned previously, that increasing the solvent ratio produces *epd*-trends that are closer to the Newtonian reference line, through increasing the solvent contribution to the total viscosity to 99%. With this change, the extensional viscosity becomes sharper as strain-rates approach the limit $\lambda \dot{\varepsilon} = 1/2$; to appreciate the effect of β on η_e, see Figure 7.16a (further comments on this figure are given in section 7.3.3). In this study the extensional response of the fluid is adjusted by modifying the solvent content, whilst Szabo et al. [90] adjusted the finite extensibility parameter (L) of the FENE-CR model to influence pressure-drops. For this solvent contribution ratio, focus lies on the axisymmetric configuration alone, the one that presents the cross-over.

- Pressure profiles at boundary wall; axisymmetric and planar, β = 0.99

Figure 7.17 displays the pressure-profile at the wall for the axisymmetric 4:1:4 flow. Again, the flip-over is present in the entry section, where the pressure at $We = 5$ is larger than for $We = 1$ and $We = 2$. In the exit region, the three selected levels of elasticity produce the same levels of pressure. Differences between the $\beta = 0.9$ and $\beta = 0.99$ cases are that the gap in pressure profiles, generated by increasing elasticity, is contained almost completely in the fourth quadrant (not in the third/fourth as for $\beta = 0.9$) and that this gap in $We = 1$ and $We = 2$ solutions is not *a) Oldroyd-B extensional viscosity*

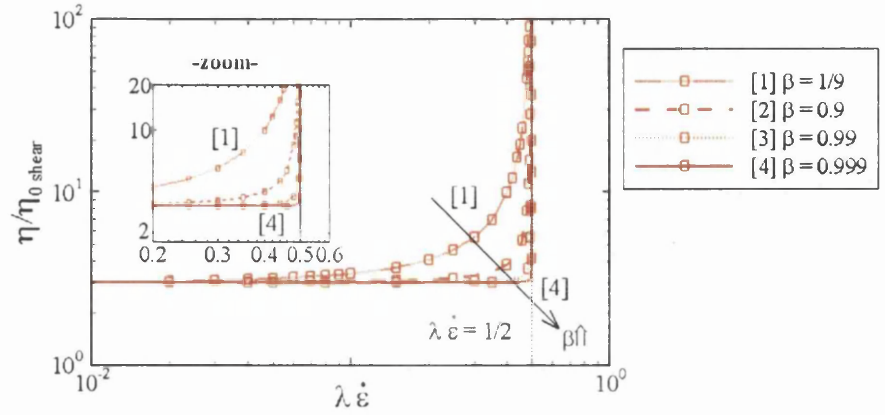

b) Shear and extensional viscosity, $\beta = 0.9$

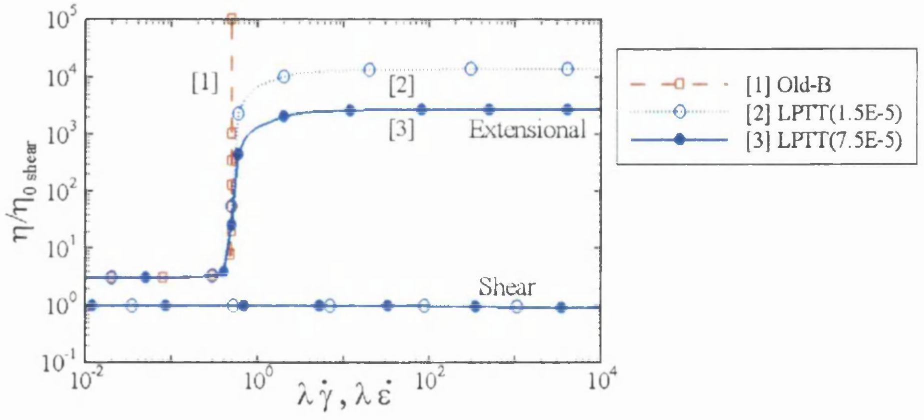

c) Shear and extensional viscosity, $\beta = 0.99$

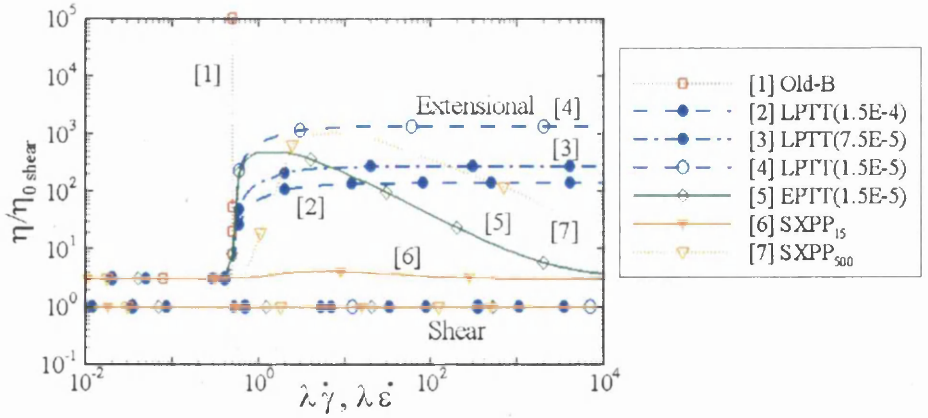

Figure 7.16. Rheological properties: Oldroyd-B, LPTT, EPTT and SXPP.

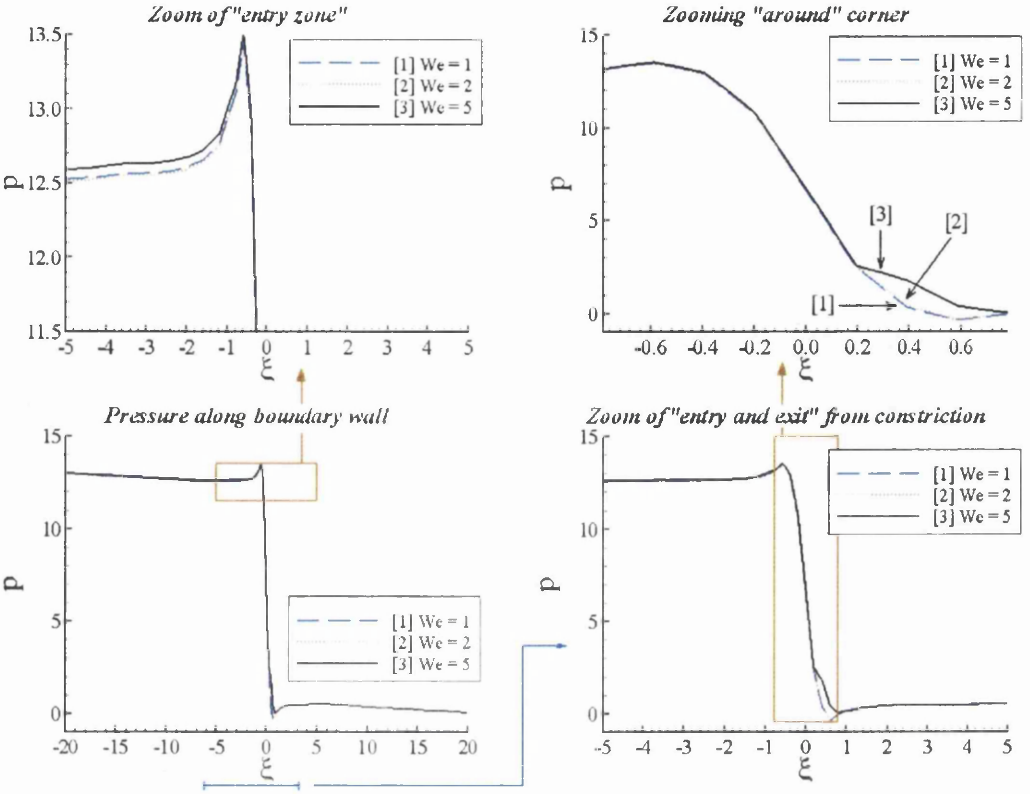

Figure 7.17. Pressure profile along *wall* increasing *We* (Oldroyd-B): $\beta = 0.99$, 4:1:4 axisymmetric.

apparent until elasticity reaches $We = 5$. At this Weissenberg number, *epd* has crossed the Newtonian reference line; through interpolation, the excess pressure-drop of the Boger fluid intercepts the reference line at a level of $We \approx 4.2$. The critical level is then $We_{crit} = 6.4$.

- *Stress and deformation-rate field data;* $\beta = 0.99$

The normal stress component τ_{11} and the deformation-rate d_{11} are plotted in Figure 7.18. This plot is for the axisymmetric flow of the Oldroyd-B model with a solvent contribution to the total viscosity of 99%. Similar response to that for setting $\beta = 0.9$ is obtained. Significant increase in τ_{11} maximum after the constriction mid-plane is observed under increasing levels of We. These maxima are in contact with the boundary wall and they increment from 0.6 ($We = 1$) to 20.8 ($We = 5$), around

τ_{11}-Axisymmetric

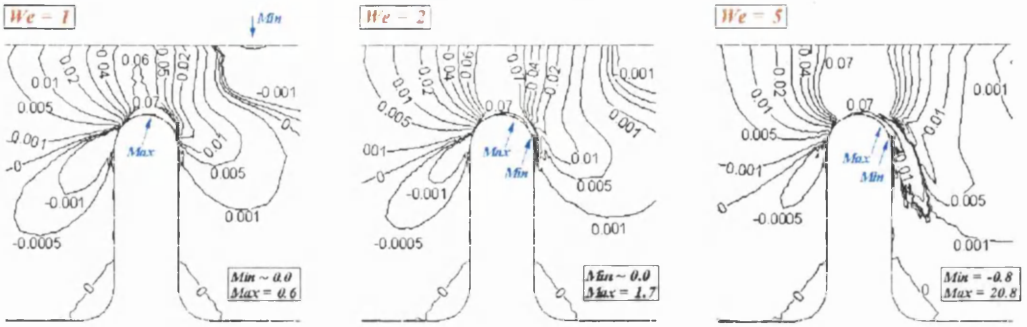

d_{11}-Planar

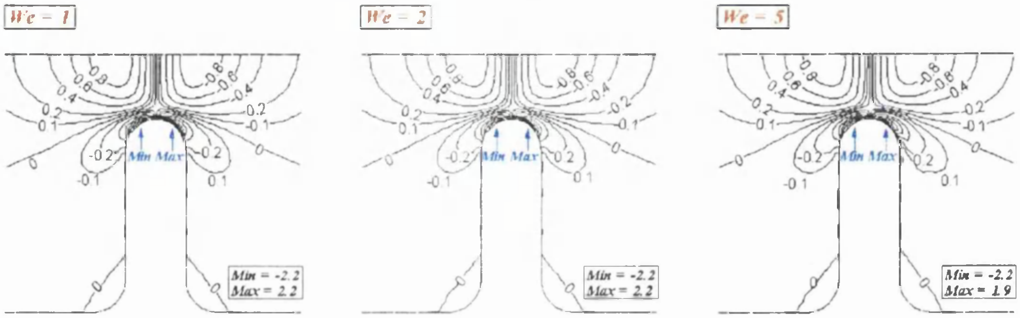

Figure 7.18. τ_{11}, d_{11} field contours (Oldroyd-B): β = 0.99, 4:1:4, axisymmetric.

thirty times (for $\beta = 0.9$ this increase is around eight times). However, peak-values ($\beta = 0.99$) are lower than those observed for $\beta = 0.9$ at any given We.

The elevation of β from 0.9 to 0.99, produces a reduction in the contribution of the polymeric viscosity, which is associated with the initial decline in *epd*-trends. That is, for larger polymeric viscosity contribution (lower β), this initial decrease of pressure-drop is larger. The fact that the *upturn* in *epd* is less visible for $\beta = 0.99$ than for $\beta = 0.9$ is regarded as a consequence of the larger contribution from the solvent, with its associated reduction in the decline of *epd* at low elasticity levels (Figure 7.3a).

Rothstein and McKinley [86] explain such initial decline in *epd* at any given polymer content level with molecular arguments. These authors interpret the decrease in pressure-drop as a result of an energy storage process, which takes place as the polymer chains are being extended. For further increments in *We* (flowrate or elasticity), the molecules reach their full extension and start behaving like rigid rods, increasing the pressure-drop (tending to an *up-turn*) via an additional viscous drag due to the presence of such rods. Part of the stress generated in the constriction is recoverable once, the contraction has been passed and the polymer chains return to their original length.

Increasing β (which is a measure of the concentration of polymer in the system), can be seen as a decrease in the number of polymer chains in the fluid. This accounts for lower decline in initial *epd*, confirming the observations obtained in the present study (Figure 7.3a). Note that with the Oldroyd-B model, there is no limiting extension of molecules and yet the *up-turn* is detected. Such response may indicate that the additional viscous drag is present when the polymer chains reach a certain length (clearly not critical), even if they can be extended further.

The deformation-rate component d_{11} is shown in Figure 7.18 for $\beta = 0.99$. It exhibits almost identical contour-lines patterns as those for $\beta = 0.9$ (Figure 7.14), with only minor differences in peak-values. Therefore, for both solvent ratios, higher deformation zones are expected near the mid-plane of the contraction and at the centreline zone, though of lower magnitude.

- *Comments on pressure-gradient: planar and axisymmetric,* β *= 1/9, 0.9, 0.99*

Centreline pressure-gradient are presented in Figure 7.19 for both axisymmetric and planar 4:1:4 configurations and for systems representing highly polymeric ($\beta = 1/9$, *Fluid-A*) to highly solvent content ($\beta = 0.9$, *Fluid-B* and $\beta = 0.99$, *Fluid-C*). Peak-values of pressure-gradients (absolute value) are located near the mid-plane. These maxima in the axisymmetric configuration double those of the planar

Axisymmetric   ***Planar***

a) β = 1/9

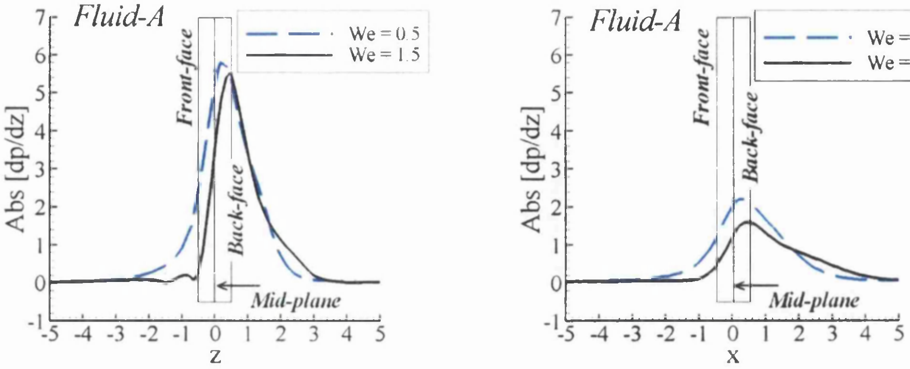

b) β = 0.9

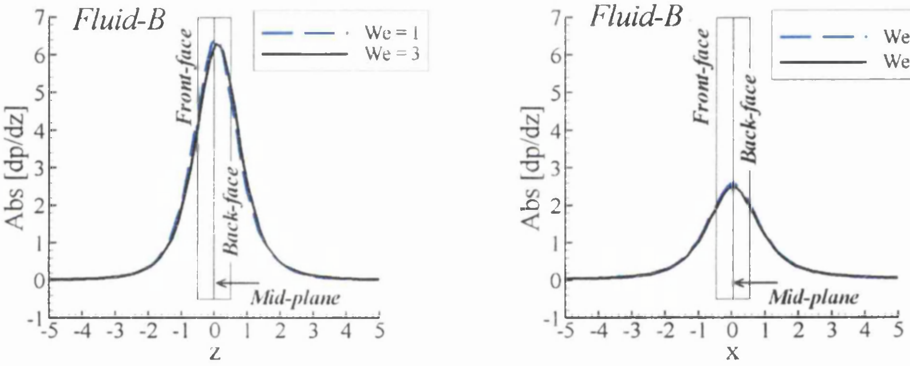

c) β = 0.99

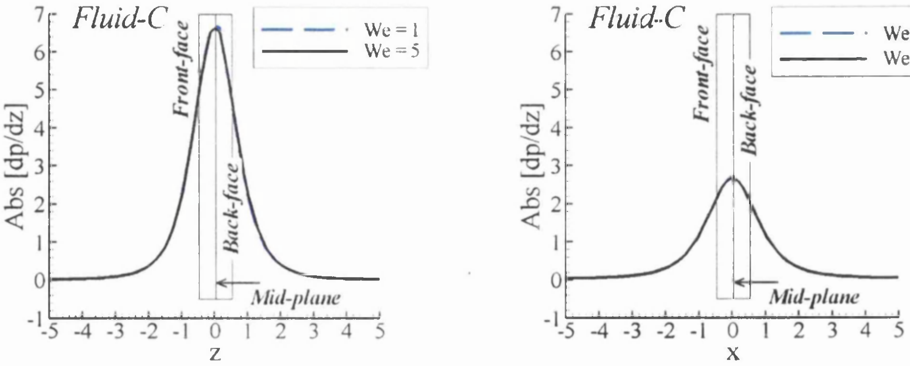

Figure 7.19. Pressure gradient at centreline (Oldroyd-B): 4:1:4 axisymmetric vs. planar; a) $\beta = 1/9$, b) $\beta = 0.9$, c) $\beta = 0.99$.

case. Pressure-gradient for *Fluid-A* exhibits a downstream shift (in direction to the back-face of the constriction) when elasticity varies from $We = 0.5$ to 1.5. A minor reduction in peak-value is also noted. As a consequence of this shift, ∇p values are reduced in the upstream when compared to the downstream section, provoking a net reduction. With increasing elasticity, pressure-gradients require longer downstream distances to relax to fully-developed conditions. In the planar case, these distances are slightly larger than for the axisymmetric configuration. For *Fluid-B* and *Fluid-C* little effect is gathered for increasing We and larger downstream lengths would not be necessary. See Binding et al. [17] for similar comments to the initial *epd*-decline.

7.3.1b Comparison with 4:1 contraction flow results: [p-p_{Newt}]-data

One goes on to study the benchmark 4:1 contraction flow in this section, see Figure 7.4. A monotonic decline of *epd* with increasing elasticity is observed; for $\beta = 1/9$ similar decay in pressure-drop is reported in literature (see for example references [2,3]). No tendency in trends to reach an *upturn* is detected in Figure 7.4. For Oldroyd-B fluids with $\beta = 0.9$ and short-dies, Aboubacar et al. [5] reported pressure-drops in planar flows similar to those for corresponding Newtonian fluids.

Considering the axisymmetric 4:1 contraction, Figure 7.20 displays the pressure (or pressure-drop due to the setting that $p = 0$ at the exit) along the boundary wall. No flip-over is observed between pressure values in the entry section (top-left plot); therefore, no *upturn* in *epd* can be detected. Increasing We produces a decrease in pressure-level at any point along the wall (see full geometry, lower-left plot). This decrease is reduced as the fluid approaches the channel-exit (lower-right plot); again, this is because of imposing vanishing pressure reference at flow-exit. Even in the entry of the contraction, no flip-over arises in pressure-trend. The response of the fluid in the axisymmetric 4:1 contraction is extremely different to that exhibited in the 4:1:4 contraction/expansion flow (Figure 7.8). Note that in the contraction, pressure-drops are around 400 units, whilst for the 4:1:4 setting, this reduces to ≈ 15 (increments in Δp-values correspond to greater dissipation in the flow).

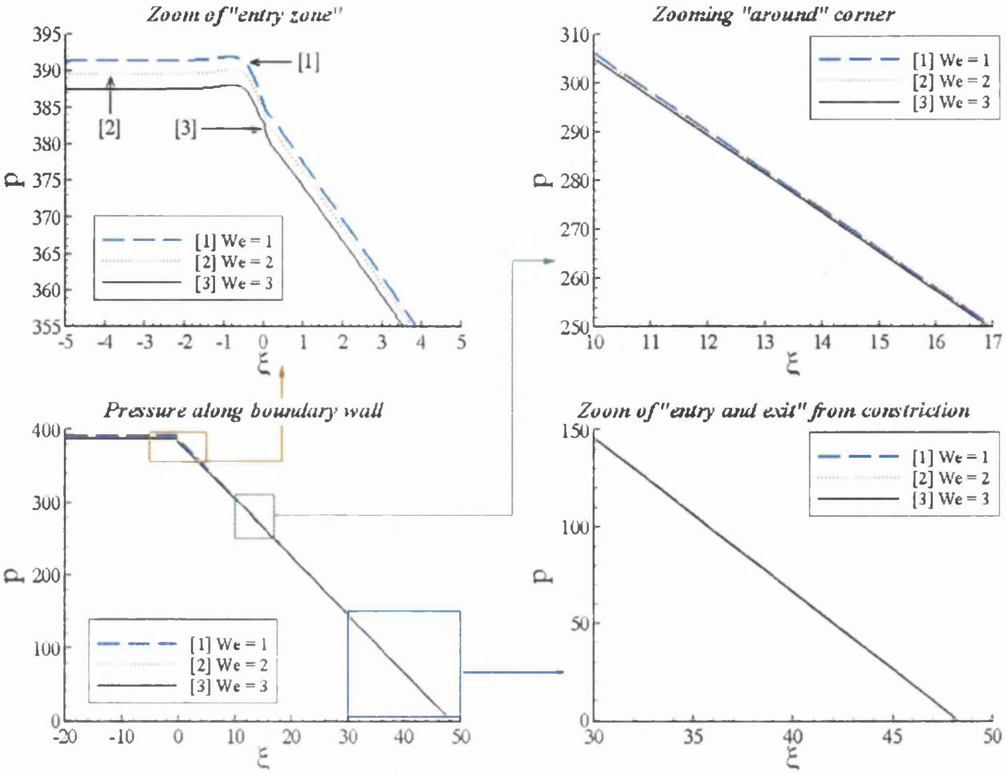

Figure 7.20. Pressure profile along *wall* increasing *We* (Oldroyd-B): $\beta = 0.9$, 4:1 axisymmetric.

An alternative calibration, [$p - p_{Newt}$], for this Boger fluid pressure-profiles is illustrated in Figure 7.21. This new variable is defined as the pressure for the Oldroyd-B fluid where an equivalent Newtonian part (the zero-reference line) has been subtracted at each point in the domain. The equivalence between both fluids lies in terms of flowrate and total shear viscosity. Figure 7.21 displays [$p - p_{Newt}$] data along the boundary wall for 4:1 contraction (left) and 4:1:4 contraction/expansion (right), with the corresponding stress component τ_{11} for both cases plotted below. In the generalized coordinate sense, both mid-plane (4:1:4 case) and 'end of rounded-corner' of the constriction (4:1) are located at $\xi = 0$.

Note in Figure 7.21, that peaks in stress and pressure occur at the same location. For the 4:1 geometry these peaks are located almost exactly at the end of the rounded-corner ($\xi \approx 0.04$ units), whilst in the 4:1:4 setting maxima take place

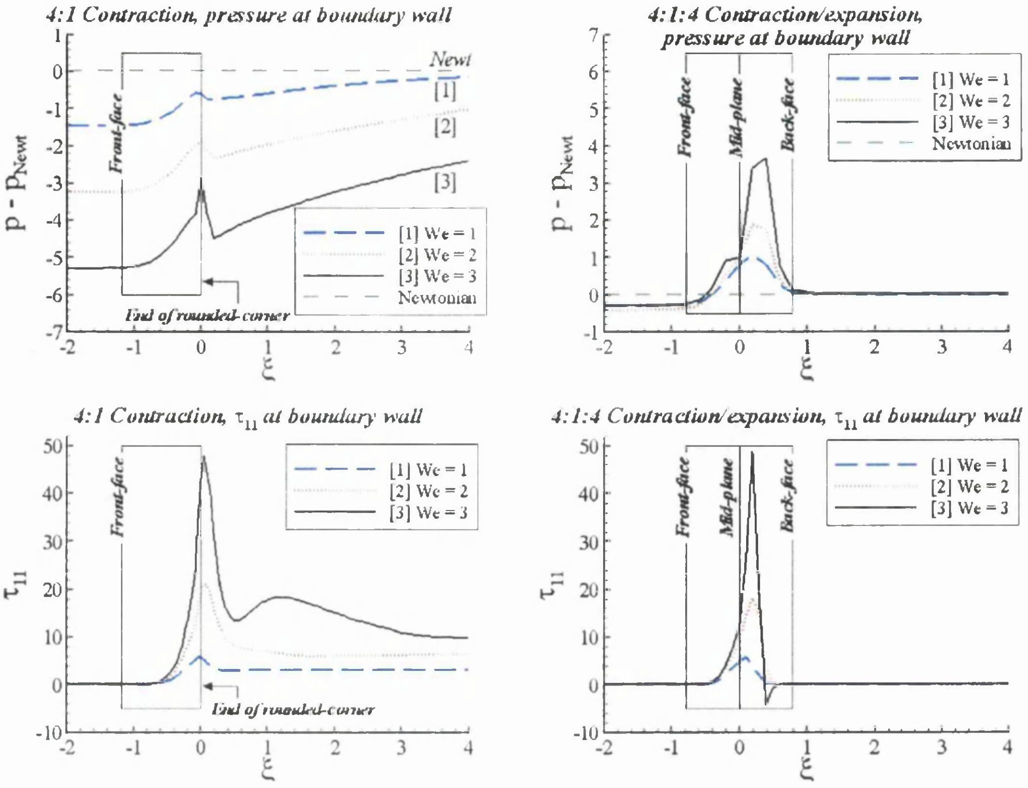

Figure 7.21. Pressure [p-p_{Newt}] and stress τ_{11} profiles along *wall* increasing *We* (Oldroyd-B): $\beta = 0.9$, 4:1 and 4:1:4 axisymmetric.

between the mid-plane and the back-face ($\xi \approx 0.2$ units). Note that even when stress-peaks are similar in magnitude between geometries at every We-level, [$p - p_{Newt}$] data is significantly different.

In the 4:1:4 case (right plots), stress and this pressure calibration have a constant value with respect to the ξ-position except in the constriction region, whilst in the 4:1 contraction, a relaxation in stress and [$p - p_{Newt}$] takes place throughout the exit channel. Due to the 4:1 flow-geometry configuration, τ_{11} recovers to the constricted-channel level away from its inlet-value.

Another aspect to observe is that in the 4:1 contraction instance, [p]-data is lower than the corresponding Newtonian case at any ξ coordinate. Contrasting response is obtained from the contraction/expansion flow, where positive [$p - p_{Newt}$] is gathered in the third and fourth quadrants, and this difference increases with We. The *upturn* in pressure-drop is associated with this positive and increasing trend in [$p - p_{Newt}$]. Note that the excessive decay in this pressure calibration with elasticity increments in the 4:1 contraction prevents the increasing peaks from crossing the Newtonian reference line. One may speculate that for positive [$p - p_{Newt}$]-data in this 4:1 flow, significantly larger elastic effects will be required, perhaps of one to two orders larger. However, this cannot be achieved with the Oldroyd-B model and available numerical methods. For the 4:1:4 instance, the *upturn* in *epd* is explained in terms of these $[p - p_{Newt}]$ peaks observed in pressure, themselves provoked by stress.

In Figure 7.22, one focuses on the 4:1:4 configuration alone, contrasting $[p - p_{Newt}]$ and stress data between planar (left plots) and axisymmetric (right plots) instances under increasing We. Here, stress generation across the constriction in the planar case is considerably reduced over that for the axisymmetric case. Pressure differentials are correspondingly suppressed in the planar case, so that no flip-over in entry $[p - p_{Newt}]$ -data is substantiated, and hence, no *upturn* is apparent.

7.3.2 Vortex development and structure (4:1:4 and 4:1)

Streamline patterns for both 4:1:4 and 4:1 axisymmetric geometries are shown in Figure 7.23 and Figure 7.24. Contour values are within $0 \le \psi \le 0.5$ outside the vortex region, over which equal increments are used ($\Delta\psi = 0.05$). For the streamline patterns in the vortex region, six contour values are chosen $[10^{-4} \le \psi \le 10^{-3}]$ in increments of 0.15^{-3}. Figure 7.23 presents streamline patterns for two solvent fraction values, $\beta = 0.99$ and $\beta = 1/9$, corresponding to highly-solvent to highly-polymeric systems, respectively. For the ($\beta = 1/9$)-case, strong vortex enhancement in cell-size and intensity is observed in the upstream channel from $We = 0.1$ to 1.5,

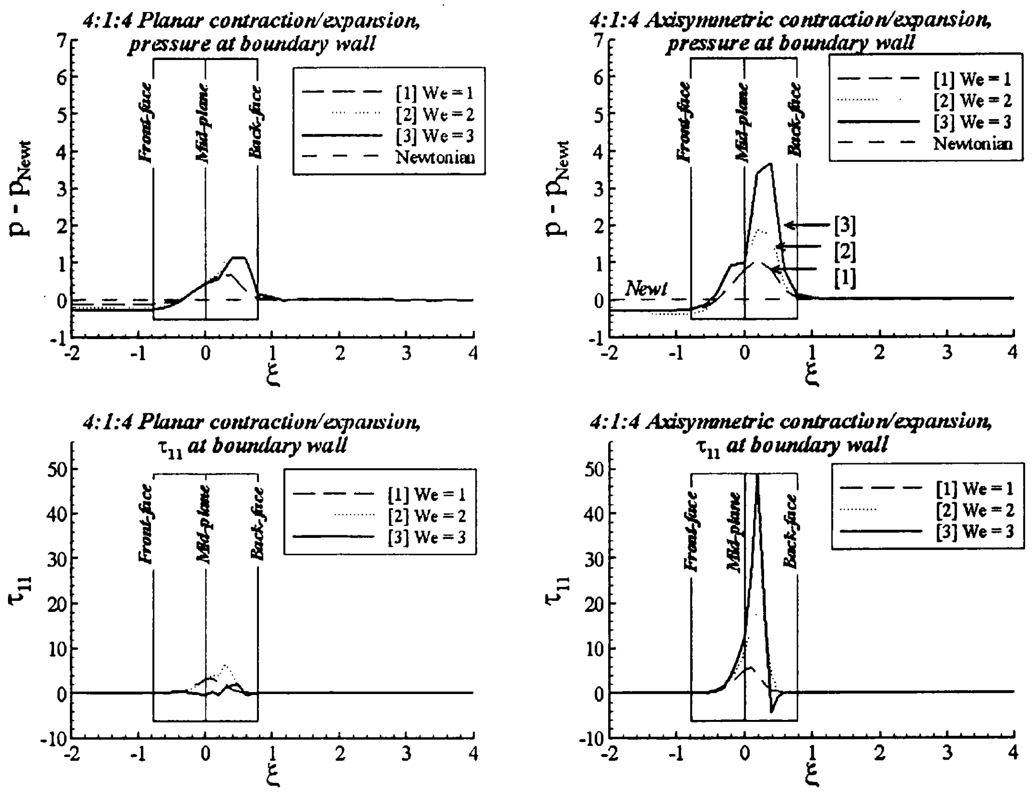

Figure 7.22. Pressure $[p\text{-}p_{Newt}]$ and stress τ_{11} profiles along *wall* increasing *We* (Oldroyd-B): $\beta = 0.9$, 4:1:4 axisymmetric and planar.

with suppression in the downstream section (almost disappearing). At the other extreme ($\beta = 0.99$), vortex variation is less visible. In terms of cell-size, minor increase can be detected in the downstream vortex for $We = 5$. Looking at intensity, the upstream vortex increases slightly and more noticeable variation is observed in the vortex after the constriction. A decay from $We = 1$ to 2 is gathered, followed by an increase from $We = 2$ to 5. The decay and increase is in direct correspondence with, and hence a signal of, the *epd* response for this beta ratio $\beta = 0.99$. As noted earlier, large stress arises over the third and fourth quadrants (after the mid-plane), where the more visible and larger vortices are detected for this highly-solvent content system.

Figure 7.24 presents the streamline patterns for $\beta = 0.9$ across the two distinct axisymmetric configurations: the 4:1:4 expansion/contraction and 4:1 contraction.

a) *β=0.99, low polymeric system*

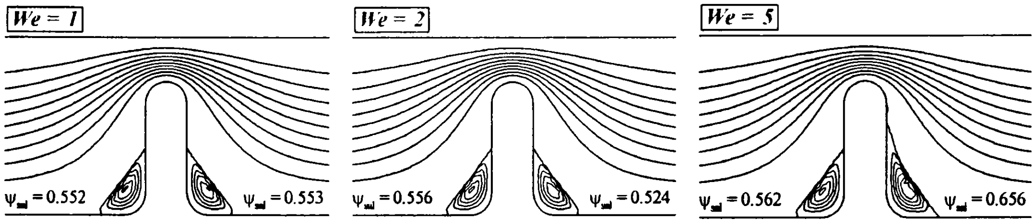

b) *β=1/9, highly polymeric system*

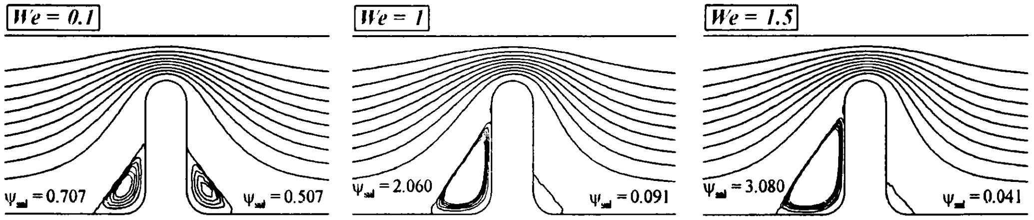

Figure 7.23. Stream function ($-\psi\times10^3$) increasing *We* (Oldroyd-B): 4:1:4 axisymmetric; a) $\beta = 0.99$, b) $\beta = 1/9$.

a) *4:1:4, axisymmetric*

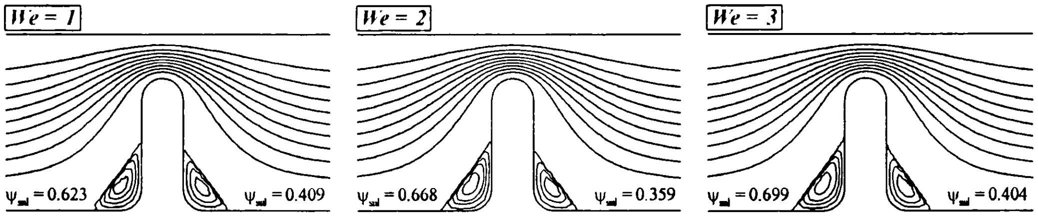

b) *4:1, axisymmetric*

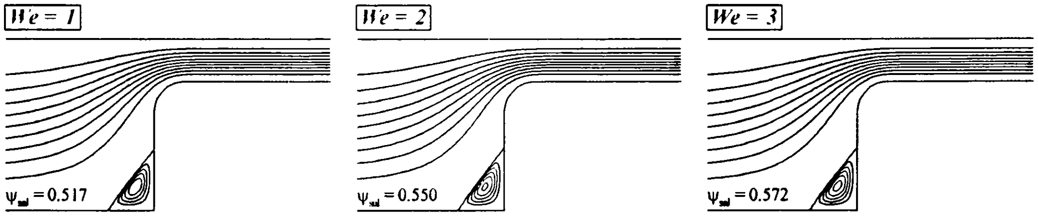

Figure 7.24. Stream function ($-\psi\times10^3$) increasing *We* (Oldroyd-B): β=0.9, axisymmetric; a) 4:1:4, b) 4:1.

Now, the upstream vortex increases in intensity with elasticity increase under both geometric configurations. In contrast with the 4:1:4 geometry and in the downstream flow section, vortex intensity is observed to decrease from $We=1$ to $We=2$, and to increase thereafter by $We=3$ (as with $\beta=0.99$ data above). It is precisely under these circumstances that an *upturn* in *epd* is observed.

7.3.3 Alternative model representations: 4:1:4 axisymmetric

To this point, all predictions have been for the Oldroyd-B model, a fluid with strong and unbounded strain-hardening response, now some alternative models capable of strong-hardening behaviour are considered. Constant shear viscosity is achieved through high solvent fractions, i.e. $\beta \to 1$. The particular models selected are the linear and exponential Phan-Thien/Tanner (LPTT and EPTT) and the single-equation pom-pom fluid (SXPP). A comparison of *epd*-data between these models, including that for the Oldroyd-B fluid is provided for the interesting case of the 4:1:4 axisymmetric flow.

Model parameters to stimulate large values of extensional viscosity are LPTT(β,ε_{PTT}), SXPP(β,ε,q) and Oldroyd-B(β). With PTT and SXPP models, the viscosity ratio β-parameter is used to control the degree of departure from the Newtonian reference base to the second plateau value. That is, the approximation to constant shear-viscosity for these shear-thinning fluids, PTT and SXPP, is within 10% for $\beta=0.9$ and 1% for $\beta=0.99$ (see comments on Figure 7.16 in Section 7.3.1a). Note that the network-based LPTT-fluid is purely strain-hardening to a limiting finite plateau (unlike Oldroyd), and so, does not support any degree of strain-softening (Figure 7.16). This fluid can be made to replicate the FENE-CR steady extensional response with its finite-extensibility control parameter (L), through the adjustment of the ε_{PTT}-parameter: $L=50$ approximately equates to $\varepsilon_{PTT}=0.02$ response, whilst $L=5$ more closely matches $\varepsilon_{PTT}=0.1$ [48]. Alternatively, the kinetic-based SXPP-fluid displays strain-hardening/softening properties, with the rise and peak of hardening controlled by both SXPP(ε,q). Here, ε controls the degree of system entanglement (molecular weight, Mw) and q the number of dangling-end side-branches to the molecular backbone chain. The alternative forms of extensional viscosity data for each model used here allows one to assess the impact of both, bounded strain-hardening over the unbounded Oldroyd response, and to distinguish between excessive and mild strain-hardening.

7.3.3a epd for Old-B, LPTT($\varepsilon_{PTT}=0.15\times10^{-4}$), LPTT($\varepsilon_{PTT}=0.75\times10^{-4}$): $\beta=0.9$

Viewing Figure 7.25a for β-variation in Oldroyd-B and LPTT models, each of the LPTT-variants track the Oldroyd-B *epd*-data in trend. The match is close, up to the local minima (*upturn*) of $We=2$. After this stage, the LPTT-fluid with greater hardening response, LPTT($\varepsilon_{PTT}=0.15\times10^{-4}$), more closely follows the rising trend (steepness) of Oldroyd-B. Once the *upturn* ($We=2$) has been reached, the relative rate-of-rise of *epd* with increasing elasticity across fluids is larger for fluids with more severe strain-hardening properties, where the Oldroyd-B model is the upper limit. In this case, if it were possible to advance elasticity from $We_{crit}\approx5$ to 9, the significant *epd* enhancement observed by Szabo et al. [90] with the FENE-CR model would be realised.

7.3.3b epd for LPTT($\varepsilon_{PTT}=0.15\times10^{-4}$): $\beta=0.95$

The trends are all replicated for LPTT($\beta=0.95$), with lower *epd* decline than for $\beta=0.9$, and slight lessening of subsequent rise. The intercept with the Newtonian reference-line thus occurs earlier at $We=4.4$, rising to a critical level $We_{crit}\approx5$. Thus, the importance of β-adjustment is clear.

7.3.3c epd for Old-B, LPTT, EPTT and SXPP models: high $\beta=0.99$

Switching from $\beta=0.9$ to a higher solvent fraction, $\beta=0.99$, a major impact on the level of *epd*-data is observed, both in initial decay rate and minima attained, *a) β-variation*

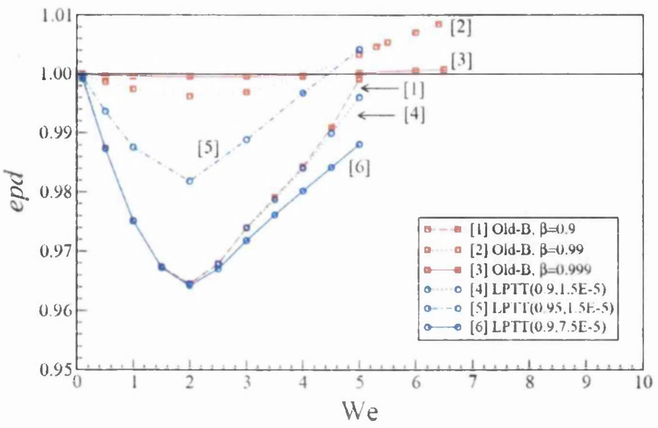

b) β=0.99

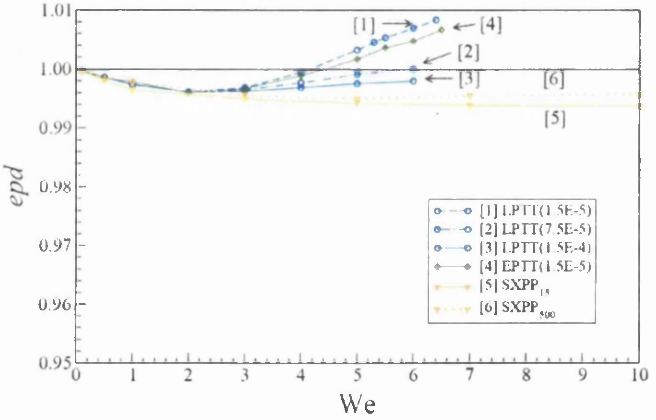

Figure 7.25. Pressure-drop (*epd*) vs. *We*: 4 :1 :4 axisymmetric; a) *β*-variation, b) $\beta = 0.99$.

see Figure 7.25b where solutions at $\beta = 0.99$ are presented. This is due to the relative proportions of solvent to polymeric components within each system and the impact this has, in particular, via decreasing polymeric stress levels. As illustrated in Figure 7.16, prior to the critical deformation rate of 0.5 units, an increase in β has the effect of lowering extensional viscosity. Table 7.2 reflects the parameters used here to investigate *epd*-response for the selected models in order to appreciate the effect of the material functions on the flow setting. The Oldroyd model displays an unbounded degree of hardening under extensional deformation and is therefore not listed.

For ($\beta = 0.99$)-data alone, once again all model variants provide similar initial decay in *epd*-data up to $We = 2$. This is a statement about common peak strain-rates experienced within the flow field, independent of β and for We up to two. Beyond the level of $We = 2$, the departure in fluid properties segregates the various types of response. The LPTT($\beta = 0.99$)-models approximate the Oldroyd-B trend-line, displaying *upturn* to various degrees and even a tendency to intercept the Newtonian reference-line. As may be expected, the fluid with the larger degree of hardening, LPTT($\varepsilon_{PTT} = 1.5\times10^{-5}$), follows the Oldroyd-B trend-line more closely and has the faster rate-of-rise in *epd*. This particular version of the PTT model supports sustained hardening properties at large deformation-rates, with similar rates of hardening uptake as for Oldroyd, and larger plateau levels as $\varepsilon_{PTT} \to 0$. The instance, with $\varepsilon_{PTT} = 1.5\times10^{-5}$, is so close to Oldroyd in hardening, that it succeeds in clearing the Newtonian reference-line, unlike the slightly larger values of $\varepsilon_{PTT} = \{0.75\times10^{-4}, 1.5\times10^{-4}\}$, lines [2] and [3] in Figure 7.25b. In contrast, the SXPP-model certainly plateaus out beyond $We = 2$, confirming limiting expectations, as above. For SXPP$_{15}$, there is no local minimum, and hence, no enhancement above the

Table 7.2. Fluid parameters for the $\beta = 0.99$ solvent fraction

	LPTT	***EPTT***	***SXPP***[§§]
Strong hardening	$\varepsilon = 0.15\times10^{-4}$	$\varepsilon = 0.15\times10^{-4}$	$\varepsilon = 0.99...,q = 500$
.	$\varepsilon = 0.75\times10^{-4}$		
.	$\varepsilon = 1.5\times10^{-4}$		
Low hardening			$\varepsilon = 0.99...,q = 15$ SXPP$_{15}$

[§§] Anisotropy parameter (α) is set to zero for both SXPP fluids.

Newtonian reference-line encountered. This fluid has reached its limiting plateau in extensional viscosity (constant level in Trouton ratio) for this range of We within the constriction zone, the flow-area of greatest impact upon *epd*. Any effect of softening is negligible for this SXPP option. SXPP$_{500}$ fluid displays severe strain-hardening at moderate strain-rates, to a peak level equivalent to that for the LPTT($\varepsilon_{PTT}=0.15\times10^{-4}$) fluid, with a decline thereafter at larger strain-rates. Here, for the SXPP$_{500}$ fluid, an *epd* minimum appears at $We=5$, though is not as prominent as for PTT and Oldroyd cases. The trend in this *epd*-curve appears more to asymptote out than to cross the Newtonian reference line. This can be associated with much lower stress maxima beyond the constriction when compared against Oldroyd and PTT solutions (see Figure 7.26, $\beta=0.99$). What is essential here is the delay in the extension-hardening regime observed with the SXPP$_{500}$ model. Then, increase in stress substantially depreciates; for example, at $\lambda_{0b}\dot{\varepsilon}\approx0.7$, LPTT($\varepsilon_{PTT}=0.15\times10^{-4}$) and EPTT($\varepsilon_{PTT}=0.15\times10^{-4}$) extensional viscosities are greater than 300 units, whilst SXPP$_{500}$ lies only around 3 units (see Figure 7.16c). Not until a deformation rate, $\lambda_{0b}\dot{\varepsilon}\approx2.0$, does the SXPP$_{500}$ fluid reach such elevated order in extensional viscosity. The *upturn* in *epd* for the PTT models can be correlated with the similarity to Oldroyd response of sharp rise in extensional viscosity (hardening) around the 0.5 unit strain-rate level. Beyond such strain-rates, the LPTT models reach a plateau, with levels of extensional viscosity of {10^3, 250, 150} units for $\varepsilon_{PTT}=\{0.15\times10^{-4},0.75\times10^{-4},1.5\times10^{-4}\}$. The tendency in *epd*-trends towards the asymptotic limits at elevated elasticity levels may be related to realising these η_e-plateau displayed by the LPTT models. For the two fluids, $\varepsilon_{PTT}=\{0.75\times10^{-4},1.5\times10^{-4}\}$, their trend-lines ([2], [3]) lie in close proximity to the Newtonian reference-line. Note that for $\varepsilon_{PTT}=1.5\times10^{-4}$, with lowest level of extensional viscosity plateau for the LPTT model, this leads to a trend-line practically parallel to the Newtonian reference-line. In the regions of deformation where extensional viscosity (and Trouton Ratio) is constant and dominates,

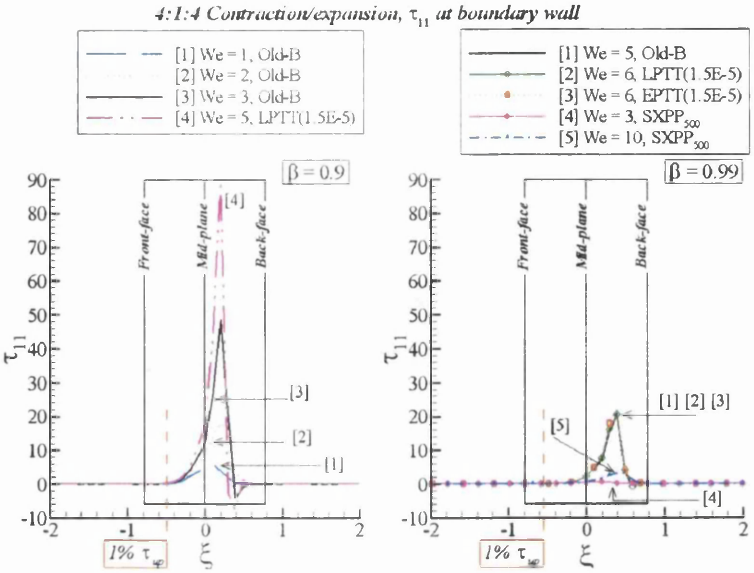

Figure 7.26. Stress profile along *wall* increasing *We*: $\beta = 0.9$ and 0.99; 4:1:4 axisymmetric.

epd-response is closer to that for an equivalent Newtonian fluid. The ratio of the resultant *epd* to the original Newtonian flow will be directly related to the enhancement in extensional viscosity.

A further comparison between the two strong-hardening/softening fluids, EPTT($\varepsilon_{PTT} = 0.15\times10^{-4}$) and SXPP$_{500}$, provides a better understanding of the influence of delayed hardening upon *epd*-trends. The delay in onset of the hardening regime provokes the lower stress values developed by SXPP$_{500}$. This can be observed in Figure 7.26 for $\beta = 0.99$-setting, where stress-peak at the wall for SXPP$_{500}$ and $We = 10$ is about five times lower than for LPTT($\varepsilon_{PTT} = 0.15\times10^{-4}$) or Oldroyd-B models at $We = 6$ or less. The rise in SXPP$_{500}$-stress as elasticity increases, indicates that the softening regime has yet to be reached. In Figure 7.26, it can be observed that the peak for $We = 10$ is about six times larger than for $We = 3$. The rise in stress may be reduced by an additional suppressive effect, identified via the more gradual increase in extension-hardening exhibited by this particular pom-pom model (SXPP$_{500}$) compared to its PTT counterparts. Observing the *epd*-curve for EPTT($\varepsilon_{PTT} = 0.15\times10^{-4}$) of Figure 7.25b, only a slight departure from the

LPTT($\varepsilon_{PTT} = 0.15\times10^{-4}$) response is noted (lines [1] and [4]). Such departure may be related to the lower η_e-maxima displayed by the EPTT model, associated also with reduction in the rate of hardening prior to the softening regime.

7.3.3d Very high β=0.999 predictions for Old-B

Considering now a system with the least departure from the Newtonian reference-line (compared to $\beta = 0.9$ and $\beta = 0.99$), due to an extremely large solvent presence, corresponding to 99.9% of the total viscosity. This case is defined by setting the viscosity ratio to $\beta = 0.999$. Even with this extremely low polymer concentration, the *upturn* in *epd* and the *cross-over* with the Newtonian reference-line can still be detected. The position of the local minima has not changed, simply rates of decay and rise up, to and beyond this stage. Trends here, are consistent with the arguments presented above.

7.3.3e Location of upstream pressure sampling point – experimental epd

Further comments are presented in this section on $[p - p_{Newt}]$-data and its impact on *epd* in the 4:1:4 axisymmetric configuration, whilst varying the β-parameter via {1/9, 0.9, 0.99} (see Figure 7.27). Recalling that for $\beta = 1/9$, there is no flip-over observed in $[p - p_{Newt}]$-entry with increasing elasticity, and hence, no *upturn*. This is the instance with only monotonic decrease in *epd*. The ($\beta = 0.9$)-case produces *upturn* in *epd*, whilst $\beta = 0.99$ gives both *upturn* and enhanced *epd*, as noted in the figure. By identifying p for Oldroyd-B as p_{Boger} for clarity, data is expressed in the form,

$$\frac{(\Delta p_{en})_{Boger} - (\Delta p_{en})_{Newt}}{(\Delta p_{en})_{Newt}} = \mathcal{P} - 1 = \frac{\Delta\left[p_{Boger} - p_{Newt}\right]_{en}}{(\Delta p_{en})_{Newt}}. \tag{7.2}$$

4:1:4 Contraction/expansion

a) Schematic representation of the sampling-point

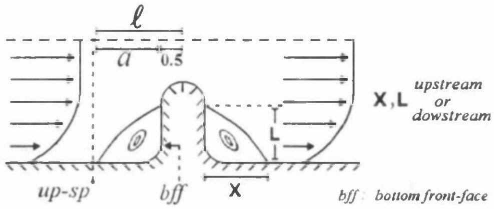

b) $\beta = 1/9$

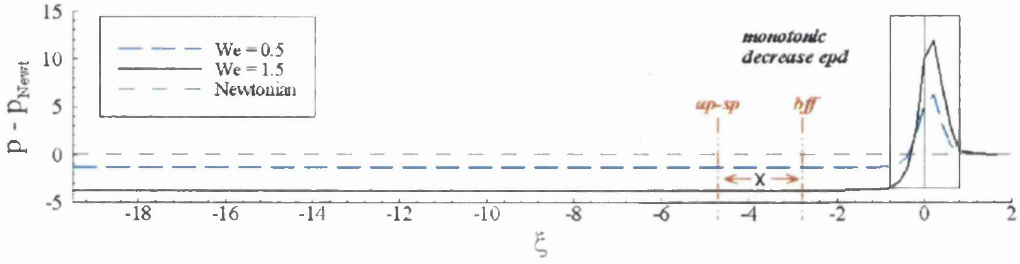

c) $\beta = 0.9$

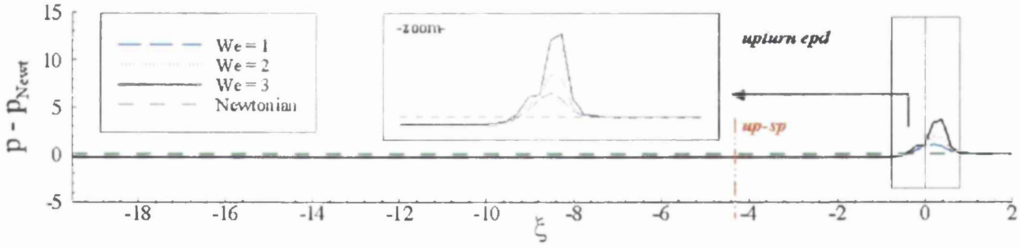

d) $\beta = 0.99$

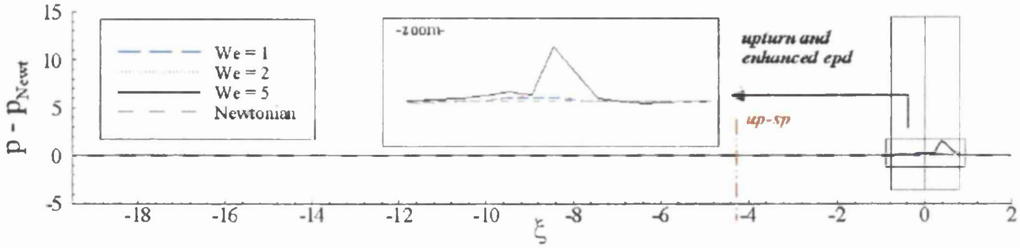

Figure 7.27. Pressure $[p\text{-}p_{Newt}]$ profiles along *wall* increasing *We* (Oldroyd-B): 4:1:4 axisymmetric; a) Schematic representation, b) $\beta = 1/9$, c) $\beta = 0.9$, d) $\beta = 0.99$.

From Figure 7.27, it may be gathered that in fully-developed inlet/exit conditions (*fd*), that $\Delta\left[p_{Boger}-p_{Newt}\right]_{fd}\approx 0$. Theoretically, under same flowrate and same shear viscosity setting for both Boger and Newtonian fluids, this statement is exact. Hence,

$$\frac{\Delta\left[p_{Boger}-p_{Newt}\right]_{en}}{\left(\Delta p_{en}\right)_{Newt}}=\frac{\Delta\left[p_{Boger}-p_{Newt}\right]}{\left(\Delta p_{en}\right)_{Newt}}=\mathcal{P}-1. \tag{7.3}$$

For enhanced *epd*, $(\mathcal{P}-1)$ must be positive and it is known that in general, $\left(\Delta p_{en}\right)_{Newt}>0$. With the calibration in the numerical scheme of $p_{Boger}^{exit}=p_{Newt}^{exit}=0$, this implies that $(\mathcal{P}-1)>0$ if and only if $\left[p_{Boger}-p_{Newt}\right]^{up\text{-}sp}>0$. Here, an upstream pressure sampling point (up-sp) can be defined (see Figure 7.27a), set at the minimum distance upstream from the mid-plane of the constriction to satisfy fully-developed flow conditions beyond the vortex region, so that $\left(p_{Boger}-p_{Newt}\right)^{inlet}=\left(p_{Boger}-p_{Newt}\right)^{up\text{-}sp}$.

Specifically, with $\Delta p=p^{inlet}-p^{exit}$,

$$\frac{\Delta\left[p_{Boger}-p_{Newt}\right]}{\left(\Delta p_{en}\right)_{Newt}}=\frac{\left(p_{Boger}-p_{Newt}\right)^{inlet}-\cancelto{0}{\left(p_{Boger}-p_{Newt}\right)^{exit}}}{\left(\Delta p_{en}\right)_{Newt}}, \tag{7.4}$$

then,

$$\frac{\left(p_{Boger}-p_{Newt}\right)^{inlet}}{\left(\Delta p_{en}\right)_{Newt}}=\mathcal{P}-1=\frac{\left(p_{Boger}-p_{Newt}\right)^{up\text{-}sp}}{\left(\Delta p_{en}\right)_{Newt}}. \tag{7.5}$$

This is a statement about the location of the *upstream pressure sampling point* (*up-sp*), which is satisfied for { $\beta=0.99$, $We=5$ } far upstream (say at some 14 units), a stage where enhanced *epd* is detected. With $\beta=0.9$, this same condition may be satisfied with a short centreline upstream distance ≈ 0.5 units, just beyond the front-face. Thus, the centreline upstream sampling distances, ℓ, and the dependency of practical *experimental epd* measurement on this distance can be re-examined, noting that ℓ is measured upstream from the mid-plane (see Figure 7.27a). Influence on *epd*-values for a range of different upstream sampling points, $\ell = \{0.5, 1.0, \psi_{up} \approx 1.5, 2.0, 14\text{-base}\}$[***], is depicted in Figure 7.28 for $\beta = 0.9$. By suitable sampling, it is possible to extract enhancement even for Oldroyd-($\beta = 0.9$). That is with $\ell \geq 0.5 + a$, $We \geq 2$ for some positive constant a, the minimum such per case considered. One recognises that in practice, valid-*epd*, should be taken at a fully-developed upstream stress location beyond the vortex regime, when falling below a set level (say 1% of stress maxima[†††], τ_{up}), see Figure 7.26.

Data is included in Figure 7.28a for the equivalent LPTT-($\beta = 0.9$) fluid, where it can be discerned that the trend is towards larger enhanced *epd* for larger We $(\rightarrow 5)$ and for $\ell \geq 1.5$ units.

In Figure 7.28b, each We-solution is re-considered and plotted as corresponding *epd* against upstream sampling distance ℓ. This identifies the scale and rapidity of the rise in *epd* at each We-state as $\ell \rightarrow 0.5$ units (constriction front-face). Clearly, this state of rise is most rapid and assists in determining the constant a per We-level[‡‡‡]. So, for example, with $We_{Old\text{-}B}$ of {1, 2, 3}, a is {0.0, 0.5, 1.5} units, rising to We_{LPTT} of 5 and a of about 3.5 units. For LPTT($\beta = 0.9$, $\varepsilon_{PTT} = 0.15 \times 10^{-4}$), $We = 5$ and $\ell = 4$, the sampling distance is outside the vortex region (delimited on the upstream wall by ψ_{up}) and which satisfies the fully-developed stress establishment criteria. If higher elasticity levels could have been reached $(We_{crit} > 5.6)$ for the LPTT($\beta = 0.9$, $\varepsilon_{PTT} = 0.15 \times 10^{-4}$), enhanced *epd* would have

---

[***] $\ell = 0.5$ corresponds to the front-face, ψ_{up} is the minimum valid ℓ.

[†††] Field variables in the centreline require longer distances to relax than those along the wall, for example, upstream pressure-gradient reach 1% of its peak-value at $z \approx -1.7$ units (see Figure 7.19c).

[‡‡‡] Clearly, it would not be difficult to provide misleading invalid *epd*-values from ℓ (or a) taken too small (too close to the constriction). There is also a $\ell_{\max}$ beyond which all *epd*-data are valid and equivalent.

a) epd vs. We

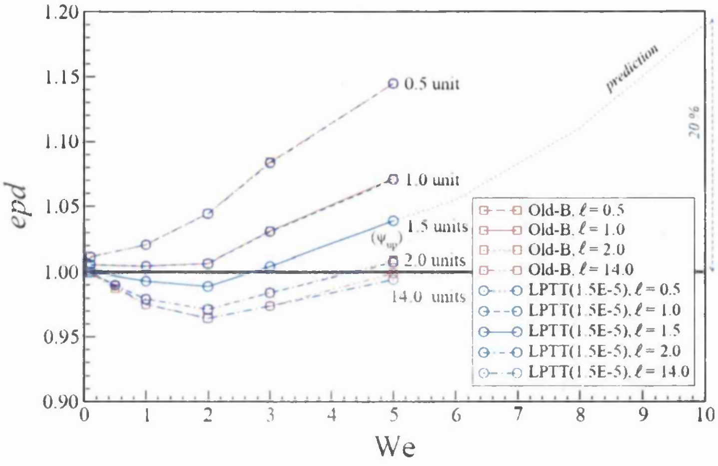

b) epd vs. ℓ

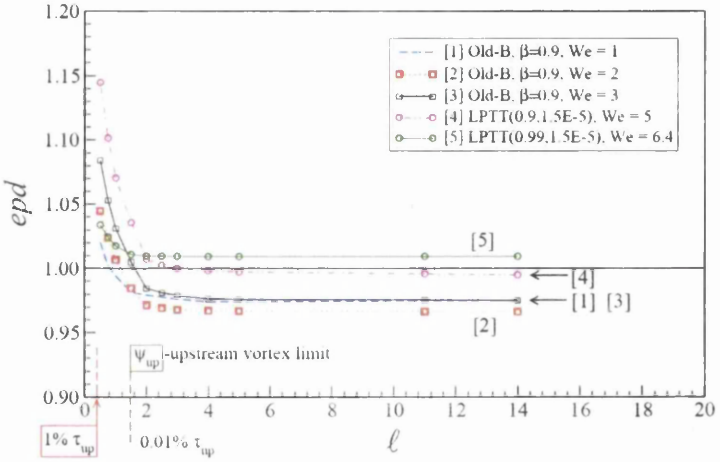

Figure 7.28. Pressure-drop (*epd*) at different sampling-points and *elasticity levels*: $\beta = 0.9$, 4:1:4 axisymmetric.

been achieved way-upstream. The importance of this analysis is to assist in guidance for pressure transducer positioning in order to obtain enhanced valid-*epd* measurements. With respect to the ($\beta = 0.9$)-solutions of Figure 7.28b, *epd*-minima is established by $\ell \approx 4$ units, with sharp *upturn* for $\ell \approx 2$ units. This is certainly beyond the ψ_{up}-measure indicated of $\ell \approx 1.5$. The subsequent sudden rise as $\ell \to 0.5$ units is common across all cases. For the LPTT($\beta = 0.99, We = 6.4$), a slightly less significant variation can be observed from the *epd*-minima ($\ell \approx 2.5$ units) towards its limit $\ell \rightarrow 0.5$ units, when compared to ($\beta = 0.9$)-cases. The terminating *epd*-value ($\ell \rightarrow 0.5$) is considerably reduced over that for LPTT($\beta = 0.9, We = 5.0$). This may be associated with τ_{11}-maxima across cases which reduce from 89.5 units for LPTT($\beta = 0.9, We = 5.0$) to 23.7 units for LPTT($\beta = 0.99, We_{crit} = 6.4$). Here, again the strong influence on *epd* is from stress reduction, lowering the extensional viscosity through increase in β.

Combining the information gathered in Figure 7.28b with Figure 7.28a and selecting $\ell \approx 1.5$ units, a prediction line following the *epd*-trend ($We, \beta = 0.9$) has been included in Figure 7.28a drawn for $We > 5$. This aids in identifying that an elasticity level of $We = O(10)$ may be necessary to gather an enhancement of $O(20\%)$.

Following the observations of Szabo et al. [90] and Cartalos and Piau [29], relating the dissipation-rate to the product of pressure-drop and flowrate, assuming equitable upstream and downstream stress distributions, a functional relationship between dissipation-rate and [$p - p_{Newt}$] is now sought. One may begin with[§§§],

$$\Delta p\, Q = \mathcal{D} \qquad \text{where} \qquad \Delta p = p^{inlet} - p^{exit}, \tag{7.6}$$

recognizing $\mathcal{D} = \int_V \boldsymbol{\sigma}{:}\nabla\mathbf{u}\,\mathrm{d}V$ over the inlet to exit flow region in question, where $\boldsymbol{\sigma}$ is the total stress and V is the fluid volume. Defining

$$\left(\Delta p\, Q = \mathcal{D}\right)_{Boger} \qquad \text{and} \qquad \left(\Delta p\, Q = \mathcal{D}\right)_{Newt}, \tag{7.7}$$

and assuming a constant flowrate configuration across the different fluid settings for simplicity, this yields,

---

[§§§] Equation (7.6) is satisfied at every instant under inertialess conditions.

$$\Delta\left[p_{Boger}-p_{Newt}\right]=\frac{\left[\mathcal{D}_{Boger}-\mathcal{D}_{Newt}\right]}{Q}, \qquad (7.8)$$

and since by calibration, $\left[p_{Boger}-p_{Newt}\right]^{exit}=0$, then

$$\left[p_{Boger}-p_{Newt}\right]^{inlet}=\left[p_{Boger}-p_{Newt}\right]^{up-sp}=\frac{\left[\mathcal{D}_{Boger}-\mathcal{D}_{Newt}\right]}{Q}, \qquad (7.9)$$

where the entry-station may be taken as the upstream pressure sampling point ($up-sp$), provided fully-developed flow conditions apply (in stress). This identifies the relationship between dissipation difference per unit flowrate, the upstream pressure differential and *epd* from equation (7.5). Since identical arguments may be applied for the separate 4:1:4 *fully-developed* flow sections, both upstream and downstream, where the relation $\Delta\left[p_{Boger}-p_{Newt}\right]_{fd}=0$ is satisfied, then, it can be concluded that there is no difference in dissipation-rate between these Boger and Newtonian fluids across such fully-developed regions. Considering the geometric complement, that is only the constriction and the upstream and downstream sections (near the constriction), where the flow is not fully-developed, the following identity may be established,

$$\frac{\left[\mathcal{D}_{Boger}-\mathcal{D}_{Newt}\right]^{constriction}}{Q}=\left[p_{Boger}-p_{Newt}\right]^{up-sp}=(\mathcal{P}-1)\left(\Delta p_{en}\right)_{Newt} \qquad (7.10)$$

Hence, seeking positive $\left[p_{Boger}-p_{Newt}\right]^{up-sp}$ to attain positive $(\mathcal{P}-1)$, also equates to establishing a positive dissipation difference across the constriction zone alone. This is so, independent of profile views along centreline or walls. Thus for the 4:1:4 flow, entry and exit channel lengths become irrelevant within the problem, beyond the establishment of fully-developed stress/flow sections.

It can also be observed empirically that $\left[p_{Boger} - p_{Newt}\right]^{up-sp}$ corresponds to a minimum entry-flow value, that is sustained as constant for each (We, β)-case through the inlet channel; this confirms the independence of 4:1:4 entry-zone length. Such a statement cannot be made for the 4:1 instance since stress values at the inlet are completely different from those at the exit.

To corroborate and validate present findings, Figure 7.29 displays *epd*-data obtained through various alternative numerical predictions in the literature for the 4:1:4 axisymmetric flow. This figure displays results from the studies of Szabo et al. [90], Binding et al. [17] and the present work. In general the agreement is most satisfactory at the two selected solvent ratios ($\beta = 1/9$ and 0.9).

7.4 Conclusions

The focus in this chapter has been to obtain physically representative pressure-drop predictions for constant shear-viscosity strain-hardening (Boger) fluids in contraction and contraction/expansion flows. The major findings of this chapter may be summarised as follows:

(*i*) Significant differences in *epd*-data have been identified between axisymmetric and planar configurations for Oldroyd-B fluids in 4:1:4 contraction/expansion flows. There and for axisymmetric settings only, enhancement above Newtonian *epd* is identified under certain circumstances. Adjusting the viscosity split ratio parameter β strongly influences the level of *epd*, with high solvent contributions providing local minima/*upturn*. This can be viewed as similar to the adjustment of the FENE-CR(L-parameter) in Szabo et al. [90], where large though finite η_e were stimulated. Some settings of Old-B(β) have been found to provide the desired enhancement in *epd*. It is reasonable to argue that β-adjustment for FENE-CR fluids is not necessary in cases where extension of the molecular

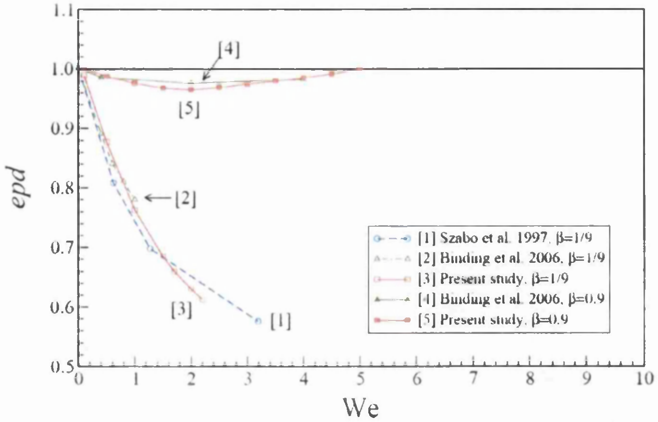

Figure 7.29. Pressure-drop (*epd*) vs. *We* (Oldroyd-B): 4:1:4 axisymmetric; scheme variation.

chains is short (low values of L - the finite extensibility parameter). Under such circumstances (with finite extension) there is decrease in the stored energy within the system. Hence, the initial decay in pressure-drop may be reduced from that for the Oldroyd-B model with unbounded extensibility. In addition, it is essential to note that the FENE-CR model shows a constant shear viscosity, whilst for PTT and SXPP simulations, a high-solvent contribution is necessary in order to represent Boger-like fluids. Recall that Oldroyd-B results for [17,90] and the present work are in excellent agreement at the level of $\beta = 1/9$ (see Figure 7.29).

(*ii*) Another important feature is that neither local minima nor *upturn* in *epd* have been observed under planar configurations, or for 4:1 contraction flows.

(*iii*) In the axisymmetric 4:1:4 contraction/expansion flow of an Oldroyd-B fluid, and when an *upturn* in *epd* is observed, this is accompanied by larger vortex intensity and cell-size in the downstream flow section, above that arising in the upstream section.

(*iv*) LPTT models follow the *epd*-trends of Oldroyd-B; adjusting the ε_{PTT}-parameter identifies the role of severe strain-hardening, and the impact of limiting the η_e-response. The larger degree of strain-hardening may be associated with the greater increase in the rise of *epd*, once an *upturn* has been captured. The pom-pom representation, with only relatively mild-hardening response, reinforces this observation. This also points to the fact that once a plateau has been reached in extensional viscosity[****], *epd* is anticipated to asymptote out to an equivalent Newtonian fluid level. The relative levels of *epd* will be related to the ratio of extensional viscosities (or Trouton ratios) involved.

(*v*) A unique feature of this study is the identification of influences from the boundary wall, and particularly so in stress. An explanation for the *upturn* in axisymmetric 4:1:4 *epd*, the single most important outcome from this work, may be found in the correlation of the extreme changes observed in the extensional stress fields, located about the constriction in the third and fourth quadrants. This stimulates some cross-stream response through stress and deformation-rate within axisymmetric 4:1:4 flows, that conveys its influence to the flow centreline, influencing the local pressure-drop accordingly. Predictions indicate that this does not happen in the planar or the 4:1 flow-settings, at least at the levels of deformation and elasticity explored. Under the comparison between the contraction/expansion and the contraction problems, one may speculate that it would be necessary to elevate deformation-rates and attainable elasticity levels by one to two orders of magnitude to stimulate *epd* enhancement in the 4:1 contraction flow. However, it is necessary to take into account that the pressure-drop (and also dissipation) for the contraction is of an order of magnitude larger than that for the contraction/expansion flow. That is, seeking larger attainable elasticity levels to stimulate larger stress peaks with greater influence on pressure, produces entry-pressure levels that fall away from the corresponding Newtonian fluid. These two influences are in conflict for the 4:1 contraction flow, which leads to the above speculation. Unfortunately, to date, it has not proven possible to attain such large elasticity levels through current numerical procedures.

[****] Equivalently, Trouton ratio for shear-thinning fluids, see pressure-drop results of Aboubacar et al. [1,2] Wapperom and Keunings [102], Alves et al. [8], Szabo et al. [90].

(*vi*) Through analysis of 4:1:4 data, the link between $[\,p - p_{Newt}\,]$-data, *epd* and dissipation-rate differences across the constriction zone has been identified. This leads one to appreciate the importance of the need to generate a positive reading of entry-flow $[\,p - p_{Newt}\,]$-minima at the upstream sampling point to extract enhanced *epd*, which equates to a positive dissipation-rate differential across the constriction. Also, the $\left[p - p_{Newt}\right]^{up\text{-}sp}$ data may be employed directly to estimate *epd* ($\mathcal{P}$). In this manner and considering LPTT as the more physically representative constitutive model for strongly strain-hardening Boger fluids, it can be appreciated how enhanced *epd* may be measured.

The implication from these finding is that if enhanced *epd* is sought, strong strain-hardening properties are crucial to raise levels of stress across the constriction. The fluid constitution and rheological properties are key. A high degree of solvent:polymeric constitution may achieve such ends, though proves a delicate matter to balance.

CHAPTER 8

Bautista-Manero Models in Planar Flows

This chapter is motivated by the need to model worm-like micellar systems that arise in oil-recovery situations. Typically, such systems exhibit Maxwellian-type behaviour in small-amplitude oscillatory shear and the saturation of shear stress in steady simple shear flow. Nevertheless, according to Manero and co-workers [61], their adequate representation through suitable rheological constitutive equations remains short of that desired. Good representation of the extensional properties of such viscoelastic fluid systems is also a necessity if one is to sensibly predict some important phenomena that arise in porous-media flow. Here the objective is the prediction and understanding of enhanced pressure-drop in viscoelastic shear-thinning systems for planar channel flows.

8.1 Introduction

Colloidal and polymeric liquid systems exhibit a variety of rheological responses, some of them with direct applications in the food, oil-extraction, cosmetics and coating industries. Particularly in oil-recovery processes, there is a need for fluids capable of transforming from low viscosity, Newtonian type to highly viscoelastic gels, and returning to low viscosity liquid form. These changes can be induced at different stages of the oil-recovery procedure. Viscoelastic surfactants systems (VES), with worm-like micellar formation, fall into this category and are being increasingly used as reservoir stimulation fluids, due to their assembly and disassembly properties.

Hydraulic stimulation of oil-wells is a technique to increase well-productivity when reservoir permeability is low. Fracturing treatment using viscoelastic gels is one such technique. This consists of transmitting hydraulic pressure to the rock to provoke fractures in the formation. Such a gel also contains particles (proppant), ceramic or sand, the whole constituting a porous proppant pack. The aim is for the gel to transport the pack into place and for the proppant to keep the fractures open upon removal of fluid pressure, via gel degradation. Polymeric fluids, used as fracturing liquids, present the inconvenience that they cannot be totally degraded and their particle size is sufficient to block the pores of the fracture, limiting the hydraulic conductivity of the pack. The use of viscoelastic surfactants systems as fracturing fluids, displaying worm-like micelles, has been a relatively new innovation. Once the proppant pack, armed with these fluids, comes into contact with hydrocarbon produced from the fracture, the internal structure reverts into small spherical micelles or microemulsions. As a consequence, the viscosity and elasticity of the fluid residues fall dramatically and they are able to easily flow from the pack. Very little pore blockage is therefore encountered, so that practically full fracture flow-back efficiency is achieved (see Boek et al. [21]).

Investigating the rheological response of wormlike micelle systems, Manero et al. [61] proposed a model similar in structure to the Oldroyd-B constitutive equation for the evolution of stress, coupled with the Fredrickson (kinetic) equation [46][*]. Such a model accounted for construction and destruction of micelles in solution, which resulted in a constitutive system capable of reproducing shear-thinning and strain-hardening/softening phenomena. The model is reported to be in excellent

---

[*] Moore [71] and Chung and Evans [34] are some examples of similar equations to that proposed by Fredrickson that accounts for structure formation and destruction.

agreement with experimental data from steady shear and small amplitude oscillatory measurements for the erucyl bis(hydroxyethyl)methylammonium chloride (EHAC) surfactant. Nevertheless, the extensional viscosity of the model gives rise to unbounded response (discontinuous structure) at finite deformation rates, and as such, presents some abnormal behaviour. Since the typical extension-rates experienced in porous-media flow can enter within this range of uncertainty, it is important to rectify this position. The original Bautista-Manero (BM) model may be represented through the following system of equations:

Extra-stress evolution,

$$\mathbf{T}+\frac{\eta}{G_0}\overset{\nabla}{\mathbf{T}}=2\eta\left(\mathbf{d}+\lambda_J\overset{\nabla}{\mathbf{d}}\right), \tag{8.1}$$

kinetic equation,

$$\frac{\mathrm{d}}{\mathrm{d}t}\left[\eta^{-1}\right]=\underbrace{\frac{1}{\lambda}\left(\frac{1}{\eta_0}-\frac{1}{\eta}\right)}_{construction}+\underbrace{k\left(\frac{1}{\eta_\infty}-\frac{1}{\eta}\right)\mathbf{T}:\mathbf{d}}_{destruction}, \tag{8.2}$$

where the relevant parameters represent the following quantities,

λ_J: retardation time (related to the solvent viscosity),
λ, k: structural parameters for relaxation time and breakdown, respectively,
η: viscosity,
η_p , μ_s: polymeric (variable) and solvent (constant) viscosities, respectively,
η_0, η_∞: viscosity at zero and very high shear-rates, respectively.
G_0: elastic modulus,

8.2 Modified Bautista Manero model

In order to overcome the unbounded extensional viscosity response of the original BM model, Boek et al. (see reference [22]), proposed a modified Bautista-

Manero (MBM) model, where the solvent and polymeric contributions are split. In this reformulation, the coefficient k/η_∞ is treated as a single parameter. The MBM constitutive equation provides a continuous extensional viscosity response, which yields the possibility of supporting physically realistic strain-hardening/softening properties, see equations (8.3)-(8.5). The reformulated system now becomes:

Viscoelastic stress evolution,

$$\boldsymbol{\tau} + \frac{\eta_p}{G_0}\overset{\nabla}{\boldsymbol{\tau}} = 2\eta_p \mathbf{d}, \tag{8.3}$$

kinetic equation[†],

$$\frac{\mathrm{d}}{\mathrm{d}t}\left(\frac{1}{\eta_p}\right) = \frac{1}{\lambda}\left(\frac{1}{\eta_0} - \frac{1}{\eta_p}\right) + \left(\frac{k}{\eta_\infty}\right)\boldsymbol{\tau}:\mathbf{d}, \tag{8.4}$$

solvent contribution,

$$\boldsymbol{\tau}_s = 2\mu_s \mathbf{d}. \tag{8.5}$$

In order to include this model within the local finite element/volume software library, capable of 2D/3D and transient computations, it is necessary to express the system of equations in dimensionless form. This defines group numbers of Reynolds and Weissenberg number, and the following non-dimensional parameters:

$$\begin{aligned} &Re = \rho\frac{\mathrm{UL}}{\mu}, \quad We = \frac{\mu}{\mathrm{G}_0}\frac{\mathrm{U}}{\mathrm{L}}, \quad \beta = \frac{\mu_s}{\mu}, \quad \phi_0 = \frac{\eta_0}{\mu}, \\ &\phi = \frac{\eta_p(t,\mathbf{x})}{\mu}, \quad \omega = \lambda\frac{\mathrm{U}}{\mathrm{L}}, \quad \xi = \left(\frac{\mathrm{k}}{\eta_\infty}\right)\mu_s\frac{\mathrm{U}}{\mathrm{L}}. \end{aligned} \tag{8.6}$$

[†] Note that in the BM model, η_0 is the total zero shear-rate viscosity, whilst in the modified version, it only accounts for the viscoelastic contribution. Then, in equations (8.6), $\mu = \eta_0$ for the BM model and for the modified version, $\mu = \eta_0 + \mu_s$.

In this manner, the MBM model may be expressed in equivalent non-dimensional form:

Momentum equation,

$$Re\left[\frac{\partial}{\partial t}\mathbf{u}+\mathbf{u}\cdot\nabla\mathbf{u}\right]=-\nabla p+\nabla\cdot\boldsymbol{\tau}+\beta\nabla^2\mathbf{u}\,, \tag{8.7}$$

stress evolution,

$$\boldsymbol{\tau}+We\,\phi\overset{\nabla}{\boldsymbol{\tau}}=2\phi\mathbf{d}\,, \tag{8.8}$$

kinetic equation,

$$\frac{d}{dt}\left(\frac{1}{\phi}\right)=\frac{1}{\omega}\left(\frac{1}{\phi_0}-\frac{1}{\phi}\right)+\left(\frac{\xi}{\beta}\right)\boldsymbol{\tau}:\mathbf{d}\,. \tag{8.9}$$

8.3 Discussion on results

Preliminary predictions have been obtained for the MBM model in a 4:1 rounded-corner planar contraction flow, under inertialess conditions ($Re=0$), with solvent/total viscosity ratio of $\beta=1/9$ (as a benchmark), and zero shear viscosity of $\phi_0=8/9$. This involved two separate cases, matching peaks in extensional viscosity corresponding to instances of strong-hardening and moderate-hardening, respectively. The comparable data (see Figure 8.1 for material functions[‡]) was drawn from that exhibited by an exponential Phan-Thien/Tanner (EPTT) fluid with $\varepsilon_{PTT}=0.02$ (strong strain-hardening) and $\varepsilon_{PTT}=0.25$ (moderate hardening), which have been discussed earlier in chapter 6. It can be observed that both models display the same response at low shear-rates. In shear viscosity, the agreement of fit is

---

[‡] The deformation rates are made non-dimensional by $\lambda_0=\eta_0/G_0$ in the MBM model.

Strong hardening
ω = 0.28, ξ = 0.1

Moderate hardening
ω = 4.0, ξ = 0.1

Shear and extensional viscosity

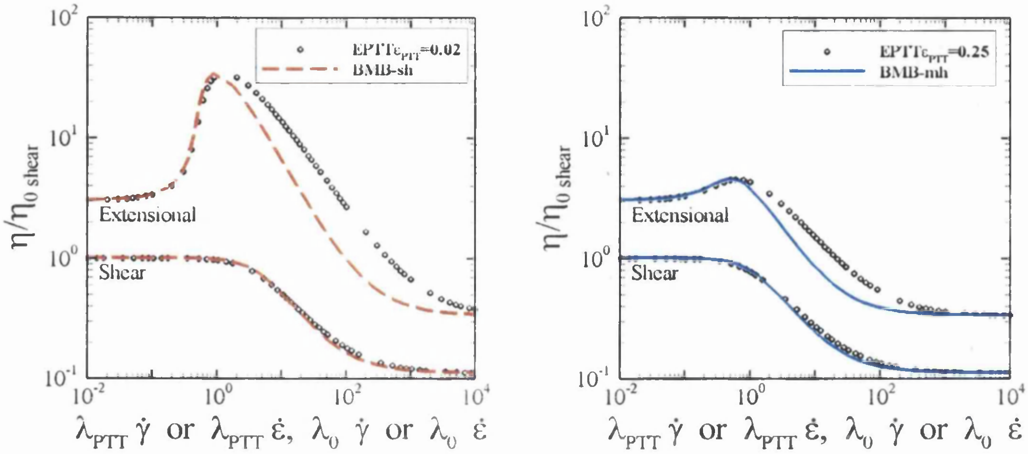

Trouton ratio

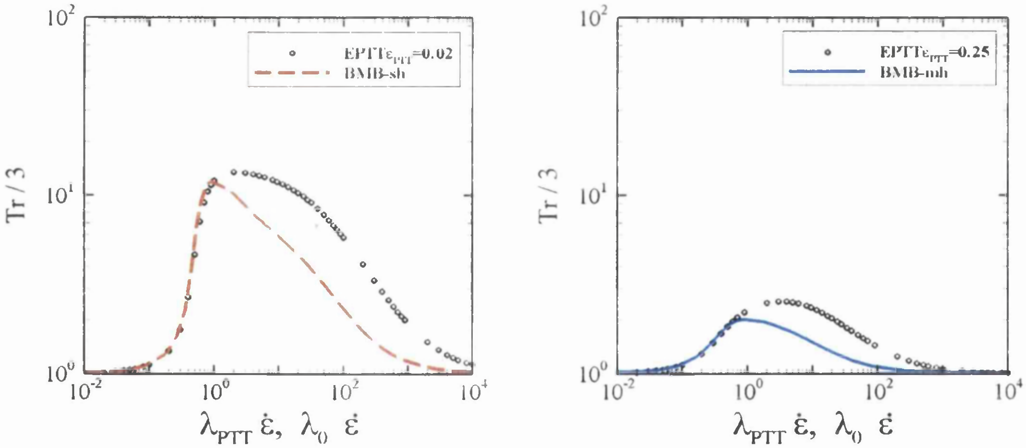

Figure 8.1. Rheometrical functions for MBM and EPTT models;

excellent throughout a wide range of deformation rates. Under moderate deformations rates, the MBM model softens more rapidly, reaching its plateau earlier than that for the corresponding EPTT fluid.

For the two sets of parameters chosen, vortex reduction is observed in cell-size and intensity, as displayed in Figure 8.2. The fluid with less degree of hardening reaches a slightly larger critical elasticity number ($We_{crit} \approx 7$) when compared to that for the strongly hardening scenario ($We_{crit} \approx 5$). This reduction in critical elasticity level attainable is a common feature observed when increasing strain-hardening inclusion, see Aboubacar et al. [3]. Under similar circumstances, the corresponding EPTT models provided vortex enhancement with increase of We whilst sustaining strongly-hardening properties, and only vortex reduction for the moderate hardening equivalent. This departure in response may be associated therefore with the more rapid strain-softening behaviour of the MBM model (which is reflected also in Trouton Ratio).

8.3.1 Material functions for the MBM model

In order to establish the influence of the various model parameters in viscometric flows, plots are presented varying η_0 (Figure 8.3), k/η_∞ (Figure 8.4), and λ (Figure 8.5).

Shear viscosity shifts from an almost constant level ($\eta_0 = 0.01$), approaching the Oldroyd-B response, to a case with extreme shear-thinning where the second plateau is reached at very high shear-rates. There is no visible effect on N_1 when the plot is presented in dimensionless form (Figure 8.3). Increasing the zero shear-rate viscosity produces an increment in the degree of strain-hardening and reduction in the level of the second plateau of extensional viscosity.

The influence of variation in k/η_∞ can be gathered from Figure 8.4. For shear viscosity, an increase in this parameter is reflected in a decrease of the shear-rate, affecting where the thinning starts and the second plateau is reached. The levels of asymptotic plateaux are independent of k/η_∞. From $k/\eta_\infty = 0.001$ to 100, the final limiting value of the first normal stress difference decreases by more than five decades ($N_1/G_0 \approx 7\times10^4$ to 7×10^{-2}) and is attained at much lower shear-rates. A similar increment in k/η_∞ lowers the degree of strain-hardening from 3×10^3 to zero,

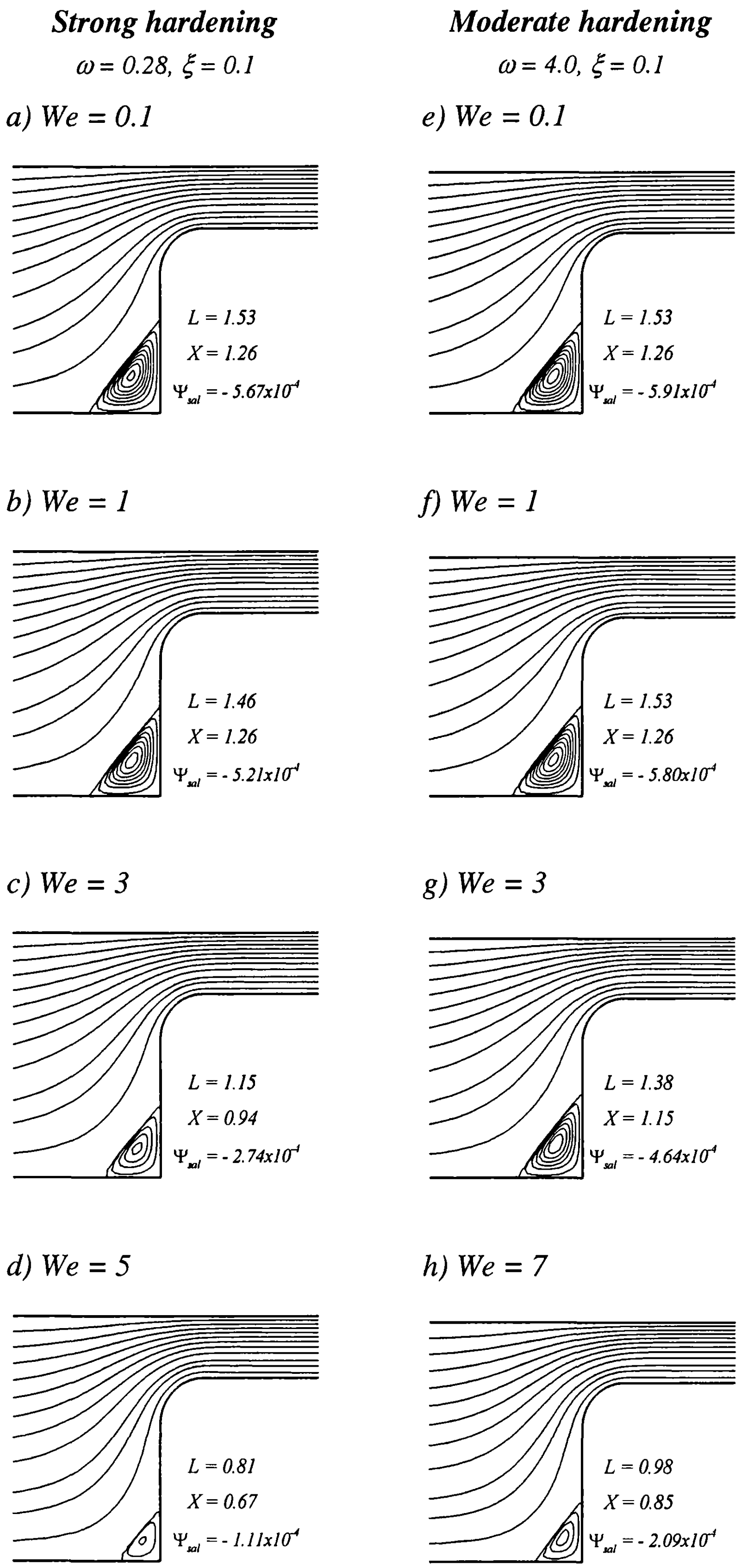

Figure 8.2. Streamlines for MBM model in 4:1 contraction flow.

a) Shear viscosity *b) First normal stress difference*

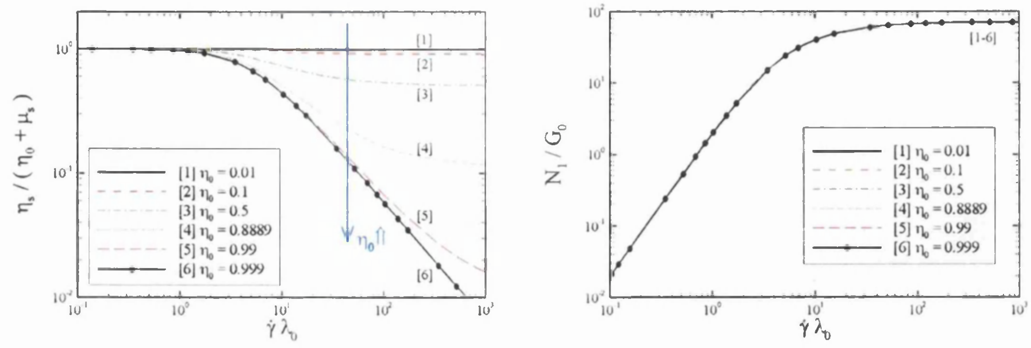

c) Uniaxial Trouton ratio *d) Uniaxial viscosity*

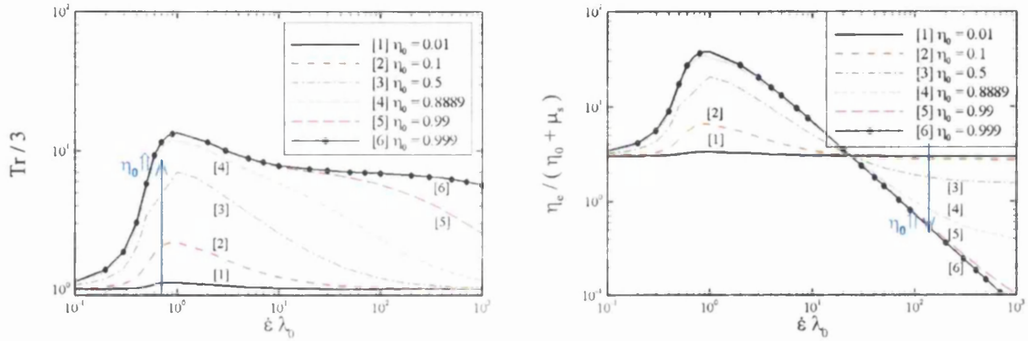

Figure 8.3. Shear and uniaxial response varying η_0: $G_0 = 1$, $k/\eta_\infty = 0.01$, $\mu_s = 1/9$, $\lambda = 0.28$.

so that for the fluid with $k/\eta_\infty = 100$, η_e decreases monotonically, softening even at very low deformation rates.

Referring to Figure 8.5, the response of the model to a change in λ somewhat replicates that dealt with under k/η_∞. It can be appreciated that the shear viscosity enters the thinning regime at lower deformations rates, and N_1 is decreased by about four decades when λ varies from 0.01 to 100. As above, an increase in λ produces a considerable increase in the degree of strain-hardening. Once the strain-rate transcends that associated with the peak in Trouton ratio (Tr), the second plateau in extensional viscosity is approached as strain-rates elevate further. Lower values of λ are observed to generate larger peaks in extensional viscosity and steeper softening

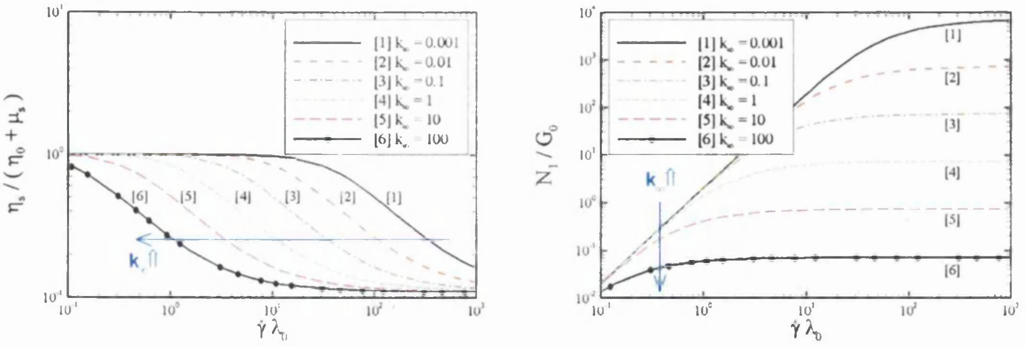

a) *Shear viscosity*

b) *First normal stress difference*

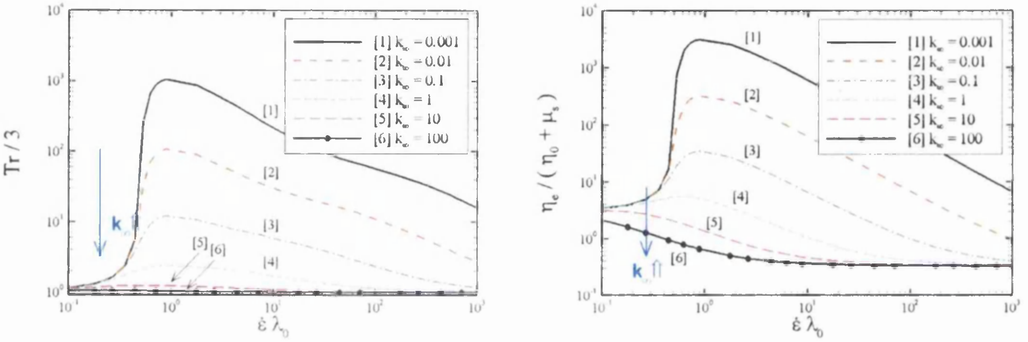

c) *Uniaxial Trouton ratio*

d) *Uniaxial viscosity*

Figure 8.4. Shear and uniaxial response varying k/η_∞: $G_0 = 1$, $\eta_0 = 8/9$, $\mu_s = 1/9$, $\lambda = 0.28$.

regimes. Note that for $\lambda \geq 10$ no strain-hardening is observed, and so no peak in extensional viscosity prevails.

8.3.2 Pressure-drop estimation in planar channels

A finite differences 1D-solution has been extracted to construct steady-state pressure-drop data for the MBM fluid in a planar channel flow. The system of equations is solved for velocity and shear-rate in the cross-stream direction (dimension H), having specified the viscosity function and a characteristic pressure-drop per unit length (L) (pressure loss within the system – see below for the equivalent analytical solution in section 8.3.3). Figure 8.6 illustrates the division of the cross-stream domain into discrete segments and nodal points, and in general, consistency and convergence under mesh refinement has been guaranteed.

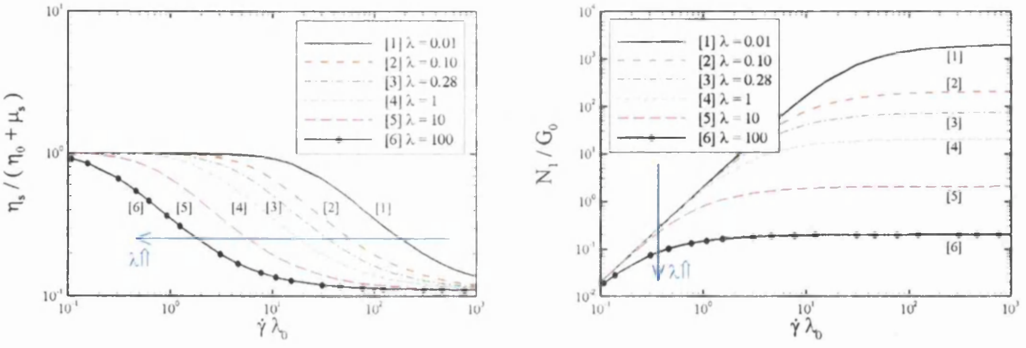
a) Shear viscosity

b) First normal stress difference

c) Uniaxial Trouton ratio

d) Uniaxial viscosity

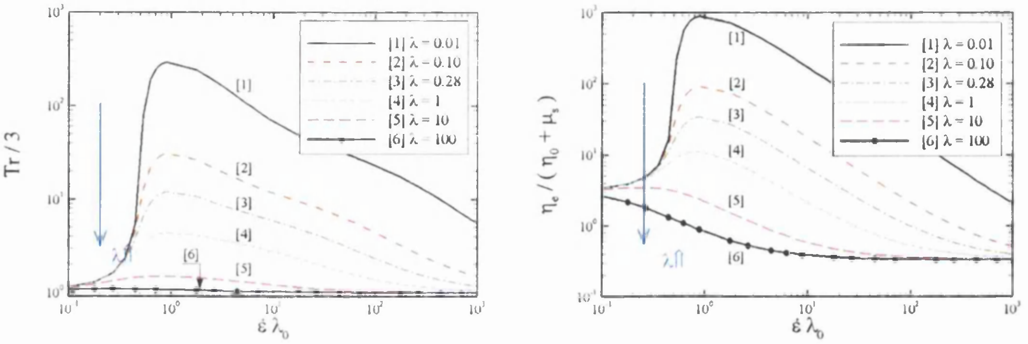

Figure 8.5. Shear and uniaxial response varying λ: $G_0 = 1$, $\eta_0 = 8/9$, $k/\eta_\infty = 0.01$, $\mu_s = 1/9$.

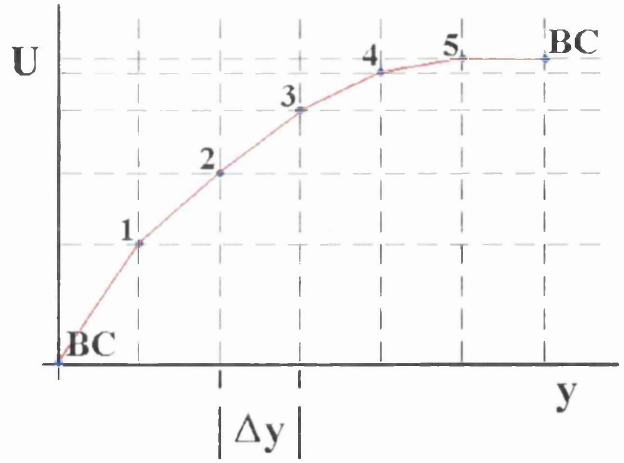

Figure 8.6. Schematic: cross-stream division of channel problem domain.

Position in the cross-stream direction lies within $-1 \le \bar{y} \le 1$, concisely represented as $\bar{y} = y/[\tfrac{1}{2}H]$.

The momentum equation for the MBM model in a planar channel ($-1 \le \bar{y} \le 1$) reduces to:

$$-\tfrac{1}{2}H\frac{\Delta p}{L}\bar{y} = \left[\eta_p + \mu_s\right]\dot{\gamma}, \qquad (8.10)$$

which satisfies the mid-channel condition,

$$\bar{y} = 0 \quad \Rightarrow \quad \dot{\gamma} = 0. \qquad (8.11)$$

The MBM viscosity in shear is given by:

$$\eta_p = \frac{1}{2\lambda k_\infty \eta_0 \dot{\gamma}^2}\left[-1 + \sqrt{1 + 4\lambda k_\infty {\eta_0}^2 \dot{\gamma}^2}\right], \qquad (8.12)$$

where the parameter (k/η_∞) is represented by k_∞ for convenience.

Assuming a given pressure-drop per unit length to conduct the parameterisation, the solution of equation (8.10) at a series of $\bar{y}$-values (y_i-positions) covering the half-channel width, yields the necessary deformation-rate profile. This profile may then be integrated by means of a Taylor series (Euler or similar scheme) to yield the corresponding velocity profile:

$$u_i = u_{i-1} + \Delta\bar{y}\ \dot{\gamma}_{i-1}. \qquad (8.13)$$

The boundary condition at the wall is no-slip,

$$\bar{y} = \pm 1 \quad \Rightarrow \quad u = 0, \qquad (8.14)$$

application of which realises:

$$u_0 = 0. \tag{8.15}$$

Equation (8.15) is necessary as a starting point for the forward numerical integration procedure of equation (8.13). This procedure may be terminated at the half-length of the channel. By definition, Δy is the mesh-segment distance between two successive points into which the domain has been divided, see Figure 8.6.

Finally, it is necessary to compute the resulting flowrate (Q), which is accomplished through quadrature applied to the integral:

$$Q = 2W\,H \int_0^1 u(\bar{y})\,\mathrm{d}\bar{y}. \tag{8.16}$$

In order to prove that algorithmic consistency and convergence upon mesh refinement with sufficient number of discrete points has been achieved, Figure 8.7 presents the solution profile using 11, 101 and 1001 points across the domain. It is evident that the three solutions are in excellent agreement.

Once the solution has been validated, the next step to meet requirements is to produce the Q vs. Δp curves for the three channels of different gap-widths (H) covering the variation of fluid parameters supplied. Table 8.1 contains the corresponding data for the fluid SF1 and Figure 8.8 is a plot covering the flowrate vs. pressure-drop calculations. Here, data is presented in dimensional form for ease of physical reference.

From Figure 8.8, monotonic increasing relationship between flowrate and pressure-drop can be observed. The curves can be superimposed almost perfectly upon each other, implying that they have exactly the same trend. However, a constant shift factor is difficult to extract as the zones where the flowrate increases faster do not start at the same level of pressure-drop. Still, one can establish a mapping as a function of H, of the start and end points of the

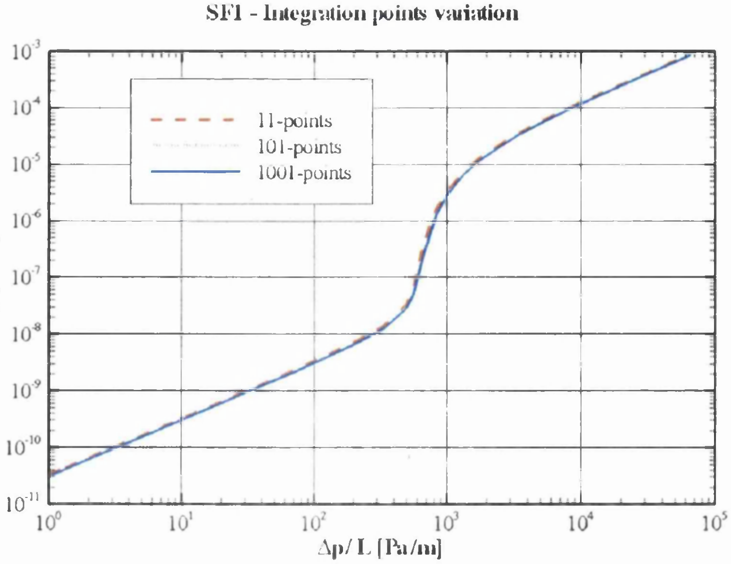

Figure 8.7. Solutions for different number of degrees of freedom.

non-linear region in pressure-drop. Linearity is upheld for low pressure-drop values (<500 Pa) and is recovered at high values ($>10^4$ Pa). For intermediate values of Δp ($500<\Delta p<10^4$ Pa), non-linear response is observed, so that the flowrate picks up a *sudden spurt*.

This non-linear response can be associated with the variation in shear-rate over the regions of parameters specified. The evidence for this is supplied below in Figure 8.9, which displays how the *steady* deformation-rate and velocity profiles evolve

Table 8.1. SF1 parameters

μ_s [Pa s]	0.0264
η_0 [Pa s]	11
k/η_∞ [Pa^{-2} s^{-1}]	0.33019
λ [s]	13.6284
G_0 [Pa]	0.44

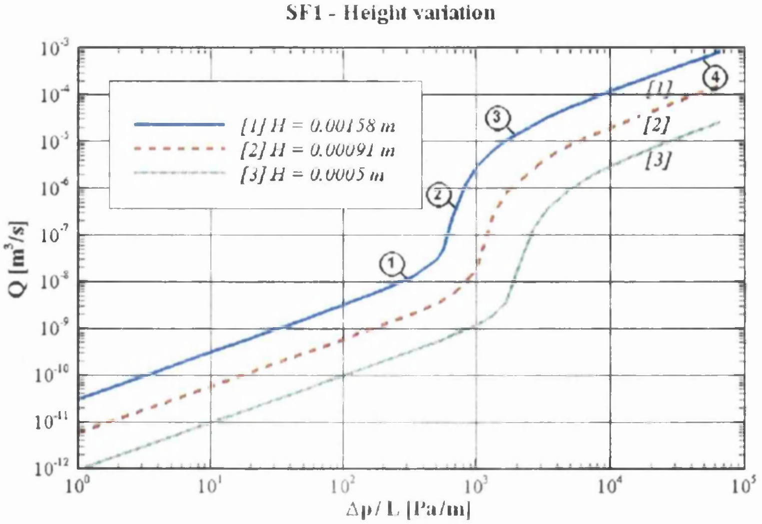

Figure 8.8. Q vs. Δp curves for channels gaps (H).

when $\Delta p/L$ increases. At $\Delta p/L = 300$ Pa/m (point 1), a linear shear-rate profile emerges (parabolic velocity distribution). Upon increase to $\Delta p/L = 700$ Pa/m (point 2), both shear-rate and velocity profiles depart from the earlier Newtonian-like pattern. The fluid near the wall is exposed to significant variation in shear-rate, in stark opposition to the conditions approaching the centreline, where shear-rates and their variation are low. Note correspondingly, that the velocity profile is practically flat in the low shear-rate centreline zone. It is precisely in this zone where the flowrate increases more rapidly with respect to incrementation in pressure-drop. Proceeding further to the next elevation station of $\Delta p/L = 2000$ Pa/m (point 3), the Q vs. Δp curve recovers its linear relationship, so that the shear-rate profile and flowrate reform the linear and parabolic trend, respectively. It is only when the significantly larger level of $\Delta p/L = 50000$ Pa/m (point 4) is reached that such trend are effectively fully recovered. The square of the Pearson coefficient[§] (r) through all

---

[§] Definition of the Pearson coefficient for n (X,Y) data is: $r = \dfrac{n(\Sigma XY) - (\Sigma X)(\Sigma Y)}{\sqrt{\left[n\Sigma X^2 - (\Sigma X)^2\right]\left[n\Sigma Y^2 - (\Sigma Y)^2\right]}}$.

Shear-rate profiles **Velocity profiles**

a) Δp/L = 300 [Pa/m]

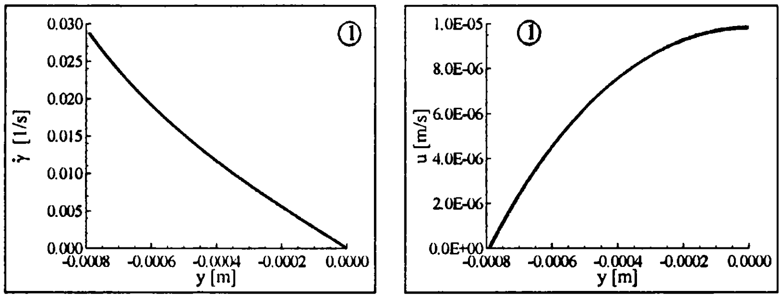

b) Δp/L = 700 [Pa/m]

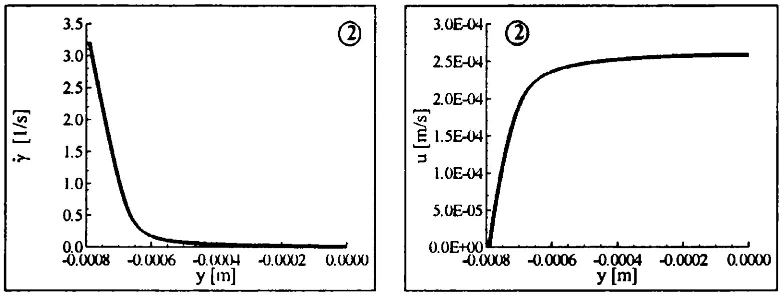

c) Δp/L = 2000 [Pa/m]

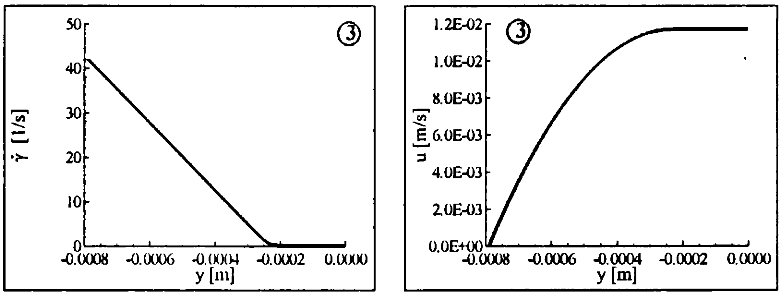

d) Δp/L = 50000 [Pa/m]

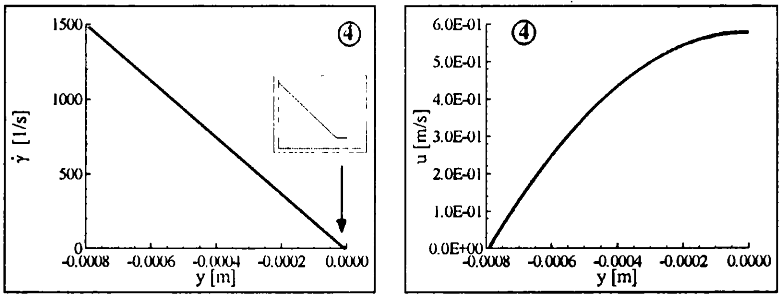

Figure 8.9. Evolution of deformation-rate and velocity profiles as Δp increases.

$\dot{\gamma}$-data points (linear regression) is a measure of proximity to linearity, an r-value of unity providing a constant slope relationship. To estimate the recovery of the linear (Newtonian) $\dot{\gamma}$-profile in cases 3 and 4, the Pearson coefficients are reported, being $r = 0.97$ for point 3 ($\Delta p/L = 2000$ Pa/m), and for point 4 ($\Delta p/L = 50000$ Pa/m), the r-value lies within the interval [0.99,1]. The point 4 r-value clearly exhibits a closer position to a constant slope-line than that for point 3.

8.3.3 An analytical solution

It has been possible to cross-check the numerical computation above for the MBM model in planar channels by appealing to a direct procedure, and thereby, extracting an analytic solution to the problem. This is accomplished by appealing to analysis for a related class of shear-thinning fluids (Oldroyd-4 constant) and shear flow in pipes performed by Walters [100]. The procedure consists in a change of variables that provides the velocity as a function of shear-rate alone.

From equation (8.10) - 'balance of forces', the cross-stream y-position as a function of the deformation-rate, expressed as:

$$y = \theta(\dot{\gamma}) = -\left[\eta_p + \mu_s\right]\frac{1}{\left(\dfrac{\Delta p}{L}\right)}\dot{\gamma}\,. \qquad (8.17)$$

Following the chain rule of differentiation, function $\theta(\dot{\gamma})$ satisfies:

$$\frac{1}{\dot{\gamma}} = \frac{\mathrm{d}y}{\mathrm{d}u} = \frac{\mathrm{d}\theta}{\mathrm{d}\dot{\gamma}}\frac{\mathrm{d}\dot{\gamma}}{\mathrm{d}u}\,. \qquad (8.18)$$

Upon integrating this relationship the velocity is extracted as:

$$u = \int \dot{\gamma}\frac{\mathrm{d}\theta}{\mathrm{d}\dot{\gamma}}d\dot{\gamma} + C\,. \qquad (8.19)$$

With the knowledge of η_p of equation (8.12), the velocity, as a function of the shear-rate, is given analytically by the derived equation (8.20):

$$u(\dot{\gamma}) = \frac{\mu_s}{2\left(\frac{\Delta p}{L}\right)}\left[\dot{\gamma}_x^{\,2} - \dot{\gamma}^2\right] + \frac{1}{2k_\infty \eta_0 \lambda \left(\frac{\Delta p}{L}\right)} Ln\left[\frac{1+\sqrt{1+4k_\infty \eta_0^{\,2} \lambda \dot{\gamma}_x^{\,2}}}{1+\sqrt{1+4k_\infty \eta_0^{\,2} \lambda \dot{\gamma}^2}}\right], \tag{8.20}$$

where $\dot{\gamma}_x$ is the solution of the boundary equation at the wall ($\bar{y} = \pm 1$).

Knowing η_p, an expansion of equation (8.17) results in a cubic polynomial for $\dot{\gamma}$ as a function of $\bar{y}$, of the form,

$$\dot{\gamma}^3 + a_1\dot{\gamma}^2 + a_2\dot{\gamma} + a_3 = 0. \tag{8.21}$$

The respective coefficients are given by:

$$a_1 = \frac{H}{\mu_s}\frac{\Delta p}{L}\bar{y},$$

$$a_2 = \frac{-(\eta_0 + \mu_s) + \frac{1}{4}H^2 k_\infty \left[\frac{\Delta p}{L}\right]^2 \eta_0 \lambda \bar{y}^2}{k_\infty \eta_0 \mu_s^{\,2} \lambda}, \tag{8.22}$$

$$a_3 = -\frac{\frac{1}{2}H\bar{y}}{k_\infty \eta_0 \mu_s^{\,2}\lambda}\left[\frac{\Delta p}{L}\right],$$

where the real root (numerically or analytically) at any particular y-position across the channel is required. In the present instance, the real root has been extracted analytically using the method of Cardano [89]:

$$a)\qquad \dot{\gamma}_{root1} = Sc + Tc - \frac{1}{3}a_1 ,$$

$$b)\qquad \dot{\gamma}_{root2} = -\frac{1}{2}\left(Sc + Tc\right) - \frac{1}{3}a_1 + \frac{1}{2}i\sqrt{3}\left(Sc - Tc\right), \tag{8.23}$$

$$c)\qquad \dot{\gamma}_{root3} = -\frac{1}{2}\left(Sc + Tc\right) - \frac{1}{3}a_1 - \frac{1}{2}i\sqrt{3}\left(Sc - Tc\right).$$

The quantities, { Sc , Tc }, necessary to evaluate these sets of solutions (roots) are defined through additional derived quantities { Qc , Rc , Dc }:

$$Qc = \frac{3a_2 - a_1^{\,2}}{9}, \qquad Rc = \frac{9a_1a_2 - 27a_3 - 2a_1^{\,3}}{54},$$

$$Dc = Qc^3 + Rc^2, \qquad Sc = \sqrt[3]{Rc + \sqrt{Dc}}, \tag{8.24}$$

$$Tc = \sqrt[3]{Rc - \sqrt{Dc}}.$$

The discriminant, Dc reveals the nature of solutions. For the case where $Dc < 0$, all three solutions are real and the following formula may be used to simplify the computation:

$$
\begin{aligned}
&a) \qquad \dot{\gamma}_{root1} = 2\sqrt{-Qc}\,cos\left[\tfrac{1}{3}\varphi\right] - \frac{1}{3}a_1\,, \\
&b) \qquad \dot{\gamma}_{root2} = 2\sqrt{-Qc}\,cos\left[\frac{\varphi + 2\pi}{3}\right] - \frac{1}{3}a_1\,, \\
&c) \qquad \dot{\gamma}_{root3} = 2\sqrt{-Qc}\,cos\left[\frac{\varphi + 4\pi}{3}\right] - \frac{1}{3}a_1\,.
\end{aligned}
\tag{8.25}
$$

appealing to

$$
\varphi = cos^{-1}\left[\frac{Rc}{\sqrt{-Qc^3}}\right]. \tag{8.26}
$$

Armed with these definitions, it is the third solution root ($\dot{\gamma}_{root3}$), given by equations (8.23)c or (8.25)c, that is equivalent to the numerical solution extracted via the proposed 1D-finite difference approximation. The deformation-rate at the wall, $\dot{\gamma}_x$, required by equation (8.20) is:

$$
a) \quad \dot{\gamma}_x = \dot{\gamma}_{root3} \quad at \quad \overline{y} = -1, \qquad\qquad b) \quad \dot{\gamma}_x = -\dot{\gamma}_{root3} \quad at \quad \overline{y} = 1. \tag{8.27}
$$

For a physical solution, that smoothly varies from $\overline{y} = -1$ to the centreline ($\overline{y} = 0$), the appropriate maximum shear rate is given by identity (8.27)a.

Similar procedures may be applied to many other common model viscosity functions (e.g. PTT and Pom-Pom), that possess a solvent viscosity component and can be expressed essentially through polynomial form in shear-rate, of integral power not greater than two (for cubics) and three for quartics. This is valid for stress evolution equations say as Oldroyd-type - see equation (8.3), where only first order terms of $\mathbf{d}$ (or $\dot{\gamma}$) appear. If the constitutive model requires second order terms of $\mathbf{d}$, numerical solutions may be required for the equivalent to equation (8.21), as quintics may appear. Third-order terms are not anticipated in the constitutive equation due to the *representation theorem* (see [56]) for tensors (*Cayley-Hamilton theorem*), which indicates that terms functionally related to $\mathbf{d}^3$, or higher, collapse to a function of $\mathbf{d}^2$, $\mathbf{d}$ and its invariants.

8.3.4 Pressure distributions

As the geometry does not present any constriction or change in direction for the flow, the steady pressure-drop is constant along the channel length, this results in a linear decay in pressure from inlet to exit. Figure 8.10 reflects this state of decay for two cases: the first is for a flowrate of $\approx 5\times10^{-6}$ m^3/s, and the second is for $\approx 5\times10^{-10}$ m^3/s. As anticipated, for channels with smaller heights (H), larger values of pressure are required to drive the flow at the same level of flowrate.

8.3.5 Transient solutions

Starting from rest, evolution field states through time are obtained by imposing a transient Oldroyd-B solution in a channel [104], at the inlet boundary (flowrate Q controlled temporal build-up). For this dynamical situation, the chosen fluid is SF2 (see Table 8.2) and the flowrate is 1.6×10^{-9} m^3/s.

Pressure-drop, velocity (centreline) and stress (boundary wall) are presented in non-dimensional terms in Figure 8.11. Pressure-drop response exhibits oscillations and is seen to reach its steady-state value faster than in velocity and stress. All evolution profiles display an overshoot. In velocity and stress, a minor undershoot is also observed before a steady-state is established.

A desirable next step would be to compute transient solutions for such fluids within a complex contraction-expansion setting, either via a flowrate controlled or a constant-force (Δp-fixed) form.

a) Pressure vs. length, SF1: low flowrate

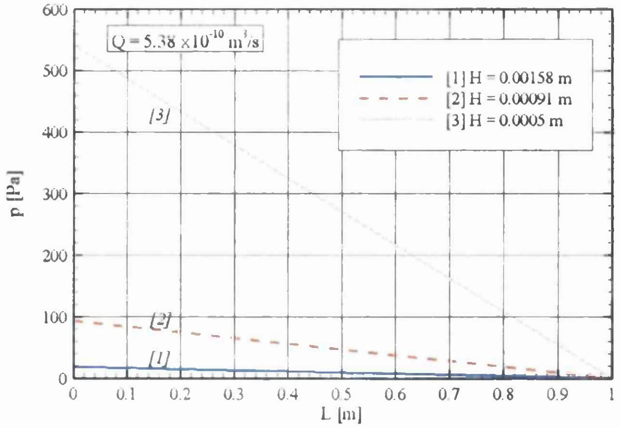

b) Pressure vs. length, SF1: high flowrate

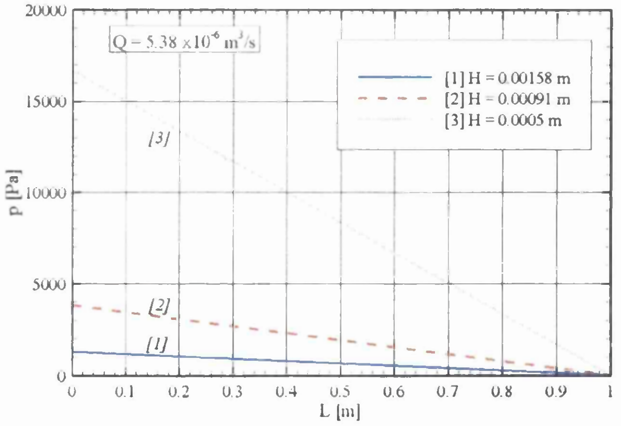

Figure 8.10. Pressure vs. length curves at fixed flowrate.

Table 8.2. SF2 parameters

μ_s [Pa s]	0.0105
η_0 [Pa s]	2.1
k/η_∞ [Pa^{-2} s^{-1}]	0.6
λ [s]	5.0
G_0 [Pa]	0.525

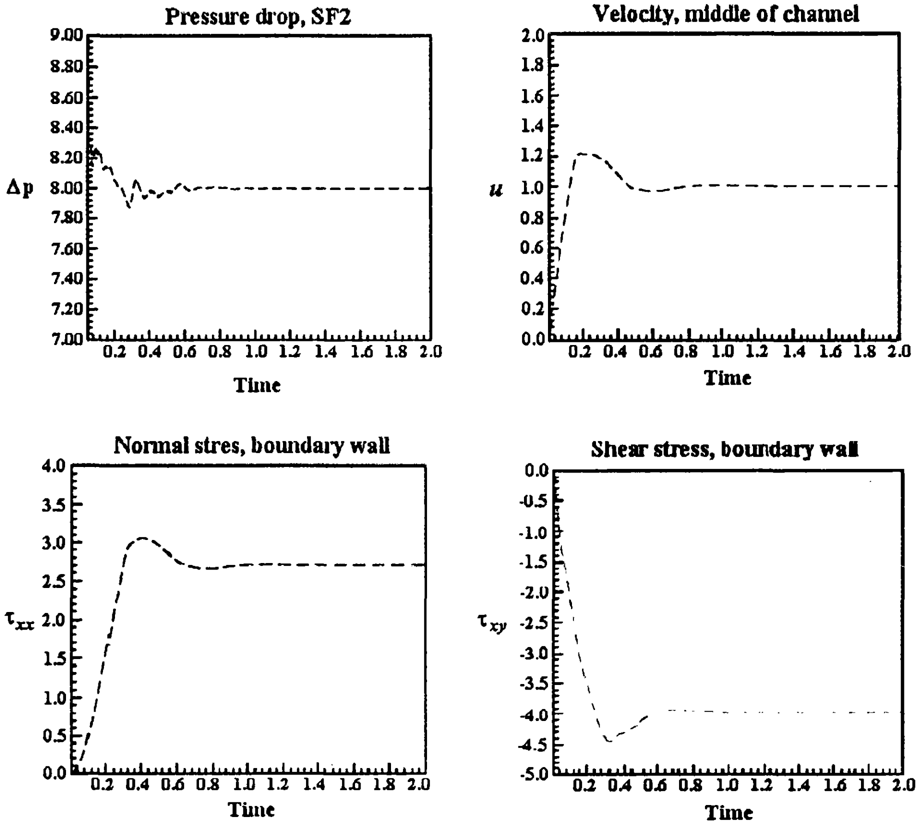

Pressure drop, SF2

Velocity, middle of channel

Normal stres, boundary wall

Shear stress, boundary wall

Figure 8.11. Transient results for the channel flow, fluid SF2.

8.4 Conclusions

Adequate representation of worm-like micellar systems was proposed via the original Bautista-Manero (BM) model. However, this model was found to exhibit unphysical extensional viscosity response. Here, the response for a modified model (MBM), introduced by Boek et al. [22] has been studied, a model that allows for a continuous viscosity in uniaxial flow.

Material functions for this new MBM version have been fitted to match two different configurations of the exponential version of the Phan-Thien/Tanner model. In contrast to the situation for pom-pom models, both extensional and shear peak viscosities of PTT models can be approximated with one set of parameters alone for each different level of hardening scenario. In rheometrical flows, a variation in k/η_∞ and λ produces almost an identical response in both viscosity and stress.

Following the procedure proposed by Walters, an analytical solution $\{u, \dot{\gamma}\}(\overline{y})$ has been derived for the MBM model in Poiseuille channel flow. The method consists in a change of variable, leaving the cross-stream position ($\overline{y}$) as a function of shear rate ($\dot{\gamma}$). This yields an integral that gives the velocity (u) in terms of the shear rate and its value at the wall. To obtain the deformation-rate at the wall, the roots of a cubic polynomial must be extracted. Finally, and for confirmation of validity, the finite difference approximation is in excellent agreement with the results obtained by the analytical solution.

Two linear trends for (Q vs. Δp)-variation have been detected in the corresponding solutions. These trends occur at low and high pressure-drops. There is a region where the flowrate increases faster, displaying a sudden spurt. The behaviour in this region has been recognized to be a result of the prevailing strong shear-thinning displayed by all such fluids studied here. As such corresponding $\dot{\gamma}$-profiles display a significant departure from the linear-form anticipated over regions of nearly constant shear viscosity. Transient solutions for channel flow have also been probed, revealing their characteristic form.

CHAPTER 9

Concluding Remarks

Simulation of planar and axisymmetric flows through channel, contraction and contraction/expansion geometries has been presented in this study. Some effort has been placed upon relating fluid response to background rheometrical properties, such as extensional and shear viscosity. In particular, vortex intensity behaviour in contraction flows exhibits a dependence on the degree of hardening. That is, for fluids displaying strain-softening under prevailing flow conditions, vortex intensity decreases in magnitude. Stress and stretch fields are also dependant on the material functions. In some instances, it is possible to discern dominant deformation regimes within a specific region. For example in contraction flows, fluid along the centreline near the contraction experiences pure elongational flow, whilst in the downstream channel, large shear rates are observed near to boundary walls (practically zero strain-rate). In the contraction corner near the wall, important shear and extensional effects are anticipated. Hence, in extension-dominated zones, extensional viscosity becomes an important parameter, and in regions of strong shear, first normal stress difference and shear viscosity govern the fluid response.

The numerical scheme employed through this study is one of hybrid finite element/finite volume (*fe/fv*) form, developed by the computational rheology

(INNFM) group at the University of Wales Swansea. In chapters 4 and 5, solutions are validated against predictions from a semi-Lagrangian pure finite volume scheme, implemented by the fluid dynamics (INNFM) group at of Cardiff University.

First, the Single eXtended Pom-Pom (SXPP) constitutive equation [96] flowing in a planar channel has been considered. This model is of a relatively new class of constitutive equations, developed mainly from physical arguments. Several modifications have been proposed since the introduction of the original model by McLeish and Larson [68]. In the planar channel, influence of the non-dimensional quantities on the flow is gathered. These quantities control the degree of hardening, the onset of shear-thinning and the viscoelastic contribution via the solvent fraction. The next step was to provide corresponding predictions for flow in planar 4:1 contraction geometries, where vortex growth, stress and stretch fields are reported for two different levels of inertia ($Re = 0$ and 1). An alternative version of the pom-pom model was also implemented, that is the λ^2XPP [76]. This gave practically identical results to those for the SXPP version.

The SXPP model presents the advantage of varying the strain-hardening response with just a minuscule variation in shear-thinning viscosity. Upon this basis, the influence of extensional viscosity was investigated for shear-thinning fluids in 4:1 contraction flows. In addition, the influence of anisotropy and the numerical difficulties introduced by this factor are observed. It was concluded that the instabilities provoked by the anisotropy parameter occur at larger deformation rates than those supported by such flows. A comparison has been included with the exponential Phan-Thien/Tanner model at two different levels of strain hardening, this has shown similar trends for fluids of comparable elongational viscosities, although for moderate hardening, a match on extensional viscosity instead of Trouton ratio provides better qualitatively agreement between both types of fluids.

The occurrence of excessive pressure-drops has been studied that arise for Boger fluids in axisymmetric contraction and contraction/expansion flows. In this work, the constitutive equation employed has been mainly the Oldroyd-B form, due to its constant shear viscosity and highly viscoelastic properties (Boger-type behaviour). In order to approximate Boger-like response with other rheological models (SXPP and PTT variants), the solvent fraction has been adjusted (excessive solvent contribution) and extremely high levels of extensional viscosity have been stimulated. Results indicate that in the case of the axisymmetric contraction/expansion, a large stress developed around the constriction is responsible for an increase in pressure when compared to its corresponding Newtonian fluid. This peak in pressure, in certain conditions, can be sufficiently large to account for an increasing trend in excess pressure-drop (*epd*). In addition, under increasing solvent fractions, the *epd*-trend crosses the Newtonian reference line, meaning that enhanced pressure-drop is derived. Stress peaks in planar contraction/expansion flows are much lower in magnitude and do not increase noticeable with elasticity. Enhanced *epd* has proven quite difficult to capture accurately through simulation; Szabo et al. [90] were the first to report enhanced *epd*, Binding et al. [17] also reported this phenomena. An original contribution from this study has been to track the pressure trend at the boundary wall, not only at the centreline. It is near the boundary-wall where the most important effects occur; some diffusion is observed at the centreline but is considerably reduced. A further contribution has been to look at an alternative calibration for pressure, $[p - p_{Newt}]$. This resembles the viscoelastic stress response and indicates the correlation between both magnitudes. Furthermore, this new calibration is useful to identify the necessary conditions to obtain enhanced *epd*. For this, the difference in dissipation rate (from [29,90]) between Boger and Newtonian fluids is compared. If the dissipation rate in the constriction zone (not in the whole geometry) is larger for the Boger fluid, then enhanced *epd* may result.

The Bautista-Manero (BM) models has been recently introduced to represent worm-like micellar systems. These systems may show highly viscoelastic properties, and in contact to oil, any viscoelastic nature can be eliminated, making them important fluids in extraction techniques. However, the original formulation of the BM model presents a deformation interval of unphysical (or undefined) extensional viscosity. This was corrected through the introduction of a modified Bautista-Manero

(MBM) model [22]. Results for the MBM model have been presented in 2D-planar channel and contraction flows. Pressure-drop for Poiseuille flow have been validated through two methods, providing essentially the same result; through a finite differences scheme and an analytical solution. The analytical solution was obtained following a procedure from Walters [100]. The trends followed by the Q vs. Δp curve are explained in terms of various zones of shear-rate covered.

The inclusion of the semi-linear version of the SXPP model may be considered, with the objective of further studies on the influence exerted through the extensional viscosity. To this end, it is possible to specify parameters for the semi-linear SXPP and linear PTT models with very weak hardening/softening properties. Hence, viscoelastic fluids can be derived with extensional viscosities close to constant, and on the other hand, both linear models can reproduce extremely high viscosity. The fluids with little variation in extensional viscosity *are not* expected to represent actual fluids. They may prove helpful in establishing the influence of elongational viscosity on results reported from numerical predictions.

APPENDIX I

SXPP model: additional detail

This appendix provides expressions for stress and related variables relevant to 2D-planar flow, proving useful under analysis when shear-rate ($\dot{\gamma}$) is known. As expressions for the constitutive model under prevailing Couette and Poiseuille flow-type conditions are the same, this functionality can be employed under both types of flow. The difference lies in $\dot{\gamma}$-profiles, linear for Couette and parabolic-type for Poiseuille flow. In addition, the fully-expanded equations for the Single eXtended Pom-Pom (SXPP) model in planar and axisymmetric flows are also included.

I.1 Non-dimensional stress relations for steady state for channel flow

The following equations are for the 2D-planar flow of the SXPP model (Cartesian frame-of-reference). They describe stress profiles for Couette and Poiseuille flow depending on the specification of shear-rate ($\dot{\gamma}$). One may adopt the following governing assumptions:

$$\begin{aligned} &v = u_y = 0, && \alpha = 0, \\ &\frac{\partial}{\partial t} = 0, && \frac{\partial}{\partial x} = 0 \ \text{except for } p. \end{aligned} \qquad \text{(AI.1)}$$

Then, stress profiles and related variables may be expressed in the form:

$$\tau_{xx} = -\left(\frac{1-\beta}{We}\right)\frac{f(\boldsymbol{\tau})-1}{f(\boldsymbol{\tau})} + 2We\frac{(1-\beta)}{f(\boldsymbol{\tau})^3}\dot{\gamma}^2, \qquad \tau_{xy} = \frac{1-\beta}{f(\boldsymbol{\tau})^2}\dot{\gamma},$$

$$\tau_{yy} = -\left(\frac{1-\beta}{We}\right)\frac{f(\boldsymbol{\tau})-1}{f(\boldsymbol{\tau})}, \qquad \tau_{zz} = -\left(\frac{1-\beta}{We}\right)\frac{f(\boldsymbol{\tau})-1}{f(\boldsymbol{\tau})},$$

$$N_1 = \tau_{xx} - \tau_{yy} = 2We\frac{(1-\beta)}{f(\boldsymbol{\tau})^3}\dot{\gamma}^2, \qquad N_2 = \tau_{yy} - \tau_{zz} = 0, \qquad \text{(AI.2)}$$

$$tr(\boldsymbol{\tau}) = -3\left(\frac{1-\beta}{We}\right)\frac{f(\boldsymbol{\tau})-1}{f(\boldsymbol{\tau})} + 2We\frac{(1-\beta)}{f(\boldsymbol{\tau})^3}\dot{\gamma}^2, \qquad \frac{\psi}{\psi_0} = \frac{1}{f(\boldsymbol{\tau})^3},$$

$$\lambda = \sqrt{\frac{1}{f(\boldsymbol{\tau})} + \frac{1}{3}\frac{We}{(1-\beta)}N_1}.$$

I.2 Fully expanded equations for the SXPP model in planar flows

1.- Polymeric stress τ_{xx} :

$$We\frac{\partial \tau_{xx}}{\partial t}+We\left(u\frac{\partial \tau_{xx}}{\partial x}+v\frac{\partial \tau_{xx}}{\partial y}+w\frac{\partial \tau_{xx}}{\partial z}\right)-2We\left(\tau_{xx}\frac{\partial u}{\partial x}+\tau_{xy}\frac{\partial u}{\partial y}+\tau_{xz}\frac{\partial u}{\partial z}\right)+\frac{\alpha We}{(1-\beta)}\left(\tau_{xx}{}^{2}+\tau_{xy}{}^{2}+\tau_{xz}{}^{2}\right)+$$
$$f(\boldsymbol{\tau})\tau_{xx}+\frac{(1-\beta)}{We}\left[f(\boldsymbol{\tau})-1\right]=2(1-\beta)\frac{\partial u}{\partial x}. \tag{AI.3}$$

2.- Polymeric stress τ_{xy} :

$$We\frac{\partial \tau_{xy}}{\partial t}+We\left(u\frac{\partial \tau_{xy}}{\partial x}+v\frac{\partial \tau_{xy}}{\partial y}+w\frac{\partial \tau_{xy}}{\partial z}\right)-We\left(\tau_{xy}\frac{\partial u}{\partial x}+\tau_{yy}\frac{\partial u}{\partial y}+\tau_{yz}\frac{\partial u}{\partial z}\right)-We\left(\tau_{xx}\frac{\partial v}{\partial x}+\tau_{xy}\frac{\partial v}{\partial y}+\tau_{xz}\frac{\partial v}{\partial z}\right)+$$
$$\frac{\alpha We}{(1-\beta)}\left(\tau_{xx}\tau_{xy}+\tau_{xy}\tau_{yy}+\tau_{xz}\tau_{yz}\right)+f(\boldsymbol{\tau})\tau_{xy}=(1-\beta)\left(\frac{\partial u}{\partial y}+\frac{\partial v}{\partial x}\right). \tag{AI.4}$$

3.- Polymeric stress τ_{yy} :

$$We\frac{\partial \tau_{yy}}{\partial t}+We\left(u\frac{\partial \tau_{yy}}{\partial x}+v\frac{\partial \tau_{yy}}{\partial y}+w\frac{\partial \tau_{yy}}{\partial z}\right)-2We\left(\tau_{xy}\frac{\partial v}{\partial x}+\tau_{yy}\frac{\partial v}{\partial y}+\tau_{yz}\frac{\partial v}{\partial z}\right)+$$
$$\frac{\alpha We}{(1-\beta)}\left(\tau_{xy}{}^{2}+\tau_{yy}{}^{2}+\tau_{yz}{}^{2}\right)+f(\boldsymbol{\tau})\tau_{yy}+\frac{(1-\beta)}{We}\left[f(\boldsymbol{\tau})-1\right]=2(1-\beta)\frac{\partial v}{\partial y}. \tag{AI.5}$$

4.- Polymeric stress τ_{zz}:

$$We\frac{\partial \tau_{zz}}{\partial t}+We\left(u\frac{\partial \tau_{zz}}{\partial x}+v\frac{\partial \tau_{zz}}{\partial y}+w\frac{\partial \tau_{zz}}{\partial z}\right)-We\left(\tau_{xz}\frac{\partial w}{\partial x}+\tau_{yz}\frac{\partial w}{\partial y}+\tau_{zz}\frac{\partial w}{\partial z}\right)-We\left(\tau_{zx}\frac{\partial w}{\partial x}+\tau_{zy}\frac{\partial w}{\partial y}+\tau_{zz}\frac{\partial w}{\partial z}\right)+$$
$$\frac{\alpha We}{(1-\beta)}\left(\tau_{xz}\tau_{zx}+\tau_{yz}\tau_{zy}+\tau_{zz}{}^{2}\right)+f(\boldsymbol{\tau})\tau_{zz}+\frac{(1-\beta)}{We}\left[f(\boldsymbol{\tau})-1\right]=2(1-\beta)\frac{\partial w}{\partial z}. \quad \text{(AI.6)}$$

5.- Extra function:

$$f(\boldsymbol{\tau})=2\frac{1}{\varepsilon}\left(1-\frac{1}{\lambda}\right)e^{\nu(\lambda-1)}+\frac{1}{\lambda^{2}}\left(1-\frac{1}{3}\alpha\frac{We^{2}}{(1-\beta)^{2}}\left(\tau_{xx}{}^{2}+\tau_{yy}{}^{2}+\tau_{zz}{}^{2}+2\tau_{xy}{}^{2}+2\tau_{xz}{}^{2}+2\tau_{yz}{}^{2}\right)\right). \quad \text{(AI.7)}$$

I.3 Fully expanded equations for the SXPP model in axisymmetric flows

1.- Component τ_{rr}:

$$We\left[\frac{\partial}{\partial t}\tau_{rr}+u_{r}\frac{\partial \tau_{rr}}{\partial r}+\frac{u_{\theta}}{r}\frac{\partial \tau_{rr}}{\partial \theta}+u_{z}\frac{\partial \tau_{rr}}{\partial z}-2\frac{u_{\theta}}{r}\tau_{r\theta}-2\tau_{rr}\frac{\partial u_{r}}{\partial r}-2\tau_{r\theta}\left(\frac{1}{r}\frac{\partial u_{r}}{\partial \theta}-\frac{u_{\theta}}{r}\right)-2\tau_{rz}\frac{\partial u_{r}}{\partial z}\right]+$$
$$\frac{\alpha We}{(1-\beta)}\left[\tau_{rr}{}^{2}+\tau_{r\theta}{}^{2}+\tau_{rz}{}^{2}\right]+f(\boldsymbol{\tau})\tau_{rr}+\frac{(1-\beta)}{We}\left[f(\boldsymbol{\tau})-1\right]=2(1-\beta)\frac{\partial u_{r}}{\partial r}. \quad \text{(AI.8)}$$

2.- Component $\tau_{\theta\theta}$:

$$We\left[\frac{\partial}{\partial t}\tau_{\theta\theta}+u_r\frac{\partial\tau_{\theta\theta}}{\partial r}+\frac{u_\theta}{r}\frac{\partial\tau_{\theta\theta}}{\partial\theta}+u_z\frac{\partial\tau_{\theta\theta}}{\partial z}+2\frac{u_\theta}{r}\tau_{r\theta}-\left(2\tau_{r\theta}\frac{\partial u_\theta}{\partial r}+2\tau_{\theta\theta}\left[\frac{1}{r}\frac{\partial u_\theta}{\partial\theta}+\frac{u_r}{r}\right]+2\tau_{\theta z}\frac{\partial u_\theta}{\partial z}\right)\right]+$$
$$\frac{\alpha We}{(1-\beta)}\left(\tau_{r\theta}^{\ 2}+\tau_{\theta\theta}^{\ 2}+\tau_{\theta z}^{\ 2}\right)+f(\boldsymbol{\tau})\tau_{\theta\theta}+\frac{(1-\beta)}{We}\left[f(\boldsymbol{\tau})-1\right]=2(1-\beta)\left(\frac{1}{r}\frac{\partial u_\theta}{\partial\theta}+\frac{u_r}{r}\right). \qquad \text{(AI.9)}$$

3.- Component τ_{zz}:

$$We\left[\frac{\partial}{\partial t}\tau_{zz}+u_r\frac{\partial\tau_{zz}}{\partial r}+\frac{u_\theta}{r}\frac{\partial\tau_{zz}}{\partial\theta}+u_z\frac{\partial\tau_{zz}}{\partial z}-\left(2\tau_{rz}\frac{\partial u_z}{\partial r}+2\tau_{\theta z}\left[\frac{1}{r}\frac{\partial u_z}{\partial\theta}\right]+2\tau_{zz}\frac{\partial u_z}{\partial z}\right)\right]+$$
$$\frac{\alpha We}{(1-\beta)}\left(\tau_{rz}^{\ 2}+\tau_{z\theta}^{\ 2}+\tau_{zz}^{\ 2}\right)+f(\boldsymbol{\tau})\tau_{zz}+\frac{(1-\beta)}{We}\left[f(\boldsymbol{\tau})-1\right]=2(1-\beta)\frac{\partial u_z}{\partial z}. \qquad \text{(AI.10)}$$

4.- Component $\tau_{r\theta}$:

$$\begin{aligned}
&We\left[\frac{\partial}{\partial t}\tau_{r\theta}+u_r\frac{\partial\tau_{r\theta}}{\partial r}+\frac{u_\theta}{r}\frac{\partial\tau_{r\theta}}{\partial\theta}+u_z\frac{\partial\tau_{r\theta}}{\partial z}+\frac{u_\theta}{r}\left(\tau_{rr}-\tau_{\theta\theta}\right)-\left(\tau_{rr}\frac{\partial u_\theta}{\partial r}+\tau_{r\theta}\left[\frac{1}{r}\frac{\partial u_\theta}{\partial\theta}+\frac{u_r}{r}+\frac{\partial u_r}{\partial r}\right]+\right.\right.\\
&\left.\left.\tau_{\theta\theta}\left[\frac{1}{r}\frac{\partial u_r}{\partial\theta}-\frac{u_\theta}{r}\right]+\tau_{rz}\frac{\partial u_\theta}{\partial z}+\tau_{z\theta}\frac{\partial u_r}{\partial z}\right)\right]+\frac{\alpha We}{(1-\beta)}\left(\tau_{rr}\tau_{r\theta}+\tau_{r\theta}\tau_{\theta\theta}+\tau_{rz}\tau_{z\theta}\right)+\\
&f(\boldsymbol{\tau})\tau_{r\theta}=(1-\beta)\left(\frac{\partial u_\theta}{\partial r}+\frac{1}{r}\frac{\partial u_r}{\partial\theta}-\frac{u_\theta}{r}\right).
\end{aligned}\tag{AI.11}$$

5.- Component $\tau_{\theta z}$:

$$\begin{aligned}
&We\left[\frac{\partial}{\partial t}\tau_{\theta z}+u_r\frac{\partial\tau_{\theta z}}{\partial r}+\frac{u_\theta}{r}\frac{\partial\tau_{\theta z}}{\partial\theta}+u_z\frac{\partial\tau_{\theta z}}{\partial z}+\frac{u_\theta}{r}\tau_{rz}-\left(\tau_{rz}\frac{\partial u_\theta}{\partial r}+\tau_{\theta z}\left[\frac{1}{r}\frac{\partial u_\theta}{\partial\theta}+\frac{u_r}{r}\right]+\tau_{zz}\frac{\partial u_\theta}{\partial z}\right)-\right.\\
&\left.\left(\tau_{\theta r}\frac{\partial u_z}{\partial r}+\tau_{\theta\theta}\left[\frac{1}{r}\frac{\partial u_z}{\partial\theta}\right]+\tau_{\theta z}\frac{\partial u_z}{\partial z}\right)\right]+\frac{\alpha We}{(1-\beta)}\left(\tau_{rz}\tau_{\theta r}+\tau_{\theta z}\tau_{\theta\theta}+\tau_{zz}\tau_{\theta z}\right)+\\
&f(\boldsymbol{\tau})\tau_{\theta z}=(1-\beta)\left(\frac{1}{r}\frac{\partial u_z}{\partial\theta}+\frac{\partial u_\theta}{\partial z}\right).
\end{aligned}\tag{AI.12}$$

6.- Component τ_{rz} :

$$We\left[\frac{\partial}{\partial t}\tau_{rz}+u_r\frac{\partial \tau_{rz}}{\partial r}+\frac{u_\theta}{r}\frac{\partial \tau_{rz}}{\partial \theta}+u_z\frac{\partial \tau_{rz}}{\partial z}-\frac{u_\theta}{r}\tau_{\theta z}-\left(\tau_{rz}\frac{\partial u_r}{\partial r}+\tau_{rz}\frac{\partial u_z}{\partial z}+\tau_{\theta z}\left[\frac{1}{r}\frac{\partial u_r}{\partial \theta}-\frac{u_\theta}{r}\right]+\tau_{r\theta}\left[\frac{1}{r}\frac{\partial u_z}{\partial \theta}\right]+\right.\right.$$
$$\left.\left.\tau_{rr}\frac{\partial u_z}{\partial r}+\tau_{zz}\frac{\partial u_r}{\partial z}\right)\right]+\frac{\alpha We}{(1-\beta)}\left(\tau_{rr}\tau_{rz}+\tau_{r\theta}\tau_{\theta z}+\tau_{rz}\tau_{zz}\right)+f(\boldsymbol{\tau})\tau_{rz}=(1-\beta)\left(\frac{\partial u_z}{\partial r}+\frac{\partial u_r}{\partial z}\right). \quad \text{(AI.13)}$$

7.- Extra function

$$f(\boldsymbol{\tau})=2\frac{1}{\varepsilon}\left(1-\frac{1}{\lambda}\right)e^{\nu(\lambda-1)}+\frac{1}{\lambda^2}\left(1-\frac{1}{3}\alpha\frac{We^2}{(1-\beta)^2}\left[\tau_{rr}{}^2+\tau_{\theta\theta}{}^2+\tau_{zz}{}^2+2\tau_{r\theta}{}^2+2\tau_{rz}{}^2+2\tau_{z\theta}{}^2\right]\right). \quad \text{(AI.14)}$$

8.- Stretch:

$$\lambda=\sqrt{1+\frac{1}{3}\frac{We}{(1-\beta)}\left[\tau_{rr}+\tau_{\theta\theta}+\tau_{zz}\right]}. \quad \text{(AI.15)}$$

APPENDIX II

Streamlines

Some of the simulation results for contraction flows in this study have been presented graphically by streamline plots. Streamlines coincide with the trajectory followed by fluid elements for steady flows. For an incompressible flow, in cartesian coordinates, continuity equation is,

$$\frac{\partial u}{\partial x}+\frac{\partial v}{\partial y}=0. \tag{AII.1}$$

Defining the "stream function" as

$$u=\frac{\partial \psi}{\partial y}, \qquad \text{and} \qquad v=-\frac{\partial \psi}{\partial x}. \tag{AII.2}$$

Obtaining the only non-zero component of the vorticity vector in 2D-flows [65],

$$\frac{\partial^2 \psi}{\partial x^2}+\frac{\partial^2 \psi}{\partial y^2}=f. \tag{AII.3}$$

Solution of equation (AII.3) gives the stream function at a position (x, y). This function ψ has the property of being constant along a streamline. It can be calculated by a finite element procedure. In addition, vortex intensity (ψ_{sal}) is the maximum ψ-value observed inside the vortex region, and it is related to the ratio of flowrates between the recirculation region and flowrate through the contraction (see Purnode and Crochet [83]).

List of Figures

2.1. Schematic representation of simple shear flow. 8

2.2. Schematic representation of uniaxial flow. 10

2.3. Idealized Pom-Pom molecule. 18

2.4. Singularities in shear viscosity for SXPP and mXPP models: $\beta = 0$, $\varepsilon = 1/3$, $q = 20$, $\alpha = 0.3$. 22

2.5. Shear and planar-extension response varying q; $\beta = 1/9$, $\varepsilon = 1/3$, $\alpha = 0.15$. 26

2.6. Transient shear and planar-extension response varying q; $\beta = 1/9$, $\varepsilon = 1/3$, $\alpha = 0.15$. 28

2. 7. Influence of β and ε on SXPP material functions: $\beta = 1/9$, $\varepsilon = 1/3$, $q = 2$, $\alpha = 0$. 30

3.1. Element grid; a) *fe* parent triangle and *fv* subcells, b) median-dual-cell configuration. 43

4.1. Channel flow; SLFV vs. *fe/fv*, *Re* = 1, $\beta = 1/9$, $\varepsilon = 1/3$, $q = 2$, $\alpha = 0.15$. 52

4.2. Channel flow; SLFV vs. *fe/fv*, *Re* = 1, *We* = 3, $\varepsilon = 1/3$, $q = 2$, $\alpha = 0.15$. 53

4.3. Channel flow; SLFV vs. *fe/fv*, *Re* = 1, *We* = 3, $\beta = 1/9$, $q = 2$, $\alpha = 0.15$. 55

4.4. Channel flow; SLFV vs. *fe/fv*, *Re* = 1, *We* = 3, $\beta = 1/9$, $\varepsilon = 1/3$, $\alpha = 0.15$. 56

4.5. Channel flow; SLFV vs. *fe/fv*, *Re* = 1, *We* = 3, $\beta = 1/9$, $\varepsilon = 1/3$, $q = 2$. 57

4.6. Polymeric stress τ_{zz} profiles: α variation; *We* = 3, $\beta = 1/9$, $\varepsilon = 1/3$, $q = 2$. 58

4.7. Dependence of pressure gradient on elasticity. $Re = 1$, $\beta = 1/9$, $\varepsilon = 1/3$, $q = 2$, $\alpha = 0.15$. 59

4.8. Shear-rate in Poiseuille flow: $We = 3$, $\beta = 1/9$, $\varepsilon = 1/3$, $q = 2$, $\alpha = 0.15$. 60

5.1. Schematic 4:1 contraction geometry: sharp-corner. 68

5.2. *fe/fv* mesh (m3) and SLFV (M4), in contraction zone. 70

5.3. Symmetry line flow results at $Re = 0$: $\beta = 1/9$, $\varepsilon = 1/3$, $q = 2$, $\alpha = 0.15$; a) $We = 0.1$, b) $We = 10$. 72

5.4. Stream function with increasing *We:* $\beta = 1/9$, $\varepsilon = 1/3$, $q = 2$, $\alpha = 0.15$; $Re = 0$ and 1. 73

5.5. Salient-corner vortex trends with increasing *We:* $\beta = 1/9$, $\varepsilon = 1/3$, $q = 2$, $\alpha = 0.15$, $Re = 0$ and 1; a) cell-size, b) intensity. 74

5.6. Backbone stretch λ-fields, increasing *We*: $\beta = 1/9$, $\varepsilon = 1/3$, $q = 2$, $\alpha = 0.15$, $Re = 0$ and $Re = 1$. 78

5.7. Normal stress τ_{xx}-fields, increasing *We*: $\beta = 1/9$, $\varepsilon = 1/3$, $q = 2$, $\alpha = 0.15$; $Re = 0$ and $Re = 1$. 79

5.8. Shear stress τ_{xy}-fields, increasing *We*: $\beta = 1/9$, $\varepsilon = 1/3$, $q = 2$, $\alpha = 0.15$; $Re = 0$ and $Re = 1$. 80

5.9. First normal stress difference (polymeric): N_1-fields, increasing *We*: $\beta = 1/9$, $\varepsilon = 1/3$, $q = 2$, $\alpha = 0.15$; $Re = 0$ and $Re = 1$. 81

5.10. Second normal stress difference N_2-fields, increasing *We*: $\beta = 1/9$, $\varepsilon = 1/3$, $q = 2$, $\alpha = 0.15$; $Re = 0$ and $Re = 1$. 82

5.11. Rate of strain d_{xx}-fields, increasing *We*: $\beta = 1/9$, $\varepsilon = 1/3$, $q = 2$, $\alpha = 0.15$; $Re = 0$ and $Re = 1$. 83

5.12. Rate of strain d_{xy}-fields, increasing *We*: $\beta = 1/9$, $\varepsilon = 1/3$, $q = 2$, $\alpha = 0.15$; $Re = 0$ and $Re = 1$. 84

5.13. Sample points used in the 4:1 contraction domain. 85

5.14. Pressure-drop vs. *We*: $\beta = 1/9$, $\varepsilon = 1/3$, $q = 2$, $\alpha = 0.15$; SLFV and *fe/fv* schemes, $Re = 0$ and 1. 86

5.15. SXPP vs. λ^2XPP profiles in planar channel flow with the *fe/fv* scheme: $We = 10$, $Re = 1$, $\beta = 1/9$, $\varepsilon = 1/3$, $q = 2$, $\alpha = 0.15$; a) velocity, b) stretch. 87

5.16. SXPP vs. λ^2XPP centreline results in planar 4:1 sharp contraction flow with the *fe/fv* scheme: $We = 10$, $Re = 0$, $\beta = 1/9$, $\varepsilon = 1/3$, $q = 5$, $\alpha = 0.15$; a) velocity, b) stretch. 88

6.1. Schematic 4:1 contraction geometry: rounded-corner. 94

6.2. Unstructured *fe*-triangular meshing in contraction zone. 95

6.3. Salient-corner vortex, increasing *We*: $Re = 0$, $\beta = 1/9$, $\varepsilon = 1/3$, $\alpha = 0.15$; $q = 2, 5, 10, 15$, a) cell-size, b) intensity. 99

6.4. Stream function and vortex data (L, X, $\psi_{sal} \times [-10^4]$), increasing *We*: $Re = 0$, $\beta = 1/9$, $\varepsilon = 1/3$, $\alpha = 0.15$; $q = 2$ and 5. 100

6.5. Stream function and vortex data (L, X, $\psi_{sal} \times [-10^4]$), increasing *We*: $Re = 0$, $\beta = 1/9$, $\varepsilon = 1/3$, $\alpha = 0.15$; $q = 10$ and 15. 101

6.6. Rate-of-strain d_{xx} and d_{xy} fields, $We = 10$: $Re = 0$, $\beta = 1/9$, $\varepsilon = 1/3$, $\alpha = 0.15$; increasing q. 103

6.7. Rate-of-strain (dxx and Γ) fields, $We = 10$: $Re = 0$, $\beta = 1/9$, $\varepsilon = 1/3$, $\alpha = 0.15$; $q = 2$ and 5. 104

6.8. Profiles along plane of symmetry, $We = 10$: $Re = 0$, $\beta = 1/9$, $\varepsilon = 1/3$, $\alpha = 0.15$; increasing q. 106

6.9. Profiles along downstream wall, $y = 3$, $We = 10$: $Re = 0$, $\beta = 1/9$, $\varepsilon = 1/3$, $\alpha = 0.15$, increasing q. 107

6.10. Stretch and firs normal stress difference (polymeric) fields, $We = 10$: $Re = 0$, $\beta = 1/9$, $\varepsilon = 1/3$, $\alpha = 0.15$; increasing q. 108

6.11. Stretch and firs normal stress difference (polymeric) fields, $We = 25$: $Re = 0$, $\beta = 1/9$, $\varepsilon = 1/3$, $\alpha = 0.15$; $q = 2$ and 5. 110

6.12. Normal stress (τ_{yy}) and shear stress fields, $We = 10$: $Re = 0$, $\beta = 1/9$, $\varepsilon = 1/3$, $\alpha = 0.15$; increasing q. 112

6.13. Normalised pressure-drop vs. *We*: $Re = 0$, $\beta = 1/9$, $\varepsilon = 1/3$, $\alpha = 0.15$; $q = 2, 5, 10, 15$. 113

6.14. Rheological properties of SXPP model, variation in α, $\beta = 1/9$, $\varepsilon = 1/3$ and $q = 15$. 114

6.15. Profiles along downstream wall, $y = 3$, increasing α: $Re = 0$, $\beta = 1/9$, $\varepsilon = 1/3$; $q = 15$, $We = 10$. 115

6.16. Rheological properties of SXPP and EPTT models: variation in q, ε and ε_{PTT}; $\beta = 1/9$, $\alpha = 0.15$. 118

6.17. Streamlines and vortex data (L, X, $\psi_{sal} \times [-10^4]$), Fluids Ia and II, strong hardening. 121

6.18. Streamlines and vortex data (L, X, $\psi_{sal} \times [-10^4]]$), Fluids III and IV, low hardening. 122

6.19. Salient-corner vortex-intensity and cell-size, increasing *We*; strong and moderate hardening fluids. 123

6.20. First and second normal stress difference (N_1, N_2) fields: $\alpha = 0.05$ (Fluid-I$_b$) and 0.15 (Fluid-I$_a$); $We = 8$. 125

7.1. Schematic diagram for a) 4:1:4 contraction/expansion, b) 4:1 contraction. 135

7.2. Zoomed mesh sections of 4:1:4 contraction/expansion and 4:1 contraction; a) coarse, b) medium, c) refined. 135

7.3. Pressure-drop (*epd*) vs. *We* (Oldroyd-B): $\beta = 0.9$ and 0.99, 4:1:4 contraction/expansion; a) axisymmetric, b) planar. 139

7.4. Pressure-drop (*epd*) vs. *We* (Oldroyd-B): $\beta = 0.9$ and 0.99, 4:1 contraction; a) axisymmetric, b) planar. 141

7.5. Pressure field plots around the contraction/expansion (Oldroyd-B): $\beta = 0.99$, $We = 2$ and 3, 4:1:4 axisymmetric, coarse, medium and refined meshes. 142

7.6. Pressure field plots around the contraction/expansion: increasing *We* (Oldroyd-B): $\beta = 0.9$, axisymmetric vs. planar. 143

7.7. Pressure profile along *centreline*: increasing *We* (Oldroyd-B): $\beta = 0.9$. 4:1:4 axisymmetric. 144

7.8. Pressure profile along *wall*: increasing *We* (Oldroyd-B): $\beta = 0.9$, 4:1:4 axisymmetric. 145

7.9. Pressure profile *along wall of constriction* zone (Oldroyd-B): $\beta = 0.9$, 4:1:4, axisymmetric vs. planar. 146

7.10. Polymeric first normal stress difference, N_1 fields (Oldroyd-B): $\beta = 0.9$, 4:1:4, axisymmetric vs. planar. 147

7.11. τ_{11} field contours (Oldroyd-B): $\beta = 0.9$, 4:1:4, axisymmetric vs. planar. 148

7.12. τ_{22} field contours (Oldroyd-B): $\beta = 0.9$, 4:1:4, axisymmetric vs. planar. 149

7.13. τ_{12} field contours (Oldroyd-B): $\beta = 0.9$, 4:1:4, axisymmetric vs. planar. 150

7.14. d_{11} field contours (Oldroyd-B): $\beta = 0.9$, 4:1:4, axisymmetric vs. planar. 151

7.15. Σ and Γ field contours (Oldroyd-B): $\beta = 0.9$, 4:1:4 axisymmetric. 152

7.16. Rheological properties: Oldroyd-B, LPTT, EPTT and SXPP. 154

7.17. Pressure profile along *wall* increasing *We* (Oldroyd-B): $\beta = 0.99$, 4:1:4 axisymmetric. 155

7.18. τ_{11}, d_{11} field contours (Oldroyd-B): $\beta = 0.99$, 4:1:4, axisymmetric. 156

7.19. Pressure gradient at centreline (Oldroyd-B): 4:1:4 axisymmetric vs. planar; a) $\beta = 1/9$, b) $\beta = 0.9$, c) $\beta = 0.99$. 158

7.20. Pressure profile along *wall* increasing *We* (Oldroyd-B): $\beta = 0.9$, 4:1 axisymmetric. 160

7.21. Pressure $[p\text{-}p_{Newt}]$ and stress τ_{11} profiles along *wall* increasing *We* (Oldroyd-B): $\beta = 0.9$, 4:1 and 4:1:4 axisymmetric. 161

7.22. Pressure $[p\text{-}p_{Newt}]$ and stress τ_{11} profiles along *wall* increasing *We* (Oldroyd-B): $\beta = 0.9$, 4:1:4 axisymmetric and planar. 163

7.23. Stream function ($-\psi \times 10^3$) increasing *We* (Oldroyd-B): 4:1:4 axisymmetric; a) $\beta = 0.99$, b) $\beta = 1/9$. 164

7.24. Stream function ($-\psi \times 10^3$) increasing *We* (Oldroyd-B): β=0.9, axisymmetric; a) 4:1:4, b) 4:1. 164

7.25. Pressure-drop (*epd*) vs. *We*: 4 :1 :4 axisymmetric; a) β-variation, b) $\beta = 0.99$. 167
7.26. Stress profile along *wall* increasing *We*: $\beta = 0.9$ and 0.99; 4:1:4 axisymmetric. 170
7.27. Pressure $[p\text{-}p_{Newt}]$ profiles along *wall* increasing *We* (Oldroyd-B): 4:1:4 axisymmetric; a) Schematic representation, b) $\beta = 1/9$, c) $\beta = 0.9$, d) $\beta = 0.99$. 172
7.28. Pressure-drop (*epd*) at different sampling-points and *elasticity levels*: $\beta = 0.9$, 4:1:4 axisymmetric. 175
7.29. Pressure-drop (*epd*) vs. *We* (Oldroyd-B): 4:1:4 axisymmetric; scheme variation. 179

8.1. Rheometrical functions for MBM and EPTT models. 187
8.2. Streamlines for MBM model in 4:1 contraction flow. 189
8.3. Shear and uniaxial response varying η_0: $G_0 = 1$, $k/\eta_\infty = 0.01$, $\mu_s = 1/9$, $\lambda = 0.28$. 190
8.4. Shear and uniaxial response varying k/η_∞: $G_0 = 1$, $\eta_0 = 8/9$, $\mu_s = 1/9$, $\lambda = 0.28$. 191
8.5. Shear and uniaxial response varying λ: $G_0 = 1$, $\eta_0 = 8/9$, $k/\eta_\infty = 0.01$, $\mu_s = 1/9$. 192
8.6. Schematic: cross-stream division of channel problem domain. 192
8.7. Solutions for different number of degrees of freedom. 195
8.8. Q vs. Δp curves for channels gaps (H). 196
8.9. Evolution of deformation-rate and velocity profiles as Δp increases. 197
8.10. Pressure vs. length curves at fixed flowrate. 203
8.11. Transient results for the channel flow. 204

List of Tables

2.1. Material function expressions of some common models 29

2.2. Influence of increasing non-dimensional numbers in shear and extensional viscosity 29

5.1. Mesh characteristics parameters, *fe/fv* and SLFV schemes 69

5.2. Mesh convergence: salient-corner vortex cell size (X), $Re = 0$ 75

5.3. Mesh convergence: salient-corner vortex cell size (X), $Re = 1$ 76

5.4. Values of stretch (λ) and first normal stress difference (N_1) at sample points, Re=0 (contraction point at $x = 0.0$, $y = 3.0$) 85

6.1. Mesh characteristics parameters 96

6.2. Mesh convergence for salient-corner vortex cell-size (X): $0.1 \leq We \leq 25$, $q = 5$ 105

6.3. SXPP and corresponding EPTT parameters; $\beta = 1/9$ 117

7.1. Mesh characteristics 136

7.2. Fluid parameters for the $\beta = 0.99$ solvent fraction 168

8.1. SF1 parameters 195

8.2. SF2 parameters 203

List of Publications

1.- J.P. Aguayo, P.M. Phillips, T.N. Phillips, B.A. Snigerev, H.R. Tamaddon-Jahromi, M.F. Webster, The Numerical Prediction of Viscoelastic Flows using the Pom-Pom Models and High-Order Finite Volume Schemes. In: J.W. Lee, S.J. Lee (Eds.), The XIVth International Congress on Rheology, The Korean Society of Rheology, Seoul, Korea, 2004, pp. CR37-31, CR37-33.

2.- M. Aboubacar, J.P. Aguayo, P.M. Phillips, T.N. Phillips, H.R. Tamaddon-Jahromi, B.A. Snigerev, M.F. Webster, Modelling pom-pom type models with high-order finite volume schemes, *Journal of Non-Newtonian Fluid Mechanics* **126** (2005) 207-220.

3.- J.P. Aguayo, H.R. Tamaddon-Jahromi, M.F. Webster, Extensional response of the pom-pom model through planar contraction flows for branched polymer melts, *Journal of Non-Newtonian Fluid Mechanics* **134** (2006) 105-126.

4.- J.P. Aguayo, P.M. Phillips, T.N. Phillips, H.R. Tamaddon-Jahromi, B.A. Snigerev, M.F. Webster, The Numerical Prediction of Planar Viscoelastic Contraction Flows using the Pom-Pom Model and Higher-Order Finite Volume Schemes - Part II, *Report No.*: **CSR 1-2006**: University of Wales, Swansea. Accepted for publication in the *Journal of Computational Physics.*

5.- J.P. Aguayo, H.R. Tamaddon-Jahromi, M.F. Webster, Excess pressure-drop estimation in contraction and expansion flows for constant viscosity, strain-hardening fluids, *Report No.*: **CSR 4-2006**: University of Wales, Swansea. Submitted to the *Journal on non-Newtonian Fluid Mechanics.*

References

[1] M. Aboubacar, J.P. Aguayo, P.M. Phillips, T.N. Phillips, H.R. Tamaddon-Jahromi, B.A. Snigerev, M.F. Webster, Modelling pom-pom type models with high-order finite volume schemes, *Journal of Non-Newtonian Fluid Mechanics* **126** (2005) 207-220.

[2] M. Aboubacar, H. Matallah, H.R. Tamaddon-Jahromi, M.F. Webster, Numerical prediction of extensional flows in contraction geometries: hybrid finite volume/element method, *Journal of Non-Newtonian Fluid Mechanics* **104** (2002) 125-164.

[3] M. Aboubacar, H. Matallah, M.F. Webster, Highly elastic solutions for Oldroyd-B and Phan-Thien/Tanner fluids with a finite volume/element method: planar contraction flows, *Journal of Non-Newtonian Fluid Mechanics* **103** (2002) 65-103.

[4] M. Aboubacar, T.N. Phillips, H.R. Tamaddon-Jahromi, B.A. Snigerev, M.F. Webster, High-order finite volume methods for viscoelastic flow problems, *Journal of Computational Physics* **199** (2004) 16-40.

[5] M. Aboubacar, T.N. Phillips, H.R. Tamaddon-Jahromi, M.F. Webster, A.J. Williams, Numerical Simulation of Contraction Flows for Boger Fluids using Finite Volume Methods. In: H. Münstedt, J. Kaschta, A. Merten (Eds.), 6th European Conference of Rheology, Erlangen, Germany, 2002, pp. 279-280.

[6] M. Aboubacar, M.F. Webster, A cell-vertex finite volume/element method on triangles for abrupt contraction viscoelastic flows, *Journal of Non-Newtonian Fluid Mechanics* **98** (2001) 83-106.

[7] M. Aboubacar, M.F. Webster, Development of an optimal hybrid finite volume/element method for viscoelastic flows, *International Journal for Numerical Methods in Fluids* **41** (2003) 1147-1172.

[8] M.A. Alves, P.J. Oliveira, F.T. Pinho, Benchmark solutions for the flow of Oldroyd-B and PTT fluids in planar contractions, *Journal of Non-Newtonian Fluid Mechanics* **110** (2003) 45-75.

[9] M.A. Alves, P.J. Oliveira, F.T. Pinho, On the effect of contraction ratio in viscoelastic flow through abrupt contractions, *Journal of Non-Newtonian Fluid Mechanics* **122** (2004) 117-130.

[10] M.A. Alves, F.T. Pinho, P.J. Oliveira, Effect of a high-resolution differencing scheme on finite-volume predictions of viscoelastic flows, *Journal of Non-Newtonian Fluid Mechanics* **93** (2000) 287-314.

[11] F.P.T. Baaijens, Mixed finite element methods for viscoelastic flow analysis: a review, *Journal of Non-Newtonian Fluid Mechanics* **79** (1998) 361-385.

[12] A. Baloch, P. Townsend, M.F. Webster, On the simulation of highly elastic complex flows, *Journal of Non-Newtonian Fluid Mechanics* **59** (1995) 111-128.

[13] H.A. Barnes, J.F. Hutton, K. Walters, *An Introduction to Rheology*, Elsevier, (1989).

[14] D. Binding, An approximate analysis for contraction and converging flows, *Journal of Non-Newtonian Fluid Mechanics* **27** (1988) 173-189.

[15] D. Binding, Further considerations of axisymmetric contraction flows, *Journal of Non-Newtonian Fluid Mechanics* **41** (1991) 27-42.

[16] D. Binding, K. Walters, On the use of flow through a contraction in estimating the extensional viscosity of mobile polymer solutions, *Journal of Non-Newtonian Fluid Mechanics* **30** (1988) 233-250.

[17] D.M. Binding, P.M. Phillips, T.N. Phillips, Contraction /expansion flows: The pressure drop and related issues, *Journal of Non-Newtonian Fluid Mechanics, Accepted Manuscript* (2005).

[18] R.B. Bird, R.C. Armstrong, O. Hassager, *Dynamics of Polymeric Liquies, Volume 1: Fluid Mechanics*, John Wiles & Sons, Inc., (1987).

[19] G.B. Bishko, O.G. Harlen, T.C.B. McLeish, T.M. Nicholson, Numerical simulation of the transient flow of branched polymer melts through a planar contraction using the 'pom-pom' model, *Journal of Non-Newtonian Fluid Mechanics* **82** (1999) 255-273.

[20] R.J. Blackwell, T.C.B. McLeish, O.G. Harlen, Molecular drag-strain coupling in branched polymer melts, *Journal of Rheology* **44** (2000) 121-136.

[21] E.S. Boek, A. Jusufi, H. Löwen, G.C. Maitland, Molecular design of responsive fluids: molecular dynamics studies of viscoelastic surfactant solutions, *Journal of Physics: Condensed Matter* **14** (2002) 9413-9430.

[22] E.S. Boek, J.T. Padding, V.J. Anderson, P.M.J. Tardy, J.P. Crawshaw, J.R.A. Pearson, Constitutive equations for extensional flow of wormlike micelles: stability analysis of the Bautista-Manero model, *Journal of Non-Newtonian Fluid Mechanics* **126** (2005) 39-46.

[23] A.C.B. Bogaerds, A.M. Grillet, G.W.M. Peters, F.P.T. Baaijens, Stability analysis of polymer shear flows using the eXtended Pom-Pom constitutive equations, *Journal of Non-Newtonian Fluid Mechanics* **108** (2002) 187-208.

[24] D.V. Boger, Short communication: A highly elastic constant-viscosity fluid, *Journal of Non-Newtonian Fluid Mechanics* **3** (1977) 87-91.

[25] D.V. Boger, Viscoelastic Flows Through Contractions, *Annual Review of Fluid Mechanics* **19** (1987) 157-182.

[26] D.V. Boger, D.U. Hur, R.J. Binnington, Further observations of elastic effects in tubular entry flows, *Journal of Non-Newtonian Fluid Mechanics* **20** (1986) 31-49.

[27] J.A. Byars, R.J. Binnington, D.V. Boger, Entry flow and constitutive modelling of fluid S1, *Journal of Non-Newtonian Fluid Mechanics* **72** (1997) 219-235.

[28] E.O.A. Carew, P. Townsend, M.F. Webster, A Taylor-Petrov-Galerkin algorithm for viscoelastic flow, *Journal of Non-Newtonian Fluid Mechanics* **50** (1993) 253-287.

[29] U. Cartalos, J.M. Piau, Creeping flow regimes of low concentration polymer solutions in thick solvents through an orifice die, *Journal of Non-Newtonian Fluid Mechanics* **45** (1992) 231-285.

[30] M.S. Chandio, Numerical Study of Model, Industrial and Free-Surface Flows. In: Computer Science, Vol. Philosophiae Doctor, University of Wales, Swansea, Swansea, U.K., 2002, p. 208.

[31] M.S. Chandio, K.S. Sujatha, M.F. Webster, Consistent hybrid finite volume/element formulations: model and complex viscoelastic flows, *International Journal for Numerical Methods in Fluids* **45** (2004) 945-971.

[32] M.D. Chilcott, J.M. Rallison, Creeping flow of dilute polymer solutions past cylinders and spheres, *Journal of Non-Newtonian Fluid Mechanics* **29** (1988) 381-432.

[33] A.J. Chorin, Numerical solution of the Navier-Stokes equations, *Mathematics of Computation* **22** (1986) 745-762.

[34] D.C.-H. Cheng, F. Evans, Phenomenological characterization of the rheological behaviour of inelastic reversible thixotropic and antithixotropic fluids, *British Journal of Applied Physics* **16** (1965) 1599-1617.

[35] T.J. Chung, *Finite Element Analysis in Fluid Dynamics*, McGraw-Hill, (1978).

[36] N. Clemeur, R.P.G. Rutgers, B. Debbaut, Numerical simulation of abrupt contraction flows using the Double Convected Pom-Pom model, *Journal of Non-Newtonian Fluid Mechanics* **117** (2004) 193-209.

[37] N. Clemeur, R.P.G. Rutgers, B. Debbaut, On the evaluation of somedifferential formulations for the pom-pom constitutive model, *Rheological Acta* **42** (2003) 217-231.

[38] F.N. Cogswell, CONVERGING FLOW AND STRETCHING FLOW: A COMPILATION, *Journal of Non-Newtonian Fluid Mechanics* **4** (1978) 23-38.

[39] F.N. Cogswell, Converging flow of polymer melts in extrusion dies, *Polymer Engineering and Science* **12** (1972) 64-73.

[40] M.J. Crochet, A.R. Davies, K. Walters, *Numerical Simulation of Non-Newtonian Flow*, Vol. **1**, Elsevier, (1984).

[41] P.J. Doerpinghaus, D.G. Baird, Pressure Profiles Along an Abrupt 4:1 Planar Contraction, *AIChE Journal* **49** (2003) 2487-2498.

[42] M. Doi, S.F. Edwards, *The Theory of Polymer Dynamics*, Oxford University Press, (1986).

[43] J. Donea, A Taylor-Galerking method for convective transport problems, *International Journal for Numerical Methods in Engineering* **20** (1984) 101-119.

[44] R.E. Evans, K. Walters, Flow characteristics associated with abrupt changes in geometry in the case of highly elastic liquids, *Journal of Non-Newtonian Fluid Mechanics* **20** (1986) 11-29.

[45] R.E. Evans, K. Walters, Further remarks on the lip-vortex mechanism of vortex enhancement in planar-contraction flows, *Journal of Non-Newtonian Fluid Mechanics* **32** (1989) 95-105.

[46] A. G. Fredrickson, A model for the thixotropy of suspensions, *AICHE Journal* **16** (1970) 436-441.

[47] D.M. Hawken, H.R. Tamaddon-Jahromi, P. Townsend, M.F. Webster, A Taylor-Galerkin-based algorithm for viscous incompressible flow, *International Journal for Numerical Methods in Fluids* **10** (1990) 327-351.

[48] M. Herrchen, H.C. Öttinger, A detailed comparison of various FENE dumbbell models, *Journal of Non-Newtonian Fluid Mechanics* **68** (1997) 17-42.

[49] C. Hirsch, *Numerical Computation of Internal and External Flows: Fundamentals of Numerical Discretization*, Vol. **1**, Wiley, (1988).

[50] G. Ianniruberto, G. Marrucci, A multi-mode CCR model for entangled polymers with chain stretch, *Journal of Non-Newtonian Fluid Mechanics* **102** (2002) 283-395.

[51] N.J. Inkson, T.C.B. McLeish, O.G. Harlen, D.J. Groves, Predicting low density polyethylene melt rheology in elongational and shear flows with "pom-pom" constitutive equations, *Journal of Rheology* **43** (1999) 873-896.

[52] D.M. Jones, K. Walters, P.R. Williams, On the extensional viscosity of mobile polymer solutions, *Rheological Acta* **26** (1987) 20-30.

[53] J.v. Kan, A second-order-accurate pressure-correction scheme for viscous incompressible flow, *SIAM Journal on Scientific and Statistical Computing* **7** (1986) 870-891.

[54] R.A. Keiller, Entry-flow calculations for the Oldroyd-B and FENE equations, *Journal of Non-Newtonian Fluid Mechanics* **46** (1993) 143-178.

[55] I.J. Keshtiban, Numerical Simulation of compressible Viscoelastic Flows. In: Computer Science, Vol. Philosophiae Doctor, University of Wales, Swansea, Swansea, U.K., 2004, p. 199.

[56] R.G. Larson, *Constitutive Equations for Polymer Melts and Solutions*, Butterworths, (1988).

[57] K. Lee, M.R. Mackley, T.C.B. McLeish, T.M. Nicholson, O.G. Harlen, Experimental observation and numerical simulation of transient "stress fangs" within flowing molten polyethylene, *Journal of Rheology* **45** (2001) 1261-1277.

[58] C.H. Macosko, *Rheology: Principles, Measurements, and Applications*, John Wiley & Sons, (1994).

[59] J.M. Maia, Theoretical modelling of fluid S1: a comparative study of constitutive models in sample and complex flows, *Journal of Non-Newtonian Fluid Mechanics* **85** (1999) 107-125.

[60] J.M. Maia, D. Binding, Influence of elongational properties on the contraction flow of polyisobutylene in a mixed solvent, *Rheological Acta* **38** (1999) 160-171.

[61] O. Manero, F. Bautista, J.F.A. Soltero, J.E. Puig, Dynamics of worm-like micelles: the Cox-Merz rule, *Journal of Non-Newtonian Fluid Mechanics* **106** (2002) 1-15.

[62] J.M. Marchal, M.J. Crochet, Hermitian finite elements for calculating viscoelastic flow, *Journal of Non-Newtonian Fluid Mechanics* **20** (1986) 187-207.

[63] J.M. Marchal, M.J. Crochet, A new mixed finite element for calculating viscoelastic flow, *Journal of Non-Newtonian Fluid Mechanics* **26** (1987) 77-114.

[64] G. Marrucci, Dynamics of entanglements: A nonlinear model consistent with the Cox-Merz rule, *Journal of Non-Newtonian Fluid Mechanics* **62** (1996) 279-289.

[65] H. Matallah, Numerical Simulation of Viscoelastic Flows. In: Computer Science, Vol. Philosophiae Doctor, University of Wales, Swansea, Swansea, U.K., 1998, p. 193.

[66] H. Matallah, P. Townsend, M.F. Webster, Viscoelastic multi-mode simulations of wire-coating, *Journal of Non-Newtonian Fluid Mechanics* **90** (2000) 217-241.

[67] J.C. Maxwell, On the dynamical theory of gases, *Philosophical Transactions of the Royal Society A* **157** (1867) 49-88.

[68] T.C.B. McLeish, R.G. Larson, Molecular constitutive equations for a class of branched polymers: The pom-pom polymer, *Journal of Rheology* **42** (1998) 81-110.

[69] J.v. Meerveld, Note on the thermodynamic consistency of the integral pom-pom model, *Journal of Non-Newtonian Fluid Mechanics* **108** (2002) 291-299.

[70] E. Mitsoulis, M. Schwetz, H. Münstedt, Entry flow of LDPE melts in a planar contraction, *Journal of Non-Newtonian Fluid Mechanics* **111** (2003) 41-61.

[71] F. Moore, The rheology of ceramic slips and bodies, *Transactions of the British Ceramic Society* **58** (1959), 470-494.

[72] H. Nguyen, D.V. Boger, The kinematics and stability of die entry flows, *Journal of Non-Newtonian Fluid Mechanics* **5** (1979) 353-368.

[73] S. Nigen, K. Walters, Viscoelastic contraction flows: comparison of axisymmetric and planar configurations, *Journal of Non-Newtonian Fluid Mechanics* **102** (2002) 343-359.

[74] P.J. Oliveira, F.T. Pinho, Plane contraction flows of upper convected Maxwell and Phan-Thien-Tanner fluids as predicted by a finite-volume method, *Journal of Non-Newtonian Fluid Mechanics* **88** (1999) 63-88.

[75] R.G.M.v. Os, T.N. Phillips, Efficient and stable spectral element methods for predicting the flow of an XPP fluid past a cylinder, *Journal of Non-Newtonian Fluid Mechanics* **129** (2005) 143-162.

[76] R.G.M.v. Os, T.N. Phillips, The prediction of complex flows of polymer melts using spectral elements, *Journal of Non-Newtonian Fluid Mechanics* **122** (2004) 287-301.

[77] R.G. Owens, T.N. Phillips, *Computational Rheology*, Imperial College Press, London, (2002).

[78] M.G.N. Perera, K. Walters, Long range memory effects in flows involving abrupt changes in geometry Part 2: the expansion/contraction/expansion problem, *Journal of Non-Newtonian Fluid Mechanics* **2** (1977) 191-204.

[79] P.M. Phillips, The Characterisation of Some Non-Newtonian Fluids and Experimental Measurements and Observations in a Contraction Expansion Geometry. In, University of Wales, Aberystwyth, 2005, p. 33.

[80] T.N. Phillips, A.J. Williams, Comparison of creeping and inertial flow of an Oldroyd B fluid through planar and axisymmetric contractions, *Journal of Non-Newtonian Fluid Mechanics* **108** (2002) 25-47.

[81] T.N. Phillips, A.J. Williams, Conservative Semi-Lagrangian Finite Volume Schemes, *Numerical Methods for Partial Differential Equations* **17** (2001) 403-425.

[82] T.N. Phillips, A.J. Williams, Viscoelastic flow through a planar contraction using a semi-Lagrangian finite volume method, *Journal of Non-Newtonian Fluid Mechanics* **87** (1999) 215-246.

[83] B. Purnode, M.J. Crochet, Flows of polymer solutions through contractions Part 1: flows of polyacrylamide solutions through planar contractions, *Journal of Non-Newtonian Fluid Mechanics* **65** (1996) 269-289.

[84] W.P. Raiford, L.M. Quinzani, P.J. Coates, R.C. Armstrong, R.A. Brown, LDV measurements of viscoelastic flow transitions in abrupt axisymmetric contractions: Interaction of inertia and elasticity, *Journal of Non-Newtonian Fluid Mechanics* **32** (1989) 39-68.

[85] J.P. Rothstein, G.H. McKinley, The axisymmetric contraction-expansion: the role of extensional rheology on vortex growth dynamics and the enhanced pressure drop, *Journal of Non-Newtonian Fluid Mechanics* **98** (2001) 33-63.

[86] J.P. Rothstein, G.H. McKinley, Extensional flow of a polystyrene Boger fluid through a 4:1:4 axisymmetric contraction/expansion, *Journal of Non-Newtonian Fluid Mechanics* **86** (1999) 61-88.

[87] I. Sirakov, A. Ainser, M. Haouche, J. Guillet, Three-dimensional numercal simulation of viscoelastic contraction flows using the Pom-Pom differential constitutive model, *Journal of Non-Newtonian Fluid Mechanics* **126** (2005) 163-173.

[88] R. Sizaire, *keyFE2 User Manual*, (2004).

[89] M. Spiegel, A.A. Rapun, *Fórmulas y Tablas de Matemática Aplicada*, McGraw-Hill, (1992).

[90] P. Szabo, J.M. Rallison, E.J. Hinch, Start-up of flow of a FENE-fluid through a 4:1:4 constriction in a tube, *Journal of Non-Newtonian Fluid Mechanics* **72** (1997) 73-86.

[91] R.I. Tanner, *Engineering Rheology*, Oxford University Press, (2000).

[92] R.I. Tanner, S. Nasseri, Simple constitutive models for linear and branched polymers, *Journal of Non-Newtonian Fluid Mechanics* **116** (2003) 1-17.

[93] R. Temam, *Theory and Numerical Analysis of the Navier-Stokes equations*, North-Holland, (1977).

[94] P. Townsend, M.F. Webster, An algorithm for the three-dimensional transient simulation of non-Newtonian fluid flows. In: NUMETA 87, Vol. 2:T12/1, Martinus Nijhoff, Dordrecht, 1987.

[95] B. Tremblay, Visualization of the flow of linear low density polyethylene/low density polyethylene blends through sudden contractions, *Journal of Non-Newtonian Fluid Mechanics* **43** (1992) 1-29.

[96] W.M.H. Verbeeten, G.W.M. Peters, F.P.T. Baaijens, Differential constitutive equations for polymer melts: The extended Pom-Pom model, *Journal of Rheology* **45** (2001) 823-843.

[97] W.M.H. Verbeeten, G.W.M. Peters, F.P.T. Baaijens, Erratum: "Differential consitutive equations for polymer melts: The extended Pom-Pom model" [J. Rheol. 45, 823-843 (2001)], *Journal of Rheology* **45** (2001) 1489.

[98] W.M.H. Verbeeten, G.W.M. Peters, F.P.T. Baaijens, Numerical simulations of the planar contraction flow for a polyethylene melt using the XPP model, *Journal of Non-Newtonian Fluid Mechanics* **117** (2004) 73-84.

[99] W.M.H. Verbeeten, G.W.M. Peters, F.P.T. Baaijens, Viscoelastic analysis of complex polymer melt flow using the eXtended Pom-Pom model, *Journal of Non-Newtonian Fluid Mechanics* **108** (2002) 301-326.

[100] K. Walters, A Note on the Rectilinear Flow of Elastico-Viscous Liquies through Straight Pipes of Circular Cross-Section, *Archive for Rational Mechanics and Analysis* **9** (1962) 411_414.

[101] K. Walters, M.F. Webster, The distinctive CFD challenges of computational rheology, *International Journal for Numerical Methods in Fluids* **43** (2003) 577-596.

[102] P. Wapperom, R. Keunings, Numerical simulation of branched polymer melts in transient complex flow using pom-pom models, *Journal of Non-Newtonian Fluid Mechanics* **97** (2001) 267-281.

[103] P. Wapperom, R. Keunings, G. Ianniruberto, Prediction of rheometrical and complex flows of entangled linear polymers using the double-convection-reptation model with chain stretch, *Journal of Rheology* **47** (2003) 247-265.

[104] N.D. Waters, M.J. King, Unsteady flow of an elastico-viscous liquid, *Rheological Acta* **9** (1970) 345-355.

[105] M.F. Webster, H.R. Tamaddon-Jahromi, M. Aboubacar, Time-Dependent Algorithms for Viscoelastic Flow: Finite Element/Volume Schemes, *Numerical Methods for Partial Differential Equations* **21** (2005) 272-296.

[106] S.A. White, D.G. Baird, Flow visualization and birefringence studies on planar entry flow behaviour of polymer melts, *Journal of Non-Newtonian Fluid Mechanics* **29** (1988) 245-267.

[107] S.A. White, D.G. Baird, The importance of extensional flow properties on planar entry flow patterns of polymer melts, *Journal of Non-Newtonian Fluid Mechanics* **20** (1986) 93-101.

[108] S.-C. Xue, N. Phan-Thien, R.I. Tanner, Three dimensional numerical simulations of viscoelastic flows through planar contraction, *Journal of Non-Newtonian Fluid Mechanics* **74** (1998) 195-245.

[109] J.Y. Yoo, Y. Na, A numerical study of the planar contraction flow of a viscoelastic fluid using the SIMPLER algorithm, *Journal of Non-Newtonian Fluid Mechanics* **39** (1991) 89-106.

[110] M. Zatloukal, Differential viscoelastic constitutive equations for polymer melts in steady shear and elongational flows, *Journal of Non-Newtonian Fluid Mechanics* **113** (2003) 209-227.

[111] O.C. Zienkiewicz, K. Morgan, *Finite elements and approximation*, Wiley, New York, (1983).

[112] M.A. Zirnsak, D.V. Boger, Axisymmetric entry flow of semi-dilute xanthan gum solutions: prediction and experiment, *Journal of Non-Newtonian Fluid Mechanics* **79** (1998) 105-136.